# MICROPLASTIC AGING: MECHANISMS, QUANTIFICATION, AND APPLICATIONS FROM LABORATORY STUDIES TO ENVIRONMENTAL SAMPLES

**YINGSHU LENG**

Thesis submitted to the University of Ottawa
in partial fulfillment of the requirements for the degree of
**Doctor of Philosophy degree in Biomedical Engineering**

uOttawa

Faculté de génie
Faculty of Engineering

Department of Chemical and Biological Engineering
University of Ottawa

# ABSTRACT

Microplastics (MPs) released into the environment rarely remain in the same state as the pristine materials used in many laboratory studies. After exposure to chemical, physical, and biological aging, they can undergo a range of physical and chemical transformations that alter their material properties. These transformations are important because they influence how MPs persist, fragment, interact with surrounding materials, and bring analytical challenges in characterizing them in matrices. A clearer understanding of MP aging is needed to interpret their environmental behaviour, evaluate their potential biological relevance, and improve methods for measuring aged particles in realistic matrices.

The measurement challenge is particularly important in environmental samples such as biosolids and soil, where MPs are often present at low concentrations, altered by aging-induced property changes, and are embedded within complex matrices. To address these challenges, a mass-based quantification method for MPs was developed and validated using a tiered analytical approach centered on modulated differential scanning calorimetry (MDSC). Calibration models for polyethylene (PE), polypropylene (PP), polyamide 6 (PA6), and polyethylene terephthalate (PET) exhibited strong linearity, high sensitivity, low limit of quantification (LOQ), and high recovery in biosolids matrices. This tiered workflow, incorporating MDSC, Raman spectroscopy, and thermogravimetric analysis (TGA), was applied to real wastewater biosolid samples, enabling mass-based quantification of multiple polymer types and demonstrating that the method can reliably measure MP burdens in complex environmental samples.

Recognizing that aging-induced transformations represent a major source of uncertainty in microplastic quantification in biosolids, an investigation of characterization of microplastic aging under controlled conditions was therefore conducted. The thermal-oxidative aging of polystyrene

(PS) resulted in surface oxidation, spectral changes consistent with ring-opening reactions, chain scission, and particle fragmentation, showing that laboratory aging can drive both chemical alteration and physical breakdown of PS particles. Building upon the findings, the work was expanded to ultraviolet C (UVC)-induced aging of PE, PP, and PET, which showed that PP was more responsive to UVC exposure than PE and PET. Thus, additional focus was placed on PP materials from different product sources and particle sizes. The characterization results demonstrate that smaller particles generally exhibited greater thermal and chemical changes, and polymer formulation modulates the depth of surface oxidation and crack propagation. Transparent PP particles exhibited more extensive surface cracking than pigmented microplastics, indicating the role of additives in mitigating UV-induced degradation. These differences suggest that material source can influence the apparent aging response of MPs, which should be considered when comparing laboratory-aged particles with environmental or consumer-derived plastics.

Rather than relying on a single aging descriptor, these variables were integrated using a principal component analysis (PCA)-based aging score to integrate structural, thermal, chemical, and spectroscopic descriptors to capture the evolution of microplastics from three aged plastics. The Shapley additive explanations (SHAP) approach was then used to examine which measured properties contributed most strongly to the aging score. By combining these descriptors, the aging score captured coordinated changes in surface oxidation, crystallinity, melting behaviour, and particle size that would be difficult to interpret using a single indicator alone. It shows the feasibility of comparing aging extent across the polymer types and laboratories.

To evaluate the biological relevance of these aging-induced changes, aged PS, PE, PP, and PET produced under similar laboratory conditions were tested using simplified in vitro assays. Cell viability, reactive oxygen species (ROS) generation, and membrane integrity were used as

endpoints. Aging-dependent differences were observed in cell viability and ROS responses, with PS showing the clearest differences between pristine and aged particles across the tested cell models. ROS responses for PE, PP, and PET were more cell-type dependent, with aging-related differences observed only in A549 cells. However, no differences in lactate dehydrogenase (LDH) release were observed for PS, suggesting that the measured responses were not associated with measurable membrane damage.

Overall, this work shows that MP aging is a coupled physical and chemical process that affects both environmental interpretation and analytical measurement. It develops mechanistic, quantitative, and analytical foundations for the study of microplastic aging and delivers a validated mass-based approach for measuring microplastic abundance in real environmental matrices.

## COPYRIGHT STATEMENT

All materials in this thesis that have previously been published in journals allow their use in graduate theses. Full references for the original publication are provided where required.

## DATA AVAILABILITY STATEMENT

The data supporting the findings of this thesis are included in the main chapters and supplementary information associated with the published manuscripts where applicable. Additional raw and analyzed datasets are available from the author upon reasonable request.

## STATEMENT OF CONTRIBUTIONS OF COLLABORATORS

I hereby declare that I am the sole author of this thesis. I designed the methodologies of the project and performed all the experiments and data analysis. The scientific guidance and editorial comments for the written work were provided by my supervisors, Dr. Xudong Cao and Dr. Shan Zou. Other academic discussions and comments that contributed to related publications are acknowledged through co-authorship in the corresponding journal papers.

# ACKNOWLEDGEMENTS

I would like to express my sincere and deepest gratitude to my supervisors, Dr. Xudong Cao and Dr. Shan Zou. I am truly grateful for the opportunity to pursue my doctoral research at the University of Ottawa (uOttawa) and the National Research Council Canada (NRC) under their supervision. Throughout my PhD journey, they provided continuous academic mentorship, patience, understanding, and generous financial support. When I encountered difficulties or felt uncertain about my direction, they were always willing to discuss problems with me and help me find a way forward. Without their support, it would not have been possible for me to complete this work.

I would also like to acknowledge the uOttawa for providing full tuition scholarships, which allowed me to focus on my research during my PhD studies. Also, I appreciate the financial support of the Ocean Program at the NRC and the Advancing a Circular Plastics Economy for Canada Program from the Government of Canada.

I sincerely thank the faculty members at uOttawa and the researchers and staff at the NRC for their technical support, instrument training, and access to research facilities. I am particularly grateful to Dr. Maohui Chen, Dr. Daniel Prezgot, Dr. Zygmunt J. Jakubek, Dr. Gregory Lopinski, Liliana Gaburici, and Brian Coleman for their invaluable assistance, insightful discussions, and constructive suggestions throughout my experimental work. I also thank all members of the Metrology Nanoscale Measurement team and Dr. Cao's lab for their help and support.

I would like to extend my thanks to my colleagues and friends, Xiaotan Zhu, Mike Deng, and Francesca Grilli, for their advice, help, and friendship throughout my PhD. I truly appreciated the many conversations and shared experiences we had.

Finally, I am deeply grateful to my family and friends. Even though we are far apart, your unconditional love, support, and encouragement have always been there. They have meant more to me than I can easily express. I would also like to thank my dog, Nova, for the quiet companionship during my long hours of writing and for the comfort she brought to everyday life throughout this journey.

This work is dedicated to everyone I love and who has loved and supported me along the way.

# TABLE OF CONTENTS

# LIST OF TABLES

# LIST OF FIGURES

# LIST OF ABBREVIATIONS AND ACRONYMS

| | |
|---|---|
| ABS | acrylonitrile butadiene styrene |
| AFM | atomic force microscopy |
| ANOVA | analysis of variance |
| AOPs | advanced oxidation processes |
| APS500 | 500 nm polystyrene dispersion after autoclave |
| APS500-S | polystyrene dispersion after autoclave and sonication |
| APS500-SP | permeate dispersion from separation after autoclave and sonication |
| APS500-SR | retentate dispersion from separation after autoclave and sonication |
| arPLS | asymmetrically reweighted penalized least squares |
| AS | artificial soil |
| ATR-FTIR | attenuated total reflectance Fourier transform infrared spectroscopy |
| CCK-8 | cell counting kit 8 assay |
| CI | carbonyl index |
| CMP | commercial microplastic powders |
| dBB | digested blank biosolids |
| DCFDA | 2′,7′-dichlorofluorescein diacetate |
| DLS | dynamic light scattering |
| DMEM | Dulbecco's Modified Eagle Medium |
| DSC | differential scanning calorimetry |
| DTG | derived thermogravimetry |
| DV | diafiltration volume |
| FPA | focal plane array |
| FTIR | Fourier transform infrared spectroscopy |
| HDPE | high-density polyethylene |
| LDH | lactate dehydrogenase |
| LDPE | low-density polyethylene |
| LOQ | limit of quantification |
| MAE | mean absolute error |
| MDSC | modulated differential scanning calorimetry |

| | |
|---|---|
| MPs | microplastics |
| NPs | nanoplastics |
| O/C | oxygen-to-carbon ratio |
| OECD | Organization for Economic Co-operation and Development |
| OM | organic matter |
| PA | polyamide |
| PBAT | poly(butylene adipate-co-terephthalate) |
| PBS | phosphate-buffered saline |
| PC | polycarbonate |
| PCA | principal component analysis |
| PDI | polydispersity index |
| PE | polyethylene |
| PET | polyethylene terephthalate |
| PLA | polylactic acid |
| PMMA | polymethyl methacrylate |
| PMP | product-derived microplastics |
| PP | polypropylene |
| PPCT | polypropylene centrifuge tubes |
| PPPB | polypropylene pipette boxes |
| PS | polystyrene |
| PS500 | pristine 500 nm polystyrene |
| PTFE | polytetrafluoroethylene |
| PU | polyurethane |
| PVA | polyvinyl alcohol |
| PVC | polyvinyl chloride |
| Py-GC/MS | pyrolysis-gas chromatography-mass spectrometry |
| Py-TD-GC/MS | pyrolysis-thermal desorption-gas chromatography/mass spectrometry |
| rBB | raw blank biosolid |
| ROS | reactive oxygen species |
| SD | standard deviation |
| SE | standard error |

| | |
|---|---|
| SEM | scanning electron microscopy |
| SHAP | Shapley additive explanations |
| $T_d$ | decomposition temperature |
| TED-GC-MS | thermal extraction desorption-gas chromatography-mass spectrometry |
| TFF | tangential flow filtration |
| TG | thermogravimetric |
| TGA | thermogravimetric analysis |
| $T_m$ | melting temperature |
| TPU | thermoplastic polyurethane |
| UV | ultraviolet |
| UVA | ultraviolet A |
| UVB | ultraviolet B |
| UVC | ultraviolet C |
| UV-Vis | ultraviolet-visible spectroscopy |
| WWTPs | wastewater treatment plants |
| XRD | X-ray diffraction |
| ZP | zeta potential |
| $\chi_c$ | crystallinity |
| $\chi_s I$ | surface crystallinity index |

# CHAPTER 1 INTRODUCTION

## 1.1 Motivation

Plastics are widely produced and used in many applications because of their lightweight, durability, and cost-effectiveness [1, 2]. Global plastic production has increased from approximately 1.5 million tons in 1950 to about 430.9 million tons in 2024 [3]. Once released into the environment, plastics undergo continuous physical, chemical, and biological degradation, leading to fragmentation into progressively smaller particles. These fragments, commonly referred to as microplastics (MPs) when smaller than 5 mm, are recognized as persistent contaminants [4]. Current estimates indicate that 10–40 million tonnes of MPs are released to the environment each year under present production and consumption trends, showing the pervasive release of plastic particles and their growing potential for widespread environmental exposure and risks to human health [5, 6]. MPs have been detected in nearly all environmental compartments, including surface waters, soils, sediments, and even remote regions [7-9]. In addition, due to their small size and persistence, MPs exhibit high mobility and reactivity, raising concerns about their environmental fate and potential exposure risks [8].

A defining characteristic of environmental MPs is that they do not remain pristine. Environmental aging of MPs occurs through processes such as ultraviolet (UV) exposure, oxidation, and mechanical abrasion, which alter particle size, surface chemistry, interior structure, and morphology. These physicochemical transformations subsequently influence aggregation behavior, sorption of co-contaminants, and environmental mobility [8]. These aging-induced transformations further complicate the extraction, identification, and quantification of MPs in complex matrices. Additionally, these aging-induced changes are expected to affect MPs and cell interactions, as surface and structural modifications govern how particles interact with cells

following human exposure. Nevertheless, most laboratory studies continue to rely on pristine particles, which limits the environmental relevance. Moreover, aging is often described qualitatively, and systematic or quantitative characterization of aging severity remains limited, making it difficult to compare results across studies and to link physicochemical transformations to environmental behaviour.

The importance of understanding the MPs' aging becomes particularly evident in the context of wastewater treatment and biosolids. During wastewater treatment, a large fraction of influent MPs is retained in sewage sludge, making biosolids an important sink for MPs, as evidenced by several field studies. Subsequent land application of biosolids, therefore, represents a key pathway for transferring microplastics into terrestrial environments [10, 11]. However, characterizing MPs in biosolids remains challenging due to the complex matrix, high organic content, and the presence of interfering components such as humic substances, residual biopolymers, and mineral particles that hinder effective separation and identification, particularly for small and low-abundance particles. As a result, reliable quantification of microplastics in biosolids is essential but remains technically challenging. Particle-counting approaches are widely used but are highly sensitive to size cutoffs, operator bias, and analytical resolution, and they do not necessarily reflect the true plastic abundance [12]. Mass-based quantification approaches provide a more representative metric of environmental exposure, but they require polymer-specific signals that can be separated from matrix background and from overlapping polymer responses [13, 14]. Thus, improving the reliability of mass-based quantification is important for measuring MPs in biosolids and for establishing more realistic baselines for environmental exposure and fate.

Based on this motivation, the thesis first addresses the analytical challenges of quantifying MPs in biosolids matrices. It then uses controlled accelerated aging as an experimental approach to

generate aged microplastic samples with measurable and comparable physicochemical changes, which are subsequently used to develop a quantitative framework for comparing aging across different plastics.

## 1.2 Research Objectives

Despite increasing attention to microplastic pollution, important knowledge gaps remain regarding how microplastics transform during environmental aging and how these transformations affect their detection and quantification in real-world matrices. These limitations hinder accurate interpretation of microplastic occurrence, behavior, and environmental impact under relevant conditions.

The overall objective of this thesis is to investigate microplastic aging and its implications for environmental characterization through an integrated experimental framework. Where relevant, exploratory cellular assays were also used to provide complementary context on how aging effects may modulate early biological responses. Specifically, the research aims to:

- develop and apply a highly sensitive mass-based approach to identify and quantify trace amounts of microplastics in complex biosolid matrices, addressing the analytical challenges posed by aged particles.
- obtain aged microplastic samples with distinguishable physicochemical properties by using controlled laboratory aging treatments.
- characterize aging-induced physicochemical changes in the laboratory-aged microplastics and establish a unified quantitative basis for comparing relative aging levels across polymers, particle sizes, and material sources.

- provide complementary biological context through exploratory *in vitro* assays to examine whether aging affects cellular responses.

## 1.3 Thesis Organization

**Chapter 1** provides the introduction, outlining the widespread use and environmental persistence of plastics, the emergence of microplastics (MPs) as contaminants, and the importance of aging in influencing their physicochemical properties, environmental fate, and biological interactions. This chapter also highlights the role of biosolids as major sinks for MPs and the analytical challenges of detecting and quantifying aged microplastics in complex matrices. The chapter concludes with the research objectives and the overall rationale for the thesis.

**Chapter 2** builds on this introduction by reviewing current knowledge of microplastic aging mechanisms and the analytical challenges associated with quantifying them in complex environmental matrices. Particular emphasis is placed on aging characterization, environmentally relevant aging processes (e.g., weathering, oxidation, biofouling, and matrix interactions), and documented difficulties in accurately measuring MPs in biosolids and other environmental samples.

**Chapter 3** presents a study that focuses on the development and application of a mass-based analytical approach to quantify microplastics in biosolid matrices using modulated differential scanning calorimetry (MDSC). This chapter addresses challenges associated with complex matrices and low plastic mass fractions, demonstrating the applicability of the method to real environmental samples. This chapter addresses a critical analytical gap and establishes the environmental relevance of subsequent polymer aging studies. This chapter is based on a peer-reviewed publication, "*Quantification of microplastics in complex environmental matrices using*

*a tiered approach with modulated differential scanning calorimetry (MDSC)*", published in the *Analytical and Bioanalytical Chemistry* in November 2025. DOI: 10.1007/s00216-025-06212-4.

**Chapter 4** investigates the thermal-oxidative aging behaviour of polystyrene (PS) microplastics. This chapter focuses on the physicochemical transformations induced by thermal-oxidative aging, including changes in morphology, particle size distribution, and chemical structure. The results provide evidence of chemical structure and morphological changes of PS microplastics and establish a foundation for subsequent aging studies. This chapter is based on a peer-reviewed publication, "*Laboratory simulated aging of polystyrene particles and characterization of the resulting nanoscale plastics*", in the *Journal of Environmental Chemical Engineering* in October 2023. DOI: 10.1016/j.jece.2023.110967.

**Chapter 5** examines ultraviolet (UV)-induced aging of multiple polymers, including polyethylene (PE), polypropylene (PP), and polyethylene terephthalate (PET), as well as PP materials from different product sources. This chapter uses UVC aging as a controlled approach to obtain aged samples with measurable physicochemical changes for comparison across polymer types and material origins and introduces a quantitative framework for assessing aging levels. This work is based on a peer-reviewed publication, "*Quantifying UVC-Induced Aging of Microplastics Using a Multivariate Aging Score*", in the *Journal of Polymers and the Environment* in March 2026. DOI: 10.1007/s10924-026-03796-5.

**Chapter 6** provides a concluding overview, summarizing the main findings and contributions of each research chapter and outlining directions for future research in microplastic aging and quantification. An appendix includes selected toxicity assays to support the environmental relevance of the study without disrupting the core focus on aging and quantification.

**Appendix A** and **Appendix C** provide supporting information for Chapters 3 and 5, respectively, including additional methodological details and supplementary data that complement the main analyses. **Appendix B** presents exploratory *in vitro* toxicity assays conducted to examine potential cellular responses associated with microplastic aging. While these cellular results provide useful contextual insight, they are included in the Appendix because they serve a complementary role to the primary focus of the thesis on aging mechanisms and analytical quantification in environmental matrices.

## References


1. Thompson RC, Swan SH, Moore CJ, vom Saal FS. Our plastic age. Philos Trans R Soc B: Biol Sci. 2009;364(1526):1973-6.
2. Crawford RJ, Martin P. Plastics engineering. 4th ed: Butterworth-Heinemann; 2020.
3. PlasticsEurope. Plastics the Fast Facts 2025. 2025.
4. Cole M, Lindeque P, Halsband C, Galloway TS. Microplastics as contaminants in the marine environment: a review. Mar Pollut Bull. 2011;62(12):2588-97.
5. Ferreira I, Venâncio C, Lopes I, Oliveira M. Nanoplastics and marine organisms: what has been studied? Environ Toxicol Pharmacol. 2019;67:1-7.
6. Thompson RC, Courtene-Jones W, Boucher J, Pahl S, Raubenheimer K, Koelmans AA. Twenty years of microplastic pollution research—what have we learned? Science. 2024;386(6720):eadl2746.
7. Geyer R, Jambeck JR, Law KL. Production, use, and fate of all plastics ever made. Sci Adv. 2017;3(7):e1700782.
8. Andrady AL. Microplastics in the marine environment. Mar Pollut Bull. 2011;62(8):1596-605.
9. Horton AA, Walton A, Spurgeon DJ, Lahive E, Svendsen C. Microplastics in freshwater and terrestrial environments: Evaluating the current understanding to identify the knowledge gaps and future research priorities. Sci Total Environ. 2017;586:127-41.

10. Nizzetto L, Futter M, Langaas S. Are Agricultural Soils Dumps for Microplastics of Urban Origin? Environ Sci Technol. 2016;50(20):10777-9.

11. Corradini F, Meza P, Eguiluz R, Casado F, Huerta-Lwanga E, Geissen V. Evidence of microplastic accumulation in agricultural soils from sewage sludge disposal. Sci Total Environ. 2019;671:411-20.

12. Cowger W, Gray A, Christiansen SH, DeFrond H, Deshpande AD, Hemabessiere L, et al. Critical Review of Processing and Classification Techniques for Images and Spectra in Microplastic Research. Appl Spectrosc. 2020;74(9):989-1010.

13. Simon M, van Alst N, Vollertsen J. Quantification of microplastic mass and removal rates at wastewater treatment plants applying Focal Plane Array (FPA)-based Fourier Transform Infrared (FT-IR) imaging. Water Res. 2018;142:1-9.

14. Rocha-Santos T, Duarte AC. A critical overview of the analytical approaches to the occurrence, the fate and the behavior of microplastics in the environment. TrAC, Trends Anal Chem. 2015;65:47-53.

# CHAPTER 2 LITERATURE REVIEW: MICROPLASTIC AGING AND ANALYTICAL CHALLENGES IN ENVIRONMENTAL MATRICES

This chapter reviews the aging of microplastics, with emphasis on environmentally aged particles and the analytical challenges associated with their characterization and quantification, particularly in complex matrices such as biosolids. Rather than attempting a comprehensive survey of the rapidly expanding literature, the discussion focuses on studies that have advanced understanding of aging-induced changes in physicochemical properties or have exposed limitations in existing analytical and quantitative methodologies. The literature discussed is intentionally limited to studies that investigate environmentally relevant aging processes (e.g., weathering, oxidation, biofouling, and matrix interactions) and that report implications for particle properties, detectability, or quantitative accuracy in complex matrices. Earlier foundational studies are cited selectively where they establish key concepts or analytical frameworks. Review articles are included to effectively contextualize broader trends, while selected primary studies are discussed to illustrate representative aging behaviours, matrix-driven complications, and persistent knowledge gaps. Collectively, these unresolved challenges provide the rationale and motivation for the research presented in this thesis.

## 2.1 Aging of Microplastics

### 2.1.1 Aging Processes in Natural and Simulated Environments

Microplastic aging refers to the progressive physicochemical transformations that plastic particles undergo after release into the environment. As shown in Figure 2.1, in natural environments, these transformations are driven by the combined action of multiple environmental stressors, including

photochemical radiation, thermal processes, biological activity, and mechanical breakage [1]. From a mechanistic perspective, environmental aging of microplastics is fundamentally governed by multiple energy sources operating concurrently in natural systems. Solar radiation, particularly ultraviolet (UV) light, represents the dominant energy source driving photo-oxidative degradation, initiating polymer chain scission and the formation of oxygen-containing functional groups that originate from the surface, and is widely recognized as the primary trigger for environmental plastic aging in both aquatic and terrestrial environments [1, 2]. Thermal energy associated with seasonal temperature variations further modulates aging kinetics by accelerating diffusion, oxidation reactions, and molecular rearrangement within polymer matrices, thereby influencing the rate and extent of structural transformation [3, 4]. In addition, mechanical energy arising from hydrodynamic forces, sediment transport, and particle-particle or particle-substrate abrasion contributes to physical fragmentation and size reduction, often acting synergistically with photochemical and oxidative processes [5]. These energy inputs act over long timescales and under variable conditions, driving complex, coupled aging pathways that shape the physicochemical alteration of microplastics in real environmental settings, making it difficult to disentangle the relative contributions of individual mechanisms. Laboratory accelerated aging is therefore commonly used to isolate selected processes, such as photo-oxidation, thermal oxidation, chemical oxidation, or mechanical abrasion, and to generate MPs with measurable changes within experimentally feasible timescales [6]. However, laboratory-aged microplastics should be interpreted as defined reference conditions rather than direct equivalents of a specific environmental exposure duration, because natural aging depends on radiation spectrum, oxygen availability, moisture, temperature, matrix contact, biological colonization, and mechanical stress [7]. As one of the most frequently used aging approaches in the literature, UV-based aging is useful

for examining photo-oxidative susceptibility, but the degradation pathway and rate are strongly dependent on exposure conditions, including wavelength, irradiance, temperature, oxygen availability, and humidity [8-10]. Polymer composition and additives can further modify UV-aging behaviour, meaning that product-derived plastics may not respond in the same way as pure polymer references [1, 11, 12]. As a result, laboratory UV exposure can generate particles with measurable aging-induced property changes, but it cannot assign an exposure time or produce the full complexity of natural aging. Studies on polypropylene further show that fragmentation may require both photooxidation and subsequent mechanical stress, indicating that UV exposure alone does not necessarily reproduce all stages of environmental particle breakdown [11]. Sunlight-based field study also show that photochemical aging can produce outcomes that are not captured by simple accelerated-dose assumptions [13].

For this reason, controlled accelerated aging and environmental aging are therefore best viewed as related, but not equivalent. Field-aged microplastics reflect the cumulative effects of variable environmental stressors, but their aging states are uncontrolled and often have unknown histories of weathering. As a result, they may show spatially heterogeneous surface oxidation, altered morphology, and changes in structural properties, which make it difficult to isolate the contribution of each aging mechanism. In contrast, laboratory-aged samples are produced under known polymer, size, and exposure conditions, allowing selected mechanisms to be linked to measurable changes, and provide reproducible materials for isolating selected aging conditions. While laboratory aging offers clear advantages in terms of experimental control and reproducibility, the environmental translation requires recognition of the differences, as natural aging histories are often far more complex than those reproduced in the laboratory.

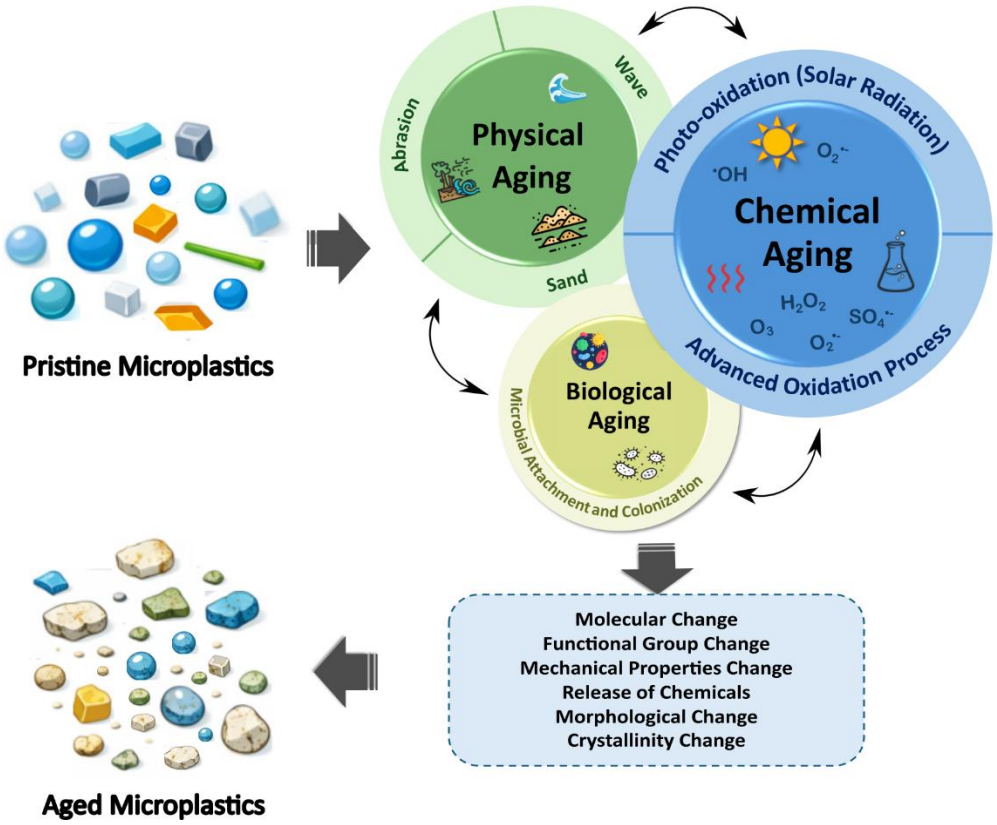


**Figure 2.1 Schematic illustration of the major degradation pathways and associated property changes of plastics during environmental aging.** Pristine microplastics are subjected to chemical, physical, and biological aging processes under environmental conditions, leading to alterations in their physicochemical properties and ultimately forming aged microplastics. Adapted from ref. [14].

### 2.1.2 Aging-Induced Property Changes

Compared with pristine microplastics, environmentally aged microplastics exhibit pronounced changes in their physicochemical properties due to prolonged exposure to natural aging processes. These changes manifest across multiple dimensions, reflecting the inherent heterogeneity of microplastics in terms of morphology, polymer composition, and degradation state [1, 2]. In environmental matrices, microplastics occur as irregular fragments, fibres, pellets, and films, each

of which may age through distinct combinations of light exposure, mechanical abrasion, and chemical oxidation, posing significant challenges for property analysis [15].

#### *2.1.2.1 Physical Characteristics*

Physical characteristics of microplastics describe the changes in surface appearance, morphology, and mechanical integrity induced by environmental aging. Field-collected microplastics from marine, coastal, and terrestrial environments consistently exhibit surface roughening, cracking, pitting, and erosion features that are absent in pristine microplastics [16-18]. These indicators capture how aging occurs at the plastic surface and morphology level changes, providing evidence of degradation progression.

Morphological changes in microplastics are most commonly characterized using electron microscopy, which allows direct observation of aging-induced surface cracking and heterogeneous erosion patterns across a range of polymers, including polyolefins recovered from beach sediments and coastal water [19-21]. As aging progresses, cracks on microplastic surfaces become increasingly rough, extend into subsurface layers, and are accompanied by a loss of mechanical integrity, making particles more susceptible to embrittlement and fragmentation. A study examining naturally aged PP films collected from beaches further linked surface oxidation to mechanical weakening, showing that increased chemical degradation coincides with enhanced fragmentation and the generation of smaller secondary particles [19]. This study established surface cracking as a key morphological indicator of physical aging in microplastics. Similar patterns in size distribution changes from the generation of secondary micro- and nanoplastics through fragmentation have also been observed in environmentally aged microplastics [20]. Such

changes in size distribution complicate the analysis by shifting microplastics toward smaller, less detectable size fractions.

Along with these morphological changes, visible colour transformation is frequently observed during microplastic aging. Several studies have proposed the yellowness index as a quantitative proxy for microplastic discoloration and degradation state [21, 22], and have further demonstrated that the degree of yellowing measured on PE pellets collected from beaches increases proportionally with the extent of environmental degradation [21]. This discoloration is generally attributed to the formation of chromophoric oxidation products and/or the oxidative degradation of phenolic antioxidants initially incorporated into the polymer matrix. It is often considered an indirect indicator of coupled physical and chemical aging processes [23].

However, physical aging characteristics primarily describe the occurrence of aging. Similar morphological features may arise from distinct aging pathways or exposure histories, and physical changes often evolve non-monotonically. Consequently, physical descriptors alone are insufficient for comparing aging severity across polymers or environments.

*2.1.2.2 Structural and Thermal Properties*

While physical characteristics primarily reveal the presence of aging on the particle surface, structural and thermal properties capture internal polymer transformations at different but closely related levels. Structural characteristics refer to changes in polymer chain organization, crystallinity, and phase structure. In contrast, thermal characteristics describe how the internal changes manifest in thermal responses, such as melting behaviour and thermal stability [6].

Environmental aging studies increasingly demonstrate that natural weathering affects not only the exterior of microplastics but also their bulk structure. A commonly proposed mechanism is that aging-driven oxidation and chain scission often occur first in amorphous regions, increasing chain mobility and enabling chemical crystallization. As a result, crystallinity may increase during early or moderate photo-oxidative aging in polyolefins [24]. However, structural change is not unidirectional. Under prolonged or more aggressive thermal aging, chain scission and morphological relaxation may compete with recrystallization, leading to decreases in crystallinity when degradation dominates over ordering [25]. This competing process is supported by evidence from long-term aging studies of PE and PP samples collected from landfill waste at different depths and over different years of storage, which show crystallinity shifts consistent with their degradation histories and environmental conditions rather than a single universal trend [26].

In parallel with structural rearrangements, aging also alters thermal characteristics, such as melting temperature and decomposition stability, providing an additional probe of bulk polymer transformation. Changes in melting temperatures and thermal stability have been reported for environmentally aged microplastics, indicating that aging influences bulk thermal performance rather than being limited to surface effects [15, 27]. For instance, De Monte et al. investigated commercial high-density polyethylene (HDPE) and PP materials exposed in situ to marine and beach conditions for 6 months. They observed measurable changes in decomposition stability and crystallinity, as accompanied by a subtle decrease in melting temperature relative to unexposed references [27]. Similarly, Maddison et al. reported that long-term natural marine aging led to measurable alterations in the thermal stability of multiple polymer types, which was attributed to bulk-phase degradation [15]. These thermal responses are mechanistically consistent with degradation-induced increases in crystal defects and structural heterogeneity. Chain scission

shortens the average chain length and broadens the distribution of crystallite populations, leading to shifts and broadening of the melting transition measured during thermal analysis [6, 28].

Overall, the changes in structural and thermal properties, such as melting temperature and crystallinity, reflect bulk polymer responses to aging, governed by competing degradation and reorganization pathways that vary across materials and aging histories [6, 26]. Consequently, changes in melting temperature or crystallinity should be interpreted with caution and, on their own, are insufficient to fully characterize the extent of microplastic aging.

*2.1.2.3 Chemical Characteristics*

Chemical characteristics of microplastics describe elemental changes in polymer composition, functional groups, and degradation products, which directly reflect oxidation reactions and molecular-level transformations occurring during aging [6, 29]. Compared with physical and structural responses, chemical characteristics provide mechanistic evidence for the reactions that drive microplastic aging [30].

A dominant chemical characteristic of microplastic aging is the formation of oxygen-containing functional groups commonly resulting from photo-oxidative and thermo-oxidative processes [31]. Numerous field studies have reported progressive increases in oxygen-containing groups, including carbonyl- and hydroxyl bands, together with the formation of carboxylic and peroxide species, and oxidation-induced alterations in aromatic ring vibrations, in naturally aged microplastics collected from marine and coastal environments, indicating cumulative oxidation during environmental aging [17, 32-34]. The carbonyl index (CI) is a commonly used chemical descriptor that quantifies the accumulation of carbonyl-containing oxidation products during aging [35]. Studies have demonstrated that CI values increase systematically with inferred exposure

duration and aging intensity most commonly in polyolefins (e.g., PE and PP) [19, 32, 33], whereas other polymers (e.g., PS, PET, PA and polyvinyl chloride (PVC)) are often reported as co-occurring within weathered microplastic assemblages showing elevated CI signatures, without polymer-specific CI being explicitly quantified [32, 36].

Furthermore, environmental evidence also links chemical oxidation to fragmentation. PP films aged on beach sand showed a strong CI-fragmentation relationship, suggesting that oxidation-driven embrittlement promotes spontaneous fragmentation beyond a critical CI threshold under realistic coastal conditions [19]. Comparable oxidation accumulation has also been reported in terrestrial settings. For instance, PE microplastics recovered from landfill matrices showed increasing CI with landfill depth and waste age, reflecting progressive oxidative degradation in long-term waste environments [37]. Long-term outdoor exposures further support these observations. Lv et al. exposed PP microplastics to different outdoor climatic conditions for up to 2 years and observed the formation of multiple carbonyl species, with CI increasing monotonically over time, demonstrating the cumulative nature of chemical oxidation during natural aging [38]. Similar transformations of surface chemistry have also been observed for microplastics collected from coastal wetlands, emphasizing that environmental aging can measurably alter chemical characteristics in situ [39].

Although chemical indices such as the CI are widely applied as quantitative descriptors of oxidation, their values are inherently method-dependent, as they are strongly influenced by spectral acquisition parameters, band selection, baseline correction, and normalization strategies [40]. Notably, this method dependence not only affects absolute values but also introduces systematic, method-dependent bias into quantitative analyses, particularly when comparing

oxidation levels across different polymers, studies, or environmental matrices. Consequently, while chemical indices can capture relative oxidation trends within a consistent analytical framework, their direct use in cross-study or cross-matrix quantitative comparisons requires careful alignment.

To summarize, physical, structural, thermal, and chemical characteristics capture complementary but partial aspects of microplastic aging. Each dimension reflects a distinct manifestation of aging, yet none alone can quantitatively or consistently describe aging severity across polymer types and exposure conditions. As a result, reliance on individual aging indicators is insufficient for consistent cross-polymer or cross-scenario assessment. This heterogeneity across descriptors motivates the need for integrated, multivariate approaches that jointly account for multiple aging dimensions, thereby providing a more robust framework for comparative aging analysis.

## 2.2 Biological Responses and Exposure Considerations of Aged Microplastics

Despite the abovementioned aging-induced changes, translating these changes into biological relevance is severely constrained by many other conditions, including particle concentrations, size distributions, and surface states encountered under environmental exposure scenarios. Therefore, evaluating biological responses provides a complementary perspective for contextualizing microplastic aging, not as a direct measure of hazard, but as an indication of how physicochemical aging may influence particle-cell interactions under environmentally relevant exposure conditions.

With the increasing detection of MPs in air, food, and consumer products, human exposure to MPs is now considered unavoidable through inhalation, ingestion, and skin contact [41]. Consequently, the biological effects of MPs, with a predominant focus on cellular-level endpoints such as reactive

oxygen species (ROS), inflammatory signalling, and membrane disruption, were primarily examined in the literature [42], as illustrated in Figure 2.2.

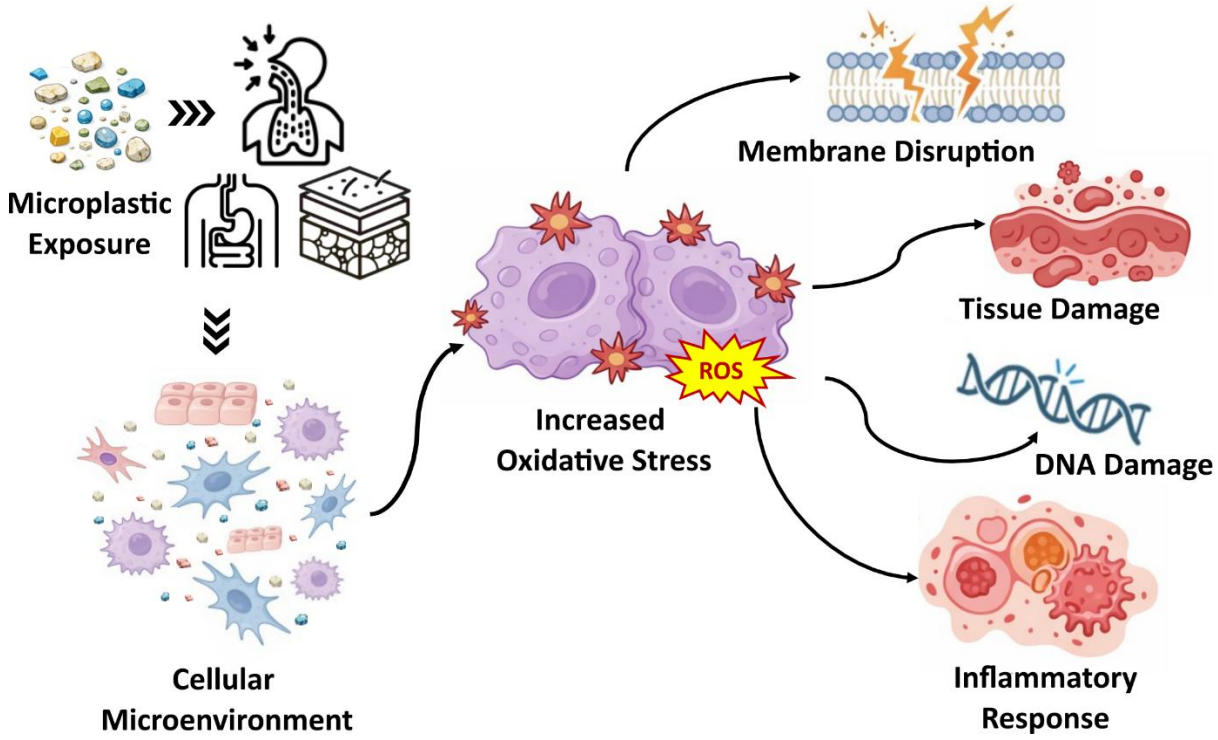


**Figure 2.2 Overview of reported human exposure routes to microplastics and their potential cellular responses.** Microplastics can enter the human body through inhalation, ingestion, and dermal contact, followed by transport to tissues and cellular environments. Upon interaction with different cell types, MPs may induce a range of cellular responses. Adapted from ref. [43].

To date, *in vitro* cell-based studies using environmentally derived or aged microplastics remain limited, but available evidence suggests that these materials can elicit qualitatively different biological responses. Rather than overt cytotoxicity, immune-relevant models, such as macrophages or dendritic cells, often exhibit inflammatory activation, including altered cytokine secretion and immune maturation marker expression, with responses strongly influenced by particle material, size, and aging state [44, 45]. In addition, studies focusing on chemical leachates

or extracts from real beach plastics have demonstrated oxidative stress and genotoxic endpoints even when direct particle-associated toxicity is modest, underscoring the importance of chemically mediated effects [46]. Evidence from consumer-product–derived particles further indicates that surface chemistry and particle size can modulate skin cell responses, although extrapolation to realistic dermal uptake remains uncertain [47].

Overall, these findings highlight that a central challenge in MPs' toxicology is the frequent mismatch between experimental exposure concentrations and environmentally relevant levels [48, 49]. Environmental exposure assessments have reported order-of-magnitude estimates of human microplastic intake that vary widely across studies, exposure pathways, and analytical methodologies. Reported intakes range from ~$10^2$ to $10^3$ particles per day, corresponding to estimated mass intakes in the ng/day to sub-µg/day range [41, 50, 51]; however, these values are highly study-dependent and reflect differences in sampled media (e.g., food, drinking water, air), particle size ranges, and detection methods. For instance, Cox et al. estimated a combined dietary and inhalation intake of ~74,000–121,000 particles per year (~200–330 particles per day) [41]. In comparison, Mohamed Nor et al. reported higher median intakes of ~883 particles/day for adults (~583 ng/day) and ~553 particles/day for children (~184 ng/day), with corresponding mass estimates that depend strongly on the particle size assumptions applied in the analysis [50]. These values are orders of magnitude lower than the tens to thousands of µg/mL commonly applied in *in vitro* toxicity studies. While high-dose studies using pristine particles provide valuable mechanistic insight, they may overemphasize hazard signals unlikely to manifest under realistic exposure conditions.

Conversely, studies conducted at environmentally relevant concentrations, particularly with environmentally sourced or aged materials, often report subtle, variable, or non-significant cellular responses. In addition, the absence of strong effects under such conditions should be interpreted as informative, reflecting the low-dose and heterogeneous nature of real-world MPs exposure rather than a lack of biological relevance. Future toxicological studies of MPs should prioritize environmentally relevant concentrations, alongside realistic particle morphologies and aging states. Incorporating chronic, low-dose exposure scenarios may better reflect real human exposure patterns than acute high-dose experiments. In addition, harmonizing dose metrics and integrating detailed physicochemical characterization with biological endpoints will be essential for improving comparability across studies. Such advances will provide a more solid foundation for interpreting cellular responses to MPs and for contextualizing toxicological findings within environmental exposure frameworks.

In all, environmental aging modifies the physicochemical and structural properties of microplastics, including surface chemistry, size distribution, and mechanical integrity. These changes can alter particle bioavailability and modes of interaction at the biological interface, underscoring the importance of considering aging when interpreting exposure and risk evidence. Additionally, human exposure to aged microplastics does not occur in isolation but is mediated through environmental reservoirs that redistribute microplastic particles. Among these, biosolids represent a critical yet analytically challenging matrix, acting as a major sink for microplastics during wastewater treatment and subsequently as a source of fertilizers to terrestrial environments [52, 53]. This positions biosolids as a key environmental context linking microplastic aging, exposure pathways, and analytical constraints, as discussed in the following section.

## 2.3 Microplastics in the Biosolid: Analytical Challenges

In complex environmental matrices such as biosolids, microplastics rarely exist as isolated particles but are instead embedded within organic- and mineral-rich matrices that strongly influence analytical outcomes. Land application of biosolids as an agricultural soil amendment represents a critical pathway for introducing microplastic particles into terrestrial ecosystems (Figure 2.3). Field studies report microplastic abundances in biosolids on the order of $10^3 – 10^5$ particles per kilogram dry weight. However, these values are strongly study-specific and site-dependent, and vary with wastewater treatment plant characteristics, sludge processing technologies, and regional regulatory frameworks governing biosolids production and land applications [52, 54-56]. Despite their importance, biosolids are among the most analytically challenging matrices for microplastic research due to their high organic content, physicochemical heterogeneity, and strong particle–matrix interactions. Systematic reviews have shown that MP concentrations span multiple orders of magnitude, a range driven not only by true environmental and site-specific variability but also by methodological divergence among studies, including differences in pre-treatment protocols, density separation media, and minimum particle size thresholds [53, 57].

The lack of consistent approaches for quantifying microplastic aging and transformation directly constrains extraction efficiency, polymer identification, and mass-based quantification. The following subsections therefore review common strategies for microplastic separation and analysis in biosolids, progressing from separation methods to identification, quantification, and remaining methodological knowledge gaps.

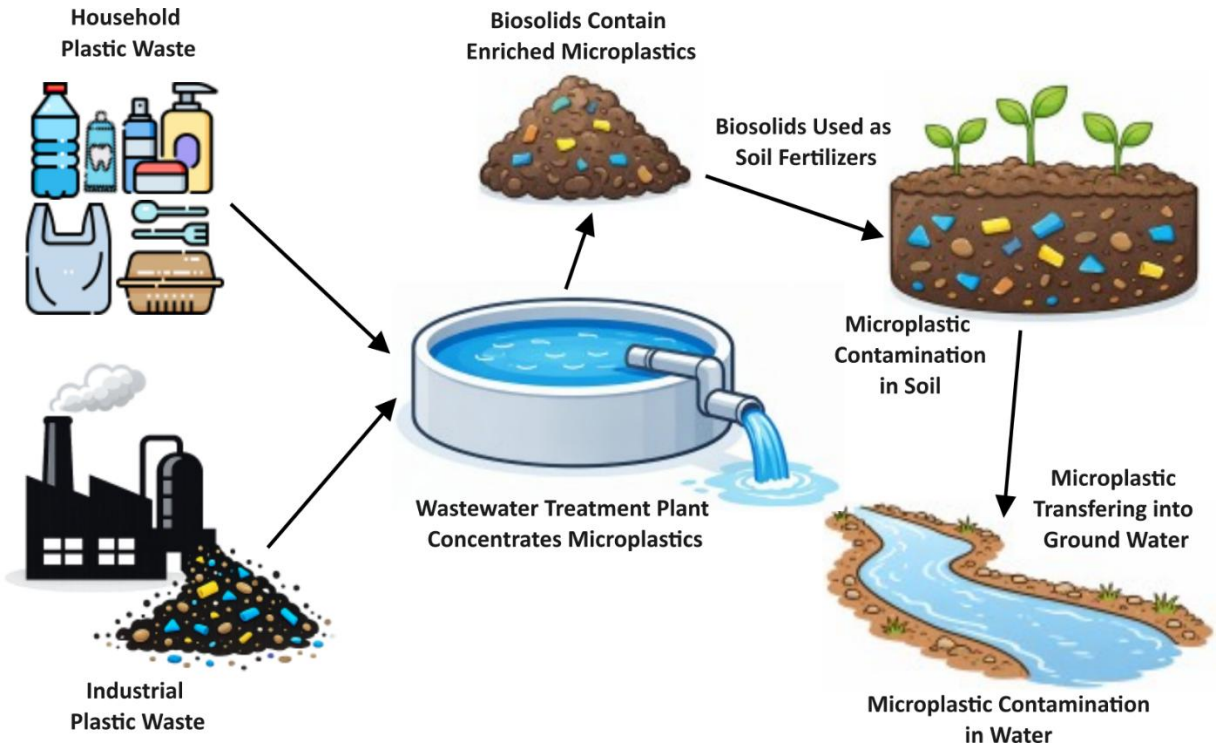


**Figure 2.3 Biosolids as a central pathway for the transfer of microplastics to terrestrial and aquatic environments.** Microplastics from household and industrial sources are captured and processed during wastewater treatment and concentrated in biosolids, which subsequently act as a major vector for microplastic input into agricultural soils and connected aquatic systems. Adapted from ref. [58].

### 2.3.1 Challenges of Microplastics Extraction from Biosolid Matrices

Biosolids are characterized by high organic content (typically on the order of tens of percent, ~50–70% volatile solids on a dry-weight basis [59]), fine mineral particles, microbial biomass, and residual chemicals, which strongly interfere with microplastic detection. In practice, MP separation from biosolids is rarely achieved by a single step. Instead, it is constrained by trade-offs between 1) sufficient matrix removal for reliable identification, 2) minimizing polymer loss and alteration during pretreatment, and 3) maintaining feasibility for routine or large-scale sample

processing. Consequently, microplastic separation in biosolids is usually interpreted as a managed compromise rather than a neutral preprocessing step. Common approaches for microplastics separation from biosolids are listed in Table 2.1. Within this framework, separation strategies are typically classified by the primary mechanism used to remove the non-plastic matrix components that are physically embedded, chemically interact with, or obscure microplastics during analysis. Among all the separation strategies, digestion is the most widely used initial step in biosolids processing.

*2.3.1.1 Digestion-based Separation*

Chemical digestion is almost universally used as the first step to selectively remove biogenic and organic components, such as proteins, lipids, polysaccharides, and humic substances, from biosolids, enabling the isolation and analysis of embedded microplastics. The purpose of digestion is not exhaustive organic matter removal, but rather sufficient matrix reduction of matrix complexity to enable downstream separation and identification of plastic particles [60]. Accordingly, "effective digestion" cannot be judged solely by the extent of organic matter removal, because digestion conditions may induce polymer- and size-dependent losses and modify plastic surface chemistry through oxidation, embrittlement, or fragmentation, particularly for environmentally aged materials. Acidic, alkaline, enzymatic, and oxidative digestions are commonly employed to target organic constituents while nominally preserving the integrity of microplastics [61-64]. Among available approaches, hydrogen peroxide-based oxidative digestion, often catalyzed by Fenton-type reactions, has been most widely adopted for sludge and biosolids [52, 61, 62, 65-67].

*2.3.1.2 Physical Separation*

Sieving and filtration are size-based separation methods that capitalize on differences in particle size. While sieving is effective for larger MPs, membrane filtration with specific pore sizes can target smaller particles [68]. Density separation is commonly combined with digestion to physically isolate MPs, relying on the distinct physical properties of MPs to separate them from environmental matrices. This separation method is based on the differences in buoyant densities between MP/NPs and surrounding natural particles. The most used techniques are density gradient centrifugation and floatation [69]. The choice of separation medium plays an important role in determining which polymers are effectively recovered. On the one hand, while low-density solutions are environmentally friendly, they can under-recover denser polymers (e.g., PET, PVC), which is why higher-density salts ($ZnCl_2$, NaI) or sequential density steps are frequently used for sludge and biosolids [62]; on the other hand, although high-density separation to treat sewage sludge could obtain overall MPs recoveries above 80%, increased co-extraction of organic residues happened, it complicates spectroscopic identification and requiring additional purification steps, particularly for large-scale biosolids analysis [62, 70].

While these methods have been widely employed and are effective for given types of microplastics, they face challenges in discriminating particles with similar physical properties or in the presence of high organic matter content [68]. In biosolids, separation efficiency is best framed as a compromise, as stronger digestion improves extraction efficiency but risks polymer modification. In comparison, denser solutions improve polymer coverage but increase co-extracted residues, cost, and handling constraints.

**Table 2.1** Advantages and key challenges of common processing steps in microplastic separation workflows for biosolid matrices*.

| Methods | Reagents | Advantages | Main challenges | Refs. |
|---|---|---|---|---|
| Oxidative digestion | $H_2O_2$, Fenton's reagent ($Fe^{2+}/H_2O_2$) | Highly effective removal of organic matter. Widely adopted and compatible with subsequent processes. | Risk of polymer degradation, surface oxidation, or fragmentation under aggressive conditions. Incomplete breakdown of humic substances/cellulose may still interfere with further identification. | [52, 61, 62, 65-67] |
| Acid/ Alkaline digestion | $HNO_3$, HCl, NaOH, KOH | Rapid degradation of biological material. Simple protocols requiring minimal specialized equipment. | Strong polymer selectivity, as some polymers (e.g., PA, PET, PU) are vulnerable to acids or bases. Potential alteration of particle surfaces and additives. | [61-63] |
| Enzymatic digestion | Protease, Pectinase, Viscozyme, Cellulase (often combined) | Mild reaction conditions that better preserve polymer integrity. | Limited effectiveness for highly complex biosolid matrices without multi-step enzyme cocktails. Time-consuming and costly. | [64] |
| Size-based separation | Stainless-steel sieves, membrane filtration | Simple, scalable, and effective for larger MPs. Enables operational size fractionation. | Poor recovery of small particles, particularly in organic-rich sludge. Filter clogging and co-retention of fine matrix particles. Final size classes are method-dependent rather than intrinsic, limiting cross-study comparability. | [52, 63, 68] |
| Density separation | NaCl, $CaCl_2$, NaI, $ZnCl_2$ | Easy operation. Physically separates MPs from matrices without degrading microplastic particles. | Low-density solutions under-recover high-density polymers. High-density reagents increase the co-extraction of organic residues. Cost, safety, and waste-disposal burden. | [62, 63, 67] |

* *Notes:* $H_2O_2$ (hydrogen peroxide), $Fe^{2+}$ (ferrous ion), $HNO_3$ (nitric acid), HCl (hydrochloric acid), NaOH (sodium hydroxide), KOH (potassium hydroxide), NaCl (sodium chloride), $CaCl_2$ (calcium chloride), NaI (sodium iodide), $ZnCl_2$ (zinc chloride), PA (polyamide), PET (polyethylene terephthalate), PU (polyurethane).

### 2.3.2 Qualitative and Quantitative Analysis of Microplastics in Biosolid

Following matrix digestion and density separation, biosolid-derived samples are substantially simplified but remain analytically complex. Residual organic matter, fine mineral particles, and heterogeneous microplastic populations continue to interfere with both polymer identification and quantitative determination. As a result, the identification and quantification of MP/NPs in biosolids are constrained not by a single instrumental limitation, but by a series of interconnected challenges, including particle size, matrix interference, sample preparation artifacts, polymer alteration, and quantitative sensitivity [71]. Also, a recent dedicated review similarly concludes that there is still no unified approach for MP characterization in sludge/biosolids, leading to incomparable datasets across studies [72].

Because biosolid- and wastewater-derived samples contain residual organic matter, mineral particles, fibres, and heterogeneous plastic fragments, no single analytical method can fully describe their microplastic content. Methods used in the literature differ in the property they measure, and the output and results are not interchangeable. For example, microscopy and imaging methods mainly describe particle recognition, size, shape, and morphology; vibrational spectroscopy is used for particle-level polymer identification; and thermal or mass-spectrometric methods provide mass-based quantification when polymer-specific signals can be resolved [71, 73]. Recent comparative studies have therefore combined or compared methods such as FTIR and Py-GC/MS to obtain both particle-based and mass-based information from MP samples extracted from wastewater [74]. Representative approaches applied to wastewater, sewage sludge, biosolids, and WWTP-related samples are summarized in Table 2.2.

**Table 2.2** Analytical approaches for microplastics in wastewater, sewage sludge, and biosolids*.

| Analytical approach | Main Output | Advantages | Limitations | Refs. |
|---|---|---|---|---|
| Optical imaging | Particle count; size class; morphology | Low cost; useful for initial screening | High false-positive and false-negative risk in organic-rich matrices; cannot confirm polymer identity | [52] |
| Nile Red fluorescence staining | Fluorescent particle count and size distribution | Rapid screening; improves the visibility of small or transparent MPs; useful when particle counts are high | Organic matter, lipids, and other hydrophobic residues can also fluoresce; staining efficiency varies with polymer types, digestion method, and matrix residue | [75] |
| ATR-FTIR spectroscopy | MPs identification based on mid-infrared absorption bands | Direct identification; suitable for larger MPs with adequate surface contact | Less suitable for small, irregular, fragile, or coated particles; matrix residues and aging can reduce spectral match quality | [52, 76] |
| Micro-FTIR / FPA-FTIR imaging | MPs identification, particle count, size distribution, and spatial mapping | Non-destructive; direct polymer identification; automated mapping; supports both abundance and size distribution | Spatial resolution and filter compatibility limit small-particle analysis; mass estimation is indirect; organic residues interfere with spectra | [52, 75, 77-79] |
| LDIR / QCL-based IR imaging | Automated polymer identification; particle size, morphology, and count | Higher throughput than conventional micro-FTIR; suitable for monitoring large numbers of particles | can be affected by fibres, cellulose, particle morphology, and matrix residues | [80] |

| | | | | |
|---|---|---|---|---|
| Raman/ Micro-Raman spectroscopy | Individual MPs identification; small-particle analysis | Higher spatial resolution than FTIR; useful for smaller particles and fibres; chemical image maps | Fluorescence from pigments, biofilms, natural organic matter; matrix residues can obscure Raman peaks; laser heating can damage particles; long acquisition time | [81-83] |
| SEM / SEM-EDS | Surface morphology, erosion, inorganic residues/fillers; primary polymer identification | High-resolution morphology; useful for observing aging patterns, such as surface damage, aggregation, and mineral residues on extracted particles | Does not directly identify polymer backbone; requires dry and treated samples; can introduce preparation artifacts; low throughput | [84] |
| Py-GC/MS | Polymer-specific mass concentration | Provides mass-based quantification; not constrained by optical size limits; less dependent on particle shape or visual recognition | Destructive; polymer markers can overlap with matrix pyrolysis products; requires careful calibration and blank correction | [85-91] |
| Sequential FTIR + Py-GC/MS | Particle number and mass; MPs identification | Allows comparison of abundance-based and mass-based results | Requires careful subsampling for direct comparison; Py-GC/MS remains destructive | [74] |
| DSC / MDSC | MPs identification based on thermal behaviour, mass-based quantification | Allows large aliquots analysis; MDSC can reduce matrix interference | MP thermal transitions can overlap and cover signals; amorphous polymers may be difficult to quantify | [92-97] |

| | | | | |
|---|---|---|---|---|
| TGA | Decomposition temperature; mass loss during heating | Provides mass estimates of MPs by mass loss during heating within the decomposition window; | Limited polymer specificity when decomposition ranges overlap; destructive | [94] |

**Note*: ATR-FTIR (Attenuated total reflectance-Fourier transform infrared spectroscopy), FPA-FTIR (Focal plane array-Fourier transform infrared spectroscopy), LDIR (Laser Direct Infrared spectroscopy), QCL-IR (Quantum cascade laser-based infrared), SEM (Scanning electron microscopy), SEM-EDS (Scanning electron microscopy-energy dispersive X-ray spectroscopy), Py-GC/MS (Pyrolysis-gas chromatography/mass spectrometry), DSC (Differential scanning calorimetry), MDSC (modulated differential scanning calorimetry), TGA (Thermogravimetric analysis).

As summarized in Table 2.2, the analytical information obtained from microplastic samples depends strongly on the technique employed. In biosolid matrices, however, the performance of all these techniques is influenced by residual organic matter, mineral particles, and the heterogeneous nature of microplastic populations. These matrix constraints affect different analytical approaches in different ways, from the initial recognition of particles to the accurate determination of their size distribution and polymer mass.

*2.3.2.1 Ambiguity in Particle Recognition*

A defining analytical challenge in biosolid microplastic analysis is that microplastics are rarely present as isolated particles. Biosolids are characterized by dense organic flocs and mineral-associated aggregates in which microplastics are often physically embedded rather than freely suspended, resulting in fundamental ambiguity in particle recognition even after digestion and density separation. Residual organic matter and fine particulates can obscure particle boundaries, making it challenging to distinguish plastics from non-plastic debris during visual or spectroscopic

screening [71]. This ambiguity is not observational but structurally linked to the matrix. Käppler et al. systematically evaluated Fourier transform infrared spectroscopy (FTIR)-based identification in complex environmental samples. They showed that residual matrix components, such as cellulose-rich organic matter with overlapping vibrational features, can generate spectra that are difficult to assign with high confidence, particularly when particles are partially covered or embedded within organic residues [98]. In biosolids, such embedding biases analyses toward particles that are more easily released during pretreatment, while particles more strongly associated with organic aggregates may remain unrecognized and therefore unaccounted for [63]. Direct evidence for this mechanism is provided by Ruffell et al., who treated biosolids as aggregate pellets rather than loose particles and demonstrated that digestion strategies explicitly designed to disintegrate aggregates substantially altered recovery outcomes. Using a tailored digestion protocol, they achieved average recoveries of approximately 95% for spiked microplastics, highlighting that particle recognition and recovery are tightly coupled to the extent to which matrix embedding is disrupted [79].

Aging processes further exacerbate this challenge by modifying particle surface chemistry and morphology. Oxidative weathering and biofilm formation increase surface roughness and polarity, enhancing the affinity of microplastics for organic coatings and matrix components, thereby reinforcing physical embedding and visual ambiguity [7]. Consequently, in biosolids, the initial step of particle recognition already integrates uncertainty arising from both matrix association and aging-driven surface modification, which propagates into downstream identification and quantification.

*2.3.2.2 Size-related Physical Constraints*

Particle size is a fundamental physical property of microplastics that directly limits the qualitative and quantitative analysis in biosolid matrices. Wastewater treatment processes promote extensive fragmentation, enriching biosolids with small microplastics and nanoplastics that are disproportionately difficult to analyze. As particle size decreases, absolute spectral signal strength declines while matrix-derived background interference remains substantial, leading to a practical lower size limit for reliable analysis.

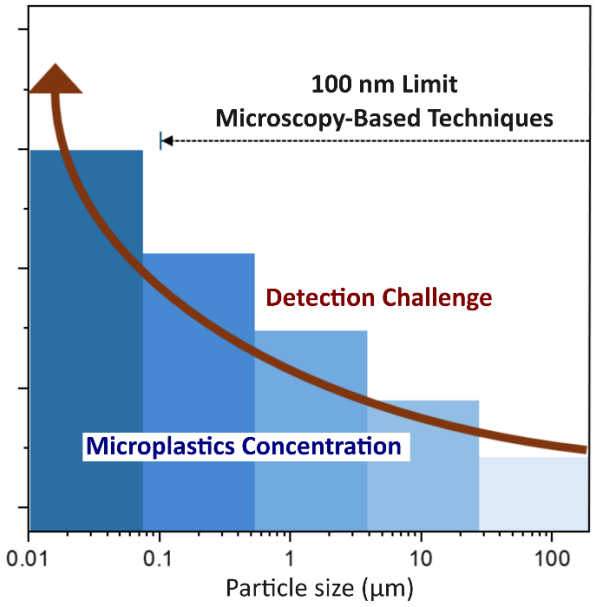


**Figure 2.4 The challenge of detecting microplastics in biosolids arising from particle size limitations.** Smaller microplastics, which are more abundant in biosolids due to extensive fragmentation during aging, are increasingly difficult to detect reliably. The dashed line indicates the approximate practical lower size limit of microscopy-based techniques. Adapted from refs. [6, 99].

As summarized in Figure 2.4, commonly used microplastic detection techniques are inherently constrained by particle size: conventional FTIR and Raman spectroscopy are typically limited to the micrometre scale due to diffraction-limited spatial resolution, whereas advanced techniques such as electron microscopy extend detection to the sub-micrometre scale. Operational size cutoffs are introduced at multiple stages of the analytical workflow, including filtration, sample handling, imaging resolution, and spectral mapping time, collectively constraining which particles are ultimately detected and reported. At the same time, microplastic size distributions in biosolids are reported to be dominated by smaller particles [99], such that the size fractions expected to be most abundant increasingly fall below practical detection limits, thereby amplifying the overall analytical challenge. Mintenig et al. reported that, even following extensive enzymatic–oxidative purification and high-density separation, polymer identification using ATR-FTIR (attenuated total reflectance-Fourier transform infrared spectroscopy) and FPA (focal plane array)-based micro-FTIR imaging was effectively constrained to particles larger than approximately 20 μm in wastewater treatment plants (WWTPs) effluents [100]. Given the higher residual organic content and particle loading typical of biosolids, comparable size fractions are expected to be at least as challenging in sludge-derived samples. However, the identification problem becomes more severe as particle size decreases, because smaller particles generate weaker absolute absorbance or scattering. At the same time, the background from the residual matrix does not scale down proportionally, so spectra from small MPs are more likely to become “borderline” under the same residual load [71, 101].

Because environmental aging could fragment larger particles into smaller size classes, this size-dependent analytical constraint becomes increasingly relevant as aging advances. Aging shifts microplastics toward finer size fractions, increasing the proportion of microplastics that approach

or fall below the practical detection limits of particle-based workflows, thereby reducing both identification confidence and sample representativeness [7]. Thus, in biosolids, aging not only alters particle properties but also renders materials analytically inaccessible due to their reduced sizes.

Raman spectroscopy is often discussed alongside FTIR due to its higher theoretical spatial resolution and its potential to access particles below 10 μm. By probing molecular structure through inelastic photon scattering, Raman spectroscopy provides non-destructive in situ identification capabilities [98]. In biosolids, however, Raman identification faces a systematic obstacle: pigments and co-extracted organic compounds frequently induce fluorescence that overwhelms Raman scattering signals. This fluorescence markedly increases the proportion of unclassifiable spectra and often necessitates more aggressive purification, which can reduce particle recovery or alter surface properties [102]. As a result, fluorescence is consistently identified as a dominant practical limitation of Raman spectroscopy in matrix-rich environmental samples, despite its theoretical advantages [103].

Finally, even when instrument quality is high, biosolid identification remains constrained by how well reference libraries represent the spectral diversity of aged particles (weathering, pigmentation, additives, surface coatings, and partial oxidation), because matrix residues and aging shift spectra away from pristine references. These practical limitations have contributed to a broader methodological shift in microplastic identification over the past decade. While early studies largely relied on manual screening for spectral identification, more recent work increasingly recognizes that identification accuracy is no longer viewed as a purely instrumental issue [104]. Studies now explicitly interrogate what determines identification accuracy: library representativeness,

algorithmic decisions, particle weathering state, and operator choices [101]. Open-access databases, such as OpenSpecy, pushed the field toward community libraries and reproducible workflows, addressing a major barrier to cross-lab comparability [105]. Complementary resources, such as SLoPP, expanded the accessible reference spectra sets, intended to improve identification robustness across polymer types and appearances [106].

*2.3.2.3 Challenges in Mass-based Quantification of Microplastics in Biosolids*

An overarching challenge in biosolid microplastic analysis is the lack of a robust, matrix-compatible mass-based quantification. Most identification workflows inherently yield particle number concentrations, whereas mass conversion requires assumptions regarding particle geometry, density, and polymer composition that are rarely valid for irregular, aged, and matrix-associated particles [107].

A primary challenge in mass-based quantification of microplastics in biosolids arises from the integrative nature of mass-based analytical techniques, which quantify all thermally or chemically responsive material within a defined analytical window rather than selectively targeting polymer signals. Unlike particle-counting approaches, mass-based quantification lacks the discrimination needed to distinguish microplastics from non-plastic components that exhibit overlapping thermal or chemical responses. As a result, accurate attribution of measured mass to microplastics becomes methodologically limited. In biosolids, residual non-plastic material may remain analytically active even after separation, further broadening background signals and complicating polymer-specific mass assignment [87, 89]. Evidence for this challenge is reflected in studies reporting substantial discrepancies or large uncertainties in mass-based measurements of sludge matrices (Table 2.3). For example, Cho et al. quantified microplastics in sewage sludge using both number-

based and mass-based approaches and reported substantial inconsistencies between the resulting estimates, which attributed part of the discrepancy between these metrics to difficulties in achieving complete matrix removal and to overlapping signals from non-plastic organic components during analysis [90]. Sample heterogeneity and the representativeness of biosolids strongly affect the mass-based quantification of microplastics. At the microgram-to-milligram-per-gram level, microplastic mass may be concentrated in a small number of particles, fibres, or agglomerates, making measured values highly sensitive to subsampling strategy and aliquot selection [108]. Another piece of evidence for this challenge is provided by Dierkes et al., who quantified microplastic mass across different sludge processing stages and demonstrated that measured microplastic loads varied substantially depending on the treatment steps, including digestion, thickening, and dewatering [89]. The markedly significant uncertainty associated with biosolids illustrates how physical state and heterogeneity can dominate measurement variability.

In addition, mass quantification in biosolids is inherently polymer-dependent, with sensitivities and limits of quantification varying by more than an order of magnitude among different polymer types (Table 2.3). As a result, the reported "total microplastic mass" is not a uniform metric but is disproportionately influenced by polymers that exhibit stronger analytical responses or occur at higher concentrations. This polymer-specific behaviour undermines direct comparison across studies unless polymer-resolved mass contributions and detection limits are explicitly reported. The examples summarized in Table 2.3 illustrate that, despite the use of different thermal- and pyrolysis-based approaches, reported mass concentrations often fall within overlapping ranges, reflecting the combined effects of polymer composition, analytical response, and reporting basis rather than systematic differences between methods. For example, Wu et al. applied a pyrolysis-thermal desorption-gas chromatography/mass spectrometry (Py-TD-GC/MS) workflow to real

sewage sludge and reported polymer-specific limits of quantification ranging from 0.57 to 14.81 µg, depending on polymer type [88]. The wide range of limit of quantification (LOQ) values indicates that specific polymers can be quantified with substantially higher sensitivity than others, enabling their contribution to the total mass to be captured more reliably. Similarly, Okoffo et al. reported total plastic concentrations of 2.8–6.6 mg/g in biosolids, with PE alone contributing approximately 2.2 mg/g, demonstrating that a single polymer can dominate total mass values depending on both abundance and analytical response [87]. These findings underscore that mass-based results in biosolids are method- and polymer-weighted rather than intrinsically comparable.

**Table 2.3** Experimental studies reporting mass-based quantification of microplastics in biosolids or sewage sludge*.

| **Material source** | **Plastic type identified** | **Quantification technique** | **LOQ** | **Mass concentration** | **Refs.** |
|---|---|---|---|---|---|
| WWTPs solid residues | PE, PS, PP | Py–GC/MS | 0.007–0.16 mg/g | 0.03– 3.3 mg/g | [89] |
| Biosolids (municipal WWTPs) | PE, PP, PVC, PS, PMMA, PC | double-shot Py-GC/MS | 0.01 – 0.09 mg/g | 2.8 – 6.6 mg/g | [87] |
| Sewage sludge from WWTPs | PP, PE, PET, PS, PMMA, PU, and PA | TED-GC-MS | N/A | Average 95.79 µg/g | [90] |
| Primary and secondary sewage sludge | PE, PP, PS, PVC, PET | Py-TD-GC/MS | 0.57–14.81 µg | primary sludge: 8714 ± 228 µg/g; secondary sludge: 3828 ± 558 µg/g | [88] |
| WWTPs | PE, PP, PET, PVC, PMMA | Py-GC/MS | 5 – 145 µg/L | 840–3116 µg/L | [91] |
| WWTPs | PE, PP, PA6, PET | DSC | 0.05 – 0.19 mg | 0.1 to 19.6 µg/L | [92, 96] |
| WWTPs | PA, PVC, PE, PC, PP, PTFE, PS, PMMA, PET | DSC | 1 mg | 0.70–0.79 µg/L | [93] |

**Note:* WWTPs (wastewater treatment plants), PE (polyethylene), PP (polypropylene), PVC (polyvinyl chloride), PS (polystyrene), PMMA (polymethyl methacrylate), PC (polycarbonate), PET (polyethylene terephthalate), PU (polyurethane), PA (polyamide), PTFE (polytetrafluoroethylene), Py-GC/MS (pyrolysis-gas chromatography-mass spectrometry), Py-TD-GC/MS (pyrolysis–thermal desorption GC/MS), TED-GC-MS (thermal extraction desorption-gas chromatography-mass spectrometry), DSC (differential scanning calorimetry).

Another key challenge in mass-based quantification is that microplastics in biosolids are usually present after natural aging. Mechanical stress, oxidative aging, additive leaching, and surface fouling during wastewater treatment and sludge processing can all alter the chemical composition and thermal behaviour of polymers. It is noted that oxidative degradation and additive loss can change pyrolysis product distributions, increase the likelihood of co-elution or altered marker yields, and thereby introduce systematic bias when pristine standards are applied to aged environmental samples [109]. In addition, the calibrations built on pristine microplastics can become systematically biased when applied to aged microplastics. Under these conditions, quantification based on Py-GC/MS using virgin PP calibration standards was predicted to underestimate PP mass by ~42% to ~49%, providing direct numerical evidence that oxidation can change marker yields sufficiently to introduce large mass errors if aging is ignored [85]. Another experimental pyrolysis study on UV-aged PE, PP, and PS further confirms that aging introduces new oxygen-containing degradation products and shifts product distributions, reinforcing the mechanistic basis for marker instability in oxidized materials when used as markers for microplastics quantification [110]. In biosolids, where aging and surface modification are ubiquitous, this challenge necessitates calibration strategies that are both aging- and matrix-aware.

In summary, mass-based quantification of microplastics in complex matrices such as biosolids remains challenging due to particle-size effects, matrix heterogeneity, and method-dependent

analytical performance. Variability in detection limits, calibration strategies, recovery corrections, and matrix interference, along with the lack of standardized protocols, suggests that reported microplastic concentrations can differ by orders of magnitude depending on the analytical approach used, even for similar sample types. Moreover, the absence of efficient mass-based quantification approaches limits the ability to interpret how aging processes systematically alter microplastic properties. It is now established that aging-induced changes in size, morphology, surface chemistry, and mechanical integrity are often interconnected and rarely independent of one another. Nevertheless, they are often evaluated using isolated metrics that provide an incomplete representation of overall aging status. Overcoming this limitation requires analytical approaches that integrate multiple property changes into a unified framework, while preserving their relative contributions and interrelationships, particularly in environmentally relevant matrices.

## 2.4 Multivariate Analysis for Quantifying the Aging Level of Microplastics

### 2.4.1 Principal Component Analysis for Aging Trajectory

Addressing this challenge requires analytical strategies that can simultaneously integrate multiple aging descriptors while preserving their relative contributions [111]. Multivariate statistical analysis provides a practical route to unify disparate measurements and evaluate their joint evolution during natural or accelerated aging. Among multivariate techniques, principal component analysis (PCA) is one of the most widely used methods for integrating heterogeneous descriptors into a reduced set of variables. It could identify which variables contribute most strongly to overall variance [112].

As shown in Table 2.4, in an aging context, PCA can compress multiple partially redundant descriptors (chemical, thermal, structural) into a smaller set of latent components and project them

into PCA space to visualize “aging trajectories” and clustering patterns under different aging conditions [113]. Recent analytical work has used characterized CI changes together with PCA to classify microplastics and probe the extent of degradation, demonstrating how chemometrics can transform complex spectral/feature sets into interpretable multivariate patterns [113, 114]. Binda et al. applied PCA to FTIR spectra of aged polyethylene. The results showed that the first principal component (PC1), which represents the dominant direction of spectral variation identified by PCA, captured most of the spectral variance and separated abiotic aging from biofouling-driven changes, enabling a comparative assessment of distinct aging states and pathways within a common multivariate framework [115]. Similarly, Ferreiro et al. combined IR spectrometry with pattern-recognition methods (including PCA) to differentiate polymer types in an aging-independent manner, highlighting how multivariate spectral structure can overcome variability introduced by aging [116]. While PCA can provide an integrated representation of aging, interpretability remains important. Environmental relevance often depends on knowing which indicators dominate the integrated score under given conditions. Explainable machine-learning tools, such as Shapley additive explanations (SHAP), offer a model-agnostic way to quantify each feature's contribution to a predicted outcome, thereby enabling the reporting of both an overall aging score and the relative influence of different characteristics within the same framework [117, 118]. Operationally, once an “aging score” is produced by a supervised model, SHAP values can be computed to quantify how much each variable contributes to each prediction and to the overall model behaviour. This feature-attribution layer is beneficial for microplastic aging because it helps determine whether the integrated score is predominantly driven by oxidation metrics, thermal weakening, or structural changes across specific aging pathways, thereby improving transparency and cross-study interpretability. Beyond materials research, SHAP has been widely adopted in environmental

modelling to diagnose dominant drivers and interactions [119, 120], illustrating its maturity as an interpretable layer for multivariate indices used in microplastics assessment.

**Table 2.4** Application of PCA in microplastic aging studies*.

| Microplastic types | Input descriptors | Key findings | Refs. |
|---|---|---|---|
| HDPE, LDPE, PP, and PS under natural sunlight exposure | Full ATR-FTIR spectral features (oxidation-related bands); CI reported for comparison | PCA of full ATR-FTIR spectra enabled integration of multiple oxidation-related features into a low-dimensional space in which samples followed systematic trajectories correlated with photochemical aging time, allowing relative aging progression to be compared across exposure conditions. | [113] |
| PLA, PS from single-use knives, PBAT from compostable bags, PE from chewing gum containers. | Full μ-FTIR and ATR-FTIR spectra; CI reported for comparison | PCA integrated degradation-induced spectral changes into a reduced feature space, enabling comparison of relative photodegradation levels when single diagnostic bands were insufficient. | [114] |
| PE fragments after UV and biofouling aging | FTIR spectral features capturing oxidation- and biofouling-related functional groups | PCA condensed FTIR spectral variation into dominant components, revealing that different aging pathways occupy distinct regions in PCA space, thereby enabling comparative assessment of aging states driven by various mechanisms. | [115] |
| PET, PMMA, PS, PP, LDPE, HDPE, PA, PC | Reflectance IR spectral features representing polymer chemistry under aging | PCA demonstrated that aging-induced spectral variability can be represented within a reduced multivariate space, providing a foundation for subsequent comparative aging analysis. | [116] |
| fragments of PP balloon ribbon, HDPE, and two PE balloon variants under humidity conditions | FTIR spectral features and bond indices (e.g., carbonyl absorbance) | PCA was used to position laboratory-aged and environmental microplastics in a common spectral space, enabling a qualitative comparison of aging between controlled aging experiments and field-collected particles. | [121] |

| | | | |
|---|---|---|---|
| PE, PP, PS, PET, PVC, ABS, PA66, PC, PTFE, PU macro/mesoplastics collected from beach | Preprocessed IR spectral features used as proxies for aging-induced changes | Distances in PCA space derived from IR spectra were used as a proxy for the extent of weathering, enabling the relative ranking of environmental plastic fragments by their degree of aging. | [122] |
| Pristine and weathered PS, HDPE, PP, PET, PMMA, Nylon | Mass-spectral features sensitive to polymer composition and degradation state | PCA projection of pristine and weathered samples into a common component space enabled systematic differentiation between aging states. | [123] |

**Note:* PCA (principal component analysis), HDPE (high-density polyethylene), LDPE (low-density polyethylene), PP (polypropylene), PS (polystyrene), PLA (polylactic acid), PBAT (poly(butylene adipate-co-terephthalate)), PET (polyethylene terephthalate), PMMA (polymethyl methacrylate), PA (polyamide), PC (polycarbonate), PVC (polyvinyl chloride), ABS (acrylonitrile butadiene styrene), PTFE (polytetrafluoroethylene), PU (polyurethane), ATR-FTIR (attenuated total reflectance Fourier-transform infrared), FTIR (Fourier-transform infrared), CI (carbonyl index)

### 2.4.2 Knowledge Gap in Microplastics Aging

Current assessments of microplastic aging predominantly rely on individual descriptors that capture specific manifestations of degradation, including changes in surface morphology, chemical functional groups, or thermal behaviour. While these indicators provide mechanistic insight, they are inherently parameter-specific and polymer-dependent, making it challenging to compare aging levels across polymers with different physicochemical properties or across particles of different sizes. For example, chemical indices such as the carbonyl index or the oxygen-to-carbon (O/C) ratio are widely used to track oxidation. Still, they are sensitive to spectral band selection and surface heterogeneity [98]. Similarly, thermal indicators such as shifts in melting temperature or changes in crystallinity are highly polymer-specific and may respond differently under identical

aging conditions. Therefore, the degree of aging inferred from one metric cannot be directly translated to another polymer or size class, even under comparable exposure histories.

As a result, the current microplastics aging study lacks a unified quantitative framework that integrates heterogeneous aging parameters into a single and comparable measure of aging level. Without such an approach, comparisons across studies remain largely qualitative or context-dependent, limiting the ability to assess relative aging severity or establish dose-response relationships between aging and downstream environmental or biological effects.

While multivariate frameworks provide a powerful means to integrate and compare aging descriptors, their interpretability ultimately depends on a mechanistic understanding of the underlying aging processes that generate these descriptors. Integrated aging scores reflect the cumulative outcomes of specific physicochemical pathways, such as photo-oxidation, thermal degradation, or mechanical abrasion, each of which operates under distinct environmental conditions and induces characteristic changes in polymer structures and properties. Consequently, evaluating the strengths and limitations of mechanistic aging approaches remains essential for contextualizing multivariate aging metrics and for linking integrated indices to environmentally relevant degradation pathways.

## 2.5 Controlled Aging Approaches and Their Limits

Although integrated and multivariate approaches enable quantitative comparison of microplastic aging states, they do not, by themselves, elucidate the specific physicochemical pathways responsible for observed degradation patterns. Controlled aging approaches are widely used in microplastic research to generate aged microplastics with measurable property changes under defined conditions. These approaches provide critical insight into isolated aging mechanisms, but

they also have important limitations because usually only one or a limited number of stressors at elevated intensity are applied. At the exposure level, it cannot reproduce the full environmental history of microplastics, because natural weathering involves variable solar spectra, day-to-night cycling, seasonal temperature changes, moisture, oxidants, dissolved organic matter, biofilm formation, and mechanical abrasion [1, 6, 124]. At the mechanistic level, however, laboratory aging can isolate specific processes that also occur in the environment, such as photo-oxidation, polymer chain scission, surface functionalization, embrittlement, and fragmentation [2, 5, 125]. Consequently, laboratory-aged microplastics should not be treated as direct simulation of environmentally aged microplastics.

### 2.5.1 Photo-Oxidative Aging

Photo-oxidation is widely recognized as a common pathway for MPs aging in the environment, particularly at the air-water and air-soil interfaces, where UV radiation and oxygen are readily available. Upon exposure to UV radiation, aging may be triggered through direct cleavage of C–C and C–H bonds or by catalyzed photo-oxidative reactions involving chromophores or additives, leading to the formation of macroradicals [126]. These radicals readily react with oxygen to generate peroxy species, which propagate oxidation via hydrogen abstraction and hydroperoxide formation [1, 126]. The subsequent breakdown of unstable oxygen-containing bonds produces secondary radicals, such as alkoxy and hydroxyl radicals, which drive further chain scission, progressively altering surface chemistry and mechanical integrity [1, 127].

Laboratory-based photo-oxidative aging experiments commonly employ artificial UV sources (UVA, UVB, or UVC) to accelerate these processes under controlled conditions. For example, Song et al. subjected PE, PP, and PS particles to prolonged UV irradiation followed by mechanical

abrasion, demonstrating that UV-induced oxidation substantially increased brittleness and fragmentation potential relative to pristine plastics [5]. Similarly, Miranda et al. applied accelerated UV aging to several polymer types and reported polymer-specific oxidation and surface cracking patterns consistent with photo-oxidative degradation [128]. To examine long-term light-driven transformation under controlled conditions, Zhu et al. aged PS microplastics under simulated solar irradiation for up to 150 days, providing a mechanistic insight into long-term light-driven aging under controlled conditions [129]. In addition, Pinlova and Nowack exposed PET to UV light, both in air and in water, over a multi-month period and reported reproducible development of progressive surface damage and cracking relevant to environmental fragmentation [130].

Despite their widespread use in laboratory photo-oxidative aging and their clear advantages in reproducibility, UV-based photo-oxidative aging approaches represent only part of the oxidative processes experienced by microplastics in the environment. Also, differences in wavelength distribution, irradiance, and exposure geometry between laboratory and natural conditions can influence oxidation depth and degradation pathways. As a result, aging-induced property changes that are generated under laboratory irradiation conditions may differ substantially from those produced in natural environments. Consequently, laboratory UV-aging should generally be interpreted as a controlled and accelerated approach for inducing photo-oxidative alteration, rather than as a direct representation of environmental solar weathering. With the rapid growth of research on plastic photo-oxidative aging, there is a need for standardized aging simulation and evaluation frameworks to ensure comparability and consistency across studies.

### 2.5.2 Chemical Oxidative Aging

In addition to photo-oxidative aging, chemical oxidation is another important pathway for accelerating microplastic aging by generating highly reactive radical species. Advanced oxidation processes (AOPs), including ozonation, Fenton reactions, and persulfate-based treatments, are widely used in laboratory studies because of their high efficiency and controllability [131].

In natural systems, such oxidative conditions can arise from chemically produced radicals, metal-catalyzed reactions, or disinfection reactions in aqueous environments. In contrast, laboratory studies often employ intensified chemical systems to accelerate these reactions under controlled conditions [30, 132]. In ozonation and Fenton systems, hydroxyl radicals (•OH) act as the primary oxidants, whereas persulfate-based systems generate both •OH and sulphate radicals ($SO_4^{\bullet -}$) [133]. These radicals can attack polymer chains, promote chain scission, and introduce oxygen-containing functional groups, thereby weakening polymer structure and accelerating aging. In some cases, radical-driven reactions may further oxidize or mineralize low-molecular-weight organic compounds released from microplastics [134]. Comparative studies have demonstrated that different AOP systems can lead to markedly different aging outcomes. Luo et al. showed that thermally activated persulfate induced stronger surface oxidation of microplastics than ozonation or Fenton treatment, likely due to differences in dominant radical species [133]. Similar conclusions were reported by Liu et al., who attributed the lower oxidation efficiency of Fenton systems to surface passivation by iron-containing precipitates [131]. In contrast, persulfate-based treatments have been shown to promote deeper structural modification and more pronounced surface roughening of PE, PP, and PS, reflecting the higher reactivity and longer lifetime of $SO_4^{\bullet -}$ relative to hydroxyl radicals [134].

Although AOPs exhibit high oxidative capacity, their strong dependence on elevated temperature and intense oxidative reactions limits their direct environmental relevance. Therefore, chemical oxidative aging is best regarded as a mechanistic acceleration approach for probing radical-driven aging pathways, rather than a direct simulation for natural aging timescales. Further studies are required to bridge the knowledge gaps between naturally occurring aging processes of microplastics and chemically induced oxidation.

### 2.5.3 Mechanical Aging and Physical Fragmentation

In natural environments, microplastics are continuously subjected to physical and mechanical stresses arising from environmental loads such as sand grains, sediments, water flow, tides, waves, and interactions with sediments or soils. Abrasion-driven aging is primarily associated with repeated tangential and normal stresses applied to the polymer surface, resulting in surface roughening, crack initiation, and plastic deformation. Once surface cracks penetrate the subsurface, localized material detachment may occur, producing secondary microplastic fragments. At the molecular scale, prolonged mechanical stress can disrupt polymer chain packing and weaken cohesive structures, rendering microplastics more brittle over time and more susceptible to subsequent fragmentation.

Sand abrasion is the most frequently applied approach to simulate physical aging in laboratory settings. More recently, to isolate abrasion as the sole driver, Ziemann et al. designed a quantitative setup in which dry sand freely slid over LDPE films for several months, explicitly targeting micro/nanoplastic release arising only from surface abrasion, indicating that solid abrasion releases debris more efficiently than fluid shear [135]. In addition to direct particle abrasion, hydraulic scouring has been shown to contribute to surface roughness, wrinkles, and cracks on plastic

particles, thereby generating secondary microplastics [136]. In practice, most abrasion experiments are conducted in combination with other aging stressors to better simulate weathering, in which polymers are first embrittled (e.g., by UV/photooxidation) and then fragmented by mechanical action. For example, Song et al. [5] demonstrated that UV pre-aged plastics exhibited substantially greater fragmentation during sand abrasion than their non-aged counterparts, with clear polymer-dependent responses. Similarly, Sun et al. showed that combined UV radiation and mechanical abrasion produced more severe surface damage and higher microplastic release from PE and thermoplastic polyurethane (TPU) films than either stressor alone [137].

Notably, the observed reduction in particle size during abrasion experiments is often attributed to the synergistic effect of oxidative aging and mechanical stress, as oxidation-induced embrittlement lowers fracture resistance and promotes crack propagation under physical loading [2, 127].

### 2.5.4 Other Aging Processes

Beyond photo-oxidative, chemical, and mechanical aging, microplastics in natural environments are also subject to additional transformation pathways that can influence their long-term physicochemical evolution, including biologically mediated aging driven by microbial activity [138] and thermally induced oxidation at elevated temperatures. Although these pathways are often slower or context-dependent, they frequently operate concurrently with other stressors and contribute to the overall aging of microplastics.

Biological aging arises from interactions between microplastics and ubiquitous microorganisms such as bacteria, fungi, and algae. Upon environmental exposure, microorganisms readily colonize plastic surfaces and form biofilms, a process governed by both material properties (e.g., surface area, hydrophobicity, and surface morphology) and surrounding environmental conditions [138,

139]. Subsequent bio-deterioration may occur as microbial growth induces surface-level reactions such as hydrolysis, protonation, or ionization, leading to fragmentation into smaller particles without immediate changes to the polymer backbone [140]. While complete biodegradation of most conventional polymers remains limited under environmental conditions, biological processes can substantially alter surface properties and modulate subsequent physicochemical aging pathways.

Thermal oxidation is another aging mechanism, particularly relevant in environments with elevated temperatures, such as soils, sediments, urban surfaces, and industrial settings. Higher temperatures increase polymer chain mobility and accelerate oxidative reactions, leading to chain scission, embrittlement, and changes in crystallinity [141, 142]. Although thermal aging is rarely isolated as a dominant pathway in environmental studies, it can amplify photo-oxidative and chemical oxidation processes by accelerating reaction kinetics and weakening polymer stability, thereby facilitating fragmentation under additional mechanical or chemical stress.

Overall, microplastic aging in natural environments is governed by the combined action of multiple interacting physical, chemical, and biological processes rather than by any single, isolated mechanism [7, 115]. Environmental variables such as solar radiation, temperature, redox conditions, hydrodynamics, and microbial activity often change simultaneously along spatial and temporal gradients, making it inherently difficult to disentangle the individual contributions of specific aging factors [143]. Consequently, while laboratory studies focusing on single stressors provide valuable mechanistic insights, they may not fully capture the coupled and dynamic nature of natural aging. Addressing this challenge requires developing experimental approaches that more closely approximate environmentally realistic conditions, as well as conducting more

investigations on microplastics aged directly in natural environments, to improve understanding of their behaviour.

## References


1. Gewert B, Plassmann MM, MacLeod M. Pathways for degradation of plastic polymers floating in the marine environment. Environ Sci Process Impacts. 2015;17(9):1513-21.
2. Andrady AL. Microplastics in the marine environment. Mar Pollut Bull. 2011;62(8):1596-605.
3. Alimi OS, Farner Budarz J, Hernandez LM, Tufenkji N. Microplastics and nanoplastics in aquatic environments: aggregation, deposition, and enhanced contaminant transport. Environ Sci Technol. 2018;52(4):1704-24.
4. Lambert S, Wagner M. Microplastics are contaminants of emerging concern in freshwater environments: an overview. In: Lambert S, Wagner M, editors. Freshwater Microplastics: Emerging Environmental Contaminants. Cham: Springer; 2018. p. 1-23.
5. Song YK, Hong SH, Jang M, Han GM, Jung SW, Shim WJ. Combined Effects of UV Exposure Duration and Mechanical Abrasion on Microplastic Fragmentation by Polymer Type. Environ Sci Technol. 2017;51(8):4368-76.
6. Shi Y, Shi L, Huang H, Ye K, Yang L, Wang Z, et al. Analysis of aged microplastics: a review. Environ Chem Lett. 2024;22(4):1861-88.
7. Binda G, Kalčíková G, Allan IJ, Hurley R, Rødland E, Spanu D, et al. Microplastic aging processes: Environmental relevance and analytical implications. TrAC, Trends Anal Chem. 2024;172:117566.
8. Zhenfeng Z, Xingzhou H, Zubo L. Wavelength sensitivity of photooxidation of polypropylene. Polym Degrad Stab. 1996;51(1):93-7.
9. Khelidj N, Colin X, Audouin L, Verdu J, Monchy-Leroy C, Prunier V. Oxidation of polyethylene under irradiation at low temperature and low dose rate. Part I. The case of “pure” radiochemical initiation. Polym Degrad Stab. 2006;91(7):1593-7.

10. Khelidj N, Colin X, Audouin L, Verdu J, Monchy-Leroy C, Prunier V. Oxidation of polyethylene under irradiation at low temperature and low dose rate. Part II. Low temperature thermal oxidation. Polym Degrad Stab. 2006;91(7):1598-605.
11. Song YK, Hong SH, Eo S, Shim WJ. Fragmentation of nano- and microplastics from virgin- and additive-containing polypropylene by accelerated photooxidation. Environ Pollut. 2023;327:121590.
12. Burrows S, Colwell J, Costanzo S, Kaserzon S, Okoffo E, Ribeiro F, et al. UV sources and plastic composition influence microplastic surface degradation: Implications for plastic weathering studies. Journal of Hazardous Materials Advances. 2024;14:100428.
13. Tuttle E, Wiman C, Muñoz S, Law KL, Stubbins A. Sunlight-Driven Photochemical Removal of Polypropylene Microplastics from Surface Waters Follows Linear Kinetics and Does Not Result in Fragmentation. Environ Sci Technol. 2024;58(12):5461-71.
14. He W, Liu S, Zhang W, Yi K, Zhang C, Pang H, et al. Recent advances on microplastic aging: Identification, mechanism, influence factors, and additives release. Sci Total Environ. 2023;889:164035.
15. Maddison C, Sathish CI, Lakshmi D, Wayne OC, Palanisami T. An advanced analytical approach to assess the long-term degradation of microplastics in the marine environment. npj Materials Degradation. 2023;7(1):59.
16. Napper IE, Thompson RC. Environmental Deterioration of Biodegradable, Oxo-biodegradable, Compostable, and Conventional Plastic Carrier Bags in the Sea, Soil, and Open-Air Over a 3-Year Period. Environ Sci Technol. 2019;53(9):4775-83.
17. Dong C-D, Chen C-W, Chen Y-C, Chen H-H, Lee J-S, Lin C-H. Polystyrene microplastic particles: In vitro pulmonary toxicity assessment. J Hazard Mater. 2020;385:121575.
18. Rowenczyk L, Jahandideh H, Lin N, Tufenkji N. Weathering of agricultural polyethylene films in cold climate regions: which parameters influence fragmentation? Environmental Science: Advances. 2024;3(3):470-9.
19. Syranidou E, Karkanorachaki K, Barouta D, Papadaki E, Moschovas D, Avgeropoulos A, et al. Relationship between the Carbonyl Index (CI) and Fragmentation of Polyolefin Plastics during Aging. Environ Sci Technol. 2023;57(21):8130-8.

20. ter Halle A, Ladirat L, Gendre X, Goudouneche D, Pusineri C, Routaboul C, et al. Understanding the Fragmentation Pattern of Marine Plastic Debris. Environ Sci Technol. 2016;50(11):5668-75.

21. Abaroa-Pérez B, Ortiz-Montosa S, Hernández-Brito JJ, Vega-Moreno D. Yellowing, Weathering and Degradation of Marine Pellets and Their Influence on the Adsorption of Chemical Pollutants. Polymers. 2022;14(7):1305.

22. Martí E, Martin C, Galli M, Echevarría F, Duarte CM, Cózar A. The Colors of the Ocean Plastics. Environ Sci Technol. 2020;54(11):6594-601.

23. Brandon J, Goldstein M, Ohman MD. Long-term aging and degradation of microplastic particles: Comparing in situ oceanic and experimental weathering patterns. Mar Pollut Bull. 2016;110(1):299-308.

24. Wu H, Zhao Y, Dong X, Su L, Wang K, Wang D. Probing into the microstructural evolution of isotactic polypropylene during photo-oxidation degradation. Polym Degrad Stab. 2021;183:109434.

25. de la Orden MU, Montes JM, Martínez Urreaga J, Bento A, Ribeiro MR, Pérez E, et al. Thermo and photo-oxidation of functionalized metallocene high density polyethylene: Effect of hydrophilic groups. Polym Degrad Stab. 2015;111:78-88.

26. Canopoli L, Coulon F, Wagland ST. Degradation of excavated polyethylene and polypropylene waste from landfill. Sci Total Environ. 2020;698:134125.

27. De Monte C, Locritani M, Merlino S, Ricci L, Pistolesi A, Bronco S. An In Situ Experiment to Evaluate the Aging and Degradation Phenomena Induced by Marine Environment Conditions on Commercial Plastic Granules. Polymers. 2022;14(6):1111.

28. Shi Y, Liu P, Wu X, Shi H, Huang H, Wang H, et al. Insight into chain scission and release profiles from photodegradation of polycarbonate microplastics. Water Res. 2021;195:116980.

29. Campanale C, Savino I, Massarelli C, Uricchio VF. Fourier Transform Infrared Spectroscopy to Assess the Degree of Alteration of Artificially Aged and Environmentally Weathered Microplastics. Polymers. 2023;15(4):911.

30. Hu J, Lim FY, Hu J. Characteristics and behaviors of microplastics undergoing photoaging and Advanced Oxidation Processes (AOPs) initiated aging. Water Res. 2023;232:119628.

31. Chamas A, Moon H, Zheng J, Qiu Y, Tabassum T, Jang JH, et al. Degradation Rates of Plastics in the Environment. ACS Sustain Chem Eng. 2020;8(9):3494-511.

32. Bayo J, Rojo D, Olmos S. Weathering indices of microplastics along marine and coastal sediments from the harbor of Cartagena (Spain) and its adjoining urban beach. Mar Pollut Bull. 2022;178:113647.
33. Okubo R, Yamamoto A, Kurima A, Sakabe T, Ide Y, Isobe A. Estimation of the age of polyethylene microplastics collected from oceans: Application to the western North Pacific Ocean. Mar Pollut Bull. 2023;192:114951.
34. Liu Z, Zhu Y, Lv S, Shi Y, Dong S, Yan D, et al. Quantifying the Dynamics of Polystyrene Microplastics UV-Aging Process. Environ Sci Technol Lett. 2022;9(1):50-6.
35. Li X, Huang D, Dong H, Wen J, Dong J, Zhang C, et al. Differential photoaging behaviors of different colored commercial polyethylene microplastics in water: The important role of color characteristics. Sci Total Environ. 2024;956:177361.
36. Celik M, Nakano H, Uchida K, Isobe A, Arakawa H. Comparative evaluation of the carbonyl index of microplastics around the Japan coast. Mar Pollut Bull. 2023;190:114818.
37. Sholokhova A, Denafas G, Ceponkus J, Omelianenko T. Microplastics in Landfill Bodies: Abundance, Spatial Distribution and Effect of Landfill Age. Sustainability. 2023;15(6):5017.
38. Lv Y, Huang Y, Kong M, Yang Q, Li G. Multivariate correlation analysis of outdoor weathering behavior of polypropylene under diverse climate scenarios. Polym Test. 2017;64:65-76.
39. Wang T, Liu D, Liu R, Yuan F, Ding Y, Tao J, et al. Weathering Process and Characteristics of Microplastics in Coastal Wetlands: A 24-Month In Situ Study. Environ Sci Technol. 2025;59(15):7667-77.
40. Almond J, Sugumaar P, Wenzel MN, Hill G, Wallis C. Determination of the carbonyl index of polyethylene and polypropylene using specified area under band methodology with ATR-FTIR spectroscopy. e-Polymers. 2020;20(1):369-81.
41. Cox KD, Covernton GA, Davies HL, Dower JF, Juanes F, Dudas SE. Human Consumption of Microplastics. Environ Sci Technol. 2019;53(12):7068-74.
42. Prata JC, da Costa JP, Lopes I, Duarte AC, Rocha-Santos T. Environmental exposure to microplastics: An overview on possible human health effects. Sci Total Environ. 2020;702:134455.
43. Mahmud F, Sarker DB, Jocelyn JA, Sang Q-XA. Molecular and Cellular Effects of Microplastics and Nanoplastics: Focus on Inflammation and Senescence. Cells. 2024;13(21):1788.

44. Hwang J, Choi D, Han S, Jung SY, Choi J, Hong J. Potential toxicity of polystyrene microplastic particles. Sci Rep. 2020;10(1):7391.
45. van den Berg AET, Plantinga M, Vethaak D, Adriaans KJ, Bol-Schoenmakers M, Legler J, et al. Environmentally weathered polystyrene particles induce phenotypical and functional maturation of human monocyte-derived dendritic cells. Journal of Immunotoxicology. 2022;19(1):125-33.
46. Hosseinzadeh M, Wang T, Morales-Caselles C, Callejas S, Eljarrat E, Porte C. Comparative toxicity of beach mesoplastics from South Spain: An in vitro approach. Chemosphere. 2024;352:141494.
47. Gopinath PM, Twayana KS, Ravanan P, John T, Mukherjee A, Jenkins DF, et al. Prospects on the nano-plastic particles internalization and induction of cellular response in human keratinocytes. Particle and Fibre Toxicology. 2021;18(1):35.
48. Wright SL, Kelly FJ. Plastic and Human Health: A Micro Issue? Environ Sci Technol. 2017;51(12):6634-47.
49. Weis JS, Palmquist KH. Reality Check: Experimental Studies on Microplastics Lack Realism. Applied Sciences. 2021;11(18):8529.
50. Mohamed Nor NH, Kooi M, Diepens NJ, Koelmans AA. Lifetime accumulation of microplastic in children and adults. Environ Sci Technol. 2021;55(8):5084-96.
51. Vianello A, Jensen RL, Liu L, Vollertsen J. Simulating human exposure to indoor airborne microplastics using a Breathing Thermal Manikin. Sci Rep. 2019;9(1):8670.
52. Crossman J, Hurley RR, Futter M, Nizzetto L. Transfer and transport of microplastics from biosolids to agricultural soils and the wider environment. Sci Total Environ. 2020;724:138334.
53. Ziajahromi S, Leusch FDL. Systematic assessment of data quality and quality assurance/quality control (QA/QC) of current research on microplastics in biosolids and agricultural soils. Environ Pollut. 2022;294:118629.
54. Mahon AM, O'Connell B, Healy MG, O'Connor I, Officer R, Nash R, et al. Microplastics in Sewage Sludge: Effects of Treatment. Environ Sci Technol. 2017;51(2):810-8.
55. Li X, Chen L, Mei Q, Dong B, Dai X, Ding G, et al. Microplastics in sewage sludge from the wastewater treatment plants in China. Water Res. 2018;142:75-85.

56. Corradini F, Meza P, Eguiluz R, Casado F, Huerta-Lwanga E, Geissen V. Evidence of microplastic accumulation in agricultural soils from sewage sludge disposal. Sci Total Environ. 2019;671:411-20.
57. Harley-Nyang D, Memon FA, Osorio Baquero A, Galloway T. Variation in microplastic concentration, characteristics and distribution in sewage sludge & biosolids around the world. Sci Total Environ. 2023;891:164068.
58. De Bhowmick G, Sarmah AK. Microplastics contamination associated with land-application of biosolids: A perspective. Curr Opin Environ Sci Health. 2022;26:100342.
59. Metcalf, Eddy A. Wastewater engineering treatment and resource recovery: McGraw-Hill Education.; 2014.
60. Cole M, Webb H, Lindeque PK, Fileman ES, Halsband C, Galloway TS. Isolation of microplastics in biota-rich seawater samples and marine organisms. Sci Rep. 2014;4(1):4528.
61. Hurley RR, Lusher AL, Olsen M, Nizzetto L. Validation of a Method for Extracting Microplastics from Complex, Organic-Rich, Environmental Matrices. Environ Sci Technol. 2018;52(13):7409-17.
62. Li X, Chen L, Ji Y, Li M, Dong B, Qian G, et al. Effects of chemical pretreatments on microplastic extraction in sewage sludge and their physicochemical characteristics. Water Res. 2020;171:115379.
63. Lares M, Ncibi MC, Sillanpää M, Sillanpää M. Intercomparison study on commonly used methods to determine microplastics in wastewater and sludge samples. Environ Sci Pollut Res. 2019;26(12):12109-22.
64. Philipp M, Bucheli TD, Kaegi R. The use of surrogate standards as a QA/QC tool for routine analysis of microplastics in sewage sludge. Sci Total Environ. 2022;835:155485.
65. Schrank I, Möller JN, Imhof HK, Hauenstein O, Zielke F, Agarwal S, et al. Microplastic sample purification methods - Assessing detrimental effects of purification procedures on specific plastic types. Sci Total Environ. 2022;833:154824.
66. Maw MM, Boontanon N, Fujii S, Boontanon SK. Rapid and efficient removal of organic matter from sewage sludge for extraction of microplastics. Sci Total Environ. 2022;853:158642.
67. Long Z, Pan Z, Wang W, Ren J, Yu X, Lin L, et al. Microplastic abundance, characteristics, and removal in wastewater treatment plants in a coastal city of China. Water Res. 2019;155:255-65.

68. Lusher AL, Munno K, Hermabessiere L, Carr S. Isolation and Extraction of Microplastics from Environmental Samples: An Evaluation of Practical Approaches and Recommendations for Further Harmonization. Appl Spectrosc. 2020;74(9):1049-65.
69. Tirkey A, Upadhyay LSB. Microplastics: An overview on separation, identification and characterization of microplastics. Mar Pollut Bull. 2021;170:112604.
70. Rani M, Ducoli S, Depero LE, Prica M, Tubić A, Ademovic Z, et al. A Complete Guide to Extraction Methods of Microplastics from Complex Environmental Matrices. Molecules. 2023;28(15):5710.
71. Ivleva NP. Chemical Analysis of Microplastics and Nanoplastics: Challenges, Advanced Methods, and Perspectives. Chem Rev. 2021;121(19):11886-936.
72. Christian AE, Köper I. Microplastics in biosolids: A review of ecological implications and methods for identification, enumeration, and characterization. Sci Total Environ. 2023;864:161083.
73. Hidalgo-Ruz V, Gutow L, Thompson RC, Thiel M. Microplastics in the marine environment: a review of the methods used for identification and quantification. Environ Sci Technol. 2012;46(6):3060-75.
74. Lee S-Y, An J, Kwon J-H. Sequential quantification of number and mass of microplastics in municipal wastewater using Fourier-transform infrared spectroscopy and pyrolysis gas chromatography-mass spectrometry. Environ Pollut. 2023;336:122452.
75. Gao Z, Cizdziel JV, Chen L. Microplastics profile in sludge from a university wastewater treatment plant and the influence of chemical digestions on Nile red stained microplastics. J Environ Chem Eng. 2023;11(3):109671.
76. Circelli L, Cheng Z, Garwood E, Yuksel K, Di Iorio E, Angelico R, et al. Comparison of ATR-FTIR and NIR spectroscopy for identification of microplastics in biosolids. Sci Total Environ. 2024;916:170215.
77. Horton AA, Cross RK, Read DS, Jürgens MD, Ball HL, Svendsen C, et al. Semi-automated analysis of microplastics in complex wastewater samples. Environ Pollut. 2021;268:115841.
78. Tagg AS, Sapp M, Harrison JP, Ojeda JJ. Identification and Quantification of Microplastics in Wastewater Using Focal Plane Array-Based Reflectance Micro-FT-IR Imaging. Anal Chem. 2015;87(12):6032-40.

79. Ruffell H, Pantos O, Robinson B, Gaw S. A method for the extraction of microplastics from solid biowastes including biosolids, compost, and soil for analysis by μ-FTIR. MethodsX. 2024;12:102761.
80. Pagliaccia B, Ascolese M, Vannini E, Carretti E, Lubello C, Gori R. Methodologic insights aimed to set-up an innovative Laser Direct InfraRed (LDIR)-based method for the detection and characterization of microplastics in wastewaters. Sci Total Environ. 2025;967:178817.
81. Fortin S, Song B, Burbage C. Quantifying and identifying microplastics in the effluent of advanced wastewater treatment systems using Raman microspectroscopy. Mar Pollut Bull. 2019;149:110579.
82. Becucci M, Mancini M, Campo R, Paris E. Microplastics in the Florence wastewater treatment plant studied by a continuous sampling method and Raman spectroscopy: A preliminary investigation. Sci Total Environ. 2022;808:152025.
83. Lessa Belone MC, Yli-Rantala E, Sarlin E, Kokko M. Microplastics in an anaerobic digester treating sewage sludge: Occurrence and factors affecting their identification with Raman spectroscopy. J Hazard Mater. 2025;491:138015.
84. Li X-y, Liu H-t, Wang L-x, Guo H-n, Zhang J, Gao D. Effects of typical sludge treatment on microplastics in China—Characteristics, abundance and micro-morphological evidence. Sci Total Environ. 2022;826:154206.
85. Toapanta T, Okoffo ED, Ede S, O'Brien S, Burrows SD, Ribeiro F, et al. Influence of surface oxidation on the quantification of polypropylene microplastics by pyrolysis gas chromatography mass spectrometry. Sci Total Environ. 2021;796:148835.
86. Xu Y, Ou Q, Wang X, Hou F, Li P, van der Hoek JP, et al. Assessing the Mass Concentration of Microplastics and Nanoplastics in Wastewater Treatment Plants by Pyrolysis Gas Chromatography–Mass Spectrometry. Environ Sci Technol. 2023;57(8):3114-23.
87. Okoffo ED, Ribeiro F, O'Brien JW, O'Brien S, Tscharke BJ, Gallen M, et al. Identification and quantification of selected plastics in biosolids by pressurized liquid extraction combined with double-shot pyrolysis gas chromatography–mass spectrometry. Sci Total Environ. 2020;715:136924.
88. Wu Z, Wu Y, Zhang Z, Dong J, Li H, Zhao X, et al. Quantitatively tracing microplastics in sewage sludge using thermodesorption gas chromatography/mass spectrometry combined with pyrolysis. J Hazard Mater. 2025;494:138652.

89. Dierkes G, Lauschke T, Becher S, Schumacher H, Földi C, Ternes T. Quantification of microplastics in environmental samples via pressurized liquid extraction and pyrolysis-gas chromatography. Anal Bioanal Chem. 2019;411(26):6959-68.
90. Cho S-J, Choi J-H, Yoon Y-S, Um N-I. Microplastic Pollution in Sewage Sludge from Wastewater Treatment Plants and Estimation of Microplastic Release. Water. 2025;17(3):387.
91. Okoffo ED, Rauert C, Thomas KV. Mass quantification of microplastic at wastewater treatment plants by pyrolysis-gas chromatography–mass spectrometry. Sci Total Environ. 2023;856:159251.
92. Bitter H, Lackner S. Fast and easy quantification of semi-crystalline microplastics in exemplary environmental matrices by differential scanning calorimetry (DSC). Chem Eng J. 2021;423:129941.
93. Lee J, Yoon S, Jang T, Choi J-H, Kim N, Kim H-O, et al. A facile approach to microplastic identification and quantification using differential scanning calorimetry. Sci Total Environ. 2024;957:177456.
94. Sorolla-Rosario D, Llorca-Porcel J, Pérez-Martínez M, Lozano-Castelló D, Bueno-López A. Study of microplastics with semicrystalline and amorphous structure identification by TGA and DSC. J Environ Chem Eng. 2022;10(1):106886.
95. Majewsky M, Bitter H, Eiche E, Horn H. Determination of microplastic polyethylene (PE) and polypropylene (PP) in environmental samples using thermal analysis (TGA-DSC). Sci Total Environ. 2016;568:507-11.
96. Bitter H, Krause L, Kirchen F, Fundneider T, Lackner S. Semi-crystalline microplastics in wastewater plant effluents and removal efficiencies of post-treatment filtration systems. Water Research X. 2022;17:100156.
97. Leng Y, Gaburici L, Cao X, Zou S. Quantification of microplastics in complex environmental matrices using a tiered approach with modulated differential scanning calorimetry (MDSC). Anal Bioanal Chem. 2025.
98. Käppler A, Fischer D, Oberbeckmann S, Schernewski G, Labrenz M, Eichhorn K-J, et al. Analysis of environmental microplastics by vibrational microspectroscopy: FTIR, Raman or both? Anal Bioanal Chem. 2016;408(29):8377-91.

99. Okoffo ED, O'Brien S, O'Brien JW, Tscharke BJ, Rauert C, Rødland ES, et al. Does size matter? Quantification of plastics associated with size fractionated biosolids. Sci Total Environ. 2022;811:152382.
100. Mintenig SM, Int-Veen I, Löder MGJ, Primpke S, Gerdts G. Identification of microplastic in effluents of waste water treatment plants using focal plane array-based micro-Fourier-transform infrared imaging. Water Res. 2017;108:365-72.
101. Primpke S, Wirth M, Lorenz C, Gerdts G. Reference database design for the automated analysis of microplastic samples based on Fourier transform infrared (FTIR) spectroscopy. Anal Bioanal Chem. 2018;410(21):5131-41.
102. Araujo CF, Nolasco MM, Ribeiro AMP, Ribeiro-Claro PJA. Identification of microplastics using Raman spectroscopy: Latest developments and future prospects. Water Res. 2018;142:426-40.
103. Huang Z, Hu B, Wang H. Analytical methods for microplastics in the environment: a review. Environ Chem Lett. 2023;21(1):383-401.
104. Cowger W, Roscher L, Jebens H, Chamas A, Maurer BD, Gehrke L, et al. Generation of macro- and microplastic databases by high-throughput FTIR analysis with microplate readers. Anal Bioanal Chem. 2024;416(6):1311-20.
105. Cowger W, Steinmetz Z, Gray A, Munno K, Lynch J, Hapich H, et al. Microplastic Spectral Classification Needs an Open Source Community: Open Specy to the Rescue! Anal Chem. 2021;93(21):7543-8.
106. Munno K, De Frond H, O'Donnell B, Rochman CM. Increasing the Accessibility for Characterizing Microplastics: Introducing New Application-Based and Spectral Libraries of Plastic Particles (SLoPP and SLoPP-E). Anal Chem. 2020;92(3):2443-51.
107. Cowger W, Gray A, Christiansen SH, DeFrond H, Deshpande AD, Hemabessiere L, et al. Critical Review of Processing and Classification Techniques for Images and Spectra in Microplastic Research. Appl Spectrosc. 2020;74(9):989-1010.
108. Chen M, Coleman B, Gaburici L, Prezgot D, Jakubek ZJ, Sivarajah B, et al. Identification of microplastics extracted from field soils amended with municipal biosolids. Sci Total Environ. 2024;907:168007.
109. Seeley ME, Lynch JM. Previous successes and untapped potential of pyrolysis–GC/MS for the analysis of plastic pollution. Anal Bioanal Chem. 2023;415(15):2873-90.

110. Ainali NM, Bikiaris DN, Lambropoulou DA. Aging effects on low- and high-density polyethylene, polypropylene and polystyrene under UV irradiation: An insight into decomposition mechanism by Py-GC/MS for microplastic analysis. J Anal Appl Pyrolysis. 2021;158:105207.
111. Koelmans AA, Redondo-Hasselerharm PE, Nor NHM, de Ruijter VN, Mintenig SM, Kooi M. Risk assessment of microplastic particles. Nature Reviews Materials. 2022;7(2):138-52.
112. Jolliffe IT, Cadima J. Principal component analysis: a review and recent developments. Philosophical Transactions of the Royal Society A: Mathematical, Physical and Engineering Sciences. 2016;374(2065).
113. Zvekic M, Richards LC, Tong CC, Krogh ET. Characterizing photochemical ageing processes of microplastic materials using multivariate analysis of infrared spectra. Environ Sci Process Impacts. 2022;24(1):52-61.
114. Conterosito E, Roncoli M, Ivaldi C, Ferretti M, De Felice B, Parolini M, et al. μ-FTIR Reflectance Spectroscopy Coupled with Multivariate Analysis: A Rapid and Robust Method for Identifying the Extent of Photodegradation on Microplastics. Anal Chem. 2025;97(6):3263-73.
115. Binda G, Zanetti G, Bellasi A, Spanu D, Boldrocchi G, Bettinetti R, et al. Physicochemical and biological ageing processes of (micro)plastics in the environment: a multi-tiered study on polyethylene. Environ Sci Pollut Res. 2023;30(3):6298-312.
116. Ferreiro B, Andrade JM, Paz-Quintáns C, Fernández-González V, López-Mahía P, Muniategui S. Weathering-independent differentiation of microplastic polymers by reflectance IR spectrometry and pattern recognition. Mar Pollut Bull. 2022;181:113897.
117. Qin L, Zhu Y, Liu S, Zhang X, Zhao Y. The Shapley Value in Data Science: Advances in Computation, Extensions, and Applications. Mathematics. 2025;13(10):1581.
118. Scott Lundberg S-IL. A Unified Approach to Interpreting Model Predictions. 31st Conference on Neural Information Processing Systems (NIPS 2017); Long Beach, CA, USA. 2017.
119. He Z, Yang Y, Fang R, Zhou S, Zhao W, Bai Y, et al. Integration of shapley additive explanations with random forest model for quantitative precipitation estimation of mesoscale convective systems. Front Environ Sci. 2023;Volume 10 - 2022.
120. Silva SJ, Keller CA, Hardin J. Using an Explainable Machine Learning Approach to Characterize Earth System Model Errors: Application of SHAP Analysis to Modeling Lightning Flash Occurrence. Journal of Advances in Modeling Earth Systems. 2022;14(4):e2021MS002881.

121. Ochoa L, Nitzberg EJ, Chant RJ, Arbuckle-Keil G, Fahrenfeld NL. Polymer weathering under simulated solar radiation and comparison to stormwater and estuarine microplastics. Chemosphere. 2025;379:144379.
122. Nayrac N, Bellenger J-P, Segura PA. Screening of polymer types and chemical weathering in macro- and meso-plastics found on lake and river beaches using a combined chemometric approach. Anal Methods. 2022;14(47):4977-89.
123. Forbes TP, Pettibone JM, Windsor E, Conny JM, Fletcher RA. Rapid Chemical Screening of Microplastics and Nanoplastics by Thermal Desorption and Pyrolysis Mass Spectrometry with Unsupervised Fuzzy Clustering. Anal Chem. 2023;95(33):12373-82.
124. Jahnke A, Arp HPH, Escher BI, Gewert B, Gorokhova E, Kühnel D, et al. Reducing Uncertainty and Confronting Ignorance about the Possible Impacts of Weathering Plastic in the Marine Environment. Environ Sci Technol Lett. 2017;4(3):85-90.
125. Andrady AL, Barnes PW, Bornman JF, Gouin T, Madronich S, White CC, et al. Oxidation and fragmentation of plastics in a changing environment; from UV-radiation to biological degradation. Sci Total Environ. 2022;851:158022.
126. Singh B, Sharma N. Mechanistic implications of plastic degradation. Polym Degrad Stab. 2008;93(3):561-84.
127. Andrady AL, Heikkilä AM, Pandey KK, Bruckman LS, White CC, Zhu M, et al. Effects of UV radiation on natural and synthetic materials. Photochem Photobiol Sci. 2023;22(5):1177-202.
128. Miranda MN, Sampaio MJ, Tavares PB, Silva AMT, Pereira MFR. Aging assessment of microplastics (LDPE, PET and uPVC) under urban environment stressors. Sci Total Environ. 2021;796:148914.
129. Zhu K, Jia H, Sun Y, Dai Y, Zhang C, Guo X, et al. Long-term phototransformation of microplastics under simulated sunlight irradiation in aquatic environments: Roles of reactive oxygen species. Water Res. 2020;173:115564.
130. Pinlova B, Nowack B. From cracks to secondary microplastics - surface characterization of polyethylene terephthalate (PET) during weathering. Chemosphere. 2024;352:141305.
131. Liu P, Qian L, Wang H, Zhan X, Lu K, Gu C, et al. New Insights into the Aging Behavior of Microplastics Accelerated by Advanced Oxidation Processes. Environ Sci Technol. 2019;53(7):3579-88.

132. Kim S, Sin A, Nam H, Park Y, Lee H, Han C. Advanced oxidation processes for microplastics degradation: A recent trend. Chemical Engineering Journal Advances. 2022;9:100213.
133. Luo H, Zeng Y, Zhao Y, Xiang Y, Li Y, Pan X. Effects of advanced oxidation processes on leachates and properties of microplastics. J Hazard Mater. 2021;413:125342.
134. Ortiz D, Munoz M, Nieto-Sandoval J, Romera-Castillo C, de Pedro ZM, Casas JA. Insights into the degradation of microplastics by Fenton oxidation: From surface modification to mineralization. Chemosphere. 2022;309:136809.
135. Ziemann S, Alberg CH, Yadav H, Qin J, Iskander SM, Rahman E, et al. Novel Release Mechanism of Microplastics and Nanoplastics by Environmentally Relevant Sand Abrasion. Environ Sci Technol. 2025;59(38):20684-94.
136. Zhang X, Liu C, Liu J, Zhang Z, Gong Y, Li H. Release of microplastics from typical rainwater facilities during aging process. Sci Total Environ. 2022;813:152674.
137. Sun J, Zheng H, Xiang H, Fan J, Jiang H. The surface degradation and release of microplastics from plastic films studied by UV radiation and mechanical abrasion. Sci Total Environ. 2022;838:156369.
138. Zettler ER, Mincer TJ, Amaral-Zettler LA. Life in the “Plastisphere”: Microbial Communities on Plastic Marine Debris. Environ Sci Technol. 2013;47(13):7137-46.
139. Amaral-Zettler LA, Zettler ER, Mincer TJ. Ecology of the plastisphere. Nature Reviews Microbiology. 2020;18(3):139-51.
140. Mohanan N, Montazer Z, Sharma PK, Levin DB. Microbial and Enzymatic Degradation of Synthetic Plastics. Frontiers in Microbiology. 2020;Volume 11 - 2020.
141. Papac Zjačić J, Tonković S, Pulitika A, Katančić Z, Kovačić M, Kušić H, et al. Effect of Aging on Physicochemical Properties and Size Distribution of PET Microplastic: Influence on Adsorption of Diclofenac and Toxicity Assessment. Toxics. 2023;11(7).
142. Ding L, Mao R, Ma S, Guo X, Zhu L. High temperature depended on the ageing mechanism of microplastics under different environmental conditions and its effect on the distribution of organic pollutants. Water Res. 2020;174:115634.
143. Ren Z, Gui X, Xu H, Xu X, Cao X. Contrasting effects of physical and chemical aging of microplastics on the transport of lead and copper in sandy soil. Environmental Research. 2025;286:122991.

# CHAPTER 3 QUANTIFICATION OF MICROPLASTICS IN COMPLEX ENVIRONMENTAL MATRICES USING A TIERED APPROACH WITH MODULATED DIFFERENTIAL SCANNING CALORIMETRY (MDSC)


## Abstract

The widespread presence of microplastics (MPs) in biosolids raises significant concerns, primarily because biosolids are commonly used as fertilizers in soil, where MPs can accumulate, disrupt soil health and microbial activity, and potentially enter the food chain. Accurate quantification of MPs in biosolids and soil remains challenging due to their low concentrations, aging-induced property variations, and complex biosolid matrices. To address these challenges, modulated differential scanning calorimetry (MDSC), a high-sensitivity, low-detection limit, and cost-effective thermal analysis approach, was employed to quantify MPs in complex biosolid matrices. Using micron-sized polyethylene (PE), polypropylene (PP), polyamide 6 (PA6), and polyethylene terephthalate (PET) spiked into biosolid matrices, MPs were quantified based on the enthalpies generated from the melting peaks. MDSC exhibited 1.4–2.5 times higher sensitivity than conventional DSC, with a theoretical limit of quantification (LOQ) as low as 7 μg/g. An averaged recovery of (93±20) % for four micron-sized plastics from three different sources using MDSC demonstrated good accuracy, confirming its reliability. To highlight its applicability to real-world samples, a tiered workflow incorporating MDSC, Raman spectroscopy, and thermogravimetric analysis (TGA) was employed to identify and quantify MPs in biosolids. These findings indicate that MDSC, especially when combined with complementary techniques, is a sensitive and accurate method for identifying and quantifying MPs in complex matrices.

## 3.1 Introduction

Microplastics (MPs), typically defined as plastic particles smaller than 5 mm, have become a primary environmental concern due to their widespread distribution and potential to disrupt both marine and terrestrial ecosystems [1, 2]. Their presence in soil and water has raised alarms as MPs can accumulate in the food chain, potentially affecting human health and biodiversity. As MP research progresses, there is a growing focus on identifying, quantifying, and understanding environmental abundance and implications of MPs. The quantification of MPs remains particularly challenging due to their broad size distributions, diverse compositions, and complex matrices [3, 4]. Biosolids, the by-products of wastewater treatment plants (WWTPs), are major accumulators of MPs [5-7], and it has been reported that there are as many as 12,000 MP particles per kg of biosolids [8]. In North America, approximately 50% of biosolids is processed and applied as fertilizer in agriculture [9], which inadvertently makes biosolids one of the primary routes for microplastics to be released into the environment [10, 11].

As global plastic production and consumption increase, unmanaged discharges into WWTPs will likely result in more MPs entering the environment [10, 12]. Although research on microplastic pollution is advancing rapidly, identifying and quantifying MPs in biosolids remains challenging [13]. This is due to 1) difficulties in extracting MPs, 2) instrumental limitations in detecting small-sized particles, and 3) the presence of organic materials and other contaminants in matrices that complicate the quantification process [14-16]. Therefore, there is a pressing need for reliable and efficient methods to identify and quantify MPs in complex matrices, such as biosolids, to better assess their environmental risks.

Existing analytical methods, such as Fourier-transform infrared (FTIR) and Raman spectroscopies, are commonly used to identify MPs based on their chemical structures [17, 18]. While both can

effectively determine the chemical characteristics of the MP samples of interest, they are often limited in quantitative measurements. While quantifications are possible through labour-intensive visual sorting or by integrating machine learning techniques, these methods frequently face challenges associated with sample heterogeneity in complex sample matrices, including biosolids [19]. Useful as they are, other techniques, such as pyrolysis gas chromatography-mass spectrometry (py-GC/MS) [20-22], are limited by high costs and interference from organic matter in the matrices, which are known to increase background noise [23]. Alternatively, thermogravimetric analysis (TGA) has also been used to quantify MPs [24, 25]. However, the TGA technique generally fails when thermal transitions overlap [26].

Differential scanning calorimetry (DSC) is a widely used technique for analyzing polymers, measuring the enthalpy changes associated with thermal transitions, primarily melting and crystallization [24, 27]. This technique allows for quantification based on the amount of heat absorbed or released [28-31]. While conventional DSC can be used to quantify polymer content in biosolids, it is limited in resolving overlapping thermal events, especially in complex samples, thus hindering its wide application in MPs analysis [28]. To address this issue, modulated differential scanning calorimetry (MDSC) has emerged as a technique that enhances detection resolution and sensitivity [32, 33]. The MDSC technique integrates conventional DSC with periodic temperature modulation, enabling simultaneous measurement responses to multiple heating rates within the same experimental setup, thereby eliminating the need for compromises between resolution and sensitivity [34]. The MDSC has been shown to enhance the analysis of MPs by separating reversible and irreversible thermal events via temperature modulation, allowing the method to distinguish overlapping thermal signals and providing a clearer understanding of complex materials [35]. This not only enhances sensitivity and resolution but also facilitates the detection

of weak transitions and the separation of overlapping thermal events [33, 34, 36], making the MDSC highly effective for identifying different polymer types in complex samples and distinguishing their crystalline and amorphous phases.

In this study, we develop and validate an MDSC-based method to both identify and quantify MPs in biosolid matrices with high detection sensitivity and low LOQ. Furthermore, a tiered workflow combining MDSC, TGA, and Raman spectroscopy is proposed to enable the characterization of trace amounts of MPs, such as PE, PP, PA6, and PET, in complex matrices, including biosolids, with enhanced efficiency and sensitivity.

## 3.2 Materials and Methods

### 3.2.1 Microplastics Preparation and Characterization

Three types of microplastics were used in this study (Table 3.1). Commercial microplastic powders (CMP) included PE (10 μm) and PP (42 μm) from Polysciences (Warrington, PA, USA), PET (20 μm) from Chemazone (Leduc, AB, Canada), and PA6 produced by blending Sigma PA6 pellets (Oakville, ON, Canada) and sieving through a 125 μm mesh. Product-derived microplastics (PMP) were sourced to reflect common consumer plastic waste: PE from laboratory wash bottles, PP from food containers, PET from disposable water bottles, and PA6 from umbrella straps. PE, PP, and PET were blended and sieved to <125 μm, while PA6 straps were cut into 1–2 mm pieces and manually pulled into ~50 μm fibres. Aged-CMPs were prepared by suspending 50 mg of CMPs in 150 mL of 0.01% polyvinyl alcohol (PVA) solution, followed by thermal aging in an autoclave and probe sonication [37], after which the suspension was filtered through 5 μm PTFE membranes (Sartorius, Aubagne, France) and dried at 50 °C.

**Table 3.1** Sources and preparation of microplastic samples for calibration and validation of the MDSC method.

| Source Type | Polymer | Material Description | Preparation / Size | Supplier/ Origin |
|---|---|---|---|---|
| **Commercial Microplastic Powders (CMP)** | PE | Powder, ~10 μm | Direct use | Polysciences Inc. (Warrington, PA, USA) |
| | PP | Powder, ~42 μm | Direct use | Polysciences Inc. (Warrington, PA, USA) |
| | PET | Powder, ~20 μm | Direct use | Chemazone Inc. (Leduc, AB, Canada) |
| | PA6 | From PA6 pellets | Blended, sieved <125 μm | Sigma (Oakville, ON, Canada) |
| **Product-derived Microplastics (PMP)** | PE | Lab wash bottles | Blended, sieved <125 μm | Consumer plastic waste |
| | PP | Food containers | Blended, sieved <125 μm | Consumer plastic waste |
| | PET | Water bottles | Blended, sieved <125 μm | Consumer plastic waste |
| | PA6 | Umbrella wrist straps | Cut 1–2 mm, pulled to ~50 μm fibres | Consumer plastic waste |
| **Aged-CMP** | PE, PP, PET, PA6 (from CMPs) | Suspended in 0.01% PVA | Autoclave + sonication, filtered (5 μm PTFE), dried at 50°C | Prepared in lab |

### 3.2.2 Microplastics Extraction from Biosolids

In this study, raw biosolids from a secondary-level wastewater treatment facility with anaerobic digestion were used; they were collected from various locations across Canada [5, 6]. To ensure laboratory biosafety, the collected biosolids were autoclaved before any further processing. For the pre-treatment, 5 grams of raw biosolids were reacted with 150 mL of 30% $H_2O_2$ (Fisher Scientific, Ottawa, ON, Canada) at room temperature until bubbling ceased, which takes up to 7 days, indicating complete digestion. Subsequently, the mixture was filtered through a Sartorius 1.2 μm PTFE filter (Aubagne, France), and the collected solid was then transferred to a saturated

$CaCl_2$ solution (density of 1.42 g/cm³) in a custom-made glass separator [38] for density separation after the mixture was allowed to settle overnight. The $CaCl_2$ solution was used because it had a higher density than most common polymers, and is considered safe and environmentally friendly. Subsequently, the supernatant– the fraction with a density <1.42 g/cm³– was filtered through a 1.2 μm PTFE filter. The retained solids were collected, dried at 50 °C, and then manually ground in a ceramic mortar and pestle for 10-20 seconds to de-agglomerate dried clumps before further analysis.

### 3.2.3 MDSC Measurement and Analysis

A DSC Q2000 (TA Instruments, New Castle, DE, USA) equipped with a refrigerated cooling system (RCS90, TA Instruments, New Castle, DE, USA) was used for the MDSC measurements. Briefly, dry samples (5-15 mg) were placed into Tzero aluminum pans (TA Instruments, New Castle, DE, USA), sealed with Tzero lids (TA Instruments, New Castle, DE, USA), and then encapsulated using a Tzero DSC sample encapsulation press (TA Instruments, New Castle, DE, USA). All crucibles and sample masses were measured using a Mettler-Toledo XPE-205 analytical balance (Oakland, CA, USA) with a readability of 0.01 mg. The DSC equipment was calibrated periodically during the measurements using indium standards. Measurements were performed under MDSC mode from 50 °C to 300 °C. Specifically, during MDSC measurements, a modulated heating rate of 0.796 °C every 60 seconds was superimposed on a constant average heating rate, yielding total heat flow data equivalent to those obtained from conventional DSC [33]. A heat-cool-heat cycle was used to erase the thermal history and water effects and to maximize the uniformity of the crystallinity of the samples [28]. Thermograms obtained from the second heating ramp were analyzed. Samples were subjected to a heating/cooling rate of 5 °C/min to enhance the

resolution of thermal transitions [39]. A nitrogen purge gas flow of 50 mL/min throughout the process.

To identify plastics in the MDSC samples, the 'peak maximum' feature in the Universal Analysis 2000 (version 4.7.0.2, TA Instruments, New Castle, DE, USA) was employed to locate the peaks of melting temperatures ($T_m$). This was followed by comparisons with a library of standard plastic melting peaks (Table A2) to identify potential plastic candidates.

To further quantify the amount of the identified plastics in the MDSC samples, each of the melting peak areas from the second heating cycle was integrated by applying linear peak integration at the onset and offset of the melting peaks of PE, PP, PA6, and PET at 79, 120, 168, 226, and 265 °C, respectively, all with an error of ± 1°C. To prepare calibration curves to establish melting peak areas vs. the corresponding plastic masses, individual and varying known amounts of PE, PP, PA6, and PET CMP were pre-mixed and subsequently spiked into a digested blank biosolids (dBB) matrix, designated as CMP-dBB mixtures hereafter. It should be noted that the "dBB matrix" refers to the biosolids obtained after digestion of the raw blank biosolid (rBB) to remove organic matter, and has been confirmed to be plastic-free via both MDSC and TGA analyses. The calibration curves were used to calculate the mass of the MP in the MDSC samples.

To evaluate potential matrix effects on polymer quantification using thermal analysis, CMP mixtures containing PE, PP, PA6, and PET were spiked into two types of environmental matrices: (1) biosolid and (2) artificial soil (AS). The samples were subjected to both conventional DSC and MDSC analysis to assess differences in thermal signal clarity. The AS matrix was a gift from the Environment and Climate Change Canada, prepared in-house according to Organization for Economic Co-operation and Development (OECD) guidelines, by mixing 10% sphagnum peat,

20% kaolin clay, and 70% silica sand by dry weight [40], resulting in an AS with a measured organic matter (OM) content of approximately 7%.

### 3.2.4 Determination of Quantification Error of MPs using Three Sources

To evaluate the accuracy and selectivity of MDSC quantification of MPs, mean absolute error (MAE) and analytical recovery were assessed using microplastic samples from three different sources — CMP, MPP, and aged-CMP — that were characterized using MDSC. Each sample consisted of mixtures of PE, PP, PA6, and PET in varying proportions, with each plastic ranging from 0.03 mg to 1.11 mg per sample. The resulting plastic mixtures were spiked with the dBB matrix so that the total sample mass (i.e., the plastic mix and the dBB matrix) was approximately 10 mg for the MDSC measurement. The MAE and analytical recovery were calculated using Eq. 3.1 and Eq. 3.2:

$$Mean\ Absolute\ Error\ (MAE, mg) = \frac{1}{n}\sum_{i=1}^{n} |(m_{measure,i} - \bar{m}_{blank}) - m_{true,i}| \quad \text{(Eq. 3.1)}$$

$$Recovery\ (\%) = \frac{1}{n}\sum_{i=1}^{n} (\frac{m_{measure,i} - \bar{m}_{blank}}{m_{true,i}} \times 100\%) \quad \text{(Eq. 3.2)}$$

where $m_{measure}$ is the measured mass of a given species of the polymer in the spiked mixture determined by the MDSC, $\bar{m}_{blank}$ is the averaged peak area of the dBB matrix measured at the onset and offset of the MPs' melting peaks (79, 120, 168, 226, and 265 °C for PE, PP, PA6, and PET, respectively); mean of six blank runs, and $m_{true}$ is the corresponding mass of the same polymer determined using an analytical balance (Mettler-Toledo, Oakland, CA, USA). Here, *n* is the total number of spiked samples that were measured; n = 10.

### 3.2.5 TGA Analysis

To validate the MDSC results, TGA analysis was conducted using a Netzsch TG 209F1 Iris system (Selb, Germany) from 40 °C to 1000 °C at a rate of 5 °C/min under an argon atmosphere (50 mL/min). Briefly, samples (3–10 mg) were placed in an empty aluminum oxide crucible for measurement. The TGA data were processed using Proteus Analysis software (version 8.0.2, Selb, Germany), with smoothing applied to the derived thermogravimetric (DTG) curves. The decomposition temperature range of plastics ($T_d$, 380–500 °C) was determined from the DTG curve, allowing for the determination of mass loss on the thermogravimetric (TG) curve. To assess the correlation between MDSC and TGA, different CMP mixtures containing equal amounts of PE, PP, PA6, and PET were spiked into the dBB matrix at 4%, 10%, and 20% per polymer (16%, 40%, and 80% total CMP), with the remaining fraction being dBB. In each sample, TGA provided the total polymer mass, determined by the total mass loss occurring within the temperature range of 380°C to 500°C for the four plastics. The mass of each polymer was determined from MDSC, and the results were summed to obtain the total mass. The relative error was determined by comparing the total mass measured by the MDSC ($m_{\mathrm{MDSC}}$) with that by the TGA ($m_{\mathrm{TGA}}$), normalized to $m_{\mathrm{TGA}}$ as the reference method, as shown in Eq. 3.3.

$$Relative\ error\ (\%) = \frac{m_{TGA} - m_{MDSC}}{m_{TGA}} \times 100\% \qquad \text{(Eq. 3.3)}$$

### 3.2.6 Raman Spectroscopy Analysis

To prepare samples for Raman analysis, 0.5 mg of the extracted materials from the tested biosolid were suspended as-is in 1 mL Milli-Q water. Then, 20 µL of the suspension was drop-cast onto a double-sided polished silicon wafer and dried in a 50 °C oven to ensure adhesion. This process was repeated three times to accumulate sufficient samples for analysis. Subsequently, Raman

spectra were acquired using a inVia™ confocal Raman microscope (Renishaw plc., UK) equipped with a 633 nm excitation laser and a 1200/mm grating (50 W). Optical images were captured using a Leica 100× objective (Concord, ON, Canada). Each Raman spectrum was recorded with a 10-second exposure time over the spectral range of 950–3200 $cm^{-1}$. A total of 25 spectra were collected per sample from randomly selected different locations. The spectra were baseline corrected using a peak analyzer function in OriginPro 2021 (OriginLab, Northampton, MA, USA). For environmental samples, the obtained spectra were compared with an in-house Raman polymer spectral library for qualitative analysis.

## 3.3 Results and Discussion

### 3.3.1 Microplastics Characterization Using MDSC and Its Comparison with Conventional DSC

It is known that MPs often exist in the environment as mixtures of various plastics and are typically embedded within complex matrices [6]. These matrices can negatively impact the accuracy of thermal analytical results, as organic and inorganic compounds within the matrices are known to lead to over- or underestimation of quantifications [41]. In the current study, we demonstrate the use of MDSC as a feasible thermal analytical method for quantifying MPs in biosolid matrices. To enhance environmental relevance and analytical accuracy, the composition of MPs in complex matrices was mimicked by spiking the dBB matrices with mixtures of CMP-PE, CMP-PP, CMP-PA6, and CMP-PET. As shown in Figure 3.1A, distinct melting peaks corresponding to the semi-crystalline phases of PE, PP, PA6, and PET were identified, allowing clear differentiation in both MDSC and conventional DSC.

Closer analysis of the thermograms revealed that at low plastic concentrations (i.e., 0.05 mg), MDSC exhibited a flatter baseline and more distinct peak shapes than conventional DSC, which is particularly true for the cases of PA6 and PET. This observation is likely due to the enhanced ability of MDSC to detect weak thermal transitions by separating overlapping thermal transitions of matrix decompositions and plastic melting [33, 42, 43], which forms the basis for quantifying MPs in complex biosolid matrices.

The thermal behaviours of individual CMPs (i.e., CMP-PE, CMP-PP, CMP-PA6, and CMP-PET) were separately characterized using the MDSC. Distinct melting points were observed at approximately (110.5±0.7) °C, (155.1±0.6) °C, (220.2±0.4) °C, and (239.5±0.3) °C for CMP-PE, -PP, -PA6, and -PET, respectively (Figure A1). It is interesting to note that for a given polymer, differences in melting point were observed when the polymer was characterized as a polymer mixture vs. individually by MDSC. This was particularly pronounced for PA6 and PET, with melting point shifting up to 7 °C and 8 °C, respectively (Figures A1C–D). Similar $T_m$ shifts of PA were also observed in a previous study [29]. Additionally, it is consistent with a recent TG study on mixed thermoplastics; PA6 and PET pairs exhibit interfacial interactions that accelerate degradation and deviate from linear superposition, particularly when contact is high, indicating that phase interactions can alter thermal behaviour in mixtures [44]. The shift in melting peaks, therefore, justifies the importance of using polymer mixtures – as opposed to individual polymers – in MPs studies to better understand polymer behaviour and achieve more accurate analytical results.

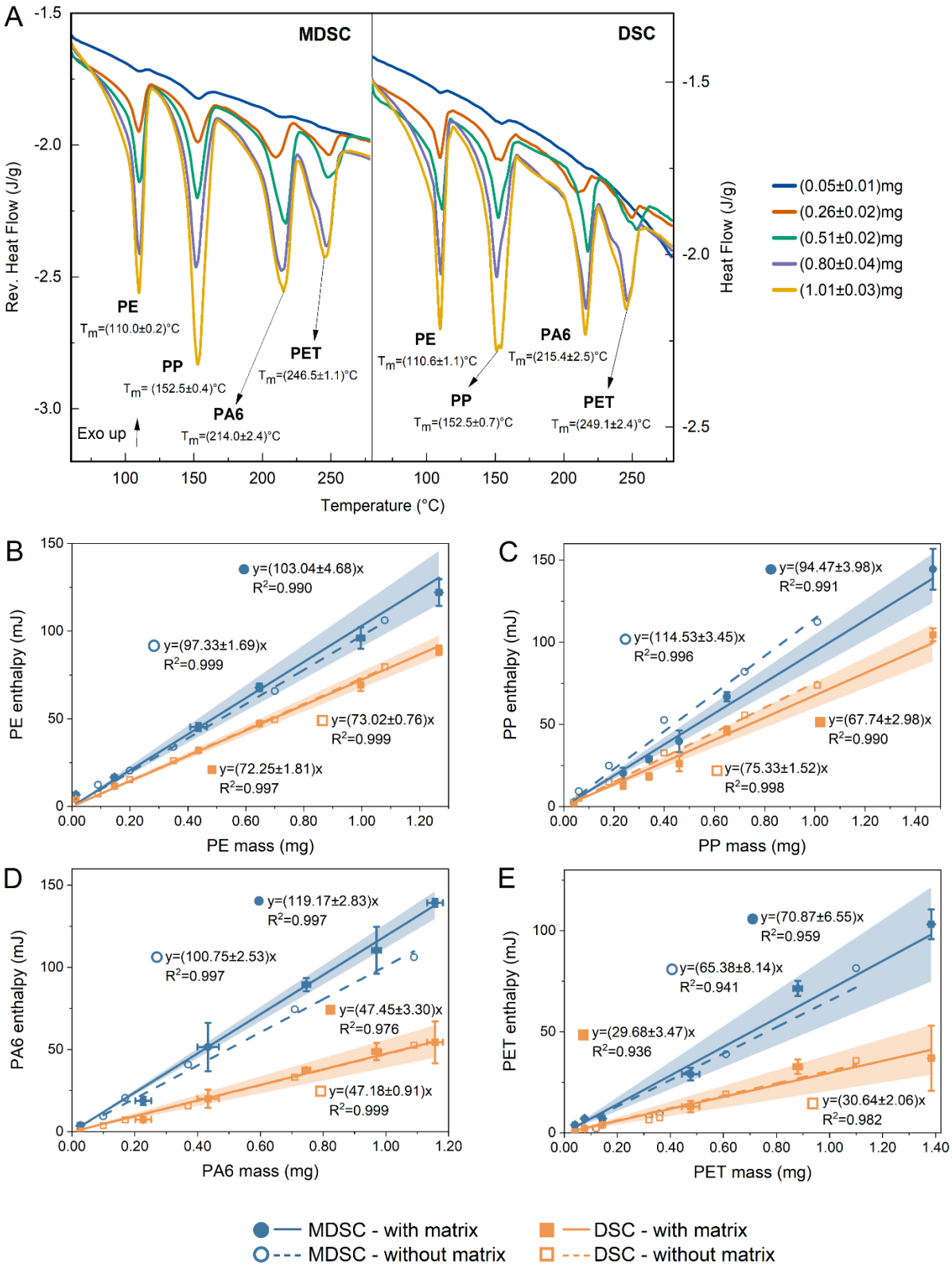
A
MDSC
DSC
Rev. Heat Flow (J/g)
Heat Flow (J/g)
Temperature (°C)
Exo up
PE
Tm=(110.0±0.2)°C
PP
Tm= (152.5±0.4)°C
PA6
Tm=(214.0±2.4)°C
PET
Tm=(246.5±1.1)°C
PE
Tm=(110.6±1.1)°C
PP
Tm=(152.5±0.7)°C
PA6
Tm=(215.4±2.5)°C
PET
Tm=(249.1±2.4)°C
(0.05±0.01)mg
(0.26±0.02)mg
(0.51±0.02)mg
(0.80±0.04)mg
(1.01±0.03)mg
B
PE enthalpy (mJ)
PE mass (mg)
y=(103.04±4.68)x
R2=0.990
y=(97.33±1.69)x
R2=0.999
y=(73.02±0.76)x
R2=0.999
y=(72.25±1.81)x
R2=0.997
C
PP enthalpy (mJ)
PP mass (mg)
y=(94.47±3.98)x
R2=0.991
y=(114.53±3.45)x
R2=0.996
y=(67.74±2.98)x
R2=0.990
y=(75.33±1.52)x
R2=0.998
D
PA6 enthalpy (mJ)
PA6 mass (mg)
y=(119.17±2.83)x
R2=0.997
y=(100.75±2.53)x
R2=0.997
y=(47.45±3.30)x
R2=0.976
y=(47.18±0.91)x
R2=0.999
E
PET enthalpy (mJ)
PET mass (mg)
y=(70.87±6.55)x
R2=0.959
y=(65.38±8.14)x
R2=0.941
y=(29.68±3.47)x
R2=0.936
y=(30.64±2.06)x
R2=0.982
MDSC - with matrix
MDSC - without matrix
DSC - with matrix
DSC - without matrix

**Figure 3.1 Identification and quantification of MPs by MDSC and conventional DSC.** (A) MDSC and conventional DSC measurements of quadruple polymer mixtures spiked in biosolids. Melting peaks of polymer mixtures are shown for mixtures spiked in biosolid matrices with total masses of 0.05±0.01, 0.26±0.02, 0.51±0.02, 0.80±0.04, 1.01±0.03 mg, at equal mass proportions of 25% each. Calibration curves for PE (B), PP (C), PA6 (D), and PET (E) in mixtures were obtained using MDSC and conventional DSC, with solid lines representing mixtures spiked into matrices and dashed lines representing mixtures without matrices, respectively. Calibration curves were derived from the melting peak areas (enthalpy). Fitting equations and $R^2$ values are provided in each plot. Error bars indicate the standard deviation (SD) of enthalpy measurements (n = 3). Shaded confidence bands correspond to ±2 SD, an approximate 95% confidence interval of measurement variability.

It is noticeable that as the mass of polymers increased, the peak area observed in the MDSC thermograms increased proportionally. To achieve quantification, the reversed heat flow resulting from the plastics' melting behaviour during the second heating ramp was utilized, as the melting of plastics is a reversible thermal behaviour, to integrate the area under each peak. Additionally, the total heat flow from the second heating ramp was generated and used as a comparative measure, equivalent to conventional DSC.

Building on this proportional relationship, calibration curves were generated by integrating peak areas under the melting peaks and plotting them against the corresponding masses of each plastic, using CMP mixtures prepared with and without dBB matrices. Figure 3.1B–E present the calibration curves for PE, PP, PA6, and PET individually, obtained during the second heating ramp by both MDSC and conventional DSC. All curves showed coefficients of determination ($R^2$) greater than 0.99, except for PA6 in matrices and for PET (with or without matrices), analyzed by conventional DSC, which exhibited lower $R^2$ values in both MDSC and DSC analyses. This is most likely attributed to the secondary reaction involving PA6 in the presence of PET during co-

heating, an observation well documented in previous studies [45]. Consistently, it has been reported that PET and PA6 show the highest deviations in recovery and the most significant relative standard deviations. Moreover, the calibration curve using PET alone spiked into dBB matrices yielded a good linear fit ($R^2 > 0.99$; Figure A2) in the absence of PA6, further supporting the notion that such secondary reactions affect quantitative reliability when analyzing mixtures containing these polymers.

A closer analysis of the calibration curves reveals that the dBB matrices did not affect the results from either MDSC or conventional DSC when the second heating ramp of the heat–cool–heat cycle was used, as evidenced by the similar slopes of curves with and without dBB matrices. However, as the compositions of matrices from different sources vary, potential matrix effects must still be carefully considered. Thus, calibration curves generated with biosolid matrices were used for all subsequent quantification.

### 3.3.2 Higher Sensitivity and Lower LOQs of MDSC

The sensitivity of MDSC and conventional DSC for plastic quantification was compared using the slopes of calibration curves [46]. MDSC exhibited consistently steeper calibration slopes across all polymers (Figure 3.1B–E), suggesting a sensitivity 1.4–2.5 times higher than that of the conventional DSC method for all polymer types investigated. This increased sensitivity arises primarily from MDSC's ability to detect subtle enthalpy changes associated with metastable crystallites that can form due to previous thermal or mechanical processing or other pre-treatments of the plastics [47]. Such enhanced detection is particularly beneficial for low-mass samples or those with weak thermal responses that might otherwise go undetected by conventional DSC.

The limit of quantification (LOQ) for each polymer was determined from the calibration curves using the standard approach: $LOQ = \frac{10 \times SD}{S}$, where *SD* is the standard deviation of the peak area

of the blank (dBB matrix) measured at the onset and offset of the MPs' melting peaks (79, 120, 168, 226, and 265 °C for PE, PP, PA6, and PET), and *S* is the slope of the calibration curve [48]. Using this approach, MDSC achieved lower theoretical LOQs than conventional DSC for all polymers, reaching as low as 0.0001 mg per measurement, corresponding to ~7 µg/g in concentration for PA6 (Table A2), confirming its higher sensitivity.

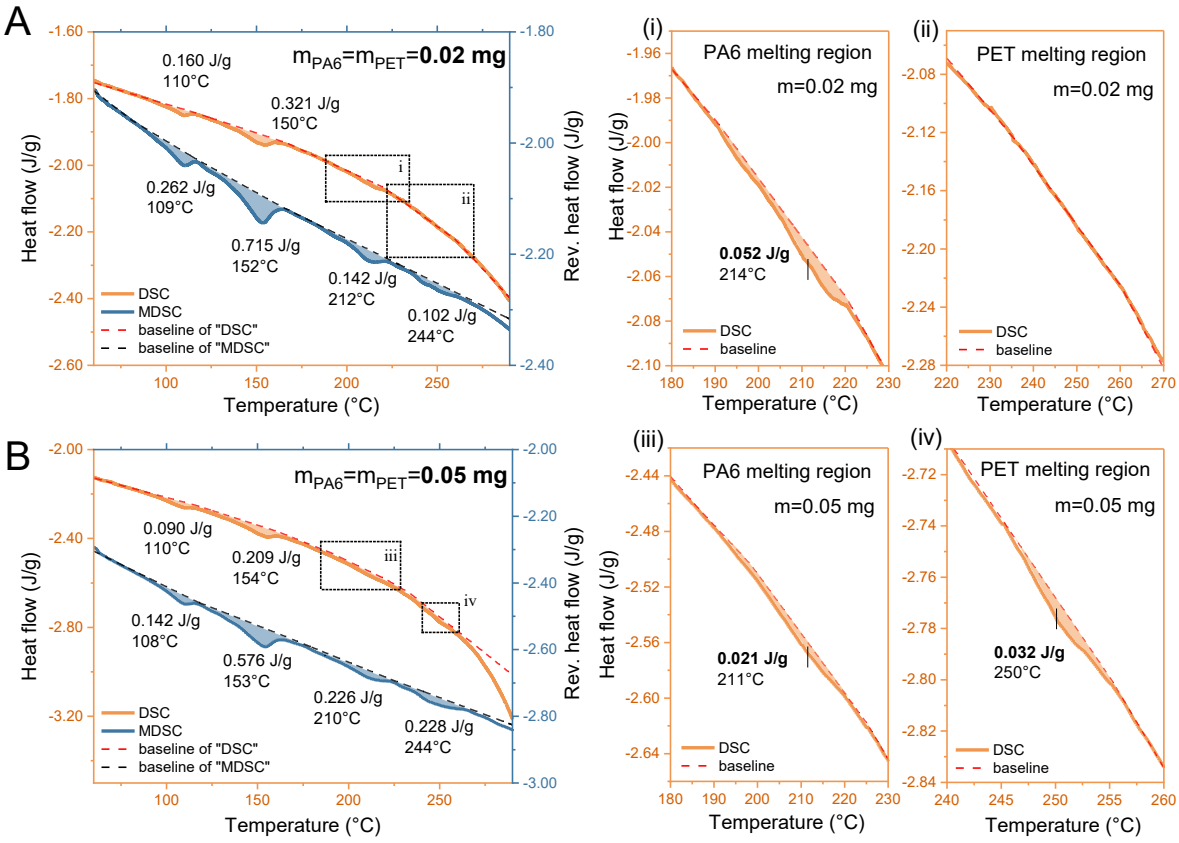


**Figure 3.2 MDSC and conventional DSC thermograms of polymer mixtures spiked in digested blank biosolid (dBB).** PA6 and PET were added in equal amounts at two total masses: (A) 0.02 mg and (B) 0.05 mg. Insets (i-iv) show enlarged views of the PA6 and PET melting regions from the conventional DSC thermograms.

For example, at a PET sample mass of 0.02 mg (Figure 3.2A), the PET melting peak at 244°C was clearly detectable in the MDSC thermogram. In contrast, no corresponding peak was observed in

conventional DSC (Figure 3.2A, ii) until the sample mass was increased to ≥ 0.05 mg (Figure 3.2B, iv). It is noticed that PA6 shows a higher melting enthalpy at the lower mass (Figure 3.2A, i and Figure 3.2B, i). This is because, with a fixed PA6: PET ratio (1:1), increased PET content enhances PET's cold crystallization and the leading tail of its melt, which affects the baseline near the PA6 melting. The lower detection threshold of MDSC is likely due to its slower underlying heating rate, which keeps the system closer to equilibrium and provides a more stable baseline for detecting weak thermal transitions [49]. In addition, MDSC can separate reversible polymer melting from non-reversible signals arising from matrix decomposition [33, 43], allowing more sensitive detection of small amounts of plastics in complex matrices such as biosolids, where incomplete decomposition of inorganic matter may otherwise obscure weak melting peaks in conventional DSC.

It should be mentioned that although the LOQs of MDSC are higher than those achieved by mass spectrometry-based methods, the lowest theoretical LOQ for PA6 at 7 μg/g is comparable to that of the Py-GC/MS [50]. While MDSC measurements require larger sample sizes (generally > 0.1 mg of dried solids per measurement), the increased sample size reduces heterogeneity in sampling, thus lowering variability in results from heterogeneous samples such as MPs in biosolids.

By isolating plastic-melting signals and performing matrix decomposition, MDSC improves sensitivity for plastic quantification. In the environmental-mimicked scenario with CMP mixtures in biosolid matrices, these low quantification limits enable the detection of MPs at trace levels. Compared to conventional DSC, MDSC provides more reliable measurements with smaller sample sizes, offering advantages for detecting increasingly pervasive MPs at minute concentrations.

### 3.3.3 Factors Affecting Sensitivity and Accuracy in MDSC Quantification

#### *3.3.3.1 Crystallinity and Aging History*

Quantifying low-crystallinity or amorphous plastics by conventional DSC is challenging because their thermal responses are weak or diffuse, lacking the sharp melting transitions and large enthalpy changes typical of highly crystalline polymers [51]. For instance, polystyrene (PS) undergoes a glass transition rather than melting. As illustrated in Figure A3, MDSC can detect the presence of PS. Still, the signal-to-noise ratio is substantially reduced, particularly in multicomponent mixtures with PE, where the melting of low-density PE (LDPE) overlaps with the PS glass transition [30]. Among the four micron-sized plastics analyzed, PE and PP displayed the highest thermal response (Figure 3.1A), owing to their defined crystallinity [28, 52]. In contrast, PET exhibited the weakest signal, consistent with its lower crystallinity fraction [28, 53].

Natural aging processes, such as UV radiation, mechanical abrasion, and chemical oxidation, often result in reduced crystallinity [54, 55], thereby diminishing thermal signals [56]. Additionally, manufacturing conditions and the presence of additives can also modify polymer crystallinity structures and affect enthalpy, resulting in reduced accuracy and sensitivity [57].

To explore how different manufacturing and aging histories affect quantification sensitivity, calibration curves were generated using micron-sized mixtures of PE, PP, PA6, and PET from the two sources of microplastics introduced earlier, PMP and aged-CMP, each spiked separately into the dBB matrix. As shown in Figure A4, the PMP set yielded the lowest calibration slopes, with PMP-PP being 59% less sensitive than CMP-PP. This reduction likely originated from broader, weaker melting peaks arising from lower crystallinity after manufacturing [58, 59]. Although the heat-cool-heat cycle (in non-isothermal crystallization) can partially restore crystallinity through re-crystallization during cooling, this effect depends on polymer-specific kinetics that are difficult

to control uniformly in mixed-plastic samples [28, 60]. Despite these challenges, MDSC retained good sensitivity in quantifying trace micron-sized plastics with varying aging and manufacturing history, by capturing weak transitions more effectively.

To evaluate the accuracy of MDSC for microplastics quantification, the measured mass from MDSC ($m_{measure}$) was compared with the actual weighed mass ($m_{true}$). Three mixtures—CMP, PMP, and aged-CMP (Table 3.1)—are each spiked into the dBB matrix at concentrations ranging from 0.03 to 1.11 mg per plastic, with 10 replicates per mixture (n = 10). Specifically, the $m_{true}$ values are obtained gravimetrically, while $m_{measure}$ values are determined by MDSC from melting peak areas and converted to mass using calibration curves. Comparisons between MDSC and gravimetric values are shown in Figure A5, and the mean absolute errors (MAE) are summarized in Table 3.2. The analytical recovery of MDSC quantification for PE, PP, PA6, and PET is presented in Figure 3.3.

**Table 3.2** Deviation of MDSC-measured microplastic mass from theoretical values for CMP, PMP, and aged-CMP*.

| Plastic types | Mean Absolute Errors (mg) | | |
|---|---|---|---|
| | **CMP** | **PMP** | **aged-CMP** |
| PE | 0.02±0.01 | 0.03±0.02 | 0.02±0.01 |
| PP | 0.04±0.02 | 0.18±0.13 | 0.05±0.03 |
| PA6 | 0.02±0.02 | 0.06±0.04 | 0.03±0.02 |
| PET | 0.04±0.03 | 0.13±0.08 | 0.06±0.05 |

**Note:* Values are (mean ± standard deviation) over n=10 independent spiked samples per mixture.

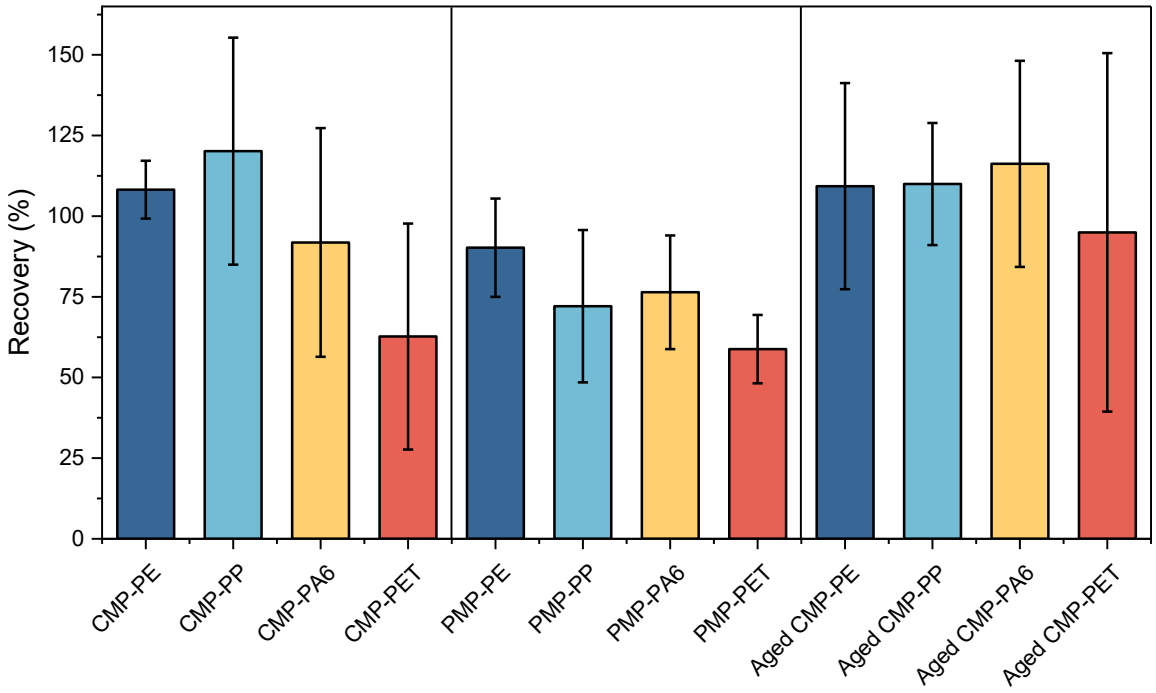


**Figure 3.3 Validation of quantification accuracy using CMP, PMP, and aged-CMP.** Spike recoveries (%) of PE, PP, PA6, and PET measured by MDSC. Bars show mean recovery and error bars denote standard deviation (SD) of 10 independent spiked samples (n=10).

Among the four plastics, PE exhibited the closest agreement across all sources (Figure A5A), with MAE consistently below 0.03 mg, and recovery averaged at 102% (Table 3.2, Figure 3.3). This likely reflects its favourable crystallization kinetics, resulting from a higher molecular weight and fewer branching points, which support the formation of a stable lattice structure and a better-defined thermal transition [61, 62]. Conversely, PP showed underestimations at higher masses (Figure A5B)—when PP was spiked at more than 0.4 mg in the matrices—particularly notable in PMP-PP, with an MAE of 0.18 mg, and recovery of 72%. A similar underestimation trend was observed in PA6 and PET (Figure 3.3 and Figures A5C-D), which consistently exhibited underestimations across the entire mass range in PMP, with recovery of 76% and 59%, respectively.

Regarding the aging effect, oxidative aging treatment induced chemical changes in the aged-CMP-PE, PP, and PA6 compared to CMP, as presented in the Fourier-transform infrared spectroscopy with attenuated total reflectance (FTIR-ATR) spectra in Figure A6. In aged CMP-PP and -PA6, a carbonyl peak around 1720 $cm^{-1}$ emerged, corresponding to C=O stretching and serving as a typical indicator of MPs oxidative aging [63, 64]. The spectral changes in aged-CMP-PE were more pronounced, with a new peak around 1200 $cm^{-1}$ suggesting the formation of new interchain interactions among PE chains due to thermal aging [65]. Although the chemical characteristic changes have been observed in PE, PP, and PA6 in aged-CMP, the measurement errors of aged-CMP did not parallel the error increment seen in PMP, especially for PP and PET. Slight overestimations were noted for PP (MAE of 0.05 mg, recovery of 110%) and PA6 (MAE of 0.03 mg, recovery of 116%), which may be due to increased crystallinity after oxidation. Since the calibration is based on the reversing melting enthalpy, which is proportional to crystallinity, the higher crystallinity of aged plastics could explain the overestimation of quantification. This observation also aligns with previous reports that oxidized PP exhibits higher crystallinity than the unoxidized ones because chemical crystallization occurs during oxidation [66, 67]. Similarly, for PA6, the oxidation enhances crystallinity, as low-molecular-weight oxidation products promote crystallization at elevated temperatures [68].

Overall, CMP mixtures consistently achieved the highest accuracy, as determined by both MAE and recovery, followed by aged-CMP, with PMP showing the largest deviations. These discrepancies may arise from additives or contaminants introduced during manufacturing, which interfere with chain mobility and disrupt crystallization [69-72]. This trend suggests that both manufacturing and post-consumer modifications can complicate crystallinity and, in turn, the precision of MDSC quantification. While PMP was consistently underestimated, variations

introduced by additives and contaminants are inevitable factors that could be present during the manufacturing process. Despite these challenges, this study establishes a foundation for applying MDSC in quantifying MPs and successfully demonstrates its efficacy and potential for more precise quantification across diverse types of plastics and sources.

*3.3.3.2 Matrix Interference in Environmental Samples*

Although the second heating ramp is commonly used to minimize matrix interference [28, 29], this approach is not always suitable for measuring plastic mixtures within complex matrices. In some cases, matrix–polymer interactions prevent recrystallization, leading to inaccurate quantification or missing signals of plastics during the second heating. For example, PA6 in a CMP mixture spiked into artificial soil (AS) failed to show a melting peak during the second heating. In contrast, the same polymer in digested biosolid did (Figure A7), suggesting that the AS matrix suppresses recrystallization. A possible cause is interfacial interactions between kaolinite and PA6 (e.g., hydrogen bonding between kaolinite surface -OH groups and PA6 amide groups), which restrict chain mobility and thereby inhibit second-heat recrystallization of PA6 [73]. Such cases highlight the importance of evaluating the first heating profile. Considering matrix variability, understanding the matrix and incorporating it as a background when establishing calibration curves is essential.

Because matrix effects can influence thermal behaviour during the second heating, ensuring a flat baseline during the first heating ramp is critical. To assess the impact of the matrix on MDSC quantification, CMP mixtures of PE, PP, PA6, and PET were spiked into raw biosolid and AS, and the samples were analyzed using both MDSC and conventional DSC. As shown in Figure 3.4, the MDSC thermograms of the first heating ramp displayed smooth baselines and clearly identifiable peaks, compared with those of conventional DSC. This improvement stems from MDSC's ability

to distinguish between reversible polymer melting and irreversible matrix degradation, thereby minimizing matrix effects. With this capability, extensive sample pre-treatment can be reduced, streamlining processing while maintaining analytical accuracy.

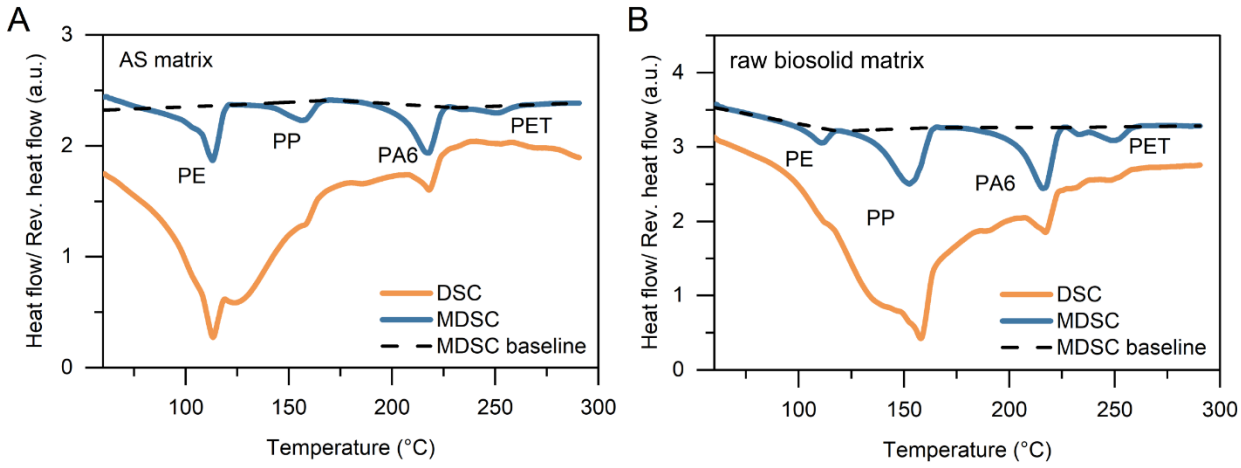


**Figure 3.4 Comparison of DSC and MDSC thermograms for microplastic mixtures in matrices.** Thermograms from the first heating ramp are shown for mixtures spiked into (A) artificial soil (AS) and (B) raw biosolids. Dashed lines indicate the baseline levels in MDSC, highlighting improved resolution and separation of polymer melting transitions compared with conventional DSC.

Taken together, these findings underscore MDSC's capacity to address two persistent obstacles in the thermal analysis of MPs: weak transitions in low-crystallinity plastics and matrix interference in environmental samples. The technique provides a streamlined, robust approach for quantifying microplastics with diverse thermal properties across diverse matrices.

### 3.3.4 Practical Strategy for MP Identification and Quantification: A Tiered Approach

When analyzing environmental samples, the diverse and complex nature of MPs necessitates combining multiple analytical techniques for accurate characterization. Due to their varying sizes, shapes, and chemical compositions, relying on a single method often falls short of providing a

comprehensive assessment [4, 74]. Recognizing these challenges, we propose a tiered approach to analyze MPs in environmental samples, integrating Raman and TGA as complementary techniques for MDSC identification and quantification.

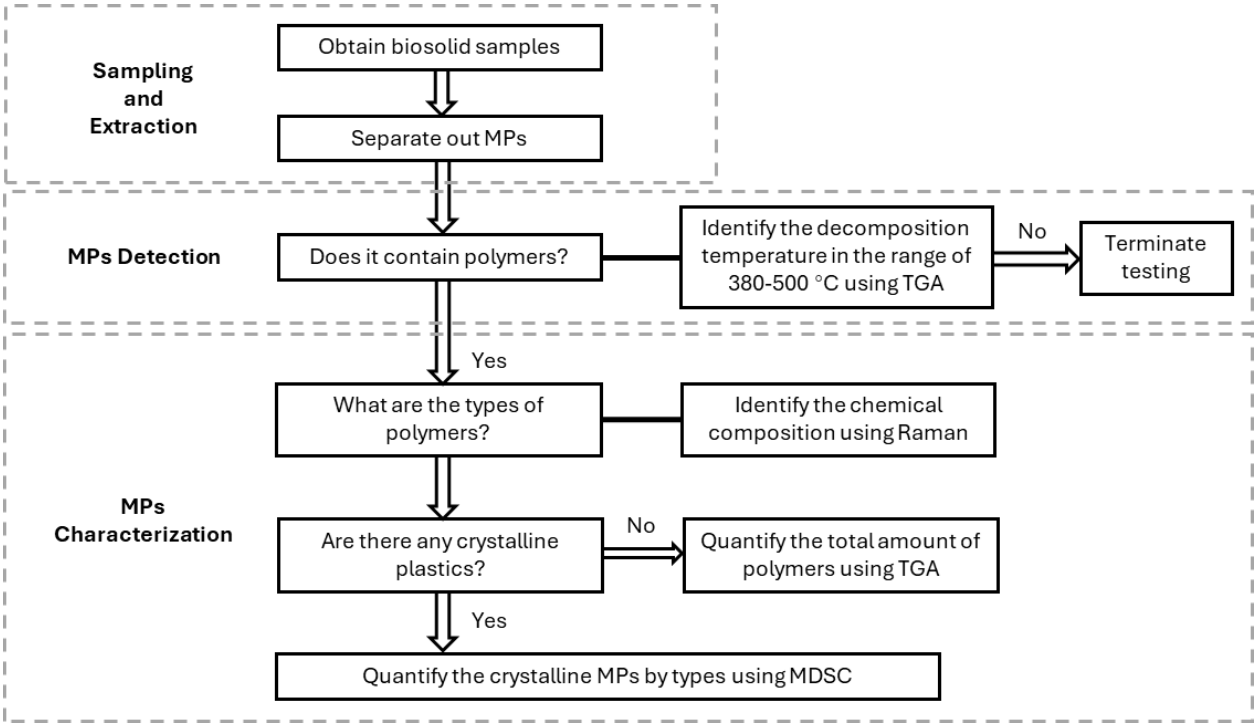


**Figure 3.5 A tiered analytical workflow for MPs analysis in biosolids.** Samples are screened for polymer presence using TGA, followed by polymer type identification with Raman spectroscopy. Crystalline MPs are quantified by MDSC, while TGA provides total polymer content, enabling complementary and comprehensive characterization.

Figure 3.5 illustrates the proposed workflow for MPs analysis in biosolids or soils. This approach begins with sample collection and separation of MPs. Initially, the presence of plastics in the samples is determined by TGA, which analyzes the degradation behaviour within the typical polymer degradation temperature range (380-500°C). Once the presence of polymers is confirmed, Raman spectroscopy is used to identify polymer types via characteristic vibrational modes that thermal methods alone cannot provide.

To determine which polymers are suitable for MDSC quantification, crystalline identity is assessed either through crystallinity-sensitive peaks in Raman spectra [75, 76], where applicable, or inferred from established material properties, since many common MPs such as PE, PP, and PET are semicrystalline under ambient conditions. Crystalline plastics can then be quantified individually using MDSC, which provides polymer-specific measurements even in the presence of complex matrix residues.

It is important to note that MDSC cannot reliably quantify amorphous plastics, such as polystyrene (PS), due to the overlap of glass transition signals with other thermal events and the lack of a sharp melting peak. In such cases, TGA and Raman are particularly valuable: TGA provides total polymer mass, including amorphous MPs [24, 30, 77], while Raman confirms their identity. This combination of MDSC and TGA could enhance understanding of MP analysis and address challenges in using MDSC to quantify non-crystalline plastics, particularly in multi-component MPs embedded in complex environmental matrices. Thus, the tiered approach leverages the strengths of each technique: MDSC resolves trace amounts of crystalline MPs with high sensitivity, Raman provides molecular specificity, and TGA complements the workflow by detecting amorphous or otherwise indistinguishable plastics.

Correlation experiments were conducted to assess the consistency and complementarity of TGA and MDSC in quantifying crystalline plastics. The CMP-dBB mixtures with PE, PP, PA6, and PET, in equal proportions of 4%, 10%, and 20% per polymer (16%, 40%, and 80% total CMP), demonstrated the complementarity of MDSC and TGA across the low-to-high concentration range. A 1:1 reference line was used as a benchmark to evaluate the correlation between the methods (Figure A8). At a higher mass ratio, MDSC and TGA agreed within 7% relative error. In contrast, at lower masses, the relative error increased to −31% to −55%, due to a broader thermal

degradation range captured by TGA, which accounts for all types of polymer decompositions within 380-500°C. At the same time, MDSC primarily resolves well-defined thermal transitions. Additionally, matrix interference could contribute to the overestimation of TGA, potentially amplifying the discrepancy between MDSC and TGA results. Overall, this validates the use of TGA as a complementary technique to MDSC for comprehensive analysis of MPs.

By explicitly combining MDSC, Raman, and TGA, this tiered approach accounts for both crystalline and amorphous plastics, compensates for matrix and aging effects, and provides a more robust and reliable workflow for quantifying MPs in complex environmental matrices [78, 79].

### 3.3.5 Application of MDSC Quantifying Microplastics in Biosolids

To advance the quantification of MPs in real-world biosolids, a tiered approach incorporated with MDSC was applied to analyze MPs extracted from three raw biosolids collected from different WWTPs. While MDSC is inherently less sensitive to matrix interferences than spectroscopic methods, extraction by digestion (to remove large amounts of cellulose that can hinder polymer identification) and density separation (to eliminate higher-density matter) further simplify the sample and provide a more consistent basis for accurate quantification.

Thermal decomposition profiles of the extracted biosolid, as determined by TGA measurements (Figure A9), revealed contributions from organic matter (200-400°C), cellulose (300-400°C), polymer decomposition (380-500°C), and inorganics (>500°C). In Sample 1, a broad degradation peak spanning 250°C to 550°C, including a strong feature at 455°C, suggested plastic degradation but overlapped with other components, making it difficult to distinguish individual plastic types. Additionally, the shoulder peak around 355°C was likely due to residual cellulose from $H_2O_2$ digestion or plastics that have undergone processing or environmental weathering [80, 81], which

reduced their thermal stability, leading to lower decomposition temperatures. However, confirming the precise origin of this peak by TGA is challenging. Similar degradation patterns were noted in Samples 2 and 3, which displayed similar behaviours, with a cellulose-related peak at ~345 °C and broad polymer signals between 380–500 °C. Overall, the TGA confirmed the presence of polymer(s) but lacked the resolution to distinguish specific plastic types.

Following the tiered approach workflow (Figure 3.5), Raman spectroscopy was used to determine the chemical structures and identify specific polymer types. By comparison with a reference library of Raman spectra previously established from standard plastics, the presence of PS, PE, PP, and PET was confirmed in all three samples. Additionally, cellulose was observed in Sample 1, and PA was observed in Sample 2. A heatmap of the spectral counts (Figure 3.6A) provided a qualitative and semi-quantitative overview of the polymer distributions across samples.

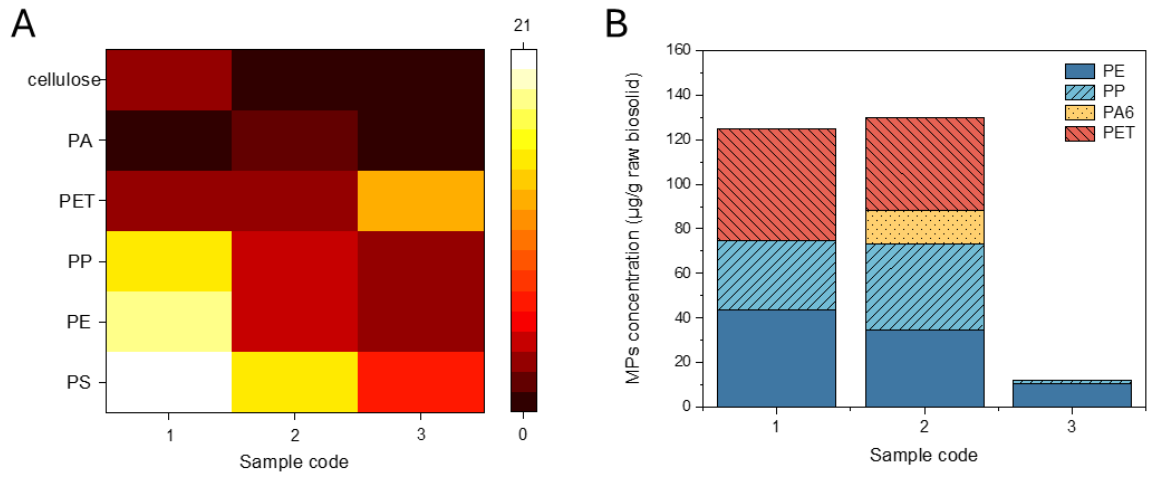


**Figure 3.6 Integrated spectroscopic and calorimetric analysis of microplastics in biosolids.** (A) Heat map showing the frequency of occurrence of polymers (or cellulose) across three biosolid samples. Occurrence frequency is defined as the number of Raman spectra in which characteristic peaks of polymers were identified. The colour scale (0-21) represents the Raman spectral counts assigned to each polymer type. (B) Concentration of MPs extracted from real-world biosolids quantified by MDSC.

For crystalline plastics—PE, PP, PA6, and PET—MDSC provided quantitative results (Figure 3.6B). As shown in Figure 3.6B, Samples 1 and 2 showed comparable total concentrations of MPs, at (125 ± 48) μg/g and (130 ± 72) μg/g, respectively, suggesting a similar overall level of MPs contamination in these biosolid sources. Their compositions, however, differed. In Sample 1, PE, PP, and PET were present at concentrations of (44 ± 30) μg/g, (31 ± 11) μg/g, and (50 ± 41) μg/g, with PET contributing the largest share. Sample 2 contained a broader mix, with PA6 detected exclusively at (15 ± 5) μg/g, followed by PET (42 ± 18) μg/g, PE (35 ± 15) μg/g, and PP (39 ± 55) μg/g, which together accounted for most of the MPs. By contrast, Sample 3 exhibited markedly lower levels of MP presence, with only PE and PP quantified at (4 ± 2) μg/g and (2 ± 2) μg/g, giving a total of (12 ± 4) μg/g. The relatively larger standard deviations (15–55 μg/g) observed in Samples 1 and 2 likely stem from the intrinsic heterogeneity of biosolids, which results in uneven MP distribution. Despite this variability, the MDSC results followed the same trends as the Raman identifications, as shown in Figure 3.6A, reinforcing the reliability of MDSC quantification in complex matrices. As for PS, although it is consistently detected by Raman, it cannot be quantified by MDSC due to its amorphous nature and the overlap with PE melting, which prevents clear resolution under current conditions.

TGA-based estimates, obtained from mass loss within the 380–500 °C temperature range (Figure A9), were consistently higher than those from MDSC (Table A3). The discrepancy was most pronounced in Sample 3, where TGA values were nearly 75-fold higher, likely indicating substantial amounts of amorphous plastics not captured by MDSC, as well as possible effects of uneven polymer distribution in the heterogeneous biosolids.

Overall, the combined application of TGA, Raman spectroscopy, and MDSC provided complementary insights into microplastic characterization: TGA confirmed the presence of

polymers and overall polymer content, Raman spectroscopy identified polymer types, and MDSC quantified the crystalline fractions. The consistency between Raman and MDSC enhanced confidence in the quantification, while comparison with TGA underscored the additional contribution of amorphous plastics. Together, this integrated approach establishes a comprehensive framework for the analysis of microplastics in complex biosolid matrices.

## 3.4 Conclusion

This study established a method for quantifying MPs using MDSC in complex biosolids. By incorporating periodic temperature modulation, MDSC enhances conventional DSC by increasing sensitivity, reducing detection limits, and facilitating the separation of weak plastic melting transitions from matrix degradation. The capability provides a smooth baseline during the first heating cycle, enabling accurate differentiation of polymer signals from complex biosolid matrices. A key observation was that PA6 recrystallization could be suppressed by the matrix, potentially leading to no detectable signal during the second heating, thereby necessitating characterization during the first heating via MDSC.

Calibration curves for PE, PP, PA6, and PET were established by integrating melting peak areas relative to mass, each showing strong linearity. Potential sources of quantification error were investigated by using three different types of MPs—CMP, MPP, and aged-CMP—and all confirmed the accuracy of MDSC measurements. The method was then employed to analyze MP concentrations in biosolids, where, within the proposed tiered workflow, Raman spectroscopy identified polymer types, and TGA verified polymer signals in the thermal range. These complementary techniques supported the MDSC quantification, and the results were consistent across all three biosolid samples, successfully confirming their MP concentrations.

This study demonstrated that MDSC provides high sensitivity, low detection limits, and reliable quantification of trace and low-crystallinity MPs in biosolids. Its application is currently limited to crystalline and semicrystalline plastics, and further research is required to reduce signal-to-noise ratios and resolve glass transition and peak overlaps to allow quantification of amorphous polymers.

## References


1. Jiang J-Q. Occurrence of microplastics and its pollution in the environment: A review. Sustain Prod Consump. 2018;13:16-23.
2. Lambert S, Wagner M. Microplastics are contaminants of emerging concern in freshwater environments: an overview. In: Lambert S, Wagner M, editors. Freshwater Microplastics: Emerging Environmental Contaminants. Cham: Springer; 2018. p. 1-23.
3. Hidalgo-Ruz V, Gutow L, Thompson RC, Thiel M. Microplastics in the marine environment: a review of the methods used for identification and quantification. Environ Sci Technol. 2012;46(6):3060-75.
4. Ivleva NP. Chemical Analysis of Microplastics and Nanoplastics: Challenges, Advanced Methods, and Perspectives. Chem Rev. 2021;121(19):11886-936.
5. Sivarajah B, Lapen DR, Gewurtz SB, Smyth SA, Provencher JF, Vermaire JC. How many microplastic particles are present in Canadian biosolids? J Environ Qual. 2023;52(5):1037-48.
6. Chen M, Coleman B, Gaburici L, Prezgot D, Jakubek ZJ, Sivarajah B, et al. Identification of microplastics extracted from field soils amended with municipal biosolids. Sci Total Environ. 2024;907:168007.
7. Walker H, Aherne J. Microplastic fate in a chronosequence of biosolid-amended agricultural soil in Southern Ontario, Canada. Eur J Soil Sci. 2024;75(5):e13592.
8. Adhikari K, Pearce CI, Sanguinet KA, Bary AI, Chowdhury I, Eggleston I, et al. Accumulation of microplastics in soil after long-term application of biosolids and atmospheric deposition. Sci Total Environ. 2024;912:168883.

9. Nizzetto L, Futter M, Langaas S. Are Agricultural Soils Dumps for Microplastics of Urban Origin? Environ Sci Technol. 2016;50(20):10777-9.
10. Okoffo ED, Donner E, McGrath SP, Tscharke BJ, O'Brien JW, O'Brien S, et al. Plastics in biosolids from 1950 to 2016: A function of global plastic production and consumption. Water Res. 2021;201:117367.
11. Crossman J, Hurley RR, Futter M, Nizzetto L. Transfer and transport of microplastics from biosolids to agricultural soils and the wider environment. Sci Total Environ. 2020;724:138334.
12. Corradini F, Meza P, Eguiluz R, Casado F, Huerta-Lwanga E, Geissen V. Evidence of microplastic accumulation in agricultural soils from sewage sludge disposal. Sci Total Environ. 2019;671:411-20.
13. Christian AE, Köper I. Microplastics in biosolids: A review of ecological implications and methods for identification, enumeration, and characterization. Sci Total Environ. 2023;864:161083.
14. Wang Z, Taylor SE, Sharma P, Flury M. Poor extraction efficiencies of polystyrene nano- and microplastics from biosolids and soil. PLoS One. 2018;13(11):e0208009.
15. Adhikari S, Kelkar V, Kumar R, Halden RU. Methods and challenges in the detection of microplastics and nanoplastics: a mini-review. Polym Int. 2022;71(5):543-51.
16. Ziajahromi S, Slynkova N, Dwyer J, Griffith M, Fernandes M, Jaeger JE, et al. Comprehensive assessment of microplastics in Australian biosolids: Abundance, seasonal variation and potential transport to agroecosystems. Water Res. 2024;250:121071.
17. Xu J-L, Thomas KV, Luo Z, Gowen AA. FTIR and Raman imaging for microplastics analysis: State of the art, challenges and prospects. TrAC, Trends Anal Chem. 2019;119:115629.
18. Käppler A, Fischer D, Oberbeckmann S, Schernewski G, Labrenz M, Eichhorn K-J, et al. Analysis of environmental microplastics by vibrational microspectroscopy: FTIR, Raman or both? Anal Bioanal Chem. 2016;408(29):8377-91.
19. Araujo CF, Nolasco MM, Ribeiro AMP, Ribeiro-Claro PJA. Identification of microplastics using Raman spectroscopy: Latest developments and future prospects. Water Res. 2018;142:426-40.
20. Hermabessiere L, Himber C, Boricaud B, Kazour M, Amara R, Cassone A-L, et al. Optimization, performance, and application of a pyrolysis-GC/MS method for the identification of microplastics. Anal Bioanal Chem. 2018;410:6663-76.

21. Gomiero A, Øysæd KB, Palmas L, Skogerbø G. Application of GCMS-pyrolysis to estimate the levels of microplastics in a drinking water supply system. J Hazard Mater. 2021;416:125708.
22. Liu Y, Li R, Yu J, Ni F, Sheng Y, Scircle A, et al. Separation and identification of microplastics in marine organisms by TGA-FTIR-GC/MS: A case study of mussels from coastal China. Environ Pollut. 2021;272:115946.
23. Silva AB, Bastos AS, Justino CI, da Costa JP, Duarte AC, Rocha-Santos TA. Microplastics in the environment: Challenges in analytical chemistry-A review. Anal Chim Acta. 2018;1017:1-19.
24. Mansa R, Zou S. Thermogravimetric analysis of microplastics: A mini review. Environ Adv. 2021;5:100117.
25. Becker R, Altmann K, Sommerfeld T, Braun U. Quantification of microplastics in a freshwater suspended organic matter using different thermoanalytical methods – outcome of an interlaboratory comparison. J Anal Appl Pyrolysis. 2020;148:104829.
26. David J, Weissmannová HD, Steinmetz Z, Kabelíková L, Demyan MS, Šimečková J, et al. Introducing a soil universal model method (SUMM) and its application for qualitative and quantitative determination of poly(ethylene), poly(styrene), poly(vinyl chloride) and poly(ethylene terephthalate) microplastics in a model soil. Chemosphere. 2019;225:810-9.
27. Lynch JM, Corniuk RN, Brignac KC, Jung MR, Sellona K, Marchiani J, et al. Differential scanning calorimetry (DSC): An important tool for polymer identification and characterization of plastic marine debris. Environ Pollut. 2024;346:123607.
28. Bitter H, Lackner S. Fast and easy quantification of semi-crystalline microplastics in exemplary environmental matrices by differential scanning calorimetry (DSC). Chem Eng J. 2021;423:129941.
29. Lee J, Yoon S, Jang T, Choi J-H, Kim N, Kim H-O, et al. A facile approach to microplastic identification and quantification using differential scanning calorimetry. Sci Total Environ. 2024;957:177456.
30. Sorolla-Rosario D, Llorca-Porcel J, Pérez-Martínez M, Lozano-Castelló D, Bueno-López A. Study of microplastics with semicrystalline and amorphous structure identification by TGA and DSC. J Environ Chem Eng. 2022;10(1):106886.

31. Majewsky M, Bitter H, Eiche E, Horn H. Determination of microplastic polyethylene (PE) and polypropylene (PP) in environmental samples using thermal analysis (TGA-DSC). Sci Total Environ. 2016;568:507-11.
32. De Meuter P, Rahier H, Van Mele B. The use of modulated temperature differential scanning calorimetry for the characterisation of food systems. Int J Pharm. 1999;192(1):77-84.
33. Knopp MM, Löbmann K, Elder DP, Rades T, Holm R. Recent advances and potential applications of modulated differential scanning calorimetry (mDSC) in drug development. Eur J Pharm Sci. 2016;87:164-73.
34. Verdonck E, Schaap K, Thomas LC. A discussion of the principles and applications of Modulated Temperature DSC (MTDSC). Int J Pharm. 1999;192(1):3-20.
35. Blaine R. An Introduction to Lifetime Testing by Thermogravimetry. J Test Eval. 2014;42(6):1360-5.
36. Coleman NJ, Craig DQM. Modulated temperature differential scanning calorimetry: A novel approach to pharmaceutical thermal analysis. Int J Pharm. 1996;135(1):13-29.
37. Leng Y, Chen M, Cao X, Zou S. Laboratory simulated aging of polystyrene particles and characterization of the resulting nanoscale plastics. J Environ Chem Eng. 2023;11(5):110967.
38. Nakajima R, Tsuchiya M, Lindsay DJ, Kitahashi T, Fujikura K, Fukushima T. A new small device made of glass for separating microplastics from marine and freshwater sediments. PeerJ. 2019;7:e7915.
39. Wunderlich B. Thermal analysis of polymeric materials. Berlin: Springer; 2005.
40. OECD. OECD Guidelines for the Testing of Chemicals, Section 2: Test No. 222: Earthworm Reproduction Test (Eisenia fetida/Eisenia andrei). Paris; 2016.
41. Wenzel M, Renner G, Pruin L, Wolf C, Kube C, Schram J, et al. Assessment of sample pre-treatment strategies to mitigate matrix effects for microplastics analysis using thermoanalytical techniques. TrAC, Trends Anal Chem. 2024;181:117997.
42. Gill PS, Sauerbrunn SR, Reading M. Modulated differential scanning calorimetry. J Therm Anal. 1993;40(3):931-9.
43. Righetti MC. Crystallization of Polymers Investigated by Temperature-Modulated DSC. Materials. 2017;10(4):442.

44. Netsch N, Schröder L, Zeller M, Neugber I, Merz D, Klein CO, et al. Thermogravimetric study on thermal degradation kinetics and polymer interactions in mixed thermoplastics. J Therm Anal Calorim. 2025;150(1):211-29.
45. Coralli I, Giorgi V, Vassura I, Rombolà AG, Fabbri D. Secondary reactions in the analysis of microplastics by analytical pyrolysis. J Anal Appl Pyrolysis. 2022;161:105377.
46. Sensitivity: International Union of Pure and Applied Chemistry (IUPAC); 2019 [3.0.1:[
47. Chau J, Garlicka I, Wolf C, Teh J. Modulated DSC as a tool for polyethylene structure characterization. J Therm Anal Calorim. 2007;90(3):713-9.
48. Lister AS. 7 - Validation of HPLC Methods in Pharmaceutical Analysis. In: Ahuja S, Dong MW, editors. Separation Science and Technology. 6: Academic Press; 2005. p. 191-217.
49. Gill P, Moghadam TT, Ranjbar B. Differential scanning calorimetry techniques: applications in biology and nanoscience. J Biomol Tech. 2010;21(4):167-93.
50. Dierkes G, Lauschke T, Becher S, Schumacher H, Földi C, Ternes T. Quantification of microplastics in environmental samples via pressurized liquid extraction and pyrolysis-gas chromatography. Anal Bioanal Chem. 2019;411(26):6959-68.
51. Wesolowski M. Chapter 5 - DSC of Low Molecular Mass Organic Materials and Pharmaceuticals. In: Menczel JD, Grebowicz J, editors. The Handbook of Differential Scanning Calorimetry: Butterworth-Heinemann; 2023. p. 485-658.
52. Ronca S. Chapter 10 - Polyethylene. In: Gilbert M, editor. Brydson's Plastics Materials (Eighth Edition): Butterworth-Heinemann; 2017. p. 247-78.
53. Di Lorenzo ML. Crystallization of Poly(ethylene terephthalate): A Review. Polymers. 2024;16(14):1975.
54. Iñiguez ME, Conesa JA, Fullana A. Recyclability of four types of plastics exposed to UV irradiation in a marine environment. J Waste Manag. 2018;79:339-45.
55. Liu P, Zhan X, Wu X, Li J, Wang H, Gao S. Effect of weathering on environmental behavior of microplastics: Properties, sorption and potential risks. Chemosphere. 2020;242:125193.
56. Uheida A, Mejía HG, Abdel-Rehim M, Hamd W, Dutta J. Visible light photocatalytic degradation of polypropylene microplastics in a continuous water flow system. J Hazard Mater. 2021;406:124299.

57. Martinho SD, Fernandes VC, Figueiredo SA, Vilarinho R, Moreira JA, Delerue-Matos C. Laboratory Studies about Microplastic Aging and Its Effects on the Adsorption of Chlorpyrifos. Polymers. 2023;15(16):3468.
58. Murata T, Qiu JH, Sakai E, Wu XL, Kudo M. Morphology Change of extrusion molded crystalline polymer by rolling process. Adv Mater Res. 2012;391:595-9.
59. Raharjo WP, Ariawan D, Diharjo K, Raharjo WW, Kusharjanta B. Weathering Degradation of Polyolefin. Techniques and Innovation in Engineering Research. Vol. 1: BP International; 2022. p. 97-145.
60. Ozawa T. Kinetics of non-isothermal crystallization. Polymer. 1971;12(3):150-8.
61. Wang L, Zhang R, Chen S, Yang Q. Influence of Molecular Structure on Crystallization Kinetics and Performance of Polyethylene of Raised Temperature Resistance. J Macromol Sci Part B Phys. 2024;63(10):877-88.
62. Khoshsefat M, Dechal A, Ahmadjo S, Mortazavi SMM, Zohuri G, Soares JBP. Amorphous to high crystalline PE made by mono and dinuclear Fe-based catalysts. Eur Polym J. 2019;119:229-38.
63. Shi Y, Shi L, Huang H, Ye K, Yang L, Wang Z, et al. Analysis of aged microplastics: a review. Environ Chem Lett. 2024;22(4):1861-88.
64. Campanale C, Savino I, Massarelli C, Uricchio VF. Fourier Transform Infrared Spectroscopy to Assess the Degree of Alteration of Artificially Aged and Environmentally Weathered Microplastics. Polymers. 2023;15(4):911.
65. Bergeron C, Perrier E, Potier A, Delmas G. A Study of the Deformation, Network, and Aging of Polyethylene Oxide Films by Infrared Spectroscopy and Calorimetric Measurements. Int J Spectrosc. 2012;2012(1):432046.
66. Margolin AL, Vorontsov NV, Monakhova TV, Popov AA. Thermal oxidation of blends of polypropylene and polyamide 6/66. Effect of inhibition. Polym Degrad Stab. 2024;220:110627.
67. Yu F, Wu Z, Wang J, Li Y, Chu R, Pei Y, et al. Effect of landfill age on the physical and chemical characteristics of waste plastics/microplastics in a waste landfill sites. Environ Pollut. 2022;306:119366.
68. Shu Y, Ye L, Yang T. Study on the long-term thermal-oxidative aging behavior of polyamide 6. J Appl Polym Sci. 2008;110(2):945-57.

69. Yao S, Cao H, Arp HPH, Li J, Bian Y, Xie Z, et al. The role of crystallinity and particle morphology on the sorption of dibutyl phthalate on polyethylene microplastics: Implications for the behavior of phthalate plastic additives. Environ Pollut. 2021;283:117393.
70. Fitaroni LB, de Oliveira ÉC, Marcomini AL, Paranhos CM, Freitas FL, Cruz SA. Reprocessing and Solid State Polymerization on Contaminated Post-consumer PET: Thermal and Crystallization Behavior. J Polym Environ. 2020;28(1):91-9.
71. Veroneze IB, Onoue LA, Cruz SA. Thermal Stability and Crystallization Behavior of Contaminated Recycled Polypropylene for Food Contact. J Polym Environ. 2022;30(8):3474-82.
72. Ma Y, Wang X, Tian M, Zhang L, Yang W, Xie P. Effect of process parameters on the performance of PA6 products fabricated by rotational molding. Polym Eng Sci. 2023;63(11):3762-70.
73. Raji M, Bouhfid R. Effects of bleaching and functionalization of kaolinite on the mechanical and thermal properties of polyamide 6 nanocomposites. RSC advances. 2020;10(9):4916-26.
74. Yang L, Zhang Y, Kang S, Wang Z, Wu C. Microplastics in soil: A review on methods, occurrence, sources, and potential risk. Sci Total Environ. 2021;780:146546.
75. Stuart BH. Polymer crystallinity studied using Raman spectroscopy. Vib Spectrosc. 1996;10(2):79-87.
76. Doumeng M, Makhlouf L, Berthet F, Marsan O, Delbé K, Denape J, et al. A comparative study of the crystallinity of polyetheretherketone by using density, DSC, XRD, and Raman spectroscopy techniques. Polym Test. 2021;93:106878.
77. Procházková P, Kalčíková G, Maršálková E, Zlámalová Gargošová H, Kučerík J. Innovative approach for quantitative determination of ingested microplastics by Daphnia magna: use of differential scanning calorimetry and thermogravimetry. J Therm Anal Calorim. 2024;150:1303–10.
78. Ainali NM, Bikiaris DN, Lambropoulou DA. Aging effects on low- and high-density polyethylene, polypropylene and polystyrene under UV irradiation: An insight into decomposition mechanism by Py-GC/MS for microplastic analysis. J Anal Appl Pyrolysis. 2021;158:105207.
79. Madadian E, Simakov DSA. Thermal degradation of emerging contaminants in municipal biosolids: The case of pharmaceuticals and personal care products. Chemosphere. 2022;303:135008.

80. Majder-Łopatka M, Węsierski T, Ankowski A, Ratajczak K, Duralski D, Piechota-Polanczyk A, et al. Thermal Analysis of Plastics Used in the Food Industry. Materials. 2022;15(1):248.
81. Luo H, Zhao Y, Li Y, Xiang Y, He D, Pan X. Aging of microplastics affects their surface properties, thermal decomposition, additives leaching and interactions in simulated fluids. Sci Total Environ. 2020;714:136862.

# CHAPTER 4 LABORATORY SIMULATED AGING OF POLYSTYRENE PARTICLES AND CHARACTERIZATION OF THE RESULTING NANOSCALE PLASTICS


## Abstract

Plastics are increasingly produced and used worldwide for their easy accessibility and cost-effectiveness. However, the improper discarding of plastics has caused pollution in our ecosystems due to their slow degradation rate in the natural environment. While the worldwide production of polystyrene (PS) is estimated to be around 21 million tons (8% among all types of polymers), the percentage of observed PS in environmental samples is inconsistent with the production. To this end, we hypothesize that the chemical composition of PS may have been altered when undergoing weathering in the natural environment, making fewer PS candidates identified. To test this hypothesis and understand the potential fate and behaviour of PS after aging, we performed lab-accelerated aging processes on pristine PS particles. After thermal aging and probe sonication, the size distribution of 500 nm polystyrene (PS500) was brought to around 200 nm, as measured by dynamic light scattering (DLS). The morphology of processed PS was examined by atomic force microscopy (AFM), further confirming that the shape changed. Less than 3% of PS500 did not undergo distinct structural changes, while a ring-opening reaction induced by the conjugated C=C bond breakage, followed by the C-H bond breakage, was observed in 40% of the particles after the aging process, whereas the rest underwent chemical changes to different extents. These physical and chemical changes introduced by the simulated aging process help to understand the possible fate of microplastics found in the environment, which emphasizes the importance of weathering factors in micro/nanoplastics research.

## 4.1 Introduction

Since the 1940s, when plastics entered mass production, they have become one of the most common materials in daily life because of their low price and durability [1]. Different types of plastics are used in a wide variety of life scenarios due to their specific physical and chemical properties. For example, polyethylene (PE) is used for plastic bags, films, containers, and home decoration materials; polypropylene (PP) is used for car trim and tubes; polystyrene (PS) is used as a high-strength plastic for furniture and food packaging; and polyethylene terephthalate (PET) is used as a common material for plastic containers including water bottles [2, 3].

Unfortunately, the wide application of plastic has led to a large amount of plastic waste, which has created serious environmental concerns. Particularly, smaller-sized plastics such as microplastics (MPs, 100 nm to 5 mm) and nanoplastics (NPs, 1−100 nm) [4-7] have been found in face washes, scrubs [8, 9], tea bags [10], and even bottled water and food [11-14]. Their complex properties and wide distribution make it inevitable for humans to be exposed to micro/nanoplastics, and also make recycling and monitoring of plastic wastes increasingly difficult to manage.

In addition, the weathering effects on plastic waste make it difficult to accurately determine the types and amounts of polymers in plastic waste. Among the most commonly used plastics, PE and PP make up 36% and 21% of all plastics production [15], respectively; and as expected, PE and PP account for most of the detected microplastic wastes in the aquatic and terrestrial environment [16-19]. In contrast, while PS accounts for 8% of the global plastics production and makes up 90% of the total plastic demand in the food packaging and insulation industries, as well as the most used polymer in laboratory analysis [15, 20], it is not commonly detected and reported in the assessment of environmental plastics. For example, while a large number of PE and PP particles of different sizes were detected in floodplain soil using Fourier-transform infrared spectroscopy (FTIR), for

the PS, only particles in the small size range (125 μm−1 mm) were identified in the samples [21]. Similarly, in another FTIR-based study, it was reported that the most abundant polymers found in turtle, cetacean, and fish guts were low-density PE and polyamide (PA), but not PS [20]. Although it has been noted in the literature that there is a discrepancy between the amount of PS produced and the amount extracted from the environment, it is also interesting to mention that no research has been done to solve this gap.

It is well established that PS undergoes weathering upon entering the environment under different conditions, such as ultraviolet (UV) irradiation, oxidation, thermal degradation and biodegradation [22-24], and that the weathering of the PS results in alterations to the chemical structures of the original PS material. Since the natural aging processes take up to decades, accelerated aging conditions in the laboratory are deliberately carried out to simulate and speed up the aging process. As shown in Table 4.1, there are different pathways to mimic natural aging in laboratories, and it is evident that the aged micro/nanoplastics are significantly altered from their pristine plastic properties.

**Table 4.1** Examples of accelerated aging processes on plastics and their effects.

| Type of plastics | Particle size | Aging methods | Effects on plastics | Refs. |
|---|---|---|---|---|
| **PS** | 487.3 ± 18.3 nm | Ozone and UV light | The surface appeared to have a much rougher morphology; surface property changes led to irreversible adsorption of contaminants through polar interactions, which enhanced the adsorption of pollutants to the PS particles. | [25] |
| **PS** | 28 nm | Freeze-thaw cycles | Size distribution shifted from 10–100 nm towards larger sizes of 100–1000 nm or greater; agglomerates that did not easily break down formed, thereby reducing their mobility and transport in suspension. | [26] |
| **PS** | 100-300 μm | Photo-oxidation and stirring | MP fragments ranging from 10-200 μm and containing carboxyl groups and peroxides were formed; an average volume decreases by 99.8% was assumed. | [27] |
| **PS** | 2.0–5.0, 1.25–2.0, 0.5–1.25, 0.3-0.5, and < 0.3 mm | Thermal oxidation | PS chemically degraded at a high temperature; hyperthermophilic bacteria attacked and oxidized plastic structures, leading to effective bio-oxidation and biodegradation. | [28] |
| **PS** | 1 μm | Air, pure water, and seawater at 75°C | Morphology of the PS particles displayed nicked shapes and slight cracking phenomena; initial degradation of C=C on the benzene ring and the generation of C=O after air aging; the adsorption capacity was enhanced. | [29] |
| **PP film** | - | Photo-activated oxidation | Hydrophilicity and adhesion properties of PP improved after oxidation; PP and metal could be firmly bonded by simple oxidation treatment. | [30] |

| | | | | |
|---|---|---|---|---|
| **PE pipe** | - | Chlorine dioxide solution at 20 or 40°C | Failure with brittle cracking after 5-15 years of exposure was predicted by modelling. | [31] |
| **HDPE, LDPE, PET, PP, PS mixture** | powder: average 300 μm; pellets: avr. 3 mm | Simulated marine and dry conditions | Chemical structures changed in five types of plastics resulted in cracks and fractures, crystallinity decrease, and roughness increase. | [32] |

As heating processes are often used in wastewater treatment plants, the extracted micro/nanoplastics from wastewater likely would have been exposed to high temperatures [28, 33, 34] and undergone oxidation that makes plastics weaker and more prone to fragmentation [35-37]. To mimic PS aging in the laboratory, an autoclave is used to simulate the thermal aging of PS, as high-temperature treatment, and probe sonication is used to simulate the natural oxidation process of the PS, as high-power sonication is known to generate hydroxyl free radicals (HO•) to create an oxidative environment [38, 39]. In this work, a combination of autoclave and probe sonication was used to age the PS and to help understand the changes that may occur after aging.

## 4.2 Materials and Methods

### 4.2.1 Materials and Aging Sample Preparation

To prepare PS dispersion samples for aging tests, a 2.7% w/w PS stock dispersion (500 nm, PS500, Polyscience Int., Warrington, PA, USA) was diluted in water (Milli-Q water filtered using MilliporeSigma 0.22 μm filter) to obtain a final concentration of 142 μg/mL. The untreated PS500 was the negative control. Three replicate samples were prepared for the experiment. To avoid plastic contamination from other sources during sample preparation, all samples were processed

and stored in clean glass containers that were carefully rinsed multiple times using Milli-Q water beforehand.

To mimic the thermal degradation of PS500, an autoclave was applied as an in-lab accelerated method. Specifically, 150 mL PS500 dispersion (142 μg/mL) was autoclaved at 121˚C for 50 minutes (Amsco 2021, Mentor, OH, USA). The autoclaved PS500 (hereinafter annotated as APS500) was cooled down to room temperature before further processing.

Subsequently, probe sonication was performed using ahigh-intensity processor (130W, Cole-Parmer, Quebec City, QC, Canada), with a ¼ inch probe. The probe was kept halfway into the dispersion, as the probe position is also one of the factors affecting sonication behaviour [40]. Process conditions, such as concentration of the dispersion and sonication energy (tuned by sonication power and time), were optimized. Specifically, autoclaved APS500 samples were diluted into different concentrations (i.e., 7, 14, 28, 57, and 142 μg/mL in water). For each of the APS500 samples, 30 mL of the dispersion was sonicated for 15 s with 15 s pauses in between to avoid overheating, for a total sonication duration of 70 min; in addition, 100 μL aliquots were carefully withdrawn from the dispersion after every 10 min during the sonication for further analysis. Throughout the sonication process, samples were kept in an ice-water bath. Samples obtained from the sonication were annotated as APS500-S.

### 4.2.2 Separation and Enrichment

It was found that after 50 min of sonication, small-sized particles started to show up in the solution. To collect the fragmented PS particles, the sonicated APS500-S particles were separated and enriched using a Repligen KrosFlo® KR2i Tangential Flow Filtration (TFF) System (Waltham, MA, USA). Specifically, the TFF separation process was carried out by applying 25–40 DV (diafiltration volumes) constant-volume buffer exchange, using a 165 $cm^2$ 650 nm hollow fibre

filter (Repligen, Waltham, MA, USA) at a flow rate of 100 mL/min with 15.0 psi back pressure. The retentate that contained particle sizes larger than 650 nm was indicated as APS500-SR. The permeate with particle sizes smaller than 500 nm after the separation process was collected for further enrichment (going through a concentration process). For each process, the TFF system, including tubing and filters, was flushed with Milli-Q water three times to eliminate cross-contamination. For the enrichment, the collected permeates were pumped at 200 mL/min with 15.0 psi back pressure through a 115 $cm^2$ 750 kD filter. The enriched permeate (i.e., APS500-SP) in the final volume of around 10 mL was collected for further characterization.

### 4.2.3 Characterization of PS500 and Processed Particles

To characterize the size distribution, dynamic light scattering (DLS) measurements were carried out for each PS500, APS500, APS500-S, and their aliquots during the probe sonication process. The polydispersity index (PDI), Z-average, and surface charge of PS500 and processed dispersions were determined using a ZetaSizer Nano ZS (Malvern Panalytical Ltd, UK). For the DLS measurements, the dispersions were diluted to 10 μg/mL in 10 mM NaCl and equilibrated at 25 ˚C for 3 min. Size measurements were conducted using ZEN0040 cuvettes (Malvern Panalytical Ltd, UK), with 13 runs and 10 s acquisition time for each. The average diameter was reported. Triplicate measurements were conducted for each sample. The PDI from 0 to 1 corresponds to the dimensional heterogeneity from monodispersity to high polydispersity in plastic suspensions. For Zeta-potential measurements, dispersions were injected in DTS1070 cuvettes (Malvern Panalytical Ltd, UK), with 10 runs for each under 148 mV voltage.

AFM was used to characterize their morphology after aging processes. Briefly, a drop casting approach with 30 μL of dispersions was used to prepare samples on a mica substrate (Ted Pella, Redding, CA, USA), and the substrates were placed on a shaker with a spin rate of 150 rpm for 15

min. The samples were further dried for 10 s with a dry nitrogen stream. The height images were collected with an atomic force microscope (NanoWizard II, JPK Instruments, Goleta, CA, USA). Intermittent contact mode was used with a silicon AFM tip (HQ: XSC11/AL BS, MikroMasch; typical radius 8 nm, 2.7 N/m spring constant). Large-sized images (100 μm × 100 μm) at different locations on the specimen were recorded to verify the overall morphology and homogeneity of the PS samples. A series of smaller images (30 μm × 30 μm) was then acquired with a resolution of 512 pixels × 512 pixels. A scan rate of 1.0−1.2 Hz and a Z-piezo range of 3.5 μm were applied. Before imaging samples, the AFM was calibrated using height standards (VLSI Standards, Inc.; STS3 series with four different step heights of 18, 44, 100, and 180 nm).

For the chemical composition characterization, Raman spectra were acquired using an inVia™ confocal Raman microscope (Renishaw plc., UK) equipped with a 633 nm excitation laser and a 1200/mm grating (50W). Samples were prepared by spin-coating PS dispersions on a polished silicon substrate. Optical images were captured with a 100X lens (Leica, Germany). Each spectrum was scanned using a 10-second exposure time over the range from 950 to 3200 $cm^{-1}$. Twenty spectra were collected from each sample at random (and different) locations, and triplicate samples were scanned.

### 4.2.4 Data Analysis

For size and zeta-potential measurement, Zetasizer v7.13 (Malvern Panalytical Ltd, UK) was used for data analysis. The statistical analysis was conducted using SPSS v28.0.1.1 (IBM Corp., Armonk, NY, USA). Student's t-test and one-way ANOVA were used to analyze differences among groups, and a p-value $< 0.05$ was considered significant. AFM images were flattened using a first-order polynomial fit by JPKSPM Data Processing software (JPK Instruments, Goleta, CA, USA). Raman spectra collection was performed using WiRE 5.2 (Renishaw, Manchester, UK),

and baseline correction was processed by peak analyzer using Origin 2021 (OriginLab, Northampton, MA, USA).

## 4.3 Results and Discussion

### 4.3.1 Effect of Autoclave Thermal Aging on PS

The autoclave was first used as a high-temperature and high-pressure method to age PS500, which is well-reported and commonly used for the thermal aging of plastics [41-43]. It is a process whereby microplastic particles are placed in an elevated-temperature and pressure environment to simulate the effects of weathering caused by sunlight exposure and high temperatures in the natural environment. This treatment results in physical changes to microplastics, such as surface degradation and altered mechanical properties. Critical parameters for autoclaving include temperature, pressure, and processing time [44]. Higher temperatures and longer treatment times result in more significant changes in the properties of the microplastics that replicate prolonged exposure to the environment. It is well known that temperature plays an important role in aging phenomena, since higher temperatures may accelerate the aging process [45, 46].

The most important factor in determining whether the fragmentation of plastic formed is to evaluate its size and size distribution, followed by the comparison of its surface charge and morphology changes. The size distribution and zeta potential were characterized by DLS. Compared to the Z-avr of PS500 (508 nm, Table 4.2), after the autoclave treatment, the Z-avr of APS500 increased to 639 nm. This indicates that the size distribution in the dispersion has become broader ($p < 0.001$), and the amount of agglomeration may have increased after the in-lab accelerated weathering treatment. The commercial pristine PS500 particles are originally coated with the carbonyl group; therefore, it is expected that the PS dispersion is negatively charged, as

shown in Table 4.2. In contrast, the surface charge of the PS decreased ($p < 0.05$) after the autoclave, suggesting that some carbonyl coating was broken off from the PS beads during the autoclave [47]. However, it is evident that the dispersion is still highly stable after the autoclave.

**Table 4.2** Mean hydrodynamic size and Zeta potential (ZP) analysis of PS dispersion*.

| **Samples** | **$d_{h,\ Z\text{-}avr}$/nm** | **PDI** | **ZP/mV** |
|---|---|---|---|
| **PS500** | 508±4 | 0.14±0.01 | -97±1 |
| **APS500** | 639±17 | 0.21±0.01 | -89±2 |

**Note:* $d_{h,\ Z\text{-}avr}$: hydrodynamic size by Z-averaging. Analyses were performed by dynamic light scattering, and data are represented as means ± standard error (SE), n=3.

Possible particle aggregation may have occurred as a result of the autoclave, as suggested by the increased Z-avr and the wider size distribution (PDI increased). The nanoparticles are prone to degradation at elevated temperatures. As a result, the properties of the nanoparticles change, leading to aggregation and flocculation. Also, surfactants contained in nanoparticle formulations have been reported to have a significant effect on particle aggregation after autoclaving [48]. To further confirm whether aggregation took place after the autoclave, we performed morphology characterization using AFM. It is clear from Figure 4.1A and C that aggregates of PS particles can be seen in both PS500 and APS500. In both cases, the particles show a regular morphology of spherical shapes, suggesting that the morphology of individual particles does not change significantly after autoclave treatment.

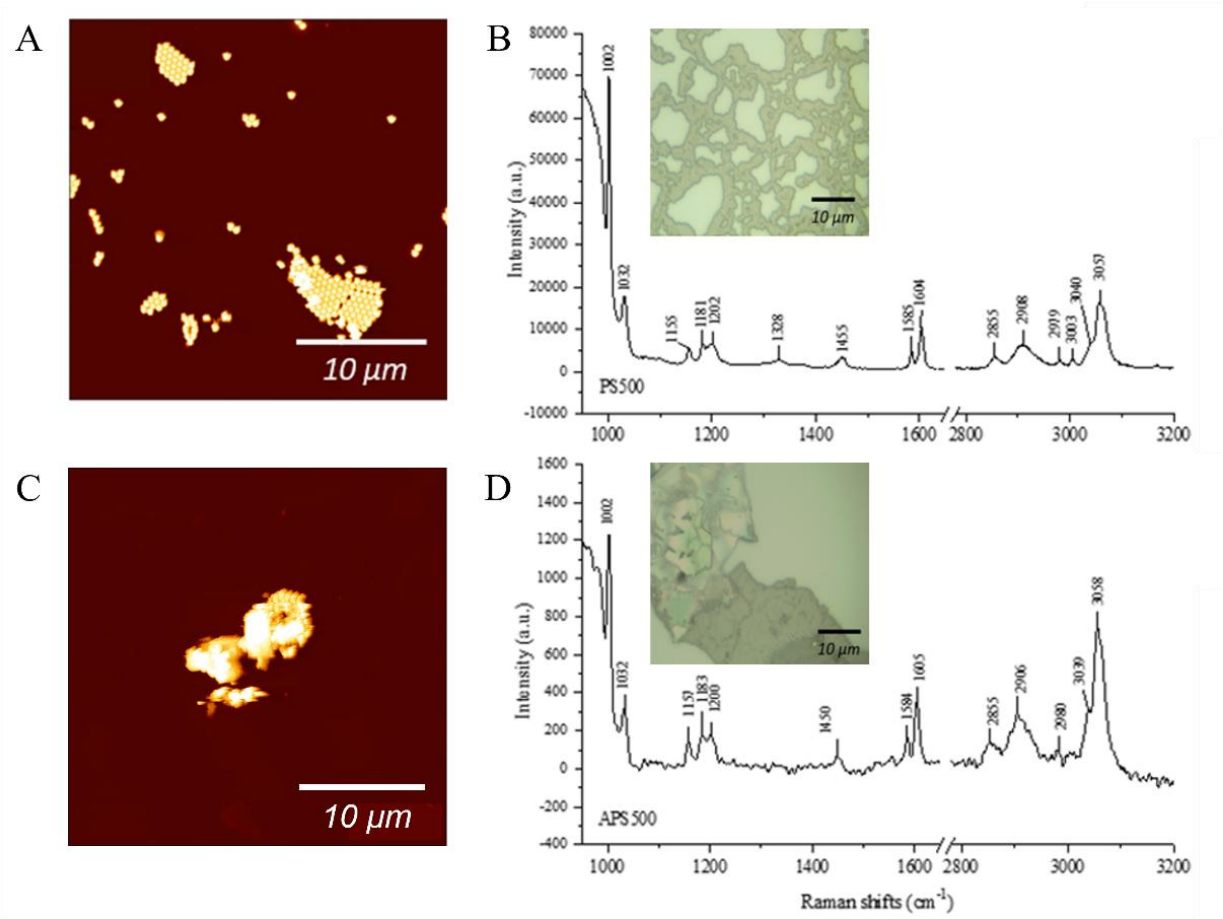


**Figure 4.1 AFM images, Raman spectra, and optical images (insets) of PS dispersions.** (A, B) pristine PS500, AFM color scale: 0-500 nm; (C, D) APS500, AFM color scale: 0-700 nm.

To investigate if the weathering process changes the chemical structure of PS, Raman microscopy was used for a micron-scale morphology check and chemical composition characterization. It can be seen from Figure 4.1B inset that the original PS500 particles were homogeneously packed and displayed a uniform arrangement. However, after the autoclave aging, the particles formed larger aggregates (Figure 4.1D inset). As for the chemical composition, Figure 4.1B presents a typical Raman spectrum of PS. Peaks around 950 $cm^{-1}$ are from the silicon substrate. For APS500 (Figure 4.1D), there is no significant shift in the peak positions, except for the disappearance of the peaks

at 1328 $cm^{-1}$ and 3003 $cm^{-1}$. This suggests that the structure of PS has not changed significantly after the autoclave. It is worth noting that the signal-to-noise ratio of APS500 has become much smaller due to the irregular agglomeration formed by non-spherical particles. The uneven baseline may result in the missing identification of weak peaks with lower intensity, which can also be the reason for the missing two peaks. It is shown in the literature that the level of Raman intensity quantitatively represents the amount of chemical groups [49]. Thus, some of the functional groups have dropped after the autoclave aging process, which would likely account for the unstable binding between the chemical bonds.

### 4.3.2 Effect of Probe Sonication

With the advantages of high energy and easy operation, sonication is a promising method for the application of particle fragmentation and degradation in dispersion. In the natural environment, microplastics are subjected to mechanical stresses from waves and turbulence (especially in the ocean), which will result in fragmentation [50]. Parameters of probe sonication include the duration of sonication, the input energy, and the amplitude. Prolonged sonication times and higher energy levels may lead to microplastic fragmentation and size reduction [51], which is similar to the mechanical forces they experience in the environment. The principle of ultrasound fragmentation is based on its cavitation in liquids. High-power sonication produces a large number of cavitation bubbles in the liquid, and the cavitation bubbles collapse and implode, giving rise to effects such as shock waves and high pressure in order to disperse particles in suspensions [52-54]. In addition, the sonication process also generates HO• free radicals that are highly oxidative [38, 39]. To mimic the formation of smaller-sized particles, sonication was used to generate the fragmentation of plastics. During the 70 min processing time, the energy delivered by the probe sonicator is about 50 kJ. The APS500 was diluted to different concentrations, and each of the

diluted dispersions was sonicated for 70 minutes. The 7 μg/ml APS500 after 70 minutes of sonication was defined as APS500-S. The sizes of sonicated APS500 at different concentrations with increasing sonication energy are shown in Figure 4.2.

Overall, the size of APS500 particles tended to decrease gradually as the sonication energy increased. This can be attributed to the presence of an increased number of cavitation bubbles within the PS dispersion, particularly around the sonication probe, when higher energy levels are employed. When these bubbles expand beyond a certain threshold size, the cushioning effect provided by the gas molecules inside them becomes insufficient, leading to a forceful collapse and a consequent rapid reduction in particle size [52, 53].

Among the five groups of different concentrations, the APS500 at 142 μg/mL did not show a noticeable size change ($p > 0.05$) after applying an energy of about 50 kJ. The size-changing trends of the three groups of 57, 28, and 14 μg/mL were not significantly different from each other ($p > 0.05$), with size reduction ranging from 100-150 nm (particle sizes 350−400 nm). The most pronounced particle size change was observed in 7 μg/mL APS500 ($p < 0.01$), where the particle size distribution was reduced to about 150 nm, suggesting that lower concentrations result in more effective particle breakage. This can be explained by the fact that the shockwave intensity experienced by individual particles is more pronounced in dispersions containing few particles. In high-concentration dispersions, the sonication energy is primarily dissipated through interparticle collisions. Conversely, in low-concentration dispersions, the attenuated interparticle collisions due to the reduced number of particles lead to a greater emphasis on particle-shockwave interactions as the dominant mode of fragmentation. This intensified interaction between particles and shockwaves results in a higher degree of fragmentation efficiency at low concentrations [55].

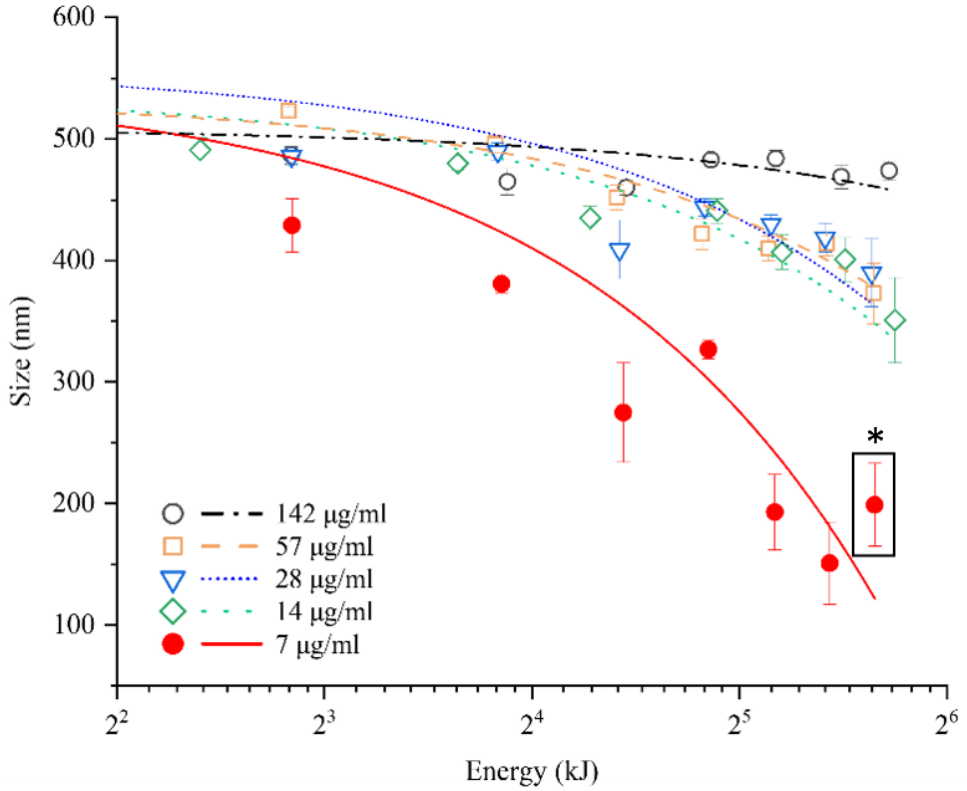


**Figure 4.2 Size change of APS500 in different concentrations correlated to the energy of probe sonication.** Polynomial fits were applied in solid lines. The star (*) refers to the size of the product APS500-S.

As the 7 µg/ml APS500 after 70 minutes of sonication showed the highest breakage efficiency, it is considered to be the optimized aging condition, from which we define the yielded product as APS500-S. In order to compare the probe sonication efficiency with and without autoclave, a direct 70-minute probe sonication without autoclave was carried out on PS500, whose product was called PS500-S. In Figure 4.3, the Z-avr PS500-S was reduced from 531 nm to 396 nm, indicating that some PS500 were broken down to below 400 nm after sonication. Interestingly, for autoclaved APS500 after 70 min sonication (APS500-S), the Z-avr peak shifted from 615 nm to 342 nm. It is noteworthy that peaks of 220 nm and 91 nm appeared in APS500-S.

In DLS measurements, the incident light scattered by dispersed particles is proportional to the sixth power of its radius at approximately < 1/10 of the laser wavelength (*i.e.,* < 100 nm), so the intensity of the scattered light for larger size particles would be dominant when the two groups of particles are in the number ratio around 1:1. This Rayleigh scattering principle would not directly apply to larger sized particles (e.g., sixth power for > 500 nm), however, the trend would still hold true. It is reported by Filipe et al. that in the mixture of 100 and 400 nm particles, the peak of 100 nm particles appears when their number ratio reaches 15:1 [56]. Since the size of the starting PS is 500 nm, when a signal peak around 100 nm appears in the DLS results (peak at around 91 nm in Figure 4.3D), we consider that the PS suspension has a larger percentage of small-sized fragments; that is, a solution with a large yield of plastic fragments for subsequent separation was produced.

Compared to the original pristine PS500, the probe sonication efficiently broke down APS500, resulting in a significant particle size reduction of APS500-S (Figure 4.3D). Since the large-sized particles are more easily broken compared to the small-sized ones when applying the same energy [57], the breakage efficiency may be higher on aggregates. Because the elevated temperatures and pressures provide the energy needed for the hydrolysis reaction that breaks the carbonyl bonds in microplastics, it is likely that the chemical bonds are no longer stable after high-temperature exposure, which led to the breakage of the particles [29]. However, these conjectures need to be further confirmed with morphology and chemical composition using AFM and Raman techniques.

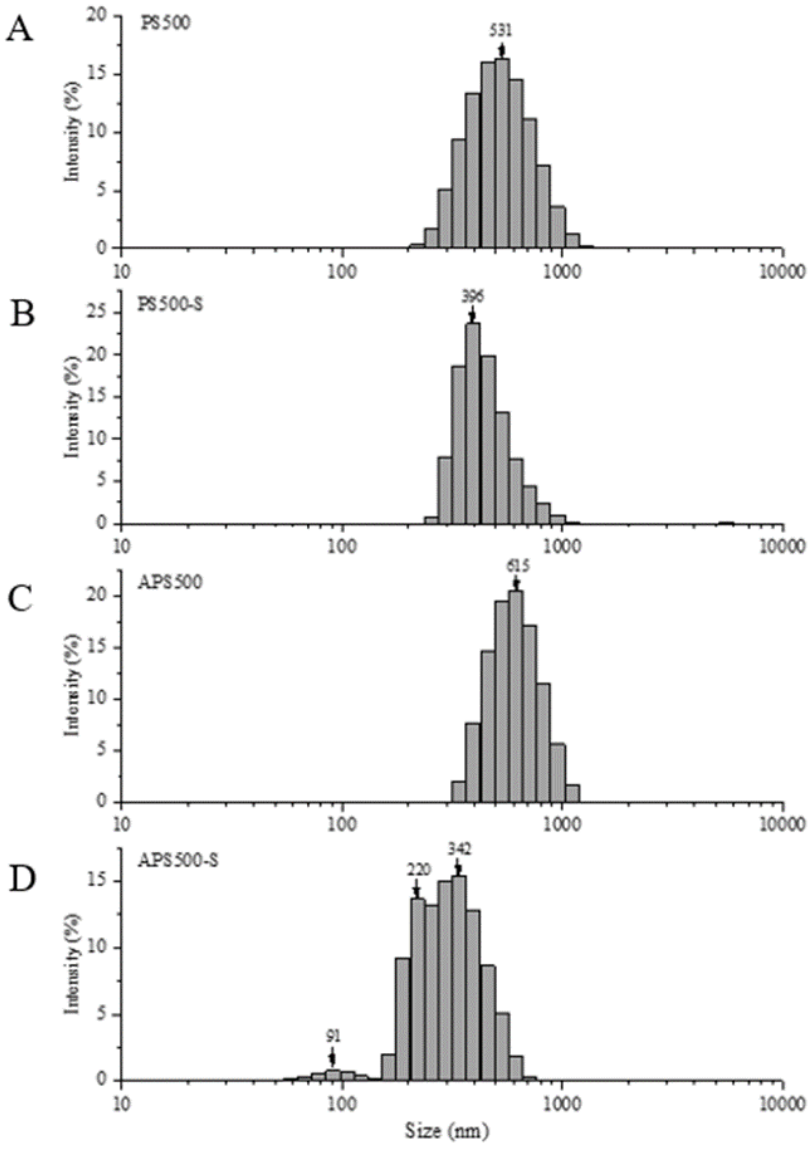


**Figure 4.3 Size distribution histograms of the mean hydrodynamic size of PS dispersions.** (A) pristine PS500; (B) sonicated PS500 (PS500-S); (C) autoclaved PS500 dispersion (APS500); (D) autoclaved and sonicated PS500 dispersion (APS500-S).

### 4.3.3 Size and Morphology Characterization

It was quite a surprise to find larger-sized particles in sonicated APS500-S (Figure 4.3D), which we speculated was due to aggregates of broken APS500-S accumulating when the sonication process was paused. Also, compared to APS500, the elevated PDI in APS500-S can prove its wide particle size distribution. To separate out the large agglomerates, as well as any possible contamination due to the probe deterioration that may have been introduced during sonication, the TFF process was introduced. By using TFF separation, it can meanwhile have the effect of purifying the sample and collecting the small-sized particles into the permeate, which we defined as APS500-SP.

**Table 4.3** DLS and Zeta potential analysis of measured hydrodynamic diameters and zeta-potential (ZP) of PS dispersions*.

| Samples | $d_{h,Z\text{-}avr}$/nm | PDI | ZP /mV |
|---|---|---|---|
| **APS500-S** | 539±61 | 0.56±0.04 | -26±0 |
| **APS500-SP** | 487±8 | 0.37±0.03 | -23±1 |
| **APS500-SR** | 775±18 | 0.31±0.02 | -22±1 |

**Note*: $d_{h,\ Z\text{-}avr}$: hydrodynamic size by Z-averaging. Analyses were performed by Dynamic Light Scattering, and data are represented as means ± standard error (SE), n=3.

During the TFF process, the fluid flows tangentially across the membrane surface at 100 mL/min. The transmembrane pressure generated by the fluid enables some particles in the suspension to go through the membrane (permeate), while the retentate is circulated back into the system [58-60]. The ultrafiltration also scours the membrane surface, so that the cake layer is not easily formed on the membrane surface, and the particles in the feed liquid will not block the membrane, which can

make it maintain a stable filtration rate. Since the number of DV is high, a large volume of Milli-Q water had to be added during the generation of the permeate, resulting in APS500-SP being significantly diluted after the separation process. To obtain a dispersion that satisfies the concentration for further characterization, an enrichment step processed by TFF was followed.

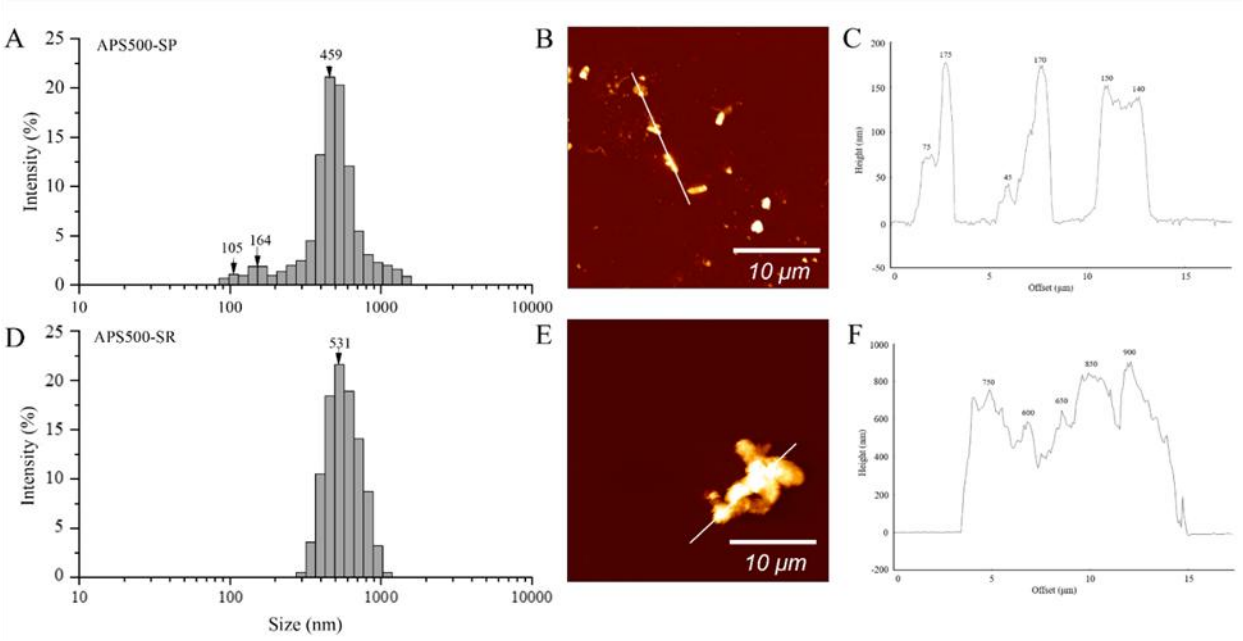


**Figure 4.4 Characterization of permeate and retentate of APS500-S after TFF separation.** Size distribution by DLS (A, D), AFM images (B, E), and height profiles (C, F) of samples prepared from dispersions of permeates (noted as APS500-SP) and retentate (APS500-SR). The vertical axis in C and F indicates the height of the particles in the area crossed by the white line in B and E, respectively. AFM colour scales in B and E: 0-200 nm, C and F: 0-800 nm.

A 650 nm pore size filter was used for the separation step. Ideally, those smaller-sized PS fragments would be collected in the permeate, and those larger aggregates would remain in the retentate. Indeed, two small signals of 105 nm and 164 nm are observed for the permeate APS500-SP samples after separation (Figure 4.4A), indicating a successful separation of small-sized particles in permeate. In the dispersion of retentate (Figure 4.4C), there is no signal of any small-

sized particles and only one peak at 531 nm, indicating that the large particles were dominant in retentate with no or very little number of small particles.

For enrichment purposes, a filter with 750 kD (60-70 nm) pore size was used to remove small molecules (i.e., water, surfactant, and other coating molecules) in the system. In APS500-SP (Figure 4.4A), it is noted that the sizes that peaked at 105 and 164 nm are slightly shifted and different from the size distribution before separation, which were 91 and 220 nm (Figure 4.3D). Meanwhile, a peak of the highest intensity was present at 459 nm. This may be due to the re-aggregation of small particles in the dispersion. Since a 750 kD filter was used for enrichment, some of the coating molecules, such as surfactant in the PS500 dispersion, are likely to be removed, which leads to a dispersion in which the system is no longer stable, and the particles start to aggregate. The zeta-potential of the permeate and retentate (Table 4.3) also decreased to below -30 mV, which could also support the notion that the dispersion started to appear unstable after sonication and TFF separation. This is reasonable because, after fragmentation, the particles no longer maintain a smooth surface morphology due to the random fragmentation, which causes an increase in surface area that might lead to their high reactivity and inter-particle interaction in dispersion [61]. Moreover, it has been confirmed by several studies that the smaller the particle size, the larger the relative surface energy, and the more likely aggregation is to form [62, 63].

The characterization of the fragmented particles by DLS showed a size distribution of 100 nm in APS500-S and APS500-SP, which is below the resolution of optical microscopy. To further characterize the breakage of PS500 beads, we performed AFM for morphological assessment. After the sonofragmentation, as shown in Figure 4.4B, the particles exhibited 3D agglomeration. The cross-section of these aggregates showed a height range of 45−175 nm. The large range of

heights from the cross-section analysis inferred that the PS500 particles were broken after sonication, and possibly re-agglomerated.

### 4.3.4 Chemical Composition Characterization

To investigate whether and how much the chemical structure has changed after the aging process, we used Raman spectroscopy to determine the chemical structure changes after autoclaving and sonicating APS500-S dispersions. APS500 and APS500-SP dispersions were deposited on silicon substrates; a total of 20 sites per sample were investigated for the identification of PS characteristic peaks, and the three spectra in Figure 4.5 are three representative types of spectra of all sites examined for the APS500-SP. The Raman resolution is around 300 nm with the 633 nm laser we used (0.61 λ/NA) [64, 65]. However, the individual particle size distribution of the aged APS500-S is around 150 nm, which is half of the Raman resolution; therefore, measurement of single particle fragments is likely to be subject to artificial error due to the inability to accurately locate the particle position. Thus, to obtain Raman signals with stronger intensity and resolution, we targeted and analyzed the aggregated coffee ring area and larger-size agglomerates (roughly around 1−10 μm) in the field of view.

Only 2 out of 60 locations (3%) show the spectrum in Figure 4.5A, which displays peaks of ring breathing (1002 $cm^{-1}$), C-H in-plane deformation (1031 $cm^{-1}$), C=C stretch (1585 $cm^{-1}$), and ring skeletal stretch (1604 $cm^{-1}$), comprising a typical pristine PS spectrum. In the C-H stretching region, the peak at 3067 $cm^{-1}$ also indicates an aromatic C-H stretch for PS. In Figure 4.5B, the peaks at 1455 and 1585 $cm^{-1}$ are missing (in a blue dashed frame), which represent the Raman shift of $CH_2$ in-phase twist, scissoring, and C=C stretching, respectively [66, 67]. The absence of these signals is likely explained by the oxidized degradation induced by sonication. Ultrasonication is one of the advanced oxidation processes in water, which generates bulk HO• and H• in dispersion

[38, 68]. The HO•, as an oxidant that can shear chemical bonds randomly, creates the conditions for the ring-opening reaction of the benzene. During the reaction, the free HO• first attack the C=C bond on the benzene ring, followed by the C-H vibration, eventually leading to the ring opening of benzene [29, 39, 69], which explained the 24 out of 60 locations (40%) missed benzene ring signals at both fingerprint (around 1000 $cm^{-1}$) and C-H stretching region (around 3060 $cm^{-1}$) in Figure 4.5C (in red dash frame).

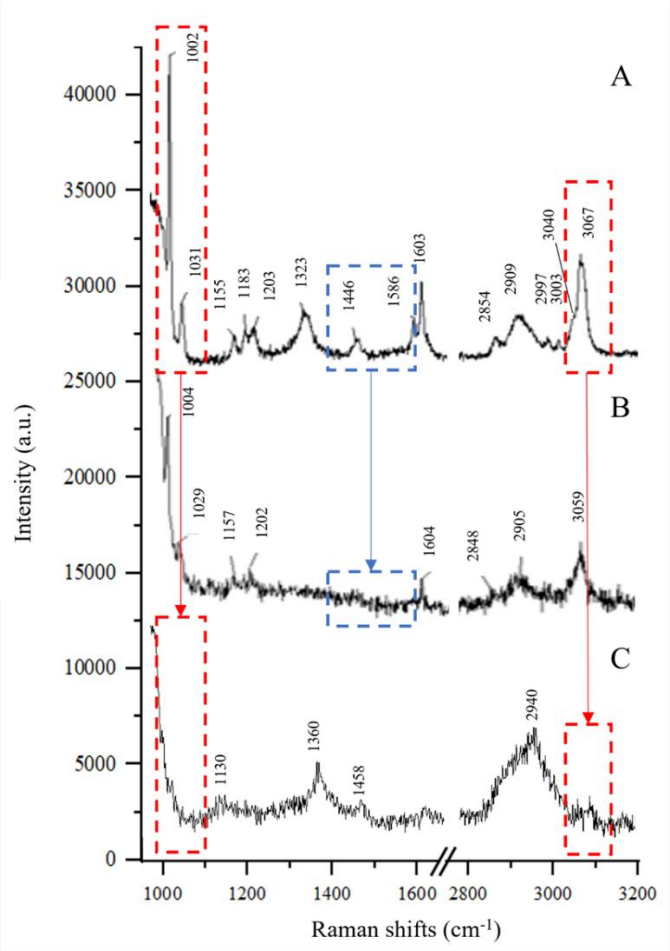


**Figure 4.5 Raman spectra identified in APS500-SP.** (A) polystyrene; (B) degraded polystyrene missing signals of CH2 in-phase twist, scissoring, and C=C stretching; (C) degraded polystyrene missing signals of the benzene ring.

Despite the high accuracy of chemical characterization using Raman, these changes in chemical bonding suggest that the use of a single technique for the identification of plastics is not sufficient. For environmental microplastics with complex properties, a combination of multiple characterization techniques to complement each other is necessary (e.g., FTIR and Raman). Simulation and understanding of the products of different types of plastics under different weathering conditions are needed to more effectively monitor the property changes for accurate identification of micro/nanoplastics.

While the physicochemical characterization demonstrates pronounced aging-induced changes in PS microplastics, the extent to which these transformations translate into acute cellular responses remains uncertain. To examine this boundary, supplementary *in vitro* experiments were conducted and are summarized in Appendix B.

## 4.4 Conclusion

The changes in particle size, size distribution, and chemical composition of nominal 500 nm PS particles before and after the aging process were investigated by applying accelerated aging processes such as heating, elevated pressure treatments, and oxidation with ultrasonic crushing. Our results revealed that under autoclave conditions (121°C, 10 MPa), PS particles in dispersion underwent morphological changes and partial aggregations. After mechanical fragmentation and oxidation simulated by 1 h of probe sonication, the particles were broken down to smaller sizes with increasing sonication energy. We also found that the fragmentation of PS particles by probe sonication was inversely correlated with the concentration of the dispersions, and the size could be reduced to about 150 nm at a low concentration of 7 μg/mL. AFM height imaging and analyses confirmed the breakage of particles after the sonofragmentation process. However, the particles and fragments started to reaggregate in the dispersion after the sonication process. Furthermore,

the chemical bonds of PS became less stable under the combined effect of autoclave and probe sonication, likely due to a ring-opening reaction of benzene induced by the sonication. These findings suggest that PS undergoes significant structural changes during the aging process, which may help explain the imbalance between usage and extracted PS from plastic wastes. Our results also highlight the importance of considering natural weathering and environmental variables when assessing the risks associated with microplastics and nanoplastics. In future studies, we plan to investigate the effects of weathering on different types of plastics and their behaviour under different weathering pathways.

## References


1. Thompson RC, Swan SH, Moore CJ, vom Saal FS. Our plastic age. Philos Trans R Soc B: Biol Sci. 2009;364(1526):1973-6.
2. Chen Y, Awasthi AK, Wei F, Tan Q, Li J. Single-use plastics: Production, usage, disposal, and adverse impacts. Sci Total Environ. 2021;752:141772.
3. Awoyera P, Adesina A. Plastic wastes to construction products: Status, limitations and future perspective. Case Stud Constr Mater. 2020;12:e00330.
4. Ferreira I, Venâncio C, Lopes I, Oliveira M. Nanoplastics and marine organisms: what has been studied? Environ Toxicol Pharmacol. 2019;67:1-7.
5. Sun X, Yuan X, Jia Y, Feng L, Zhu F, Dong S, et al. Differentially charged nanoplastics demonstrate distinct accumulation in Arabidopsis thaliana. Nat Nanotechnol. 2020;15(9):755-60.
6. Nguyen B, Claveau-Mallet D, Hernandez LM, Xu EG, Farner JM, Tufenkji N. Separation and analysis of microplastics and nanoplastics in complex environmental samples. Acc Chem Res. 2019;52(4):858-66.
7. Mattsson K, Jocic S, Doverbratt I, Hansson LA. Chapter 13 - Nanoplastics in the Aquatic Environment. In: Zeng EY, editor. Microplastic Contamination in Aquatic Environments. Amsterdam: Elsevier; 2018. p. 379-99.

8. Enfrin M, Lee J, Gibert Y, Basheer F, Kong L, Dumée LF. Release of hazardous nanoplastic contaminants due to microplastics fragmentation under shear stress forces. J Hazard Mater. 2020;384:121393.
9. Hernandez LM, Yousefi N, Tufenkji N. Are There Nanoplastics in Your Personal Care Products? Environ Sci Technol Lett. 2017;4(7):280-5.
10. Hernandez LM, Xu EG, Larsson HC, Tahara R, Maisuria VB, Tufenkji N. Plastic teabags release billions of microparticles and nanoparticles into tea. Environ Sci Technol. 2019;53(21):12300-10.
11. Shruti V, Pérez-Guevara F, Elizalde-Martínez I, Kutralam-Muniasamy G. Toward a unified framework for investigating micro (nano) plastics in packaged beverages intended for human consumption. Environ Pollut. 2021;268:115811.
12. Mason SA, Welch VG, Neratko J. Synthetic polymer contamination in bottled water. Front Chem. 2018;6:407.
13. Kedzierski M, Lechat B, Sire O, Le Maguer G, Le Tilly V, Bruzaud S. Microplastic contamination of packaged meat: Occurrence and associated risks. Food Packag Shelf Life. 2020;24:100489.
14. Li Y, Li W, Jarvis P, Zhou W, Zhang J, Chen J, et al. Occurrence, removal and potential threats associated with microplastics in drinking water sources. J Environ Chem Eng. 2020;8(6):104527.
15. Stubbins A, Law KL, Muñoz SE, Bianchi TS, Zhu L. Plastics in the Earth system. Science. 2021;373(6550):51-5.
16. Wessel CC, Lockridge GR, Battiste D, Cebrian J. Abundance and characteristics of microplastics in beach sediments: insights into microplastic accumulation in northern Gulf of Mexico estuaries. Mar Pollut Bull. 2016;109(1):178-83.
17. Lo HS, Xu X, Wong CY, Cheung SG. Comparisons of microplastic pollution between mudflats and sandy beaches in Hong Kong. Environ Pollut. 2018;236:208-17.
18. Korez Š, Gutow L, Saborowski R. Microplastics at the strandlines of Slovenian beaches. Mar Pollut Bull. 2019;145:334-42.
19. Erni-Cassola G, Zadjelovic V, Gibson MI, Christie-Oleza JA. Distribution of plastic polymer types in the marine environment; A meta-analysis. J Hazard Mater. 2019;369:691-8.

20. López-Martínez S, Morales-Caselles C, Kadar J, Rivas ML. Overview of global status of plastic presence in marine vertebrates. Glob Chang Biol. 2021;27(4):728-37.
21. Scheurer M, Bigalke M. Microplastics in Swiss Floodplain Soils. Environ Sci Technol. 2018;52(6):3591-8.
22. Alimi OS, Farner Budarz J, Hernandez LM, Tufenkji N. Microplastics and nanoplastics in aquatic environments: aggregation, deposition, and enhanced contaminant transport. Environ Sci Technol. 2018;52(4):1704-24.
23. Azizi SMM, Haffiez N, Zakaria BS, Dhar BR. Thermal Hydrolysis of Sludge Counteracts Polystyrene Nanoplastics-Induced Stress during Anaerobic Digestion. ACS ES&T Eng. 2022;2(7):1306-15.
24. Liu P, Qian L, Wang H, Zhan X, Lu K, Gu C, et al. New Insights into the Aging Behavior of Microplastics Accelerated by Advanced Oxidation Processes. Environ Sci Technol. 2019;53(7):3579-88.
25. Liu J, Zhang T, Tian L, Liu X, Qi Z, Ma Y, et al. Aging Significantly Affects Mobility and Contaminant-Mobilizing Ability of Nanoplastics in Saturated Loamy Sand. Environ Sci Technol. 2019;53(10):5805-15.
26. Alimi OS, Farner JM, Tufenkji N. Exposure of nanoplastics to freeze-thaw leads to aggregation and reduced transport in model groundwater environments. Water Res. 2021;189:116533.
27. Meides N, Menzel T, Poetzschner B, Löder MGJ, Mansfeld U, Strohriegl P, et al. Reconstructing the Environmental Degradation of Polystyrene by Accelerated Weathering. Environ Sci Technol. 2021;55(12):7930-8.
28. Chen Z, Zhao W, Xing R, Xie S, Yang X, Cui P, et al. Enhanced in situ biodegradation of microplastics in sewage sludge using hyperthermophilic composting technology. J Hazard Mater. 2020;384:121271.
29. Ding L, Mao R, Ma S, Guo X, Zhu L. High temperature depended on the ageing mechanism of microplastics under different environmental conditions and its effect on the distribution of organic pollutants. Water Res. 2020;174:115634.
30. Jia Y, Chen J, Asahara H, Asoh TA, Uyama H. Polymer surface oxidation by light-activated chlorine dioxide radical for metal–plastics adhesion. ACS Appl Polym Mater. 2019;1(12):3452-8.

31. Colin X, Audouin L, Verdu J, Rozental-Evesque M, Rabaud B, Martin F, et al. Aging of polyethylene pipes transporting drinking water disinfected by chlorine dioxide. Part II—Lifetime prediction. Polym Eng Sci. 2009;49(8):1642-52.
32. Fernández-González V, Andrade-Garda JM, López-Mahía P, Muniategui-Lorenzo S. Impact of weathering on the chemical identification of microplastics from usual packaging polymers in the marine environment. Anal Chim Acta. 2021;1142:179-88.
33. Alimi OS, Claveau-Mallet D, Kurusu RS, Lapointe M, Bayen S, Tufenkji N. Weathering pathways and protocols for environmentally relevant microplastics and nanoplastics: What are we missing? J Hazard Mater. 2022;423:126955.
34. Jagadeesh N, Sundaram B. A review of microplastics in wastewater, their persistence, interaction, and fate. J Environ Chem Eng. 2021;9(6):106846.
35. Sullivan KP, Werner AZ, Ramirez KJ, Ellis LD, Bussard JR, Black BA, et al. Mixed plastics waste valorization through tandem chemical oxidation and biological funneling. Science. 2022;378(6616):207-11.
36. Hanun JN, Hassan F, Jiang J-J. Occurrence, fate, and sorption behavior of contaminants of emerging concern to microplastics: Influence of the weathering/aging process. J Environ Chem Eng. 2021;9(5):106290.
37. Andrady AL, Barnes PW, Bornman JF, Gouin T, Madronich S, White CC, et al. Oxidation and fragmentation of plastics in a changing environment; from UV-radiation to biological degradation. Sci Total Environ. 2022;851:158022.
38. Madhavan J, Theerthagiri J, Balaji D, Sunitha S, Choi MY, Ashokkumar M. Hybrid advanced oxidation processes involving ultrasound: an overview. Molecules. 2019;24(18):3341.
39. Babu SG, Ashokkumar M, Neppolian B. The Role of Ultrasound on Advanced Oxidation Processes. Top Curr Chem. 2016;374(5):75.
40. No Y, Son Y. Effects of probe position of 20 kHz sonicator on sonochemical oxidation activity. Jpn J Appl Phys. 2019;58(SG):SGGD02.
41. Beißmann S, Stiftinger M, Grabmayer K, Wallner G, Nitsche D, Buchberger W. Monitoring the degradation of stabilization systems in polypropylene during accelerated aging tests by liquid chromatography combined with atmospheric pressure chemical ionization mass spectrometry. Polym Degrad Stab. 2013;98(9):1655-61.

42. Cotes C, Arata A, Melo RM, Bottino MA, Machado JP, Souza RO. Effects of aging procedures on the topographic surface, structural stability, and mechanical strength of a ZrO2-based dental ceramic. Dent Mater. 2014;30(12):e396-e404.
43. Luyt A, Gasmi S, Malik S, Aljindi R, Ouederni M, Vouyiouka S, et al. Artificial weathering and accelerated heat aging studies on low-density polyethylene (LDPE) produced via autoclave and tubular process technologies. Express Polym Lett. 2021;15(2):121-36.
44. Abdel-Raouf ME-S, Mahmoud Abdel-Raheim AR, El-Saeed SM. Thermo-Catalytic Versus Thermo-Chemical Recycling of Polystyrene Waste. Waste and Biomass Valorization. 2013;4(1):37-46.
45. Huang Y, Paul DR. Effect of temperature on physical aging of thin glassy polymer films. Macromolecules. 2005;38(24):10148-54.
46. Cangialosi D, Boucher VM, Alegría A, Colmenero J. Physical aging in polymers and polymer nanocomposites: recent results and open questions. Soft Matter. 2013;9(36):8619-30.
47. Bhattacharjee S. DLS and zeta potential–what they are and what they are not? J Control Release. 2016;235:337-51.
48. Memisoglu-Bilensoy E, Hincal AA. Sterile, injectable cyclodextrin nanoparticles: Effects of gamma irradiation and autoclaving. Int J Pharm. 2006;311(1):203-8.
49. Colomban P, Slodczyk A. Raman intensity: An important tool to study the structure and phase transitions of amorphous/crystalline materials. Opt Mater. 2009;31(12):1759-63.
50. Taheri S, Shoshtari-Yeganeh B, Pourzamani H, Ebrahimpour K. Investigating the pollution of bottled water by the microplastics (MPs): the effects of mechanical stress, sunlight exposure, and freezing on MPs release. Environmental Monitoring and Assessment. 2022;195(1):62.
51. Lu Y, Riyanto N, Weavers LK. Sonolysis of synthetic sediment particles: particle characteristics affecting particle dissolution and size reduction. Ultrason Sonochem. 2002;9(4):181-8.
52. Sander JRG, Zeiger BW, Suslick KS. Sonocrystallization and sonofragmentation. Ultrason Sonochem. 2014;21(6):1908-15.
53. Jordens J, Appermont T, Gielen B, Van Gerven T, Braeken L. Sonofragmentation: Effect of Ultrasound Frequency and Power on Particle Breakage. Cryst Growth Des. 2016;16(11):6167-77.

54. Gao JX, Huang HQ, Li XX, Du FH, Li LB, Li JS. Breakage and Particle Size Redistribution in an Ultrasound-Intensified Leaching Process. Chem Eng Technol. 2015;38(9):1665-70.

55. Li C, Lin J, Shen L, Bao N. Quantitative analysis and kinetic modeling of ultrasound-assisted exfoliation and breakage process of graphite oxide. Chem Eng Sci. 2020;213:115414.

56. Filipe V, Hawe A, Jiskoot W. Critical evaluation of Nanoparticle Tracking Analysis (NTA) by NanoSight for the measurement of nanoparticles and protein aggregates. Pharm Res. 2010;27(5):796-810.

57. Gibson JH, Hon H, Farnood R, Droppo IG, Seto P. Effects of ultrasound on suspended particles in municipal wastewater. Water Res. 2009;43(8):2251-9.

58. Busatto S, Vilanilam G, Ticer T, Lin W, Dickson DW, Shapiro S, et al. Tangential flow filtration for highly efficient concentration of extracellular vesicles from large volumes of fluid. Cells. 2018;7(12):273.

59. Musumeci T, Leonardi A, Bonaccorso A, Pignatello R, Puglisi G. Tangential flow filtration technique: An overview on nanomedicine applications. Pharm Nanotechnol. 2018;6(1):48-60.

60. Van Reis R, Gadam S, Frautschy LN, Orlando S, Goodrich EM, Saksena S, et al. High performance tangential flow filtration. Biotechnol Bioeng. 1997;56(1):71-82.

61. Gogate P, Shaha S, Csoka L. Intensification of cavitational activity in the sonochemical reactors using gaseous additives. Chem Eng J. 2014;239:364-72.

62. He YT, Wan J, Tokunaga T. Kinetic stability of hematite nanoparticles: the effect of particle sizes. J Nanopart Res. 2008;10(2):321-32.

63. Waychunas GA, Kim CS, Banfield JF. Nanoparticulate iron oxide minerals in soils and sediments: unique properties and contaminant scavenging mechanisms. J Nanopart Res. 2005;7(4):409-33.

64. Sobhani Z, Zhang X, Gibson C, Naidu R, Megharaj M, Fang C. Identification and visualisation of microplastics/nanoplastics by Raman imaging (i): Down to 100 nm. Water Res. 2020;174:115658.

65. Zhang W, Fang Z, Zhu X. Near-field Raman spectroscopy with aperture tips. Chem Rev. 2017;117(7):5095-109.

66. Kellar EJ, Galiotis C, Andrews EH. Raman vibrational studies of syndiotactic polystyrene. 1. Assignments in a conformational/crystallinity sensitive spectral region. Macromolecules. 1996;29(10):3515-20.

67. Zhou X, Liu R, Hao L, Liu J. Identification of polystyrene nanoplastics using surface enhanced Raman spectroscopy. Talanta. 2021;221:121552.
68. Liu L, Xu M, Ye Y, Zhang B. On the degradation of (micro) plastics: Degradation methods, influencing factors, environmental impacts. Sci Total Environ. 2022;806:151312.
69. Zhou L, Wang R, Liu Y, Zhang Y, Zhou J, Qu G, et al. Plasma-induced conversion of polystyrene nanoplastics in water: Intermediates release, toxicity, and disinfection byproducts formation. Chem Eng J. 2022;433:134543.

# CHAPTER 5 QUANTIFYING UVC-INDUCED AGING OF MICROPLASTICS USING A MULTIVARIATE AGING SCORE


## Abstract

Microplastics continue to weather as they linger in the environment, yet the roles of polymer type and product formulation in shaping their aging trajectories remain poorly defined. In this work, we examined how commercial polyethylene (PE), polypropylene (PP), and polyethylene terephthalate (PET) microplastics respond to ultraviolet C (UVC) irradiation across doses from 0 to 40 MJ $m^{-2}$. Among the three materials, PP changed the most rapidly: its carbonyl index (CI) rose sharply, its melting temperature ($T_m$) dropped from 157 °C to 141 °C, and its crystallinity ($\chi_c$) declined from 76% to 52%. In contrast, PE and PET showed only modest alterations in their chemical and thermal signatures. Imaging by scanning electron microscopy further highlights the divergence in aging behavior—PP surfaces developed widespread cracks and generated secondary fragments, whereas the other polymers remained comparatively intact. Given that surface oxidation precedes bulk destabilization, we incorporated an infrared (IR)-based surface-crystallinity index ($\chi_s$I) to quantify these early chemical-structural changes. The influence of formulation is investigated using two PP laboratory wastes—transparent centrifuge tubes and blue pipette-tip boxes—both of which show progressive surface cracking, increasing CI, and $T_m$ depression as the UVC dose rises, with the colored material aging faster than the transparent PP. Because aging manifests through several properties that do not evolve in parallel, direct comparisons across polymers and products are challenging. An approach based on principal component analysis integrates CI, $T_m$, $\chi_c$, and $\chi_s$I into a single quantitative aging score. This unified metric provides an approach for harmonized evaluation of aging levels across polymer types, product formulations, and physicochemical properties. The resulting framework facilitates direct comparisons between materials and provides

predictive assessment of microplastic transformation under environmental or laboratory exposure conditions.

## 5.1 Introduction

Microplastics (MPs, <5 mm) are now ubiquitous in marine, freshwater, soil, and wastewater matrices. They originate from the fragmentation and degradation of larger plastic debris in the environment through processes such as mechanical abrasion, photodegradation, chemical oxidation, and biodegradation. Once MPs enter aquatic and terrestrial environments, they undergo continuous environmental aging driven by sunlight, oxidants, and mechanical abrasion [1]. Such aging leads to a range of physicochemical property changes, including reduced particle size, surface roughening, formation of carbonyl, hydroxyl, and carboxyl groups, and alterations in thermal behaviour and crystalline structures. These transformations modify microplastic transport, aggregation, interactions with contaminants, pollutant sorption, and potential uptake by biota, while also affecting the reliability and sensitivity of detection in environmental samples [1]. Additionally, the pronounced heterogeneity of environmental microplastics in terms of polymer composition, colour, morphology, size, and additive content complicates the quantification and comparison of aging, as these characteristics strongly influence degradation pathways, rates, and the expression of physicochemical changes. Most previous studies have focused on differences in aging behaviours among polymer types [2], while systematic quantification of aging variations within a single polymer due to formulation factors (e.g., colourants, additives) remains limited. Despite the rapid growth of MPs research, robust quantitative metrics describing “how aged” MPs samples are across polymers, product origins, or particle sizes are still lacking. To better quantify and compare microplastic aging, there is a need to standardize studies around robust indicators and

analytical techniques that integrate complementary physical, chemical, and mechanical metrics into multivariate factors that more fully describe the progression of aging [3, 4]. Accurately capturing this complexity requires a combination of complementary physical, chemical, and mechanical measurements integrated into multivariate frameworks. Such multi-technique approaches enable fast, high-throughput quantification of aging and improve comparability across studies.

Plastic waste in the environment is subjected to multiple concurrent aging processes, including hydrolysis, photo-oxidation, thermo-oxidation, mechanical degradation, and biodegradation [5], among which photo-oxidative aging is one of the dominant pathways for polyolefins with C–C backbones [6, 7]. Laboratory accelerated aging is therefore widely used to reproduce these complex environmental weathering processes under controlled and reproducible conditions to obtain aged MPs within practical time frames. In contrast, natural weathering often requires months to years to occur and is difficult to standardize across studies [8-10]. Commonly applied laboratory aging approaches include ultraviolet (UV) irradiation (e.g., UVA, UVB, or UVC), thermal and thermo-oxidative exposure, chemically induced oxidation, and biologically mediated aging [10]. Although UVC does not reach the ground level due to atmospheric absorption, its higher photon energy enables more rapid cleavage of surface chemical bonds over short exposure times than ultraviolet A (UVA) or ultraviolet B (UVB) [11], making it an efficient approach for accelerated aging studies. Also, in engineered systems, for example, high-energy UVC at 254 nm from low-pressure mercury lamps is routinely used for disinfection in wastewater treatment plants, indicating that MPs may encounter brief but intense UVC exposures [9, 12]. Consequently, UVC irradiation has become a practical and widely adopted method for producing environment-relevant aged MPs in the laboratory.

UV-aging studies typically expose microplastics either in aqueous media or in air [13, 14]. For hydrophobic polymers such as polyethylene (PE), polypropylene (PP), and polyethylene terephthalate (PET), maintaining homogeneous aqueous suspensions during UV exposure generally requires surfactants, which stabilize the particles and modify their surface properties and transport behaviour [15, 16]. To avoid these surfactant-induced effects and ensure uniform, well-defined irradiation, MPs in this study were exposed to UV in air.

Across UV-based and chemically driven aging pathways, polymers such as PE, PP, and PET undergo oxidation initiated by excited states of photoactive chromophores (e.g., hydroperoxides, carbonyl-containing species, and other impurities/additives) and subsequent free-radical chain reactions. These processes promote the cleavage of covalent bonds, the formation and accumulation of oxygenated functional groups (e.g., carbonyl, hydroxyl, carboxyl species), and progressive surface-to-bulk oxidation [8, 13, 17-21]. These processes increase carbonyl index (CI), alter crystallinity, and promote fragmentation into smaller particles. Beyond polymer type, material formulation and processing history also play an important role in governing aging behaviour [22]. For example, the oxidative aging of colored polystyrene (PS) products is strongly colour-dependent, with white and yellow PS exhibiting the fastest oxidation, reflected by surface O/C ratios and carbonyl signals increasing at rates approximately 1.2–1.8 times and 1.2–5.5 times higher, respectively, compared with red, blue, and black materials [23].

Multiple indicators are therefore used to characterize polymer aging. Changes in thermal behaviour, including shifts and broadening of melting temperature ($T_m$) and variations in crystallinity ($\chi_c$), reflect chain scission and lamellar reorganization, oxidation of amorphous regions, and recrystallization. Li et al. reported a continuous decrease in $T_m$ for LDPE, HDPE, and PP films with increasing UVB exposure, attributed to reduced molar mass and lamellar disruption

[24]. While Canopoli et al. observed approximately two-fold increases in crystallinity for landfill-aged PE and PP relative to fresh plastics, as determined by differential scanning calorimetry (DSC) analysis [25]. On the chemical side, the CI has long been used as an indicator of photo-oxidation in polyolefins [26], defined as the ratio of the infrared absorption of carbonyl groups at around 1720 $cm^{-1}$ relative to a reference peak. Consistent increases in CI have been documented across UV-aging studies. For instance, the CI value in PP mask materials increased from 0.14–0.17 under mild conditions to approximately 0.45 under photoaging at elevated temperature [27]. Similarly, Gao et al. observed a continuous increase in CI for PE and PP aged microplastics under UVA in seawater [13], further supporting that CI rises reflecting progressive photo-oxidation.

In addition to the carbonyl groups, other infrared absorption bands provide useful indicators of aging, including the broad hydroxyl stretch (3100–3500 $cm^{-1}$) and the C–H band at 888 $cm^{-1}$ associated with vinylidene groups, each of which can be expressed as an index relative to an unchanging reference peak [28]. Crystallinity can also be inferred through IR spectroscopy. In PP, certain bands respond to crystalline content; for example, the 998 $cm^{-1}$ band increases with crystallinity, whereas reference bands such as 974 $cm^{-1}$ remain largely invariant [29]. Therefore, the intensity ratio of the 998/974 $cm^{-1}$ peak pair provides a measure proportional to crystallinity. Lanyi et al. used this approach alongside DSC and X-ray diffraction (XRD) to assess bulk and surface crystallinity gradients in PP [30]. Building on this approach, we use the same crystallinity-sensitive peak ratio to establish the surface crystallinity index ($\chi_s I$) by employing attenuated total reflectance Fourier-transform infrared spectroscopy (ATR-FTIR). Since ATR-FTIR has an estimated penetration depth of ~2 μm, the measurement is considered more sensitive to surface crystallinity than to bulk crystallinity, compared with DSC.

While the availability of these physical and chemical indicators makes it challenging to compare results across studies, the absence of standardized approaches that harmonize aging metrics across polymer types, product sources, and particle sizes further complicates the task. Individual measurements, such as CI, $T_m$, $\chi_c$, $\chi_s I$, and size reduction, capture only isolated facets of aging, and different properties often evolve at non-parallel rates. As a result, environmental assessment and risk evaluation require integrated, quantitative metrics that reflect the overall degree of aging in a manner applicable across polymers and formulations [3, 4].

Multivariate statistical analysis offers a route to unify disparate measurements and evaluate their contributions to natural or accelerated aging. Principal component analysis (PCA) has been used to reduce dimensionality, visualize multivariate trends, and classify or regress complex datasets [31]. By transforming data using covariance matrices, PCA weights each feature according to its contribution to overall variance, highlighting the most influential variables. In polymer and plastics research, it has been applied to polymer classification [32], analysis of IR spectroscopy [33], interpretation of mass spectrometry data [34], and evaluation of changes in physicochemical properties [35]. Integrating thermal, chemical, and structural measurements in a multivariate framework allows these complementary aging indicators to be assessed together. It helps capture the complex, non-parallel changes that occur across polymer types and formulations. To further confirm how each variable contributes within this framework, Shapley additive explanations (SHAP) were used to analyze the relative influence of each feature on the aging score. SHAP is derived from the Shapley value, which is a method in cooperative game theory for distributing a total value among cooperating players based on their individual contributions. It has been widely adopted in machine learning as a model-agnostic approach for explaining the contribution of individual features to the outputs of a model [36].

Notwithstanding these advances, standardized and quantitative frameworks that capture the multidimensional nature of microplastic aging across polymer types, product formulations, and particle sizes remain lacking. To address this gap, we develop a fast, high-throughput, multi-technique approach that combines complementary thermal, chemical, and structural measurements into a single, interpretable aging score. Using this framework, we monitored the aging progression of micro-sized PE, PP, and PET, as well as MPs generated from laboratory waste, under controlled UVC irradiation in air. The resulting quantitative aging score enables direct comparison of aging level across polymers and product sources, treating polymer aging as a measurable, integrative parameter and providing a unified system to answer "how much aging has occurred?" across diverse microplastic samples.

## 5.2 Materials and Methods

### 5.2.1 Microplastics Preparation

Commercial plastic powders: PE (average size 10 μm) and PP (average size 42 μm) were purchased from Polysciences (Warrington, PA), and PET (average size 20 μm) was purchased from Chemazone (Leduc, AB). Two PP-based lab consumables used in this study were: (i) PP centrifuge tubes (PPCT, transparent) and (ii) PP pipette boxes (PPPB, opaque blue). Each material was manually cut into 2–4 mm flakes using scissors. Flakes were dispersed in 200 mL of Milli-Q water with 5 mL of ethyl alcohol (95%, Commercial Alcohols Inc., Brampton, ON, Canada) to aid dispersion. The suspension was then subjected to mechanical fragmentation using a laboratory blender operated at high speed for 30 min, following a pulsed protocol of 30 s blending and 10 s pause to produce fragmentation while preventing overheating. The suspensions were filtered through a 5 μm stainless-steel mesh, and the retained material was oven-dried at 50 °C to constant mass. Dried particles were sieved through stainless-steel meshes to obtain different size classes.

Particles smaller than 5 mm were further subdivided into fractions differing by approximately one order of magnitude using mesh sizes of 500, 250, and 125 μm, yielding the 250–500 μm and <125 μm fractions. Accordingly, three PP size groups were defined for subsequent experiments: large (L), 2–4 mm in edge length; medium (M), 351±181 μm (average ± SD); and small (S), 97±44 μm (average ± SD).

### 5.2.2 UVC Aging Process

Approximately 150 mg of each polymer powder or PP microplastic fraction was placed into individual quartz vials (Aireka Scientific Co., Hong Kong, P.R. China), with nine vials typically irradiated per batch. Samples were exposed to 254 nm UVC in air using 18 W low-pressure mercury lamps (Rayonet, Branford, CT) arranged circumferentially around the vials to ensure uniform irradiation [37, 38]. Temperature was continuously monitored at the center of the sample plane during exposure and remained between approximately 50 and 56 °C. All experiments were conducted under ambient atmospheric conditions. UVC irradiance at the sample plane was measured prior to each experiment using a radiometer (Newport, Irvine, CA). After reaching a stable output, power ($P$, mW) was recorded radially from the center at twelve angles in 30° increments and averaged to obtain effective power. Irradiance ($P/A$, W $m^{-2}$) was calculated as the measured power ($P$) divided by the active sensor area ($A$) ($8.3 \times 10^{-5}$ $m^2$). The cumulative UVC radiant exposure (dose) ($H$, MJ $m^{-2}$) was obtained using Eq. 5.1:

$$H = \frac{P \times t}{A} \quad \text{(Eq. 5.1)}$$

where $t$ is the exposure time (s).

UVC irradiation was applied as an energetically accelerated aging method, in which high-energy photons were used to increase the rate of photo-oxidative degradation under controlled conditions. A maximum cumulative dose of 60 MJ $m^{-2}$ was applied, which corresponds to a few months to

about one year of natural UV exposure in terms of radiant energy (typically on the order of ~190-340 MJ $m^{-2}$ per year, depending on the location) [39-41]. Four to six aliquots (~25 mg each) were taken from each vial at predefined intervals to monitor changes at progressively increasing UVC doses.

### 5.2.3 Surface Morphology Observation and Size Distribution Analysis

Surface morphology of all MP materials was examined using a Phenom Pro desktop scanning electron microscopy (SEM, Thermo Scientific, Phoenix, AZ). SEM imaging was conducted at 5 kV and 2800× magnification. Particle size for the commercial polymers was measured from SEM images. In contrast, PPCT and PPPB particles were measured from optical images acquired using an ECHO Revolve R4 microscope (Discover Echo, San Diego, CA) with a 4× objective. Ten randomly selected fields of view were analyzed, yielding 300 particles to minimize sampling bias. Image analysis was performed in ImageJ (National Institutes of Health, Bethesda, MD).

Since particles exhibited irregular shapes, size was represented using the mean Feret diameter. The Feret diameter is the distance between two parallel tangents drawn along a specified direction; it is commonly used to characterize changes in average molar mass during polymer degradation [42]. In this study, the mean Feret diameter was calculated as the average of the maximum and minimum Feret diameters for each particle.

### 5.2.4 Melting Temperature and Crystallinity Analysis

Differential scanning calorimetry (DSC Q2000, TA Instruments, New Castle, DE) equipped with a refrigerated cooling system (RCS90, TA Instruments, New Castle, DE) was used to characterize thermal properties of the polymer samples. Dry plastics (2–5 mg) were placed into Tzero aluminum pans, sealed with Tzero lids using a Tzero DSC sample encapsulation press (all from

TA Instruments, New Castle, DE). Crucible and sample masses were measured using an XPE-205 analytical balance (Mettler-Toledo, Oakland, CA) with a readability of 0.01 mg. The DSC equipment was calibrated periodically during the measurements using indium standards.

Measurements were performed under modulated differential scanning calorimetry (MDSC) mode to resolve reversing (e.g., melting) and non-reversing (e.g., decomposition) thermal events [43, 44]. A constant heating rate of 10 °C/min was used, with a temperature modulation amplitude of 0.796 °C every 60 s. Temperature ranges were selected according to polymer type, with PE heated from 50 to 150 °C, PP from 50 to 200 °C, and PET from 150 to 300 °C. A nitrogen purge of 50 mL/min was maintained throughout the analysis. Thermograms from the first heating ramp were used for data interpretation.

To identify the plastic melting temperature ($T_m$) in the samples, the 'peak maximum' feature in the Universal Analysis 2000 (version 4.7.0.2, TA Instruments, New Castle, DE) was employed to locate the peaks of $T_m$ from the first heating cycle of the reversed thermogram. The peak determination follows the polymer-specific onset and offset windows of 63–130 °C for PE, 95–170 °C for PP, and 185–270 °C for PET, with an error of ± 1 °C.

To determine crystallinity ($\chi_c$), the melting peak area from the first heating cycle of the reversed thermogram was integrated using linear baseline correction, with the onset and offset temperatures set to the same values used for $T_m$ determination for PE, PP, and PET. The crystallinity is calculated by dividing the obtained peak area, corresponding to the heat of fusion ($\Delta H_m$), by the heat of fusion value for 100% perfectly crystalline polymer ($\Delta H_0$, PE: 297 J/g; PP: 207 J/g, PET: 140 J/g) [45], as shown in Eq. 5.2.

$$\%Crystallinity\ (\chi_c) = \frac{\Delta H_m}{\Delta H_0} \times 100\% \qquad \text{(Eq. 5.2)}$$

### 5.2.5 Carbonyl Index and Surface Crystallinity Index Analysis

ATR-FTIR was performed using a Bruker InvenioX FTIR equipped with a Bruker Platinum ATR accessory containing a diamond element (Bruker Optics, Ettlingen, Germany). Measurements were carried out by dispersing a small amount of powder onto the ATR element or a single piece of plastic for the large samples and pressing against the element. This was repeated 3 times for each measurement. FTIR spectra were collected from 600–4000 $cm^{-1}$ at a resolution of 4 $cm^{-1}$ with a coaddition of 32 scans.

All spectra were pre-processed by asymmetrically reweighted penalized least squares (arPLS) [46] using the pybaselines Python package (Python 3.12.3) [47]. The carbonyl index was used as an indicator of oxidation extent by comparing the peak area ($A$) of the carbonyl peak within the range of 1660–1860 $cm^{-1}$ and a reference peak which was agnostic to photooxidation, and varied by polymer (Eq. 5.3):

$$Carbonyl\ Index\ (CI) = \frac{A_{1720\ cm^{-1}}}{A_{reference}} \quad \text{(Eq. 5.3)}$$

Peak areas were obtained over a local baseline established by first subtracting a line between the first and last points of the integration region, then integrating absorbance via the trapezoid method. The reference peaks were at 1455 $cm^{-1}$ for PP and 1460 $cm^{-1}$ for PE [9]. For PET, the ester backbone already gives a strong intrinsic carbonyl band [48], so the carbonyl peak was integrated over 1620–1860 $cm^{-1}$, with the reference peak at 1410 $cm^{-1}$.

The change in surface crystallinity index ($\chi_s$I) of PP, evaluated by ATR-FTIR, was determined as the ratio of the peak heights at 998 $cm^{-1}$ and 974 $cm^{-1}$ (Eq. 5.4), with a common baseline.

$$Surface\ Crystallinity\ Index\ (\chi_s I) = \frac{h_{998\ cm^{-1}}}{h_{974\ cm^{-1}}} \quad \text{(Eq. 5.4)}$$

### 5.2.6 Aging Score Framework

A metric summarizing the overall change in observed measurements, $T_m$, $\chi_c$, CI, and $\chi_s I$, was calculated through a multivariate statistical approach based on principal component analysis (PCA). The procedure for obtaining this value was as follows: each measured quantity (feature) was taken as the change in each aged sample relative to the control (unaged) sample, yielding Δfeature. Because the features have different scales and units, all variables were normalized using standard z-score normalization on a per-feature basis. PCA was applied to the scaled data using scikit-learn (v1.7.1) on Python 3.12.3. Each sample is represented by a principal component score ($z$), described in $n$ dimensions, where $n \leq$ the number of features, i.e., $z = (z_1, z_2 \ldots z_n)$. A baseline point was established by taking the mean of the principal component scores of the control samples, which collapsed to a single PC score since Δfeatures were used, and all initial values for the control samples were set to 0. A weighted Euclidean distance between the PC score of any given sample ($z_i$) and the PC score of the baseline point ($z_0$) was calculated, where each principal component ($z_n$) was weighted by its explained variance ratio ($\lambda_n$). The aging score was calculated as Eq. 5.5:

$$Aging\ Score = \sqrt{\sum_{n=1}^{k} \lambda_n \left(z_{i,n} - z_{0,n}\right)^2} \quad \text{(Eq. 5.5)}$$

where $z_{i,n}$ and $z_{0,n}$ represent the scores of the n-th principal component for the sample and baseline reference, respectively; $\lambda_n$ is the explained variance ratio of the n-th principal component, and k denotes the number of principal components retained. The baseline reference ($z_0$) was defined as the centroid of pristine microplastic samples in the PCA space.

The impact of each feature on the aging score was examined using Shapley values. Shapley additive explanations (SHAP) were applied to the aging score function using a kernel approach via the SHAP package (v0.48).

### 5.2.7 Data Analysis

Data analysis was performed to evaluate aging-induced changes in the chemical, thermal, and morphological properties of the polymers. All measurements were performed using three independent replicate samples (n = 3). Reported values are presented as mean ± standard deviation (SD), and error bars shown in the figures represent the corresponding standard deviation, unless otherwise stated.

Linear regression analysis was performed using GraphPad Prism 10.6.1 (GraphPad Software, San Diego, CA) to evaluate aging-induced trends in carbonyl index, melting temperature, and crystallinity as a function of UVC exposure. An ordinary least-squares linear model with an unconstrained intercept was fitted to individual replicate data for each polymer. The significance of exposure-dependent trends was assessed by testing whether the regression slope differed from zero using the associated t-test. Differences in trend magnitude among descriptors were evaluated by comparing regression slopes with an F-test; $p < 0.05$ was considered significant.

Statistical analyses were applied where discrete group comparisons were appropriate. In particular, particle size distributions between pre- and post-UVC samples were compared using the nonparametric Mann-Whitney test, with $p < 0.05$ considered significant.

## 5.3 Results and Discussion

### 5.3.1 Polypropylene Undergoes the Most Pronounced UVC Aging

The aging responses of PE, PP, and PET to UVC irradiation were assessed using chemical, thermal, and morphological analyses. Differences in monomer composition and polymer architecture strongly influenced the extent of degradation. PE and PP are polyolefins with saturated hydrocarbon backbones, whereas PET is a polyester with an aromatic ester backbone. These

structural variations determine how readily a polymer reacts with oxygen, undergoes chain scission, and experiences lamellar order or surface changes.

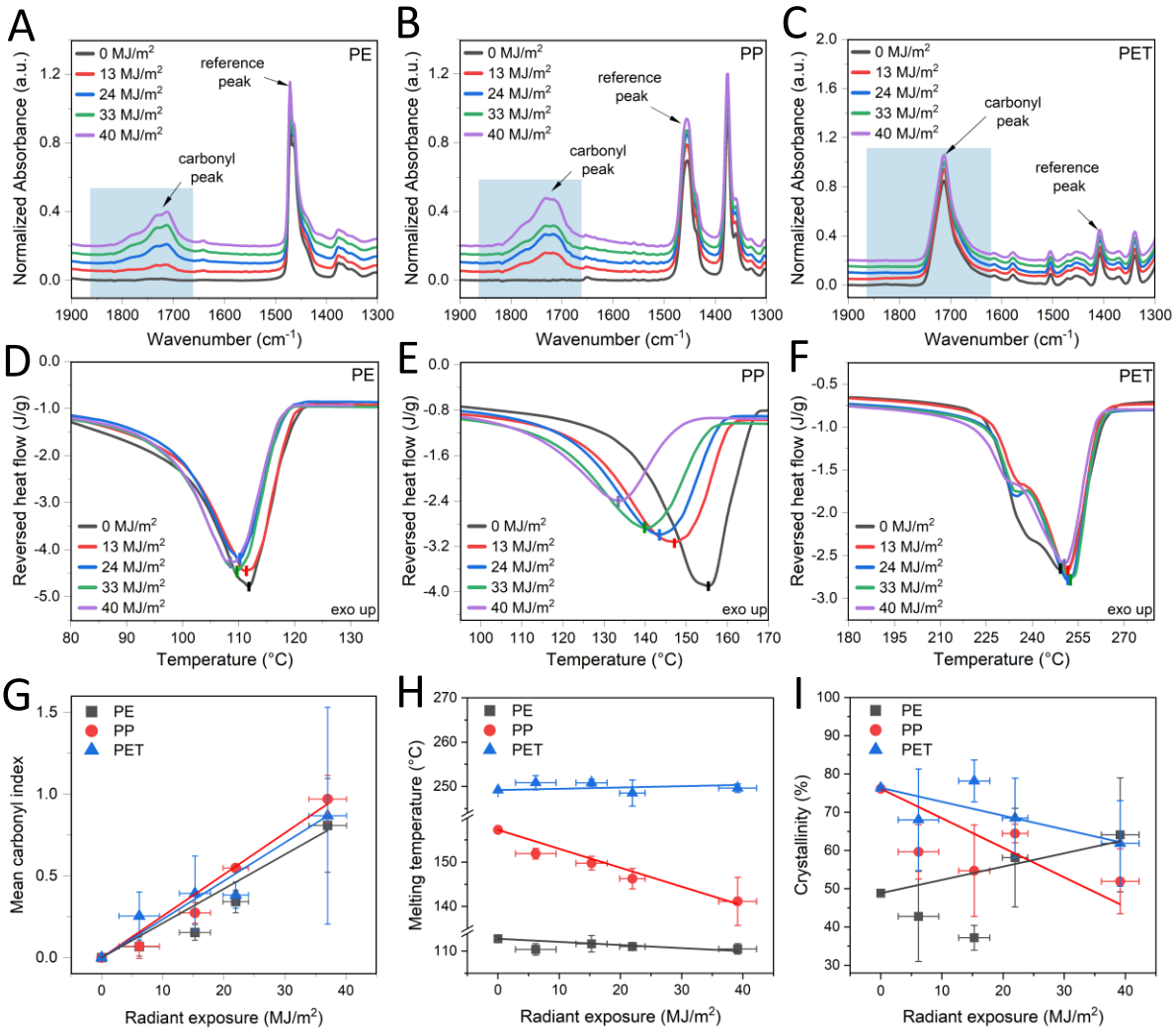


**Figure 5.1 Chemical and thermal property changes of PE, PP, and PET pre- and post-UVC irradiation (0 and 40 MJ m$^{-2}$).** (A-C) ATR-FTIR spectra in the 1900–1300 cm$^{-1}$ region and (D-F) MDSC thermograms of PE, PP, and PET under UVC exposure up to 40 MJ m$^{-2}$. DSC heat flow is presented with the exothermic direction oriented upward (exo up). Changes in carbonyl indices (G), melting temperature (H), and crystallinity (I) of PE, PP, and PET under UVC exposure up to 40 MJ m$^{-2}$. The solid lines correspond to linear fits applied to each dataset. The error bars represent the standard deviation calculated from three replicate samples (n=3).

ATR-FTIR was used to track oxidation, particularly the formation of carbonyl groups. ATR-FTIR spectra of PE, PP, and PET show increasing carbonyl-band intensity with higher UVC exposure (Figure 5.1A–C), and integration of this band yields a rising carbonyl index, confirming the occurrence of oxidation. Because the carbonyl peak at 1720 $cm^{-1}$ represents a mixture of photo-oxidation products, integration of the peak area was employed rather than peak height to better quantify the full extent of photochemical changes [28]. For PE and PP, the carbonyl region appears as a developing band on an otherwise low-carbonyl baseline, such that the emergence and integrated area of the 1720 $cm^{-1}$ region are straightforward indicators of new photo-oxidation products. For PET, by contrast, the ester carbonyl is an inherent feature of the backbone; the 1720 $cm^{-1}$ region therefore represents a mixture of intrinsic and newly formed carbonyl species, which limits the interpretability and quantitative comparability of CI across polymers. Although alternative PET oxidation proxies, such as acid carbonyl bands and hydroxyl stretching modes, have been reported in the literature, CI is retained here to maintain a consistent oxidation-related descriptor across polymers within this study.

For each polymer, CI increases approximately linearly with dose over the tested range (Figure 5.1G), enabling a simple comparison of oxidation rates based on the CI-dose slope. Using the same integration approach and polymer-specific reference peaks, we find that PP has the steepest CI-dose slope, indicating the most rapid accumulation of carbonyl functionality under identical irradiation conditions. PET exhibits a higher slope than PE, despite the visual spectral comments above; this apparently paradoxical outcome likely reflects normalization artifacts in PET because of its pre-existing ester carbonyl signal and the increased sensitivity of the CI calculation to baseline or reference-peak variability in that polymer. Importantly, CI values are measured relative to polymer-specific reference peaks and therefore are not absolute cross-polymer concentrations;

the slope metric is the appropriate comparator for oxidation susceptibility across polymers in this dataset [49].

The spectral trends are consistent with UVC-driven formation of oxygen-containing groups via radical pathways (peroxy and alkoxy intermediates) and subsequent chain-end or backbone functionalization [50, 51]. The comparatively strong spectral response of PP reflects its higher density of tertiary C–H sites and chromophoric susceptibility to radical formation relative to PE. At the same time, the intrinsic carbonyl baseline of PET alters how newly formed oxidation products manifest in spectra [52]. In this study, PET degraded more slowly under UVC aging in air because PET degradation primarily proceeds via ester-bond cleavage and the formation of carboxylic end groups via photo-induced and hydrolysis-assisted processes in water [53]. Those hydrolytic pathways are limited in dry UVC-in-air conditions.

Upon UV aging, peroxide formation cleaves covalent bonds, inducing chain scission and generating low-molecular-weight fragments or monomeric species, which in turn affect the thermal stability of the plastic [5]. DSC is commonly used to characterize such thermal behaviour [54], as changes in molecular mobility and chain packing manifest as shifts or broadening in thermal transitions such as melting temperature ($T_m$). As shown in Figure 5.1D–F, PP exhibited a clear shift and broadening of the melting endotherm, with $T_m$ falling from 157°C to 141 °C. Among the three polymers, PP showed a significantly faster Tm decrease with UV dose than PE and PET ($P < 0.0001$), whereas PE and PET show only modest changes and remain near their original $T_m$ over the same dose range (Figure 5.1H).

Bulk crystallinity changes ($\chi_c$) derived from MDSC melting enthalpy (Figure 5.1I) further confirm that PP experiences the largest crystallinity loss (76% to 52%), consistent with lamellar disruption and partial loss of ordered crystalline domains. This $\chi_c$ reduction in PP is significantly greater than

that observed for PE and PET ($p < 0.05$). The observed PP thermogram evolution ($T_m$ depression and $\chi_c$ loss) is consistent with chain scission disruption of lamellar orders. At the same time, shorter chain fragments can also recrystallize into less perfect lamellae, with broadened and shifted melting behaviour [55, 56]. The near-stability of PE and PET thermograms suggests that UVC-induced chain scission or structural reorganization is either slower in these polymers or predominantly occurs at the surface, below the bulk-sensitive DSC detection threshold. Overall, the divergent thermal responses indicate that UVC exposure more strongly perturbs the bulk crystalline structure of PP than that of PE or PET under the experimental conditions used.

The observed thermal changes imply that chain scission and lamellar disruption are accompanied by surface-level manifestations, such as cracking and fragmentation, which can be directly visualized. SEM images reveal polymer-specific surface responses: PP develops pronounced cracking and secondary fragments after UVC exposure, PE shows slight surface flaking, and PET remains largely unchanged (Figure 5.2A). These morphological observations are complemented by particle size analysis, which provides an additional indicator of microplastic aging, as UV-induced embrittlement and cracking can lead to fragmentation into smaller particles [57]. Consistent with the morphology changes in SEM images, post-UVC size distributions shifted toward smaller particles for PP and PET (Figure 5.2B–D), with the largest decrease observed for PP from (38.4±19.7) μm to (16.4±11.5) μm (Figure 5.2C).

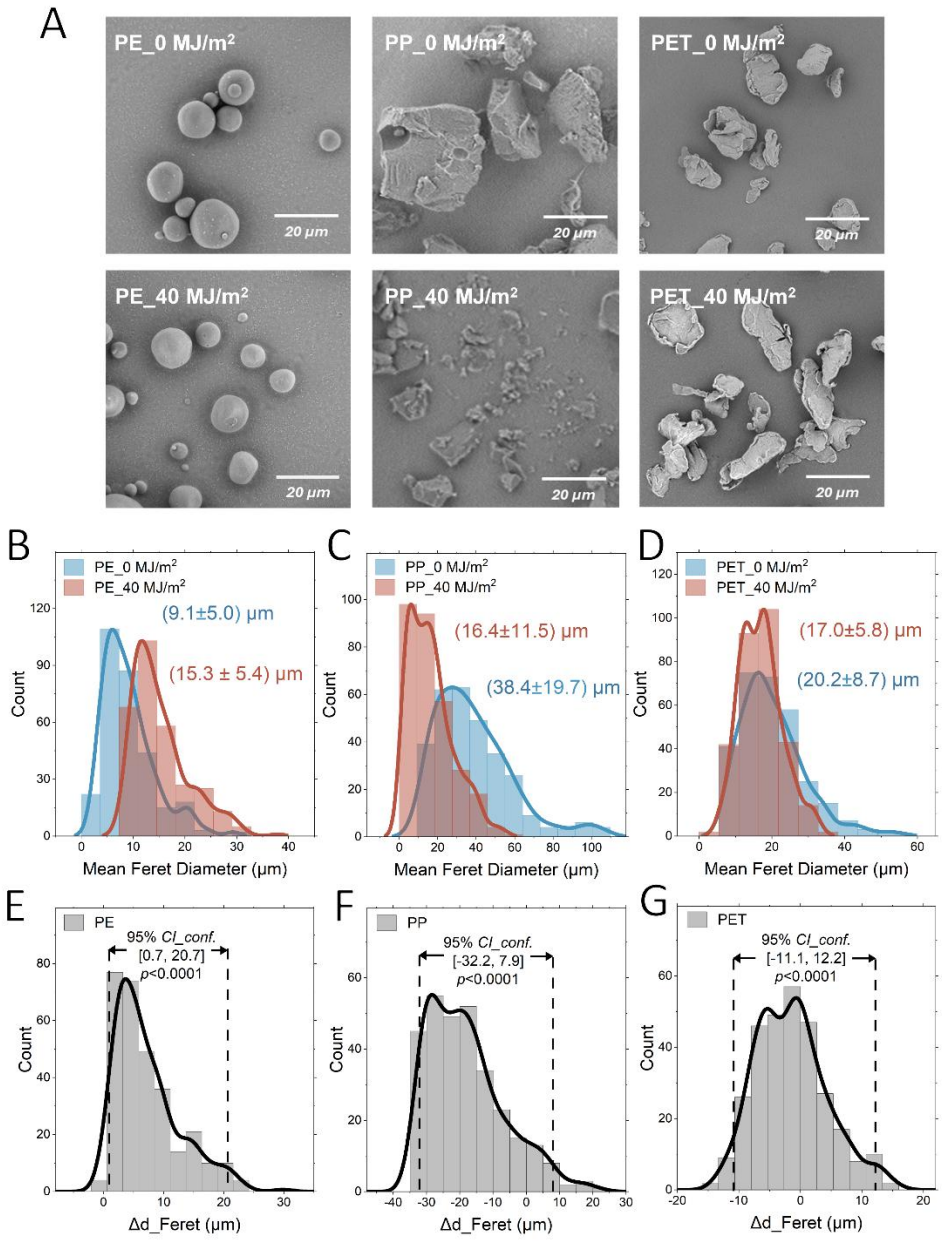


**Figure 5.2 Morphology changes and particle size distributions of PE, PP, and PET pre- and post-UVC irradiation (0 and 40 MJ m$^{-2}$).** (A) SEM images of PE, PP, and PET pre- and post-UVC irradiation. (B–D) Histograms with overlaid kernel density curves showing the size distributions of 300 particles for each polymer, with mean and standard deviation indicated. (E–G) Distribution of size shifts for PE, PP, and PET post-UVC irradiation. Dashed lines indicate the 95% confidence intervals (*CI_conf.*), and statistical analysis using the Mann–Whitney test shows highly significant differences between pre- and post-UVC samples ($p < 0.0001$ for all cases).

This pattern aligns with previous reports showing that PP undergoes more advanced surface cracking and oxidation than PE under comparable UV irradiation [58]. The observed fragmentation is consistent with a photo-oxidative degradation mechanism, in which UV-induced chain scission and surface embrittlement generate fractures that evolve into crack networks and secondary fragments. These fragments act as stress concentrators, further accelerating size reduction [58, 59]. To facilitate a direct, polymer-independent comparison of UV-induced fragmentation, we analyzed the size shift between pre- and post-UVC samples rather than the raw size distributions. As shown in Figure 5.2E–G, nonparametric tests confirmed significant pre/post differences for all plastics (Mann–Whitney, $p < 0.0001$), with PP exhibiting the largest median decrease and a broader negative tail in the size-shift distribution (Figure 5.2F), indicating both a greater extent and higher heterogeneity of fragmentation.

For more UV-resistant polymers like PET, cracking and fragmentation were not dependable visual indicators under the applied conditions, reinforcing the need to rely on chemical and thermal metrics to capture aging [60, 61]. These results show that PP displays internally consistent chemical, thermal, and physical responses indicative of advanced aging, PE exhibits limited oxidation and early surface changes with weak thermal effects, and PET remains comparatively resistant within the tested UVC dose range. It should be noted that detailed formulations of the commercial plastic powders were not provided by the manufacturers. Therefore, the observed aging behaviour reflects the combined effects of polymer chemistry and formulation-specific additives, rather than intrinsic polymer susceptibility alone.

### 5.3.2 Chemical and Thermal Characteristics of Aged PP

The aging rate of polymers is determined not only by their intrinsic molecular structure but also by additives and the polymerization or processing techniques used during manufacture to enhance material performance. In commercial plastics, stabilizers and antioxidants are commonly incorporated to improve colour, processability, and mechanical properties, thereby increasing resistance to degradation [5, 62]. Among these, colourants can strongly influence environmental durability by modifying photodegradation pathways, and the loss of pigments from the bulk can further weaken the polymer [63, 64]. To explore how these formulation factors affect UVC-induced aging, two representative laboratory plastic wastes were selected: transparent disposable polypropylene centrifuge tubes (PPCT) and opaque blue pipette tip boxes (PPPB). Additionally, the size, shape, and thickness of plastic items strongly influence their fragmentation patterns and aging behaviour. This is further illustrated by cross-sectional oxidation profiles, in which ATR-FTIR measurements taken at different depths in a larger-size fraction of PP materials show higher carbonyl peak areas near the surface and progressively lower levels toward the interior (Figure C1), indicating that oxidation proceeds inward from the exterior. Such surface-initiated oxidation implies a possible size dependence. Also, smaller particles (< 500 nm), owing to their higher surface-area-to-volume ratios, are generally more susceptible to degradation, as enhanced surface exposure accelerates oxidative reactions [65, 66].

Bulk thermal properties, assessed by MDSC, demonstrated size-dependent structural effects. With increased UVC exposure, the leftward shift of the melting peaks and the reduction in peak area indicate decreased $T_m$ and $\chi_c$ (Figure C2), consistent with chain scission, lamellar thinning, and partial loss of order domains, which reduce the thermal stability of the semi-crystalline structure [67, 68]. A pronounced size effect was observed in $T_m$ (Figure 5.3A and E), where small-sized

PPCT-S and PPPB-S exhibited the largest $T_m$ decreases (18 °C and 23 °C, respectively), followed by medium and large fractions (S > M > L). This size dependence was particularly clear for PPPB, where the small fraction showed a much stronger $T_m$ depression ($P < 0.0001$), and a more moderate but still significant effect for PPCT ($p < 0.05$), likely due to their higher surface area-to-volume ratio, greater oxidized surface fraction, and increased susceptibility to lamellar disruption, in agreement with previous microplastics aging studies [57].

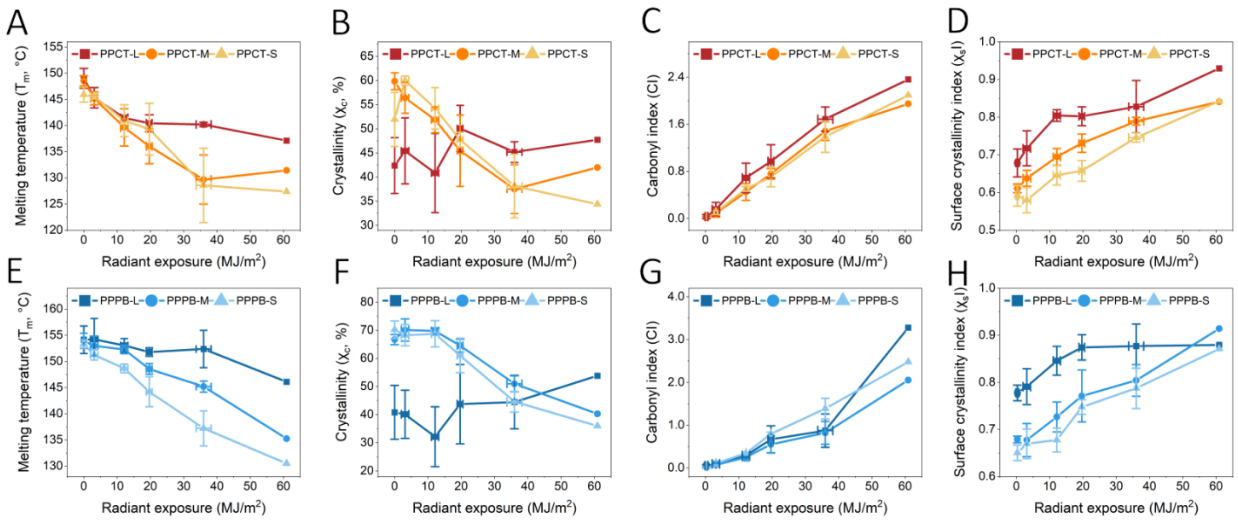


**Figure 5.3 Changes in melting temperature ($T_m$), crystallinity ($\chi_c$), carbonyl index (CI), and surface crystallinity index ($\chi_s I$) of polypropylene lab consumables under increasing UVC dose.** (A–D) PPCT and (E–H) PPPB. Error bars represent the standard deviation from triplicate samples (n=3). Data points at 60 MJ $m^{-2}$ correspond to an exploratory, late-stage aging condition and were obtained from a single sample; therefore, error bars are not shown for this exposure.

Changes in $\chi_c$ followed a more complex trend. As shown in Figure 5.3B and F, the medium and small fractions of both PPCT and PPPB showed overall $\chi_c$ reduction after 60 MJ $m^{-2}$ UVC exposure, confirming progressive disruption of crystalline lamellae [68]. Across the full exposure range, these $\chi_c$ changes were statistically significant for both PPCT and PPPB ($p < 0.0001$). In the

large size fraction, PPCT-L showed a slight increase in $\chi_c$ during early exposure at 3 MJ $m^{-2}$ before decreasing at 12 MJ $m^{-2}$, followed by partial recovery at 20 MJ $m^{-2}$ and gradual decline at higher doses. In comparison, PPPB-L exhibited an initial decrease at a low UVC dose of 12 MJ $m^{-2}$, followed by an increase at higher exposure levels. This transient recrystallization aligns with literature-reported mechanisms in which initial chain scission allows short-chain lamellae to reorganize before further oxidative degradation dominates [67]. The medium- and small-size fractions tended to exhibit smoother, near-linear decreases in $\chi_c$, and no evident size-dependent pattern was observed, suggesting that once surface oxidation reaches a critical extent, further crystallinity loss proceeds more uniformly in smaller particles.

ATR-FTIR analysis revealed a systematic increase in CI with increasing UVC irradiation exposure across all polypropylene materials and three size classes, demonstrating a clear dose-dependent oxidation response (Figure 5.3C and G). Linear analyses of CI versus dose revealed material-specific trends: for the medium and small size fractions, PPCT and PPPB particles exhibited nearly identical CI growth, whereas in the large size fraction, PPPB displayed a sharp increase at more prolonged exposure (60 MJ $m^{-2}$), suggesting an accelerated oxidation process. Interestingly, for the surface crystallinity index, $\chi_s$I showed an overall increasing trend across all size fractions (Figure 5.3D and H), in contrast to the trends observed in $\chi_c$. While $\chi_c$ decreases as bulk lamellae are disrupted, $\chi_s$I increases because the surface chain scission generates shorter and more chain segments that are more capable of reorganizing into surface-localized ordered regions [69]. This contrasting behaviour highlights the importance of distinguishing bulk versus surface-sensitive metrics when assessing polymer aging. For PPPB, however, the increase in $\chi_s$I began to level off beyond 20 MJ $m^{-2}$, likely due to surface oxidation, which reduces chain mobility and limits further ordering. Notably, PPPB exhibited significant size dependence in both CI ($p < 0.01$) and $\chi_s$I ($p <$

0.001), whereas no significant size dependence was detected for PPCT. The discrepancy between PPPB and PPCT may further reflect formulation differences, as pigments and stabilizer packages are known to strongly modulate PP degradation depth profiles, which are often governed by oxygen-diffusion-limited surface reactions [70]. Additionally, given the surface-sensitive nature of ATR-FTIR measurements, which probe approximately the outer 2 μm of samples, the calculated CI and $\chi_s$I mainly represent surface oxidation that can be similar across sizes.

### 5.3.3 Surface Morphology and Particle Size Evolution of PP

Building on the chemical and thermal changes, the two PP materials with distinct additive compositions and coloration provide a basis for comparing their morphological changes and particle-size evolution under controlled UVC exposure.

The surface morphology and size change of PPCT and PPPB in large (L), medium (M), and small (S) size fractions under UVC are shown in Figure 5.4. For the large fractions (PPCT-L and PPPB-L), initially smooth and featureless surfaces developed dense crack networks after UVC irradiation (Figure 5.4A), indicating that UV-induced degradation affected the entire exposed surface and that the materials had become sufficiently embrittled for mechanical stresses to be relieved through crack formation [59]. Notably, PPCT-L tended to form finer and more continuous crack patterns, whereas PPPB-L exhibited wider and shallower cracks. This difference is likely associated with formulation-level variations, including pigment incorporation and stabilizer packages, which may influence both the depth and uniformity of oxidation as well as the distribution of mechanical stresses within the surface layer [17, 64, 71], although contributions from other formulation- or history-dependent factors cannot be excluded.

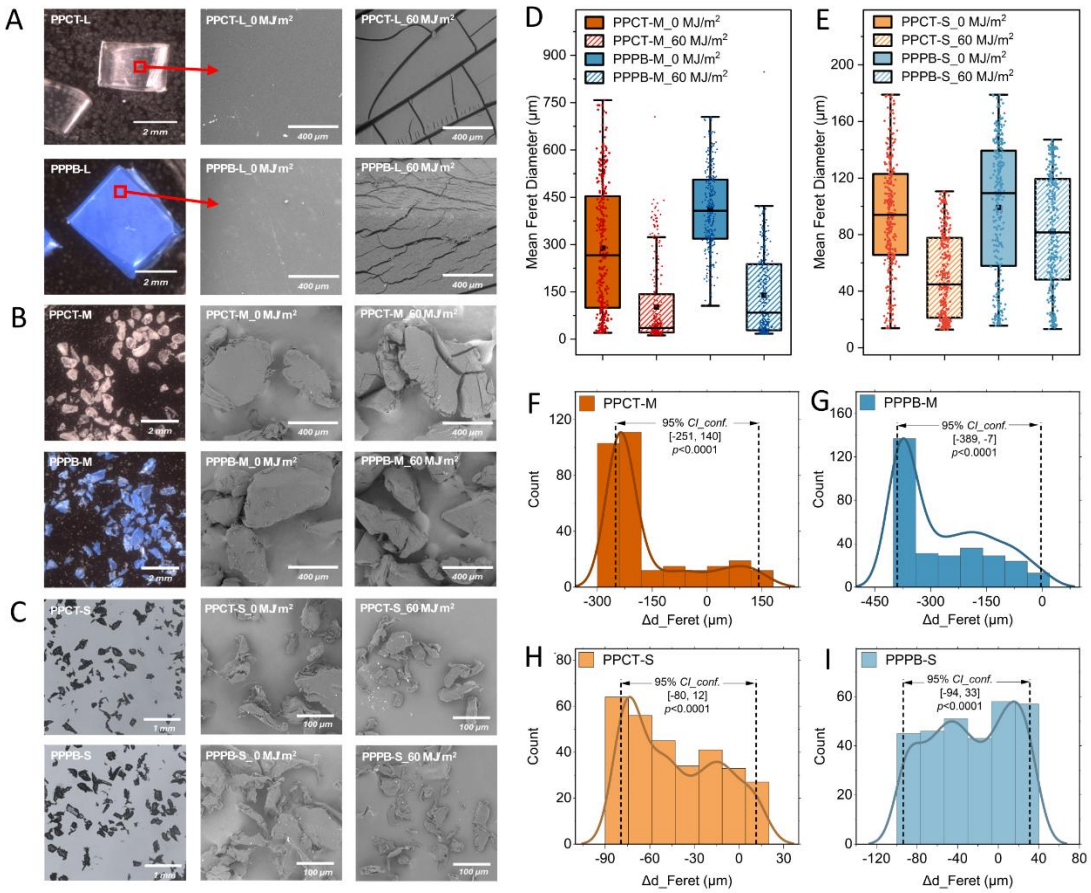


**Figure 5.4 Morphology and size distribution change.** SEM images of PPCT and PPPB in (A) large, (B) medium, (C) small sizes pre- and post-UVC (0 and 60 MJ $m^{-2}$) exposure. (D–E) Box plot of size distributions of PPCT and PPPB samples in medium and small sizes. Mean values (■), medians (─), interquartile range (25–75%), and minimum-maximum values (n=300) are presented. (F–I) Distribution of size shifts for PPCT-M, PPPB-M, PPCT-S, and PPPB-S post UVC irradiation. The dashed line represents the 95% confidence intervals (*CI_conf.*), and statistical analysis using the Mann–Whitney test indicated highly significant differences between pre- and post-UVC (0 and 60 MJ $m^{-2}$) samples ($p < 0.0001$ for all cases).

In the medium-size fraction (M, Figure 5.4B), PPCT-M also displayed apparent intergranular cracks after UVC irradiation, accompanied by an 86% decrease in mean Feret diameter from a median of 266 µm to 36 µm (Figure 5.4D). By contrast, PPPB-M retained a comparatively

smoother surface with only limited defect formation, and its mean Feret diameter decreased by 66%, from 407 µm to 139 µm. While specific stabilizer systems were not independently characterized, the observed difference suggests that transparent PPCT reaches an embrittled state at lower cumulative exposure than blue PPPB, indicating formulation-level effects, such as the absence of UV-shielding pigments [64].

For the small size fraction (S, Figure 5.4C), however, SEM imaging becomes less sensitive to surface features due to the resolution limit and contrast artifacts. Despite this limitation, particle size analysis showed that PPCT-S decreased by 52%, from 94 µm to 45 µm, and PPPB-S decreased by 25%, from 109 µm to 82 µm (Figure 5.4E), indicating that substantial fragmentation also happened in the smallest particles. Both PPCT and PPPB showed minimal observable changes in surface morphology at this scale, implying that aging in small particles primarily proceeds through the detachment of fine fragments rather than the formation of prominent cracks.

Statistical analysis (Figure 5.4F–I, Mann–Whitney test) confirmed that all pre- *vs.* post-UVC size changes were significant ($p < 0.0001$). Although the maximum particle sizes remained high after aging (e.g., PPPB-M up to 847 µm), the bulk of each distribution shifted toward smaller sizes.

Overall, these morphological and particle size observations demonstrate that UVC-induced aging of PP is strongly influenced by both product origin and particle size. Large particles develop distinct crack networks whose characteristics depend on the formulation. In contrast, medium and small particles primarily reflect aging through a measurable reduction in particle size rather than through uniformly visible surface cracking.

### 5.3.4 Multidimensional Aspects of Polymer Aging

The results from our multi-technique approach (chemical, thermal, morphological) suggest that UVC-induced aging of PP proceeds through an interdependent cascade: surface oxidation weakens the polymer, which propagates into the bulk crystalline structure, ultimately facilitating fragmentation. This mechanistic view aligns with emerging experimental evidence that couples chemical alteration to physical disintegration under realistic aging conditions. For instance, Meides et al. reported that both stabilized and non-stabilized PP particles undergo exponential molecular-weight loss and produce large numbers of small particles under accelerated weathering [71]. Similarly, when bulk PP was exposed to natural seawater and environmental-like UV radiation, it released substantial quantities of secondary microplastics (50–5000 μm), far more than those produced by comparable bio-based plastics under the same conditions [72]. In our experiments, the observed $T_m$ depression and loss of $\chi_c$ for PP (especially in smaller particles) suggest that lamellar order is compromised early during aging. This structural destabilization likely underlies the transition from chemical modification to physical failure.

One plausible explanation for the polymer-specific differences in surface response is differential absorption of UVC (254 nm) light. Ultraviolet-Visible (UV-Vis) spectroscopy measurements on PP, PE, and PET thin films showed distinct absorbance behaviours under 254 nm irradiation [73], indicating polymer type-dependent spectral sensitivity. These differences in absorbance may influence the extent of surface degradation under UVC by modulating the amount of photon energy absorbed and made available to drive photochemical bond scission or subsequent oxidative reactions. However, this explanation should be treated with caution. In comparable experiments measuring microplastic formation under 254 nm irradiation, PP produced fewer particles than PET, indicating that absorption alone does not entirely dictate fragmentation [74]. In other words,

while differential UVC absorption is likely a contributing factor to polymer-specific degradation, it is not the sole determinant—consistent with the broader understanding of polymer photodegradation processes [75].

Interestingly, the relationship between oxidation and fragmentation is not universal. In a recent study, environmental variables including humidity, temperature, and UV dose were evaluated across different polymer types. Although photo-oxidation is common, the generation of secondary micro- and nanoplastics depends strongly on both polymer identity and the aging conditions [76]. It is also shown that in the absence of mechanical stress, oxidation alone leads to only limited fragmentation [76, 77]. In addition, environmental matrices, such as catalytic (iron-bearing minerals), modulate degradation and may promote deeper oxidation, leading to more rapid progression to embrittlement and fracture beyond that observed in pure polymer [72, 78]. In practice, commercial PP items (e.g., colored or pigmented plastics) may thus age or fracture differently than unpigmented lab resins, complicating simple extrapolation from pristine materials.

Given the diversity of degradation pathways and outcomes, reliance on a single metric (e.g., carbonyl index) is insufficient to assess "how aged" a microplastic is, or its potential to fragment. Instead, the data and literature strongly support a multidimensional, integrated "aging score" approach that combines chemical (e.g., CI), thermal, structural (e.g., $T_m$, $\chi_c$, $\chi_s$I), and morphological (e.g., particle size) indicators.

### 5.3.5 Aging Score: Correlation of Polymer Chemical, Thermal, Structural, and Morphological Properties

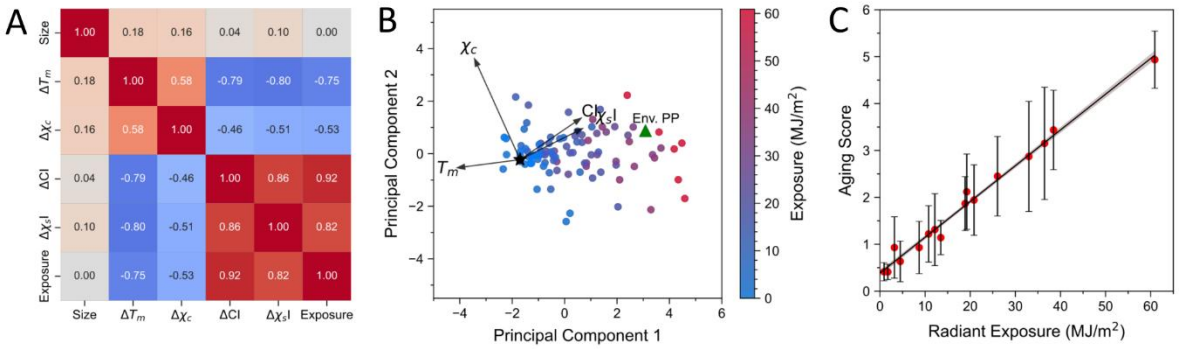


**Figure 5.5 Multidimensional analysis of PP microplastic aging metrics.** (A) Pearson correlation matrix displaying the correlations among the initial size and changes in $T_m$, $\chi_c$, CI, and $\chi_s I$. The colour scale ranges from -1 (strong negative correlation) to +1 (strong positive correlation), with values near zero indicating no linear relationship. (B) Principal component analysis derived from $\chi_c$, $T_m$, CI, and $\chi_s I$ for all PPPB and PPCT measurements, showing the first two principal components. Each point represents an individual sample, with the black star symbol representing the control sample. Arrows show the loading vectors of the variables; their orientation and length reflect the direction and relative contribution of each property to the principal components. The Env. PP represents an environmental PP fragment that was not included in PCA model construction and serves as an independent application of the aging score. (C) An aging score is calculated as the weighted Euclidean distance from any point to the control point.

The diversity of measured properties highlights the multidimensional nature of microplastic aging. It raises the question of which metrics most reliably capture degradation/plastic aging, and whether they can be synthesized into a single, interpretable measure. Although fragmentation and size reduction are important aspects of microplastic aging, morphological metrics were not incorporated into the aging score in this study. The proposed aging score was intentionally defined using bulk, ensemble-averaged chemical and structural descriptors, while morphology reflects

particle-level size distributions and can vary strongly with sampling and imaging conditions. Integrating these heterogeneous data types into a single score would require standardized distribution descriptors and different weighting strategies. Thus, only initial size, $\Delta T_m$, $\Delta CI$, $\Delta \chi_c$, and $\Delta \chi_s I$ were analyzed. Pearson correlation analysis (Figure 5.5A) indicates that the initial particle size has minimal influence on the evolution of chemical, thermal, or structural properties, suggesting that surface and bulk responses are decoupled mainly from particle size within the studied range. The remaining measured quantities, or features, are observed to correlate with the cumulative UV dose (radiant exposure) and with one another. Changes in each feature relative to the control sample ($\Delta T_m$, $\Delta CI$, $\Delta \chi_c$, and $\Delta \chi_s I$) improve comparability across samples and strengthen correlations. Notably, CI and $\chi_s I$ are strongly positively correlated, with Pearson correlation coefficients (r) > 0.80 with respect to radiant exposure and with each other, reflecting the coupling between surface oxidation and near-surface crystallinity. In contrast, $T_m$ shows a stronger negative correlation with exposure ($r = -0.75$), whereas $\chi_c$ exhibits a weaker negative correlation ($r = -0.53$) and weaker correlations with other features, consistent with differential sensitivity of bulk crystallinity versus surface properties. Although both $\chi_c$ and $\chi_s I$ quantify crystallinity, they respond differently to UVC exposure: $\chi_c$ is negatively correlated, whereas $\chi_s I$ is positively correlated, due to the bulk versus surface sensitivity of the measurements.

Principal component analysis (PCA, Figure 5.5B) reduces this multidimensional dataset to key axes of variance, with the first two components capturing ~90% of the variation. The first principal component (PC1) explains the most variance (in this case, 75%), with the second component (PC2) explaining less (15%), and the remaining components explain the remainder (Figure C3). The weights of each feature toward each principal component (loading) also provide information about their importance (Figure C3). The loading vectors shown in Figure 5.5B indicate that $T_m$, CI, and

$\chi_s$I dominate the PC1, while $\chi_c$ contributes primarily to the PC2. The black star symbol in Figure 5.5B represents the control samples, which collapse to a single point as each sample actually represents the difference from the control values. As the colour gradient shows, samples with increased radiant exposure lie further from the control point, primarily along the PC1.

This can be utilized to establish a harmonized multivariate metric for the degree of aging in the sample. By measuring the distance of each sample from the control point in principal component space, we obtain an aging score that represents the overall change in properties (Figure 5.5C). This distance is calculated as the weighted Euclidean distance, where directions along each principal component are weighted by their explained variance. Weighting by explained variance ensures that poorly correlated or low-variance features have minimal impact on the score, while strongly correlated, high-variance features dominate. The resulting aging score exhibits a near-linear relationship with exposure time ($R^2 = 0.987$), providing a robust, predictive measure of cumulative degradation. It is noted that because the aging score is derived from multivariate relationships within a specific dataset, it is intended for comparative interpretation within a given experimental system rather than as an absolute metric transferable across studies without recalibration.

The contributions of individual features to the aging score were further evaluated using Shapley additive explanations (SHAP), which quantify the impact of each feature on the predicted score for every sample [79]. SHAP distributes the “total outcome” among all input variables according to their marginal contributions, and can be applied in a model-agnostic manner.

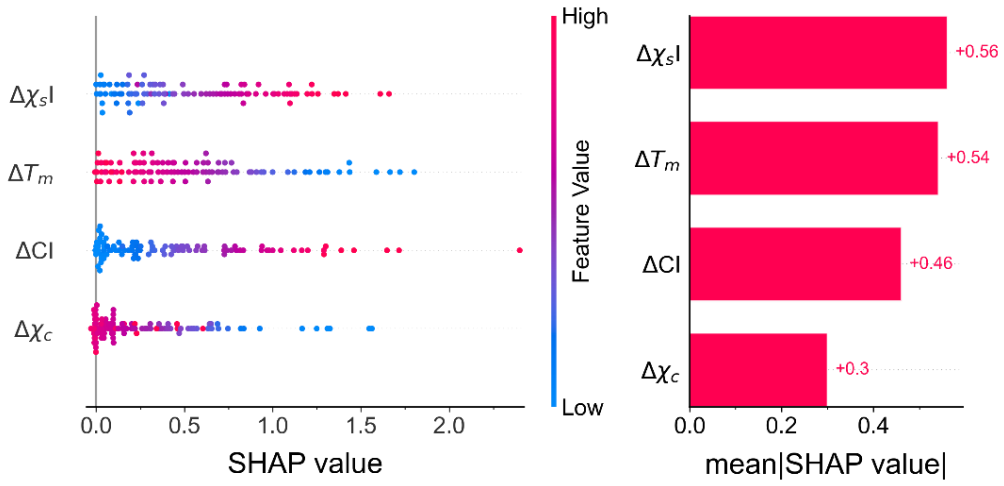


**Figure 5.6 SHAP summary plot showing the contribution of different features ($\chi_s$I, $T_m$, CI, $\chi_c$) to the aging score.** Each point represents a sample, and the horizontal spread reflects the Shapley value, indicating the impact magnitude on the aging score. The right panel shows a SHAP bar plot ranking the average feature importance.

As shown in Figure 5.6, the SHAP analysis largely agrees with the PCA results, confirming that $\chi_c$ is the least influential feature, with an average Shapley value of 0.3. Interestingly, CI receives a lower SHAP value than $T_m$ and $\chi_s$I, despite having the strongest correlation with UVC exposure (Figure 5.5A). This apparent discrepancy arises from the non-linear, sample-level sensitivity of each feature. At low exposure doses, CI shows minimal change and clusters near baseline values, resulting in smaller marginal contributions to the aging score [49]. In contrast, $\chi_s$I, which captures changes in surface crystallinity, and $T_m$, which reflects bulk thermal disruption, show more consistent contributions across the entire exposure range, giving them greater SHAP importance. A similar pattern is observed for $\chi_c$, whose changes are modest relative to surface or thermal metrics.

The SHAP analysis thus provides complementary, mechanistic insight beyond PCA. While PCA emphasizes the features that contribute most to overall variance, SHAP identifies which features actually drive the aging score on a per-sample basis. For instance, even if CI dominates variance across the dataset, its low sensitivity at early exposure levels reduces its impact for individual samples. By combining PCA and SHAP, we gain a more nuanced understanding of how chemical, thermal, and structural properties jointly govern the progression of microplastic aging. These results highlight that surface-sensitive metrics ($\chi_s$I) and bulk thermal indicators ($T_m$) are the most informative for predicting cumulative degradation, while bulk crystallinity ($\chi_c$) plays a comparatively minor role.

Overall, the results (Figure 5.6) emphasize the importance of integrating multiple complementary features into the aging score: features with different sensitivities and measurement depths contribute differently across the exposure spectrum, and SHAP allows us to quantify their relative contributions in a statistically robust, interpretable manner.

This aging score metric can also be applied to compare the previously measured commercial PE, PP, and PET powders and environmentally plastic waste samples (Figure C4). The use of Δfeatures relative to the control facilitates the comparison of properties such as $T_m$ and $\chi_c$, which differences in initial polymer properties would otherwise confound. For some features, such as CI, differences in initial values across polymers cannot be entirely avoided; reference peaks were therefore selected to render CI values roughly comparable in scale. A surface-sensitive metric analogous to $\chi_s$I could not be established for these plastics, so the analysis of multi-polymer datasets proceeded using three features (CI, $T_m$, and $\chi_c$). This framework, however, is flexible and can accommodate any number of measured quantities. When applied to commercial plastic powders (PE, PP, and PET; Figure C4), the PCA loadings and explained variance differ from the PP-only analysis

(Figure 5.5), reflecting intrinsic differences in feature variability across polymer types. Regardless of these differences, the overall aging score reproduces the same relative trends observed in Figure 5.1: PP exhibits the most significant increase in aging score relative to the control, followed by PE and PET at comparable, lower rates. These results demonstrate that the aging score provides a practical, quantitative summary of microplastic degradation and a general indication of the degree of aging across polymers.

The establishment of the aging score also provides a metric for the overall degree of aging in environmental samples. For instance, an environmentally sourced polypropylene fragment (Env. PP, green triangle, Figure 5.5B) exhibited measured values of CI, $T_m$, $\chi_c$, and $\chi_s$I equal to 1.28, 142.8°C, 43.3%, and 1.02, respectively, which fall within the range of the artificially aged PP samples. Since no dedicated control sample was available, the average values for each feature across all measured control samples were used to calculate Δ-values, enabling consistent comparison. The resulting aging score of 4.2 corresponds to approximately ~50 MJ $m^{-2}$ of UVC irradiation, demonstrating that this approach can contextualize environmental fragments relative to controlled laboratory aging. This also holds in the multi-polymer dataset, where environmental samples of PE and PP were found to have consistent degrees of aging to laboratory-aged samples (red and blue star symbols in Figure C4A). With a sufficient number of environmental samples, this metric can be used to compare degrees of weathering across different samples, allowing quantitative assessment of variability in real-world polymer degradation. The reliability of such comparisons depends on the sample population, and artificially aged samples can serve as a calibration set to establish Δ-values and variance weights.

Taken together, the analyses in Figures 5.5, 5.6, and C4 illustrate how the various measurements shape the aging score. The correlation analysis highlights groups of properties that change in

parallel, the PCA arranges these linked changes into significant variation patterns, and the SHAP analysis pinpoints each feature's contribution to the final score across samples. Both the multi-polymer comparison and the environmental fragment demonstrate how the framework handles differences in baseline properties and incomplete feature sets. These results define the operational behaviour and practical boundaries of the aging score within the dataset used in this study, supporting its application as a descriptive tool for contextualizing environmental samples relative to aging.

## 5.4 Conclusion

This study elucidates the coupled chemical, structural, and physical degradation of polypropylene under UVC exposure, providing a mechanistic framework that connects surface oxidation, bulk lamellar destabilization, and particle fragmentation. Our analyses demonstrate that oxidative modification at the polymer surface initiates a cascade of structural perturbations that propagate inward, weakening the bulk crystalline network and predisposing particles to mechanical failure. This mechanistic link is enhanced in smaller particles, where higher surface-to-volume ratios increase the contribution of surface oxidation to bulk destabilization. This emphasizes the role of particle geometry in degradation. Formulation-specific effects further modulate degradation pathways. Transparent PPCT particles, lacking UV-absorbing pigments, undergo finer and more continuous crack formation compared with blue PPPB, where stabilizers and colorants partially mitigate stress concentration and slow crack propagation. These observations underscore the role of additives in controlling both oxidative penetration and mechanical response, consistent with prior studies showing that polymer formulations can tune radical formation kinetics and energy dissipation.

Comparison with more UV-resistant polymers, such as PE and PET, confirms that backbone chemistry dictates the extent of bulk disruption; their semi-crystalline and aromatic structures confer resistance to lamellar disorder and fragmentation. This differential susceptibility emphasizes that laboratory UVC aging of PP cannot be extrapolated to all polymers without accounting for chemical structure, particle size, and formulation.

The integrated "aging score" approach developed here offers a robust, quantitative measure of cumulative degradation by combining chemical (i.e., CI), thermal, and structural (i.e., $T_m$, $\chi_c$, $\chi_s$I), and morphological (i.e., particle size) metrics. By weighing features by variance and relevance, the aging score effectively summarizes multidimensional changes, enabling cross-comparison among particles of different sizes, formulations, and polymers. Strong correlations between the aging score and radiant exposure validate its potential as a predictive tool under diverse environmental conditions. The "aging score" concept, with further validation, may inform future studies on environmental microplastic formation, support standardization of laboratory aging protocols, and improve risk assessment strategies for polymer degradation in real-world settings.

## References

1. Liu S, Li L, Liu S, Liu L, Xiao X, Zhou D, et al. Reactive oxygen species-induced microplastics aging: Implications for environmental fate and ecological impact. TrAC, Trends Anal Chem. 2024;173:117648.
2. Castelvetro V, Corti A, Biale G, Ceccarini A, Degano I, La Nasa J, et al. New methodologies for the detection, identification, and quantification of microplastics and their environmental degradation by-products. Environ Sci Pollut Res. 2021;28(34):46764-80.
3. Shi Y, Shi L, Huang H, Ye K, Yang L, Wang Z, et al. Analysis of aged microplastics: a review. Environ Chem Lett. 2024;22(4):1861-88.

4. Baby MG, Gerritse J, Beltran-Sanahuja A, Wolter H, Rohais S, Romero-Sarmiento M-F. Aging of plastics and microplastics in the environment: a review on influencing factors, quantification methods, challenges, and future perspectives. Environ Sci Pollut Res. 2025;32(3):1009-42.

5. Dimassi SN, Hahladakis JN, Yahia MND, Ahmad MI, Sayadi S, Al-Ghouti MA. Degradation-fragmentation of marine plastic waste and their environmental implications: A critical review. Arab J Chem. 2022;15(11):104262.

6. Tang L, Wu Q, Qu B. The effects of chemical structure and synthesis method on photodegradation of polypropylene. J Appl Polym Sci. 2005;95(2):270-9.

7. Beltrán-Sanahuja A, Casado-Coy N, Simó-Cabrera L, Sanz-Lázaro C. Monitoring polymer degradation under different conditions in the marine environment. Environ Pollut. 2020;259:113836.

8. Xu Y, Ou Q, van der Hoek JP, Liu G, Lompe KM. Photo-oxidation of Micro- and Nanoplastics: Physical, Chemical, and Biological Effects in Environments. Environ Sci Technol. 2024;58(2):991-1009.

9. Campanale C, Savino I, Massarelli C, Uricchio VF. Fourier Transform Infrared Spectroscopy to Assess the Degree of Alteration of Artificially Aged and Environmentally Weathered Microplastics. Polymers. 2023;15(4):911.

10. Liu P, Shi Y, Wu X, Wang H, Huang H, Guo X, et al. Review of the artificially-accelerated aging technology and ecological risk of microplastics. Sci Total Environ. 2021;768:144969.

11. Hurtado Macias A, Román-Aguirre M, Talamantes RP, Soto KM, Reyes Araiza JL, Méndez-Lozano N, et al. Comparative study between UVB 313 nm, UVC 254 nm, and far UVC 222 nm light on the aging of polyamide 66. Heliyon. 2024;10(20):e39415.

12. Hijnen WAM, Beerendonk EF, Medema GJ. Inactivation credit of UV radiation for viruses, bacteria and protozoan (oo)cysts in water: A review. Water Res. 2006;40(1):3-22.

13. Gao L, Su Y, Mehmood T, Wang Z, Peng L, Zhang N. UVA-induced weathering of microplastics in seawater: surface property transformations and kinetics. Front Mar Sci. 2025;12:1519668.

14. Galea J, Agius Anastasi A, Vella DA, Briffa SM. UV Aging of PET Microplastics in a Custom-Built Weathering Chamber Replicating Mediterranean Conditions. ACS Omega. 2025;10(33):37486-94.

15. Seghers J, Cella C, Pequeur E, La Spina R, Roncari F, Valsesia A, et al. Approaches for the preparation and evaluation of hydrophilic polyethylene and polyethylene terephthalate microplastic particles suited for toxicological effect studies. Anal Bioanal Chem. 2025;417(12):2589-602.
16. Jiang Y, Yin X, Xi X, Guan D, Sun H, Wang N. Effect of surfactants on the transport of polyethylene and polypropylene microplastics in porous media. Water Res. 2021;196:117016.
17. Andrady AL, Barnes PW, Bornman JF, Gouin T, Madronich S, White CC, et al. Oxidation and fragmentation of plastics in a changing environment; from UV-radiation to biological degradation. Sci Total Environ. 2022;851:158022.
18. Julienne F, Lagarde F, Delorme N. Influence of the crystalline structure on the fragmentation of weathered polyolefines. Polym Degrad Stab. 2019;170:109012.
19. Rostampour S, Cook R, Jhang S-S, Li Y, Fan C, Sung L-P. Changes in the Chemical Composition of Polyethylene Terephthalate under UV Radiation in Various Environmental Conditions. Polymers. 2024;16(16):2249.
20. Pinlova B, Nowack B. From cracks to secondary microplastics - surface characterization of polyethylene terephthalate (PET) during weathering. Chemosphere. 2024;352:141305.
21. Su X, Liu M, Dai H, Dou J, Lu Z, Xu J, et al. Novel insight into the aging process of microplastics: An in-situ study in coastal wetlands. Water Res. 2024;248:120871.
22. Li X, Huang D, Dong H, Wen J, Dong J, Zhang C, et al. Differential photoaging behaviors of different colored commercial polyethylene microplastics in water: The important role of color characteristics. Sci Total Environ. 2024;956:177361.
23. Su J, Ruan J, Luo D, Wang J, Huang Z, Yang X, et al. Differential Photoaging Effects on Colored Nanoplastics in Aquatic Environments: Physicochemical Properties and Aggregation Kinetics. Environ Sci Technol. 2023;57(41):15656-66.
24. Li C, Jiang B, Guo J, Sun C, Shi C, Huang S, et al. Aging Process of Microplastics in the Aquatic Environments: Aging Pathway, Characteristic Change, Compound Effect, and Environmentally Persistent Free Radicals Formation. Water. 2022;14(21):3515.
25. Canopoli L, Coulon F, Wagland ST. Degradation of excavated polyethylene and polypropylene waste from landfill. Sci Total Environ. 2020;698:134125.
26. Kato Y, Carlsson DJ, Wiles DM. The photo-oxidation of polypropylene: Some effects of molecular order. J Appl Polym Sci. 1969;13(7):1447-58.

27. Carreiras-Suárez S, Domínguez-Ramos L, Lazzari M. Study of the Long-Term Aging of Polypropylene-Made Disposable Surgical Masks and Filtering Facepiece Respirators. Polymers. 2023;15(4):1001.
28. Rajakumar K, Sarasvathy V, Thamarai Chelvan A, Chitra R, Vijayakumar CT. Natural Weathering Studies of Polypropylene. J Polym Environ. 2009;17(3):191-202.
29. Heinen W. Infrared determination of the crystallinity of polypropylene. J Polym Sci. 1959;38(134):545-7.
30. Lanyi FJ, Wenzke N, Kaschta J, Schubert DW. A method to reveal bulk and surface crystallinity of Polypropylene by FTIR spectroscopy - Suitable for fibers and nonwovens. Polym Test. 2018;71:49-55.
31. Wold S, Esbensen K, Geladi P. Principal component analysis. Chemom Intell Lab Syst. 1987;2(1):37-52.
32. Lukasiak BM, Zomer S, Brereton RG, Faria R, Duncan JC. Pattern recognition and feature selection for the discrimination between grades of commercial plastics. Chemom Intell Lab Syst. 2007;87(1):18-25.
33. Mitchell G, France F, Nordon A, Tang PL, Gibson LT. Assessment of historical polymers using attenuated total reflectance-Fourier transform infra-red spectroscopy with principal component analysis. Herit Sci. 2013;1(1):28.
34. Watanabe R, Nakamura S, Sugahara A, Kishi M, Sato H, Hagihara H, et al. Revealing Molecular-Scale Structural Changes in Polymer Nanocomposites during Thermo-Oxidative Degradation Using Evolved Gas Analysis with High-Resolution Time-of-Flight Mass Spectrometry Combined with Principal Component Analysis and Kendrick Mass Defect Analysis. Anal Chem. 2024;96(6):2628-36.
35. Song D, Gao J, Li X, Lu L. Evaluation of aging behavior of polypropylene in natural environment by principal component analysis. Polym Test. 2014;33:131-7.
36. Qin L, Zhu Y, Liu S, Zhang X, Zhao Y. The Shapley Value in Data Science: Advances in Computation, Extensions, and Applications. Mathematics. 2025;13(10):1581.
37. Yao J, Qian H, Yan Z, Zhao X, Gao N, Zhang Z. Insight into the effect of UVC-based advanced oxidation processes on the interaction of typical microplastics and their derived disinfection byproducts during disinfection. J Hazard Mater. 2024;472:134597.

38. Lin J, Yan D, Fu J, Chen Y, Ou H. Ultraviolet-C and vacuum ultraviolet inducing surface degradation of microplastics. Water Res. 2020;186:116360.
39. Diepens M, Gijsman P. Outdoor and accelerated weathering studies of bisphenol A polycarbonate. Polym Degrad Stab. 2011;96(4):649-52.
40. Andrady AL, Heikkilä AM, Pandey KK, Bruckman LS, White CC, Zhu M, et al. Effects of UV radiation on natural and synthetic materials. Photochem Photobiol Sci. 2023;22(5):1177-202.
41. Rostampour S, Jhang SS, Hsu J-K, Cook R, Li Y, Fan C, et al. Evaluating the Environmental Factors on Microplastic Generation: An Accelerated Weathering Study. Microplastics. 2025;4(1):13.
42. Syranidou E, Karkanorachaki K, Barouta D, Papadaki E, Moschovas D, Avgeropoulos A, et al. Relationship between the Carbonyl Index (CI) and Fragmentation of Polyolefin Plastics during Aging. Environ Sci Technol. 2023;57(21):8130-8.
43. Knopp MM, Löbmann K, Elder DP, Rades T, Holm R. Recent advances and potential applications of modulated differential scanning calorimetry (mDSC) in drug development. Eur J Pharm Sci. 2016;87:164-73.
44. Leng Y, Gaburici L, Cao X, Zou S. Quantification of microplastics in complex environmental matrices using a tiered approach with modulated differential scanning calorimetry (MDSC). Anal Bioanal Chem. 2025.
45. Blaine RL. Thermal Applications Note: Polymer Heats of Fusion. TA Instruments; 2002.
46. Baek S-J, Park A, Ahn Y-J, Choo J. Baseline correction using asymmetrically reweighted penalized least squares smoothing. Analyst. 2015;140(1):250-7.
47. Erb D. Pybaselines: A Python Library of Algorithms for the Baseline Correction of Experimental Data. 2022.
48. Miranda MN, Sampaio MJ, Tavares PB, Silva AMT, Pereira MFR. Aging assessment of microplastics (LDPE, PET and uPVC) under urban environment stressors. Sci Total Environ. 2021;796:148914.
49. Rouillon C, Bussiere PO, Desnoux E, Collin S, Vial C, Therias S, et al. Is carbonyl index a quantitative probe to monitor polypropylene photodegradation? Polym Degrad Stab. 2016;128:200-8.

50. García-López EI, Aoun N, Marcì G. An Overview of the Sustainable Depolymerization/Degradation of Polypropylene Microplastics by Advanced Oxidation Technologies. Molecules. 2024;29(12):2816.
51. Chamas A, Moon H, Zheng J, Qiu Y, Tabassum T, Jang JH, et al. Degradation Rates of Plastics in the Environment. ACS Sustain Chem Eng. 2020;8(9):3494-511.
52. Abang S, Wong F, Sarbatly R, Sariau J, Baini R, Besar NA. Bioplastic classifications and innovations in antibacterial, antifungal, and antioxidant applications. J Bioresour Bioprod. 2023;8(4):361-87.
53. Khairul Anuar NFS, Huyop F, Ur-Rehman G, Abdullah F, Normi YM, Sabullah MK, et al. An Overview into Polyethylene Terephthalate (PET) Hydrolases and Efforts in Tailoring Enzymes for Improved Plastic Degradation. Int J Mol Sci. 2022;23(20):12644.
54. Höhne GWH, Hemminger WF, Flammersheim HJ. Applications of Differential Scanning Calorimetry. In: Höhne GWH, Hemminger WF, Flammersheim HJ, editors. Differential Scanning Calorimetry. Berlin, Heidelberg: Springer; 2003. p. 147-244.
55. Chiapasco M, Valsecchi M, Hill G, Wallis C, Porter AE, Giuliani F. Impacts of Photooxidation on Commercially Available Homo and Copolymers of Polypropylene on Their Microstructure and Mechanics: A Cross-Sectional Analysis. Nano Select. 2025;6(1):e202300082.
56. Rabello MS, White JR. Crystallization and melting behaviour of photodegraded polypropylene — I. Chemi-crystallization. Polymer. 1997;38(26):6379-87.
57. Wu X, Zhao X, Chen R, Liu P, Liang W, Wang J, et al. Size-dependent long-term weathering converting floating polypropylene macro- and microplastics into nanoplastics in coastal seawater environments. Water Res. 2023;242:120165.
58. Bonifazi G, Fiore L, Pelosi C, Serranti S. Evaluation of plastic packaging waste degradation in seawater and simulated solar radiation by spectroscopic techniques. Polym Degrad Stab. 2023;207:110215.
59. Cai L, Wang J, Peng J, Wu Z, Tan X. Observation of the degradation of three types of plastic pellets exposed to UV irradiation in three different environments. Sci Total Environ. 2018;628-629:740-7.
60. Hoseini M, Stead J, Bond T. Ranking the accelerated weathering of plastic polymers. Environ Sci Process Impacts. 2023;25(12):2081-91.

61. Gijsman P, Meijers G, Vitarelli G. Comparison of the UV-degradation chemistry of polypropylene, polyethylene, polyamide 6 and polybutylene terephthalate. Polym Degrad Stab. 1999;65(3):433-41.
62. Hahladakis JN, Velis CA, Weber R, Iacovidou E, Purnell P. An overview of chemical additives present in plastics: Migration, release, fate and environmental impact during their use, disposal and recycling. J Hazard Mater. 2018;344:179-99.
63. Dimassi SN, Hahladakis JN, Daly Yahia MN, Ahmad MI, Sayadi S, Al-Ghouti MA. Insights into the degradation mechanism of PET and PP under marine conditions using FTIR. J Hazard Mater. 2023;447:130796.
64. Key S, Ryan PG, Gabbott SE, Allen J, Abbott AP. Influence of colourants on environmental degradation of plastic litter. Environ Pollut. 2024;347:123701.
65. Xue Z, Yu X, Ke X, Zhao J. A novel route for microplastic mineralization: visible-light-driven heterogeneous photocatalysis and photothermal Fenton-like reaction. Environ Sci Nano. 2024;11(1):113-22.
66. Born MP, Brüll C, Schüttrumpf H. Implications of a New Test Facility for Fragmentation Investigations on Virgin (Micro)plastics. Environ Sci Technol. 2023;57(28):10393-403.
67. Wu H, Zhao Y, Dong X, Su L, Wang K, Wang D. Probing into the microstructural evolution of isotactic polypropylene during photo-oxidation degradation. Polym Degrad Stab. 2021;183:109434.
68. Boronat C, Correcher V, García-Guinea J, Bravo-Yagüe JC. Ultraviolet C radiation on polypropylene: A potential way to reduce plastic pollution. Polym Degrad Stab. 2024;225:110784.
69. Delbruel V, Lajoie H, Steiner V, Gérard J-F, Duchet-Rumeau J, Chevalier J. Effects of polypropylene compositions and processing conditions on its aging resistance under tropical environments. Polym Degrad Stab. 2024;228:110883.
70. Turton TJ, White JR. Effect of stabilizer and pigment on photo-degradation depth profiles in polypropylene. Polym Degrad Stab. 2001;74(3):559-68.
71. Meides N, Mauel A, Menzel T, Altstädt V, Ruckdäschel H, Senker J, et al. Quantifying the fragmentation of polypropylene upon exposure to accelerated weathering. Microplast Nanoplast. 2022;2(1):23.

72. Niu Z, Curto M, Le Gall M, Demeyer E, Asselman J, Janssen CR, et al. Accelerated fragmentation of two thermoplastics (polylactic acid and polypropylene) into microplastics after UV radiation and seawater immersion. Ecotoxicol Environ Saf. 2024;271:115981.
73. Hebner TS, Maurer-Jones MA. Characterizing microplastic size and morphology of photodegraded polymers placed in simulated moving water conditions. Environ Sci Process Impacts. 2020;22(2):398-407.
74. Mikac L, Csáki A, Zentai B, Rigó I, Veres M, Tolić A, et al. UV Irradiation of Polyethylene Terephthalate and Polypropylene and Detection of Formed Microplastic Particles Down to 1 μm. ChemPlusChem. 2024;89(2):e202300497.
75. Suh D, Hockett Sherlock S, Dukes KC, Perencevich EN, Marra AR. Impact of UV-C on material degradation: a scoping literature review. Antimicrob Steward Healthc Epidemiol. 2025;5(1):e199.
76. Pfohl P, Santizo K, Sipe J, Wiesner M, Harrison S, Svendsen C, et al. Environmental degradation and fragmentation of microplastics: dependence on polymer type, humidity, UV dose and temperature. Microplast Nanoplast. 2025;5(1):7.
77. Polruang S, Asokbunyarat V, Bouthong P, Rizqa F, Somprasong A. Simulated environmental weathering of expanded polystyrene foam and polypropylene under UV and wave agitation. Sci Rep. 2025;15(1):38649.
78. Song YK, Hong SH, Eo S, Shim WJ. Fragmentation of nano- and microplastics from virgin- and additive-containing polypropylene by accelerated photooxidation. Environ Pollut. 2023;327:121590.
79. Lundberg SM, Lee S-I. A Unified Approach to Interpreting Model Predictions. 31st Conference on Neural Information Processing Systems (NIPS 2017); Long Beach, CA, USA. 2017.

# CHAPTER 6 CONCLUSIONS AND FUTURE DIRECTIONS

## 6.1 Conclusions and General Discussion

This thesis brings together environmental aging characteristics and laboratory-accelerated aging experiments to provide a coherent basis for assessing microplastic aging. Collectively, the findings demonstrate that the aging state fundamentally conditions both the physicochemical behaviour of microplastics and the reliability of their analytical detection, particularly in complex environmental matrices.

Across the studies presented, a consistent conclusion emerges: microplastic aging is a coupled and multi-dimensional transformation rather than an isolated physical or chemical process. Aging-induced changes observed in biosolid-derived microplastics, thermally and oxidatively aged polystyrene (PS), and ultraviolet C (UVC)-exposed polyethylene (PE), polypropylene (PP), and polyethylene terephthalate (PET) consistently show concurrent changes in crystallinity, thermal transitions, surface chemistry, and particle morphology. The observed alteration of polymer-specific spectral and thermal features indicates that analytical workflows established on pristine polymers may not apply to environmentally aged microplastics, particularly in complex matrices such as biosolids, where high organic content and heterogeneous backgrounds further obscure polymer signals and complicate mass-based quantification. As a result, these findings suggest that microplastic aging should be treated as a governing variable that shapes both particle transformation pathways and analytical uncertainty. Therefore, this work underscores the need to shift research focus from pristine polymers toward analyses that account for aging effects when interpreting microplastic occurrence, comparison, and quantification across environmental studies.

Within this context, the thesis first demonstrates the analytical feasibility of polymer-specific, mass-based quantification of mixed microplastics in biosolids using a tiered approach centred on modulated differential scanning calorimetry (MDSC). The role of each analytical technique used in the tiered approach is different but complementary. Thermogravimetric analysis (TGA) was used as a bulk screening step to assess whether polymer-like thermal decomposition signals were present in biosolid samples and whether further analysis was needed. Raman spectroscopy was used to confirm polymer identity, while MDSC enabled the quantification of the Raman-identified polymers. With improved sensitivity, lower limits of quantification, and reduced susceptibility to matrix interference, MDSC enables reliable measurement of micron-sized PE, PP, PET, and polyamide 6 (PA6) from multiple sources. Importantly, this integrative analytical approach improves the transferability of microplastic quantification in complex matrices and provides a practical method for more comparable measurements in different studies. More broadly, it emphasizes the need to align analytical methodologies with environmentally realistic environments to improve the reliability and comparability of microplastic measurements. Thus, addressing this uncertainty ultimately requires controlled laboratory aging studies that isolate and quantify aging characteristics under defined conditions.

Controlled laboratory aging experiments further show that microplastic aging is a coupled transformation in which chemical alteration and physical fragmentation happen together, and the extent of aging is governed by polymer chemistry, particle size, and formulation. Using PS as a mechanistic model, accelerated thermal-oxidative aging showed that morphological deformation and size reduction occur alongside substantial Raman spectroscopic changes, including the alteration in the characteristic aromatic ring vibrations, which are consistent with oxidative degradation and possible ring-opening reactions. However, the spectroscopic evidence alone

cannot definitively distinguish among these degradation pathways, and therefore serves primarily as an indicator of oxidative alteration rather than a direct measure of specific reaction mechanisms. When extended to comparative UVC-aging experiments, ATR-FTIR provided evidence of aging-induced chemical changes in PE, PP, and PET, particularly surface oxidation reflected by increased carbonyl bands. PP consistently exhibits a stronger and faster oxidation signature and greater thermal destabilization than PE and PET under identical exposure conditions. Also, within the same polymer, the particle size and additive composition further affect the aging behaviour. These results show that laboratory aging serves as a critical bridge between microplastic transformation processes and the analytical uncertainty observed in environmental measurements.

To quantitatively compare the heterogeneous aging responses across microplastics, this work introduces a multivariate aging score using principal component analysis (PCA) that integrates chemical, thermal, and structural properties into a unified comparative metric. In both laboratory-aged and environmentally recovered microplastics, the aging score enabled direct comparison of relative aging progressions. Also, its main value lies in reducing dependence on single aging characteristics. Carbonyl index, crystallinity, melting temperature, and spectroscopic crystallinity indicators each describe different aspects of aging and may not change in the same direction or at the same rate. Moreover, Shapley additive explanations (SHAP) analysis was used to interpret which measured descriptors contributed most strongly to the aging score in this dataset. The analysis indicated that crystallinity index ($\chi_s$I) and melting temperature ($T_m$) were major contributors to the aging of PP. This indicates that the UVC-aging trajectory of PP was not defined solely by the accumulation of oxidized surface groups. Instead, the aging score was strongly shaped by changes in surface crystalline structure and by loss of thermal stability, as reflected by the high contribution of $\chi_s$I and $T_m$, respectively. Carbonyl index remained important as evidence

of surface oxidation by photo-oxidation, but its lower relative contribution suggests that oxidation did not fully explain the differences among PP materials and size fractions. These results suggest that for semi-crystalline polymers, such as PP, structural and thermal destabilization needs to be considered besides chemical oxidation when interpreting aging. The proposed method therefore provides a scalable approach toward cross-study comparability and addressing the question of "how aged is this microplastic?", enabling a quantitative comparison of aging levels across polymers and between laboratory and environmental aging conditions, supporting more credible interpretations of aging trends.

In addition, exploratory cellular response assessments of pristine and lab-aged microplastics were conducted and are presented in Appendix B. These assays were not designed to establish a complete toxicological risk assessment, but to provide biological context for the physicochemical changes observed after aging. In general, aging alters microplastic–cell interactions in a polymer- and cell-dependent manner, with the clearest aging effects observed in oxidative stress responses. Specifically, PS showed the clearest aging-induced differences in viability and ROS responses, while ROS responses for PE, PP, and PET were more dependent on the cell model. LDH release was not significantly altered by aging for any polymer, indicating that the observed responses were not associated with measurable membrane damage under the selected assay conditions. These results suggest that, at environmentally relevant exposure levels, microplastic aging primarily modulates early sublethal stress responses rather than inducing overt cytotoxicity. The biological interpretation remains limited by short exposure durations, simplified in vitro models, and differences in particle size among the tested microplastics. While not the primary focus of this thesis, these results provide complementary context for understanding potential downstream biological implications of microplastic aging.

To summarize, the findings of this thesis demonstrate that microplastic aging is a governing source of analytical variability that directly affects the reliability and comparability of microplastics identification and quantification in environmental samples. By connecting the aging characteristics of microplastics observed in real environmental biosolid samples with controlled laboratory aging experiments and a multivariate assessment of aging, this work highlights the necessity of incorporating aging as an important factor in analytical standardization efforts and environmental risk assessments.

## 6.2 Limitations and Future Directions

While this work establishes an integrated perspective on microplastic aging and quantification in biosolids, several limitations and corresponding research directions emerge from its findings.

One important extension of this work concerns the diversity of aging pathways that microplastics undergo in the environment. The aging processes investigated here were defined as thermal-oxidative, oxidative, sonication-based, or UVC-driven conditions, which focused on single mechanisms under controlled laboratory conditions. In contrast, environmental aging typically involves multiple pathways acting sequentially or simultaneously, including photochemical, oxidative, mechanical, and biological processes. Thus, laboratory-accelerated aging does not provide a direct conversion between laboratory exposure time and environmental residence time. Future work could therefore explore combined or sequential aging scenarios to better represent realistic environmental conditions and to examine whether different pathways produce convergent or distinct aging signatures. In addition, more direct mechanistic studies are needed to distinguish the reaction pathways underlying these aging signatures. Such studies would help clarify how laboratory-aged microplastics are related to environmentally aged microplastics collected from

natural systems. This unanswered question has been highlighted in the literature as a major source of uncertainty in aging studies.

Further refinement of the multivariate aging score system also represents another promising direction. While the aging score developed in this thesis integrates chemical, thermal, and structural descriptors, future work could incorporate additional parameters such as mechanical properties, surface roughness, molecular-weight indicators, or spectroscopy-derived oxidation bands beyond carbonyls. In addition, extending the framework to include recovered environmentally aged microplastics would improve the applicability across a broader range of polymer types and aging histories, while preserving interpretability.

Another important limitation concerns the quantitative analysis of amorphous plastics. This thesis demonstrates the strengths of MDSC for thermal analysis of semi-crystalline polymers; however, mass-based quantification of amorphous plastics remains challenging. Future research could investigate whether glass transition temperature-based thermal signatures, potentially combined with spectroscopic techniques, can be developed into reliable quantitative strategies for amorphous microplastics. Establishing such approaches would significantly broaden the applicability of mass-based quantification methods to a wider range of environmentally relevant microplastics. In addition, thermal-analysis-based approaches have been increasingly recognized as complementary tools for MP analysis [1]. Recent progress in TGA-IR analysis has expanded the role of thermal methods from general mass-loss characterization toward microplastics identification and semi-quantification in biosolid matrices [2]. Further advances in TGA-FTIR analysis have incorporated automated interpretation of gas-phase FTIR spectra generated during thermal decomposition, reducing reliance on manual selection of diagnostic regions and improving polymer-specific

identification and quantification [3]. These developments point to a broader direction: combining thermal analysis with automated or machine-learning interpretation for microplastics analysis.

Finally, the biological assays provide a limited view of the biological relevance of MP aging. The assays were conducted using simplified in vitro systems, selected assays, and short exposure durations. They provide information on early cellular responses, including viability, ROS generation, and membrane integrity, but they do not capture chronic exposure, tissue-level responses, immune interactions, or realistic environmental exposure scenarios. Future work should use more environmentally representative exposure scenarios, especially for smaller microplastics, longer particle exposure durations, and additional investigation in oxidative stress, cellular uptake, and barrier function. These approaches would provide a clearer basis for linking aging-induced physicochemical changes to exposure-relevant biological responses under more realistic environmental conditions.

Overall, this thesis advances understanding of microplastic aging and its analytical implications under environmentally relevant conditions, supports more reliable assessment, and provides a basis for direct comparison between laboratory-aged and environmentally aged microplastics.

## References

1. Mansa R, Zou S. Thermogravimetric analysis of microplastics: A mini review. Environ Adv. 2021;5:100117.
2. Chen M, Coleman B, Gaburici L, Prezgot D, Jakubek ZJ, Sivarajah B, et al. Identification of microplastics extracted from field soils amended with municipal biosolids. Sci Total Environ. 2024;907:168007.
3. Prezgot D, Chen M, Leng Y, Gaburici L, Zou S. Automated Machine-Learning-Driven Analysis of Microplastics by TGA-FTIR for Enhanced Identification and Quantification. Anal Chem. 2025;97(16):8833-40.

# APPENDIX A

## A1 Measured Melting Point and Decomposition Temperature of Microplastics

**Table A1** Melting point ($T_m$) and decomposition temperature ($T_d$) of plastics measured by DSC and thermogravimetric analysis (TGA).

| Plastic types | $T_m$/°C | $T_d$/°C | Ref. |
|---|---|---|---|
| Polystyrene (PS) | - | 420 | - |
| Low-density polyethylene (LDPE) | 111 | 470 | - |
| High-density polyethylene (HDPE) | 139 | 478 | [1] |
| Polypropylene (PP) | 155 | 460 | - |
| Polytetrafluoroethylene (PTFE/Teflon) | 318 | 565 | - |
| Polyethylene Terephthalate (PET) | 239 | 435 | - |
| Polyamide 6 (PA6) | 220 | 420 | - |
| Polyvinyl chloride (PVC) | - | 300, 467 | - |

## A2 Theoretical Limit of Quantification of Microplastics

**Table A2** The theoretically calculated limit of quantification (LOQ) of polyethylene (PE), polypropylene (PP), polyamide 6 (PA6), and polyethylene terephthalate (PET) determined by MDSC and conventional DSC derived from mathematical computations.

| | MDSC | | Conventional DSC | |
|---|---|---|---|---|
| | per measurement (mg) | (μg/g) | per measurement (mg) | (μg/g) |
| PE | 0.0003 | 22 | 0.0004 | 30 |
| PP | 0.0003 | 26 | 0.0005 | 44 |
| PA6 | 0.0001 | 7 | 0.0038 | 310 |
| PET | 0.0004 | 37 | 0.0171 | 1410 |

## A3 $T_m$ of Individual Commercial Microplastic Powder

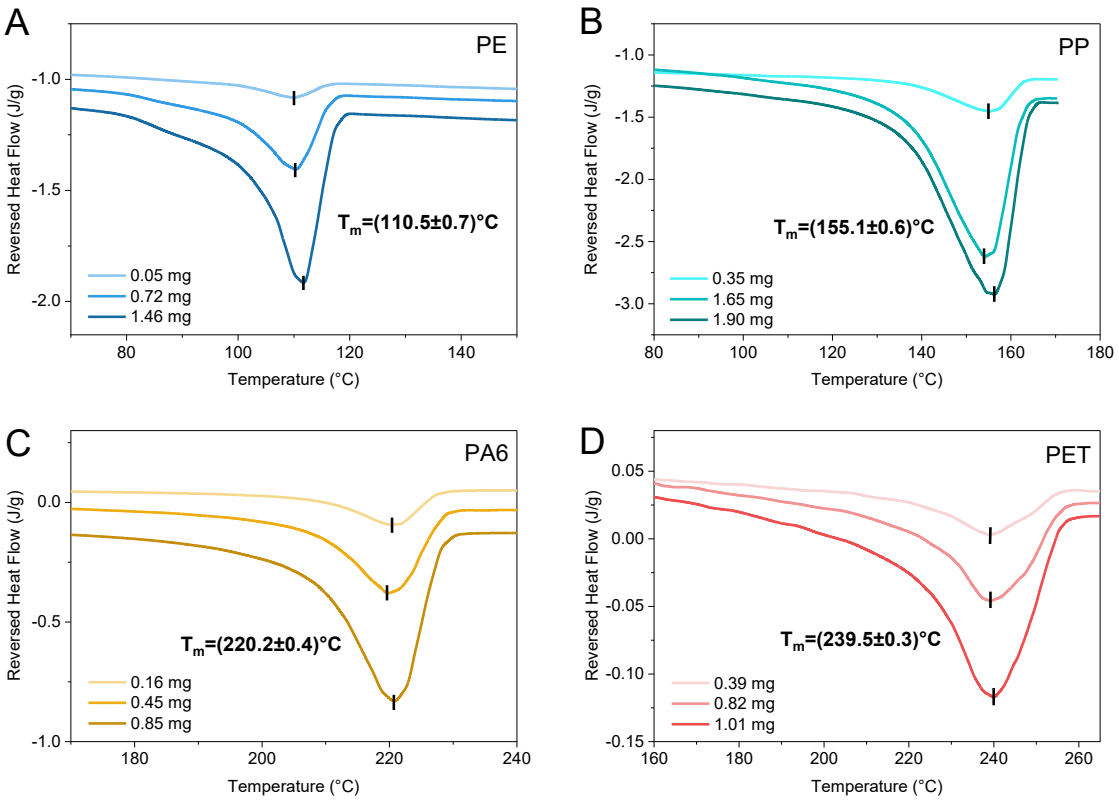


**Figure A1 MDSC thermograms of individual commercial microplastic powder (CMP).** (A) PE, (B) PP, (C) PA6, (D) PET.

## A4 Calibration Curves of PET CMP

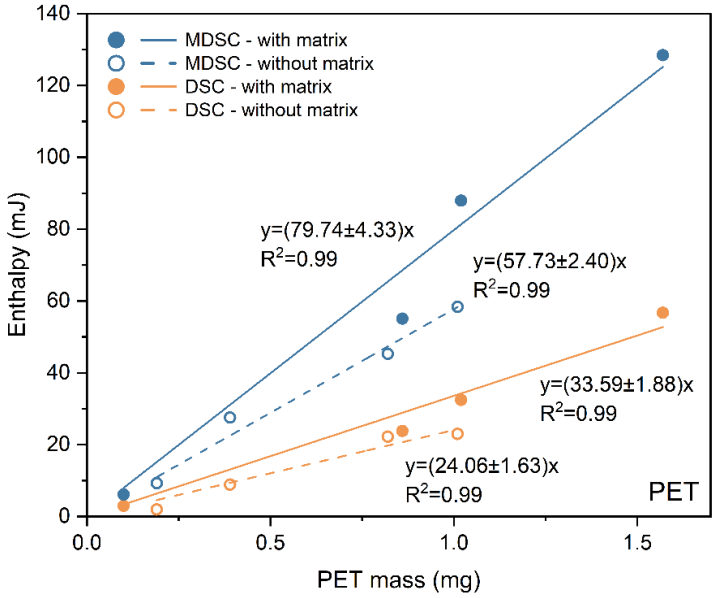


**Figure A2 Calibration curves for PET CMP.**

## A5 Thermal Signal Overlap of PS and PE

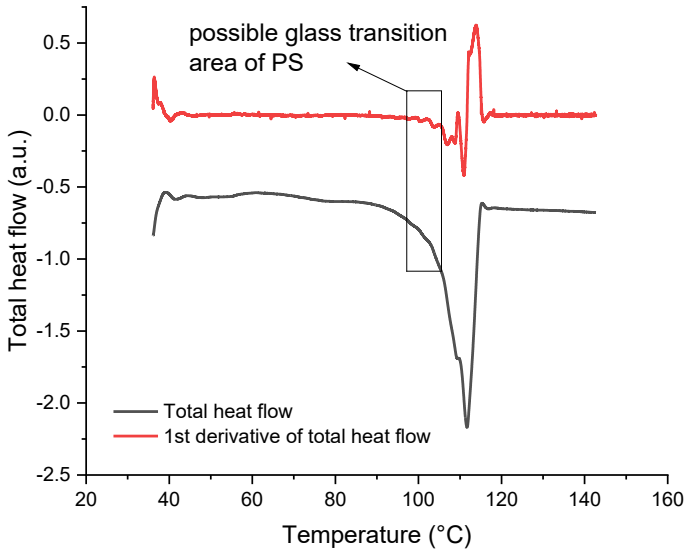


**Figure A3 Total heat flow curves (black, bottom) and 1st derivative of the total heat flow (red, top) of the PS and PE mixture (1:1 mass ratio) spiked in digested blank biosolid (dBB) obtained using DSC.**

## A6 Calibration Curves of Product-Derived Microplastics and Aged CMP

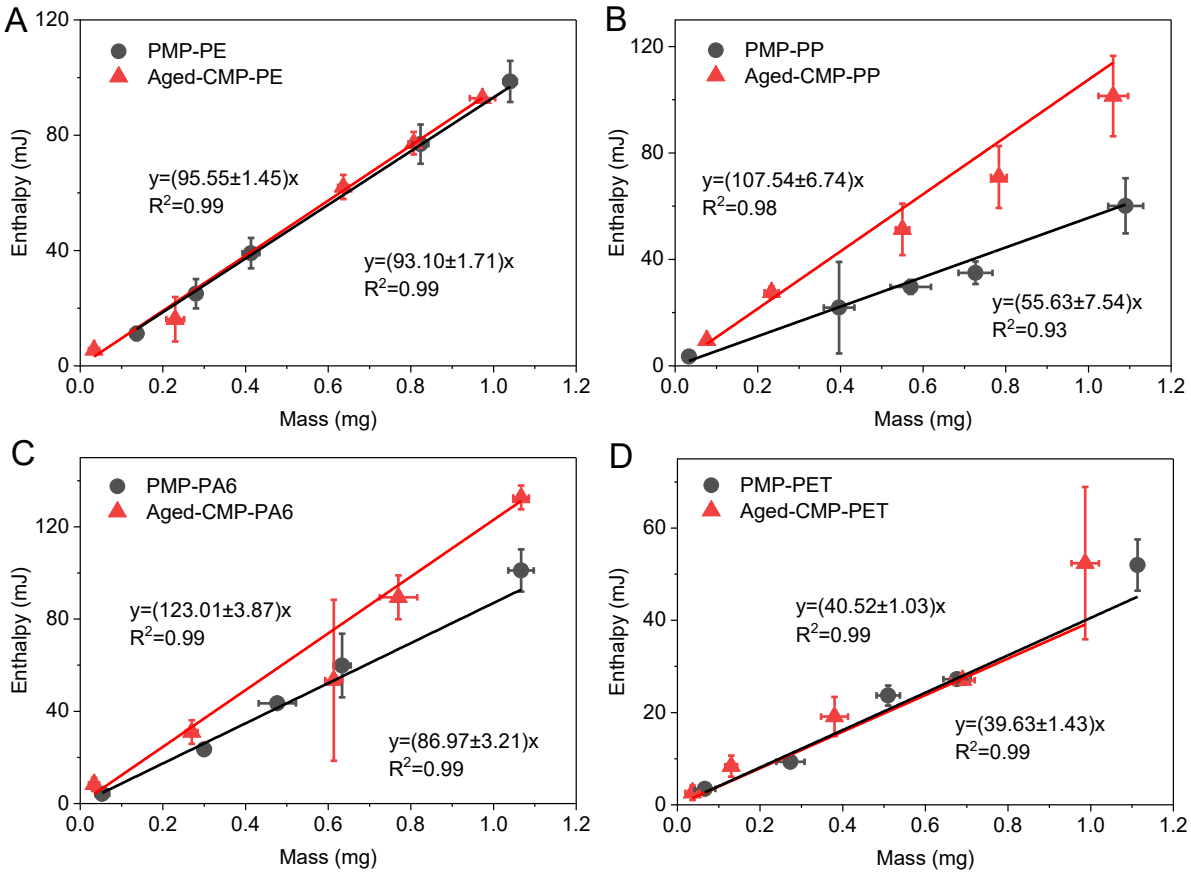


**Figure A4 Calibration curves for PE (A), PP (B), PA6 (C), PET (D) product-derived microplastics (PMP), and aged-CMP in the mixtures with dBB matrices.** Error bars indicate the SD of the enthalpy measurements, n=3.

## A7 Accuracy Validation of MDSC Quantification

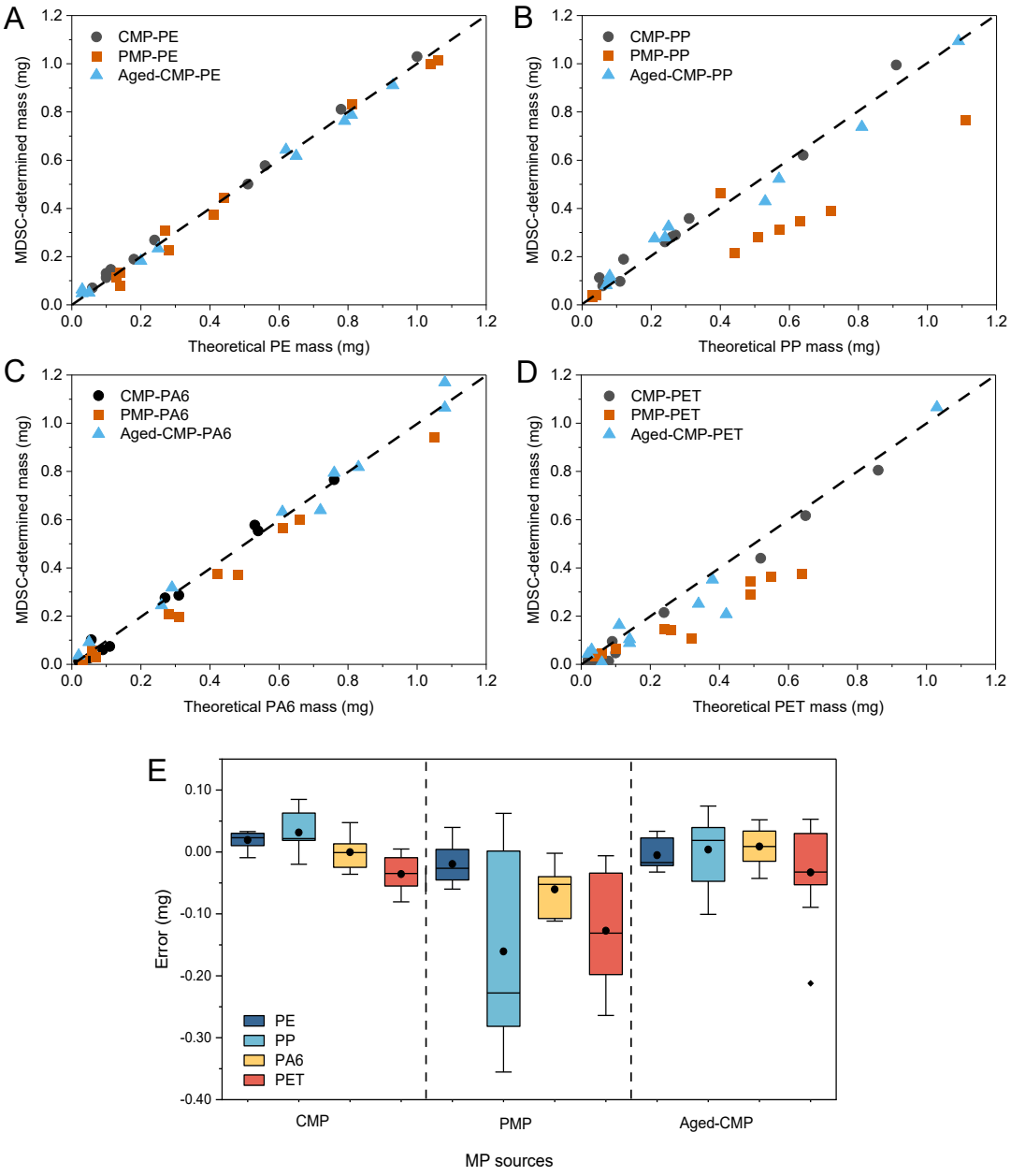


**Figure A5 Validation of the accuracy of the quantification method by using (A) PE, (B) PP, (C) PA6, (D) PET CMP, PMP, and aged CMP.** The dashed line serves as a 1:1 reference. (E) Mean absolute error of PE, PP, PA6, and PET across CMP, PMP, and aged CMP sources, with mean values (●), medians (—), interquartile range (25-75%), and minimum-maximum values presented. Ten individual spike samples were measured (n=10).

## A8 Chemical Characteristics of CMP, PMP, and Aged-CMP

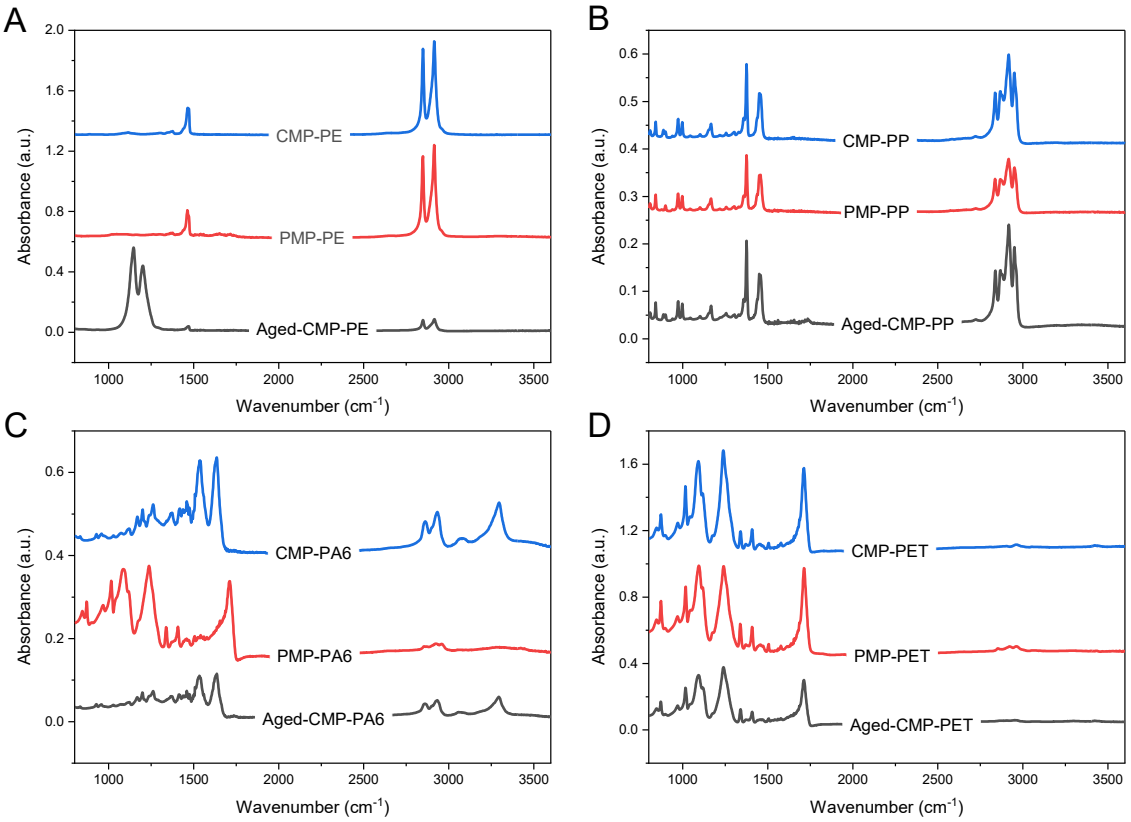


**Figure A6 ATR-FTIR spectra of micron-sized (A) PE, (B) PP, (C) PA6, (D) PET from CMP, PMP, and Aged-CMP.**

The spectra show differences in peak intensity, baseline shape, and oxidation-sensitive regions, indicating that the three material groups were not chemically identical despite sharing the same polymer identity. PP and PET showed relatively consistent polymer-specific features across the three material sources, whereas aged-CMP-PE and PMP-PA6 showed more pronounced deviations from their corresponding commercial reference spectra.

For PE (Figure A6A), all spectra showed characteristic methylene stretching bands near 2915 and 2848 $cm^{-1}$, and $CH_2$ bending near 1470 $cm^{-1}$, confirming PE identity [2]. While aged-CMP-PE

showed relatively weaker hydrocarbon bands and a more evident signal near 1165 and 1240 $cm^{-1}$, which could possibly be assigned to C-O stretching vibrations from oxygen-containing species [3]. For PP (Figure A6B), all groups of PP retained the major PP bands associated with CH3/CH2 stretching and bending vibrations, including bands near 2950–2835 $cm^{-1}$, 1455 $cm^{-1}$, 1376 $cm^{-1}$, and the crystalline region near 998–974 $cm^{-1}$ [4]. The aged CMP-PP spectrum showed a slight peak in the carbonyl region around 1740 $cm^{-1}$, indicating that oxidation happened on the surface of PP after aging [5, 6]. For PA6 (Figure A6C), spectral variability was more pronounced. CMP-PA6 and aged CMP-PA6 retained characteristic amide features, including the N–H stretching region near 3300 $cm^{-1}$, amide I around 1630–1640 $cm^{-1}$, amide II around 1530–1540 $cm^{-1}$, and C–N/amide III bands in the lower wavenumber region [7]. However, PMP-PA6 differed substantially in relative peak intensity and fingerprint-region structure, which are likely related to product source, crystallinity, moisture sensitivity, and surface changes [8]. For PET (Figure A6D), CMP-PET, PMP-PET, and aged-CMP-PET all showed the expected ester carbonyl band near 1715 $cm^{-1}$, aromatic ring vibrations near 1600–1500 $cm^{-1}$, ester C–O stretching bands near 1240 $cm^{-1}$ and 1100 $cm^{-1}$, and aromatic out-of-plane vibration near 725 $cm^{-1}$ [9]. The main PET bands remained identifiable across all three material groups, although relative intensities and baseline features differed between CMP, PMP, and aged-CMP.

Overall, ATR-FTIR provided useful evidence of polymer identity and surface chemical variation among CMP, PMP, and aged-CMP. Product-derived and aged particles may differ in surface oxidation, additives, crystallinity, and thermal history, all of which can affect melting behaviour, peak shape, and calibration reliability. The pronounced deviations observed for aged CMP-PE and PMP-PA6 support the need to validate MDSC quantification across variable material sources and aging conditions, rather than relying only on pristine commercial powders. Ultimately, ATR-FTIR

helps characterize chemical and source-related variability in the validation materials, while MDSC tests whether polymer mass quantification remains accurate despite that variability.

## A9 Interference of Soil Matrix with PA6 Recrystallization

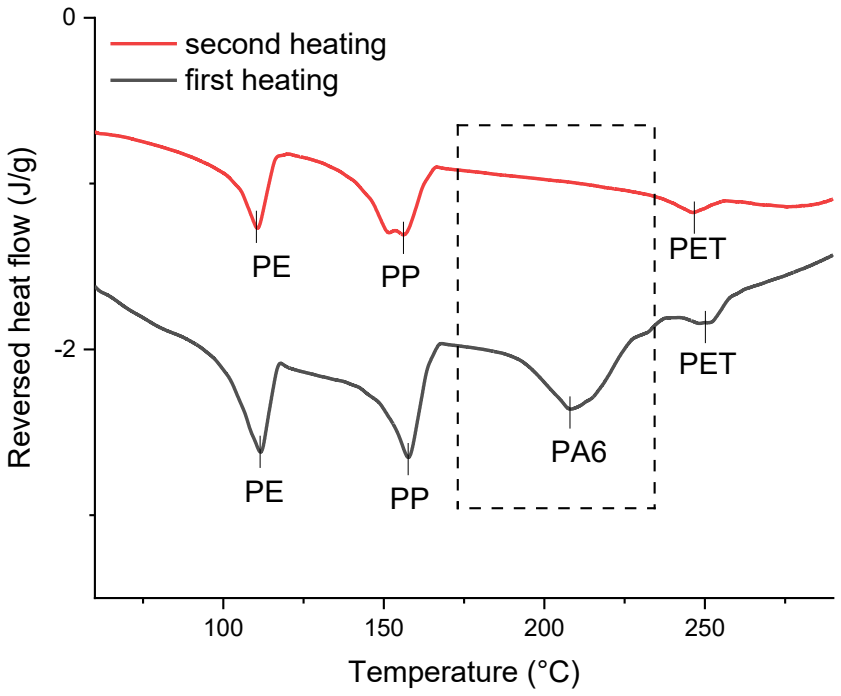


**Figure A7 MDSC thermogram of extracted CMP mixture of PE, PP, PA6, and PET from the soil matrix.**

## A10 Comparison of TGA- and MDSC-Based Mass Quantification in Spiked Biosolids

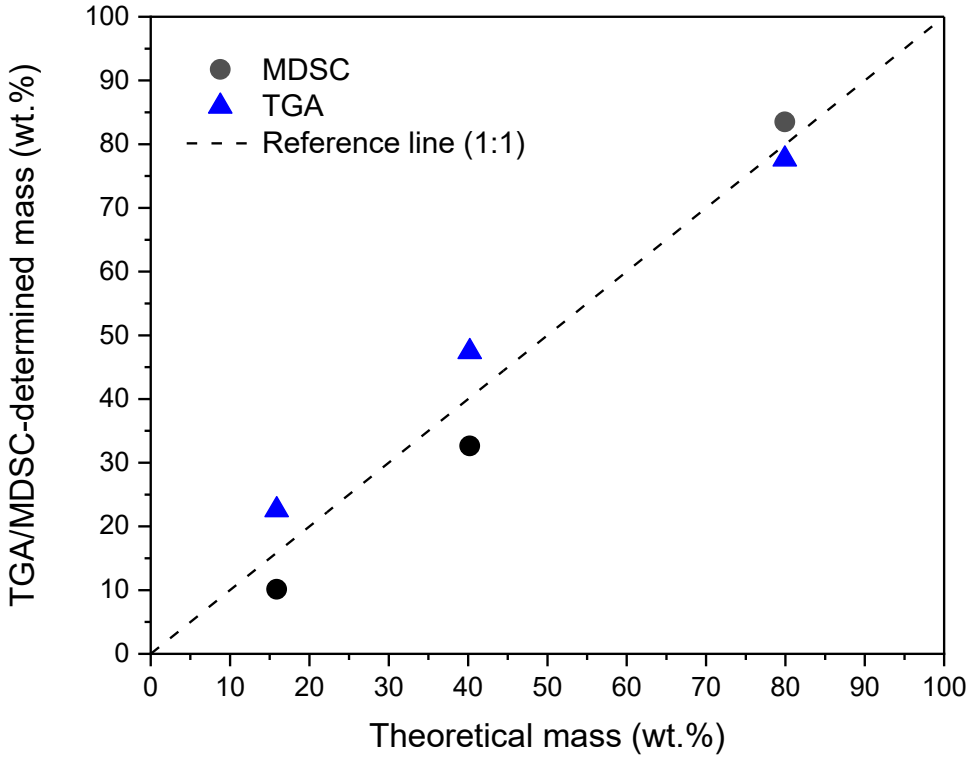


**Figure A8 Correlation of TGA- and MDSC-determined mass using plastic mixture spiked in blank biosolids.** The reference line in the plot is 1:1 (y=x).

## A11 Complex Thermal Decomposition Behaviour of Environmental Biosolids Revealed by TGA

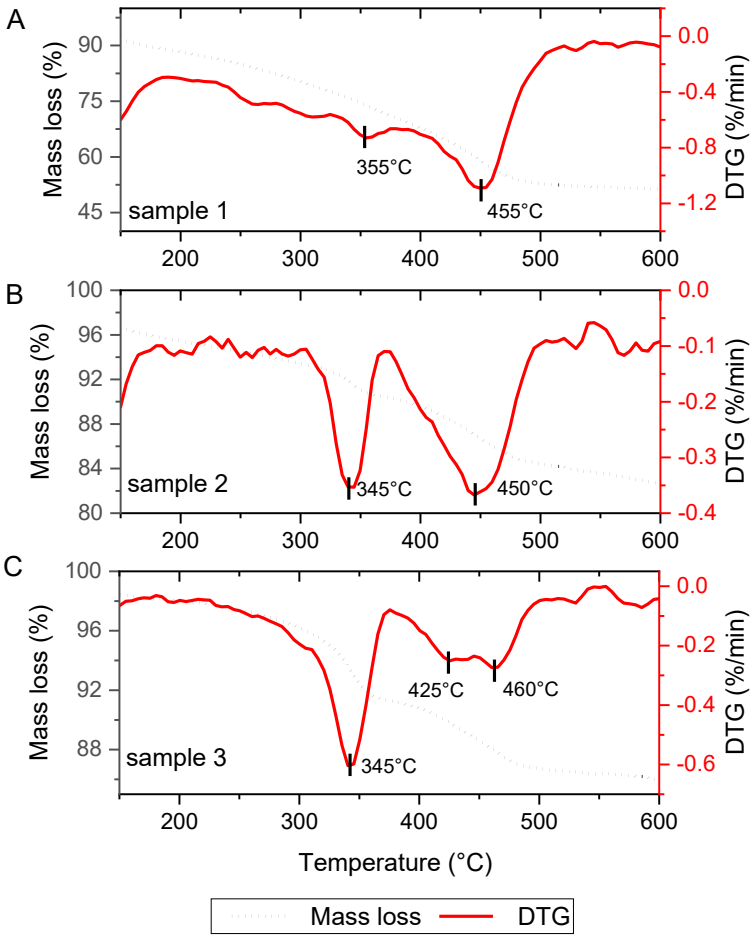


**Figure A9 TGA thermograms of environmental biosolid.** (A) sample 1, (B) sample 2, (C) sample 3. The black dotted line represents the mass loss during the heating, and the red solid line represents the first derivative of the mass-loss curve, smoothed with an 8-point window.

**Table A3** Concentration of polymers extracted from real-world biosolids quantified by TGA.

| Sample code | Sample 1 | Sample 2 | Sample 3 |
|---|---|---|---|
| Concentration of polymers (mg/g) | 5.53 | 1.47 | 1.40 |

## References


1. Sorolla-Rosario D, Llorca-Porcel J, Pérez-Martínez M, Lozano-Castelló D, Bueno-López A. Study of microplastics with semicrystalline and amorphous structure identification by TGA and DSC. J Environ Chem Eng. 2022;10(1):106886.
2. Gulmine JV, Janissek PR, Heise HM, Akcelrud L. Polyethylene characterization by FTIR. Polym Test. 2002;21(5):557-63.
3. Smak TJ, de Peinder P, Van der Waal JC, Altink R, Vollmer I, Weckhuysen BM. Oxidative Conversion of Polyethylene Towards Di-Carboxylic Acids: A Multi-Analytical Approach. ChemSusChem. 2024;17(7):e202301198.
4. Anshari R, Tsuboi M, Sato H, Tashiro K, Ozaki Y. Raman and ATR-FTIR unmask crystallinity changes and carboxylate group and vinyl group accumulation in natural weathering polypropylene microplastics. Sci Rep. 2025;15(1):2518.
5. Almond J, Sugumaar P, Wenzel MN, Hill G, Wallis C. Determination of the carbonyl index of polyethylene and polypropylene using specified area under band methodology with ATR-FTIR spectroscopy. e-Polymers. 2020;20(1):369-81.
6. Campanale C, Savino I, Massarelli C, Uricchio VF. Fourier Transform Infrared Spectroscopy to Assess the Degree of Alteration of Artificially Aged and Environmentally Weathered Microplastics. Polymers. 2023;15(4):911.
7. Ji Y, Yang X, Ji Z, Zhu L, Ma N, Chen D, et al. DFT-Calculated IR Spectrum Amide I, II, and III Band Contributions of N-Methylacetamide Fine Components. ACS Omega. 2020;5(15):8572-8.
8. Vasanthan N, Salem DR. FTIR spectroscopic characterization of structural changes in polyamide-6 fibers during annealing and drawing. J Polym Sci, Part B: Polym Phys. 2001;39(5):536-47.
9. Smith B. Infrared Spectroscopy of Polymers, VIII: Polyesters and the Rule of Three. Spectroscopy. 2022;37:25–8.

# APPENDIX B

## B1 Rationale for Cellular Response Assessment

To complement the physicochemical characterization of aged microplastics presented in Chapter 4, supplementary *in vitro* assays were conducted to determine whether probe-sonication-induced aging resulted in detectable acute cellular responses. These experiments were designed to assess the sensitivity of commonly used short-term cytotoxicity endpoints under environmentally relevant exposure scenarios, rather than to establish detailed toxicity mechanisms.

Given the frequent assumption that aging enhances the biological reactivity of microplastics, evaluating cellular responses provides valuable context for interpreting aging-related physicochemical changes. The results presented here delineate the practical boundaries of acute *in vitro* assays for resolving aging-dependent effects.

## B2 Materials and Methods

### B2.1 Aged Microplastics Preparation

PS, PE, PP, and PET microplastics were used in this study (Table B1). PE (10 μm) and PP (42 μm) were purchased from Polysciences (Warrington, PA, USA); PET (20 μm) was from Chemazone (Leduc, AB, Canada). Aged microplastics were prepared by suspending 50 mg of CMPs in 150 mL of 0.01% polyvinyl alcohol (PVA) solution, followed by thermal aging in an autoclave and probe sonication [1]. All polymers were commercially sourced consumer-grade materials and characterized prior to aging to establish baseline physicochemical and thermal properties.

The aging of PE, PP, and PET microplastics followed the same protocol as that used for the preparation of APS500-S samples described in *Chapter 4, Section 4.1 Materials and Aging Sample Preparation*. Sonication parameters, including power input, duration, pulse settings, sample

concentration, and temperature control, were identical to those reported for APS500-S in Chapter 4 to ensure methodological consistency for direct comparison between materials.

**Table B1** Sources and preparation of microplastic samples for cell work.

| Source Type | Polymer | Material Description | Preparation | Supplier/ Origin |
|---|---|---|---|---|
| **Non-aged microplastics** | PS | Dispersion Ave. 508 nm | Diluted with Milli-Q water to designed concentration | Polysciences Inc. (Warrington, PA, USA) |
| | PE | Powder, ~10 μm | Suspended in 0.01% PVA | Polysciences Inc. (Warrington, PA, USA) |
| | PP | Powder, ~42 μm | Suspended in 0.01% PVA | Polysciences Inc. (Warrington, PA, USA) |
| | PET | Powder, ~20 μm | Suspended in 0.01% PVA | Chemazone Inc. (Leduc, AB, Canada) |
| **Aged microplastics** | PS | Dispersion Ave. 487 nm | Non-aged PS autoclaved and probe-sonicated | Prepared in lab |
| | PE | Suspension Ave. 1.2 μm | Non-aged PE autoclaved and probe-sonicated | Prepared in lab |
| | PP | Suspension Ave. 8.5 μm | Non-aged PP autoclaved and probe-sonicated | Prepared in lab |
| | PET | Suspension Ave. 10.6 μm | Non-aged PET autoclaved and probe-sonicated | Prepared in lab |

*Note: PS (polystyrene), Ave. (average), PE (polyethylene), PP (polypropylene), PET (polyethylene terephthalate), PVA (polyvinyl alcohol).

### B2.2 Cell Culture and Plate Seeding

Human alveolar epithelial cells (A549), human hepatocellular carcinoma cells (HepG2), and murine fibroblasts (NIH3T3) were purchased from the American Type Culture Collection (ATCC, Manassas, VA) and used as representative *in vitro* models to reflect pulmonary exposure, hepatic metabolism, and dermal-associated cellular responses, respectively. A549, NIH3T3 and HepG-2

cells were cultured in Dulbecco's Modified Eagle Medium (DMEM) containing 10% (v/v) fetal bovine serum and 1% (v/v) penicillin–streptomycin (100 U/mL to 100 μg/mL), all purchased from Thermo Fisher Scientific (Mississauga, ON), under standard cell culture conditions (37 °C and 5% $CO_2$). Cells were incubated at $5 \times 10^4$ cells/mL in 96-well plates (Thermo Fisher Scientific, Mississauga, ON) for microplastics exposure experiments. Prior to cell exposure, microplastic dispersions were resuspended and mixed with complete cell culture medium and co-incubated with cells in 96-well plates at final concentrations of ~15 μg/mL.

**B2.3 Cell Viability Assay**

Cell viability was measured using the Cell Counting Kit 8 assay (CCK-8; Dojindo Laboratories, Kumamoto, Japan). After cells were exposed to microplastics for 24, 48, and 72 h, absorbance was measured at 450 nm using a microplate spectrophotometer (BioTek Instruments, Winooski, VT), with a reference wavelength of 600 nm to eliminate MP/NPs light scattering. Cell viability was calculated based on the relative absorbance compared to the control.

**B2.4 Intracellular ROS Quantification**

Intracellular reactive oxygen species (ROS) generation in cells exposed to microplastics was quantified using a ROS assay based on 2′,7′-dichlorofluorescein diacetate (DCFDA), purchased from Abcam, Cambridge, UK. After cells were exposed to microplastics for 24 h, 10 μM DCFDA was added to each well and incubated at 37 °C in the dark for 45 minutes. Cells were then washed twice with phosphate-buffered saline (PBS). Fluorescence signals were measured with excitation/emission wavelengths of 488/525 nm. Normalized DCF fluorescence values were calculated for the exposure group compared to the control group.

### B2.5 Membrane Integrity

Lactate dehydrogenase (LDH) release was used as an indicator of plasma membrane integrity. After cells were exposed to aged PS500 for 24 and 72 h, extracellular LDH levels in the culture medium were quantified using an LDH cytotoxicity assay kit (Abcam, ab65393, Cambridge, UK) according to the manufacturer's instructions. Membrane integrity was calculated based on the relative absorbance of LDH at 450 nm in the treated group compared to the control group.

### B2.6 Statistical Analysis

All assays were performed in triplicate, in independent experiments, and repeated three times in 6-well measurements in each experiment. Results are presented as mean ± standard deviation. Statistical comparisons between control, pristine, and aged microplastic exposures were performed using one-way analysis of variance (ANOVA) and two-way ANOVA employing GraphPad Prism 10.6.1, with $p < 0.05$ considered statistically significant.

## B3 Effects of Pristine and Aged Microplastics on Cell Viability

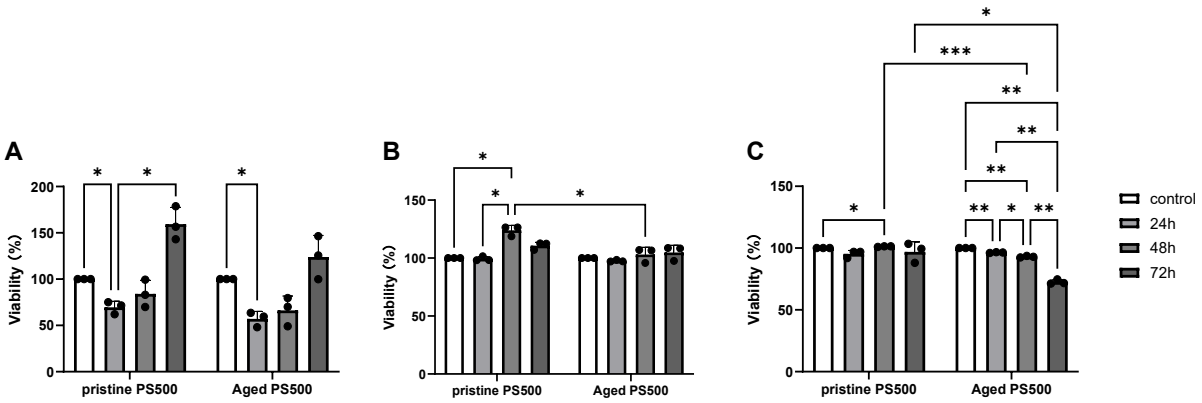


**Figure B1 Cell viability of A549 (A), HepG2 (B), and NIH3T3 (C) cells after treatment with aged PS500 microplastics for 24-, 48-, and 72-hour.** Results are displayed as mean ± SD of three independent experiments (n = 3). Statistical significance was determined with two-way ANOVA. Statistical significance is indicated as follows: *P < 0.05; **P < 0.01; ***P < 0.001; ****P < 0.0001. Only statistically significant differences are displayed in the graphs.

Exposure to 500 nm polystyrene microspheres (PS500) showed distinct, cell-type-dependent responses in cell viability (Figure B1). In A549 cells, pristine PS500 induced a significant reduction in metabolic activity after 24 h of exposure, followed by a recovery toward control levels at 72 h. However, no significant differences were observed between pristine and aged PS500 at corresponding time points (Figure B1A). A similar non-monotonic response was observed in HepG2 cells, where exposure to pristine PS500 increased metabolic activity at 48 h (Figure B1B). Such transient reductions, followed by recovery, have frequently been reported in studies of micro- and nanoplastic exposure. They are commonly attributed to an initial cellular stress response associated with particle uptake, mitochondrial perturbation, or oxidative burden, followed by metabolic adaptation and compensatory repair mechanisms rather than irreversible cell damage [2, 3]. Also, metabolic activity-based assays such as CCK-8 reflect cellular redox capacity and

mitochondrial function, which may recover or even increase during stress adaptation without corresponding changes in cell number [4, 5].

In HepG2 cells, exposure to aged PS500 resulted in significantly lower viability at 48 h compared with pristine PS500 (Figure B1B). A similar trend was observed in NIH3T3 cells, where aged PS500 induced significantly lower viability at both 48 h and 72 h compared to pristine PS500 (Figure B1C), which could be due to altered cell-particle interactions caused by aging-induced surface modifications [6]. In contrast, A549 cells did not exhibit significant viability differences between pristine and aged PS500 across all three exposure times, indicating the aging-induced effects were not uniformly expressed across the three cell models. The stronger response observed in HepG2 and NIH3T3 cells may reflect cell-type differences in metabolic state, stress regulation, and particle-cell interactions rather than particle aging alone. Because aging processes are known to introduce oxygen-containing functional groups and alter surface charge and roughness, these surface changes may modify the protein corona and potentially affect cellular uptake pathways and intracellular processing [7].

However, in a time-dependent manner, NIH3T3 fibroblasts exhibited a different response pattern (Figure B1C), with aged PS500 inducing a progressive, time-dependent decrease in viability that was not observed in A549 or HepG2 cells. This observation is consistent with previous reports showing that non-transformed fibroblast cells often display reduced adaptive capacity and higher sensitivity to prolonged particle-induced stress compared to cancer-derived cell lines, which frequently exhibit greater metabolic plasticity and stress tolerance [8].

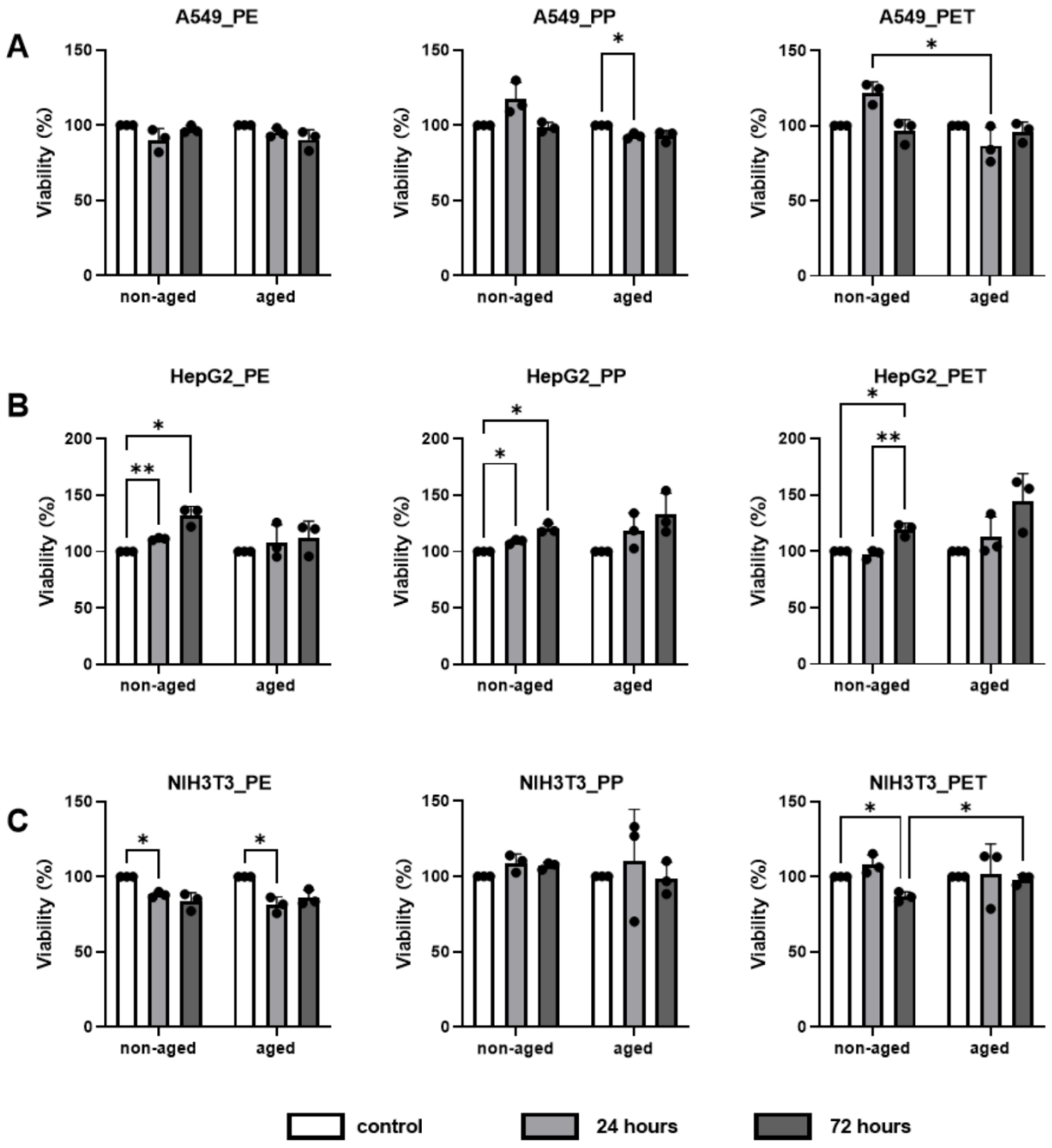


**Figure B2 Cell viability of A549 (A), HepG2 (B), and NIH3T3 (C) cells after treatment with aged PE, PP, and PET microplastics for 24- and 72-hour.** Results are displayed as the mean ± SD of three independent experiments (n = 3). Statistical significance was determined with two-way ANOVA. Statistical significance is indicated as follows: *P < 0.05; **P < 0.01; ***P < 0.001; ****P < 0.0001. Only statistically significant differences are displayed in the graphs.

For PE, PP, and PET in larger sizes, cell viability responses were generally modest (Figure B2). Exposure to PE microplastics did not produce significant differences between pristine and aged particles across cell types. No significant changes in viability were observed in A549 cells after exposure to PE (Figure B2A), whereas in NIH3T3 cells, both pristine and aged PE reduced viability at 24 hours (Figure B2C), without clear aging effects. Notably, in HepG2 cells, non-aged PE and PP produced significantly higher viability than the control at both 24 h and 72 h, but no significant difference was observed between the two exposure times (Figure B2B). This pattern indicates a sustained elevation in metabolic activity after PE and PP exposure rather than a progressive time-dependent increase. By contrast, non-aged PET produced a significant increase in viability at 72 h compared with both the control and the 24 h exposure (Figure B2B), indicating a delayed or time-dependent metabolic response, which is consistent with a previous report suggesting a hepatocyte-specific metabolic or proliferative adaptation rather than a direct cytotoxic response [9]. Also, because the viability assay used in this study is based on WST-8 reduction by cellular dehydrogenase activity, the increased absorbance more likely reflects altered cellular redox metabolism or metabolic adaptation rather than direct evidence of cell growth [10]. PET exposure revealed selective aging- and time-dependent effects, with significant differences between non-aged and aged PET observed only in A549 cells at 24 h and in NIH3T3 cells at 72 h. However, these effects vary strongly with cell model, exposure duration, and particle characteristics [11].

Overall, viability responses were modest across all three polymers. Variability appeared to be driven more strongly by cell type and exposure duration than by polymer chemistry alone. The observed non-monotonic and time-dependent viability patterns suggest that changes in metabolic activity do not necessarily reflect irreversible cytotoxicity. Instead, aging-induced differences in

microplastic-cell interactions appear to preferentially influence early stress responses, including oxidative imbalance and membrane integrity, even as viability signals may remain unchanged. Compared with PS500, the weaker responses to PE, PP, and PET may be partly explained by particle size. PS500 (500 nm) was substantially smaller than the PE, PP, and PET particles (average 9–38 μm), and smaller micro- and nanoplastics are generally reported to show greater cellular internalization and stronger biological responses than larger particles [12, 13]. Larger particles may have had less effective uptake or weaker cell-particle contact, thereby limiting the ability of aging-induced surface changes to translate into measurable viability effects. However, as direct uptake or localization measurements were not performed in this study, the mechanisms remain speculative. Further research incorporating direct measurements of particle uptake and intracellular localization would be valuable for clarifying the mechanisms underlying these cell-type-specific responses.

## B4 Intracellular ROS Generation After 24 h Exposure to Microplastics

Intracellular ROS levels measured by the DCFDA assay after 24 h exposure showed clear cell-type- and polymer-dependent responses (Figure B3).

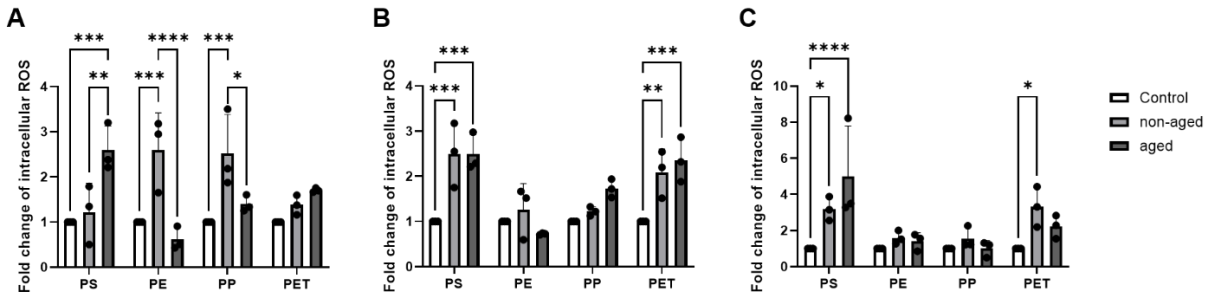


**Figure B3 Intracellular ROS levels measured by the DCFDA assay in A549 (A), HepG2 (B), and NIH3T3 (C) cells after 24-hour exposure to non-aged and aged PS, PE, PP, and PET microplastics.** Data are presented as mean ± SD of three independent experiments (n = 3). Statistical significance was determined with one-way ANOVA followed by Tukey's multiple comparisons test. Statistical significance is indicated as follows: *P < 0.05; **P < 0.01; ***P < 0.001; ****P < 0.0001. Only statistically significant differences are displayed in the graphs.

The clearest aging effect was observed for PS in A549 cells (Figure B3A), where aged PS induced a markedly higher ROS response compared to non-aged PS, reaching more than twice the ROS level of the non-aged group, likely due to aging-induced surface oxidation and defect formation that enhance particle reactivity, strengthen interactions with cellular membranes and proteins, and promote mitochondrial dysfunction-associated ROS generation [14, 15]. It is also reported that aged PS particles can show increased oxidative surface modification and enhanced airway epithelial toxicity [16]. In contrast, non-aged PE and PP showed higher ROS levels than aged particles, with ROS levels in the non-aged groups approximately twofold those of the control, whereas aged PE and PP did not change significantly from the control. One plausible explanation

is that the larger PE and PP particles had limited uptake or weaker effective contact with cells, reducing the extent to which surface changes could translate into intracellular ROS generation. In addition, aging may have altered particle dispersion, surface chemistry, or aggregation behaviour in a way that reduced effective cell exposure. PET exposure did not show a clear aging effect or ROS difference in A549 cells. These results suggest that aging does not universally enhance oxidative stress and may, for certain polyolefins, reduce effective bio-reactivity, potentially due to altered surface chemistry, aggregation behaviour, or reduced release of reactive additives [17].

In HepG2 cells, only PS and PET exposure significantly elevated ROS levels compared with controls, whereas PE and PP did not produce clear ROS changes. The increased ROS of HepG2 cells after exposure to PS and PET is consistent with previous studies that PS and PET can induce oxidative stress and mitochondrial perturbation in hepatic cell models [9, 18]. However, no significant differences were observed between non-aged and aged particles for either polymer, indicating that HepG2 cells responded to selected polymer exposures, but that the response was not primarily determined by aging effects, but by particle exposure. The HepG2 redox and metabolic responses could be activated by the microplastic itself, while any additional aging effects could either not be sufficiently large to produce a distinct ROS difference, or be buffered by cellular antioxidant and metabolic responses [18, 19].

Similarly, in NIH3T3 fibroblasts, PS exposure led to significant ROS elevation with both non-aged and aged particles compared to the control, while no difference was observed between aging states. PET induced a significant increase in ROS only in the non-aged group, whereas aged PET, PE, and PP did not differ from the control. PET particles have been reported to induce oxidative stress in NIH3T3 cells, with the magnitude of the effect strongly dependent on particle characteristics [20]. This pattern suggests that fibroblasts are sensitive to PS-induced oxidative

stress [21], while aging effects on other polymers are limited under the tested conditions. This could also be explained by the size effect because PS has a relatively smaller particle size (500 nm) compared with the other microplastics. Smaller particles provide a higher specific surface area and are more readily internalized, thereby increasing interactions with cells and enhancing oxidative stress responses [22, 23]. Larger particles have limited uptake, weaker cell-particle contact, or altered aggregation state may have reduced effective intracellular exposure [12, 13]. Because antioxidant signalling, mitochondrial function, and particle uptake were not measured in this study, the comparable ROS responses between non-aged and aged particles in HepG2 cells cannot be fully resolved. Future uptake and redox measurements would help distinguish particle exposure effects from aging effects.

Overall, these results indicate that PS is the most consistent inducer of intracellular ROS across all three cell lines, while responses to aging varied. The ROS assay identified polymer- and cell-specific oxidative responses but did not show a universal trend. Distinguishing aging effects from size or uptake effects would require direct particle uptake measurements and mitochondrial function assessment.

## B5 Cell Membrane Integrity is Preserved Following PS Microplastic Exposure

LDH release was measured after exposure only to aged PS for 24 h and 72 h in A549, HepG2, and NIH3T3 cells. No significant difference in LDH release was observed in any of the three cell models (Figure B4), indicating that there is no detectable loss of membrane integrity at the tested doses (~15 μg/mL). It has been reported that micro/nanoplastics can trigger early "stress" endpoints (e.g., ROS or antioxidant signalling) without progressing to membrane rupture, especially at short-term exposures; accordingly, LDH can remain unchanged even when other cellular responses are measurable [24, 25]. Similar *in vitro* studies report no LDH-detectable

cytotoxicity after PS particle exposure in lung epithelial models [25] and no significant LDH release (and no ROS changes) at moderate concentrations in endothelial cells exposed to 1 μm PS microplastics (with effects only emerging at very high doses)[24]. In hepatocyte models, polymer-dependent toxicity is also frequently reported, with some studies observing minimal acute damage for PS compared with other polymers under comparable particle properties [26].

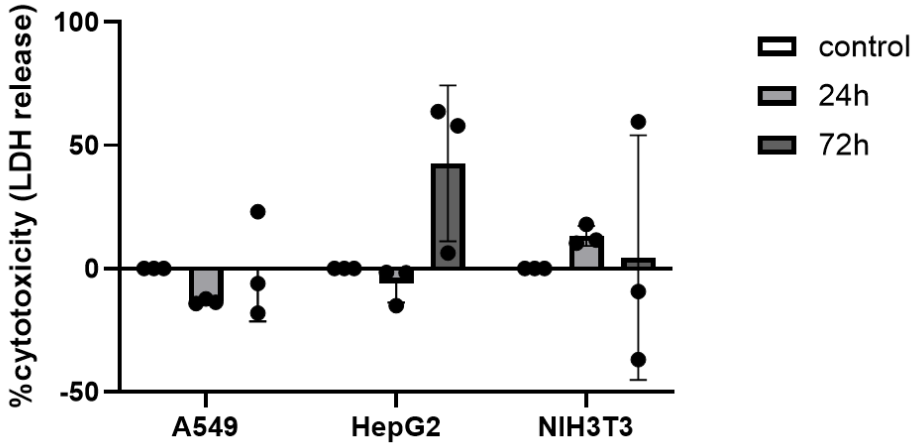


**Figure B4 Membrane integrity reflected by the amount of LDH release in A549, HepG2, and NIH3T3 cells after 24-hour and 72-hour exposure to aged PS500.** Data are presented as mean ± SD of three independent experiments (n = 3). Values near zero indicate no detectable LDH release. Statistical significance was determined with one-way ANOVA. No statistically significant differences are shown within the compared groups in the graph.

## B6 Conclusion

Across the polymers tested, PS produced the most consistent cellular responses across the three cell models (A549, HepG2, and NIH3T3). Aged PS induced the strongest intracellular ROS response in A549 cells and showed aging-induced reductions in cell viability in HepG2 and NIH3T3 cells at later exposure times at 48 h and 72 h. However, no detectable LDH release was measured across three cell models exposed to PS, indicating that these metabolic and oxidative

responses were not accompanied by measurable plasma membrane disruption under the tested conditions. Compared to PS, the larger PE, PP, and PET microplastics produced weaker and less consistent viability and ROS responses, with limited evidence of aging effects. PE and PP did not show increased ROS generation between non-aged and aged microplastics in both HepG2 and NIH3T3 cells. In A549 cells, the aged PE and PP groups produced lower ROS signals than the non-aged particles. The contrast between PS and the larger PE, PP, and PET particles suggests that particle size and effective cell-particle interaction were likely important determinants of the cellular responses. PS (500 nm) was substantially smaller than the other microplastics tested and therefore likely had a higher specific surface area and greater opportunity for cellular interaction. This may explain why PS produced clearer ROS and viability responses, whereas the larger PE, PP, and PET particles showed more limited or inconsistent effects. However, particle uptake, intracellular localization, and aggregation conditions in culture medium were not measured in this study. Therefore, the size effect interpretation should be considered a plausible explanation rather than a confirmed mechanism.

In the context of environmental monitoring and future biological assessment, these results suggest that biologically relevant microplastic exposure should not be prioritized by polymer mass or polymer identity alone. Smaller aged particles may represent a more reactive response because they are more likely to interact with cells, while larger particles with the same nominal mass may produce weaker responses if their effective cellular exposure is limited. Therefore, it is important to take particle size and particle number into consideration. Moreover, surface area measurements, alongside particle accessibility, dispersion behaviour, and protein corona formation, would better describe the amount of reactive microplastic surface available for cell contact, which may be more relevant to biological responses than bulk polymer mass. Finally, the exposure design should move

beyond short-term, single-dose tests. The present assays used an acute exposure at a defined mass concentration, which is useful for comparing particle types but does not capture the repeated or accumulated exposure scenarios more relevant to environmental MPs. Future biological assessment should therefore consider smaller aged microplastics under longer-term or repeated exposures, with dose reported not only by mass concentration but also by particle number, surface area, and delivered cellular dose.

## References


1. Leng Y, Chen M, Cao X, Zou S. Laboratory simulated aging of polystyrene particles and characterization of the resulting nanoscale plastics. J Environ Chem Eng. 2023;11(5):110967.
2. Xie L, Dai Z, Pang C, Lin D, Zheng M. Cellular glucose metabolism is essential for the reduction of cell-impermeable water-soluble tetrazolium (WST) dyes. Int J Biol Sci. 2018;14(11):1535-44.
3. Tan P, Chen B, Xu H, Cai W, He W, Liu M, et al. Co3O4 Nanosheets as Active Material for Hybrid Zn Batteries. Small. 2018;14(21):1800225.
4. Sakamuru S, Attene-Ramos MS, Xia M. Mitochondrial Membrane Potential Assay. In: Zhu H, Xia M, editors. High-Throughput Screening Assays in Toxicology. New York, NY: Springer New York; 2016. p. 17-22.
5. Kroll A, Pillukat MH, Hahn D, Schnekenburger J. Interference of engineered nanoparticles with in vitro toxicity assays. Arch Toxicol. 2012;86(7):1123-36.
6. Brouwer H, Porbahaie M, Boeren S, Busch M, Bouwmeester H. The in vitro gastrointestinal digestion-associated protein corona of polystyrene nano- and microplastics increases their uptake by human THP-1-derived macrophages. Particle and Fibre Toxicology. 2024;21(1):4.
7. Morataya-Reyes M, Villacorta A, Arribas Arranz J, Martín-Pérez J, Ferrer JF, Pastor S, et al. Exploring the impact of nanoplastics on human hepatic cells: dynamics of internalization and harmful effects in HuH-7 cells. Environ Sci Nano. 2025;12(11):4920-34.

8. Palaniappan S, Sadacharan CM, Rostama B. Polystyrene and Polyethylene Microplastics Decrease Cell Viability and Dysregulate Inflammatory and Oxidative Stress Markers of MDCK and L929 Cells In Vitro. Exposure and Health. 2022;14(1):75-85.
9. Najahi H, Alessio N, Venditti M, Lettiero I, Aprile D, Oliveri Conti G, et al. Impact of environmental microplastic exposure on HepG2 cells: unraveling proliferation, mitochondrial dynamics and autophagy activation. Particle and Fibre Toxicology. 2025;22(1):17.
10. Fan J, Schiemer T, Vaska A, Jahed V, Klavins K. Cell via Cell Viability Assay Changes Cellular Metabolic Characteristics by Intervening with Glycolysis and Pentose Phosphate Pathway. Chem Res Toxicol. 2024;37(2):208-11.
11. Kasuske ZA, Roy P, Clouse DE, Pas S, Arole K, Green M, et al. Engineered and Weathered Polyethylene Terephthalate (PET) Microplastics and Nanoplastics Induce Form and Size-Dependent Oxidative Stress, Oxidative DNA Damage, and Cytotoxicity in MCF-7 Cells. Environ Toxicol. 2026.
12. Ruan Y, Zhong Z, Liu X, Li Z, Li J, Sun L, et al. Correlation between cellular uptake and cytotoxicity of polystyrene micro/nanoplastics in HeLa cells: A size-dependent matter. PLoS One. 2023;18(8):e0289473.
13. Li Y, Tao L, Wang Q, Wang F, Li G, Song M. Potential Health Impact of Microplastics: A Review of Environmental Distribution, Human Exposure, and Toxic Effects. Environment & Health. 2023;1(4):249-57.
14. El Hayek E, Castillo E, In JG, Garcia M, Cerrato J, Brearley A, et al. Photoaging of polystyrene microspheres causes oxidative alterations to surface physicochemistry and enhances airway epithelial toxicity. Toxicol Sci. 2023;193(1):90-102.
15. Mahmud F, Sarker DB, Jocelyn JA, Sang Q-XA. Molecular and Cellular Effects of Microplastics and Nanoplastics: Focus on Inflammation and Senescence. Cells. 2024;13(21):1788.
16. El Hayek E, Castillo E, In JG, Garcia M, Cerrato J, Brearley A, et al. Photoaging of polystyrene microspheres causes oxidative alterations to surface physicochemistry and enhances airway epithelial toxicity. Toxicological Sciences. 2023;193(1):90-102.
17. Shelver WL, Billey LO, McGarvey AM, Hoselton SA, Banerjee A. The effects of concentration, duration of exposure, size and surface function of polymethyl methacrylate micro/nanoplastics on human liver cells. Ecotoxicol Environ Saf. 2024;287:117240.

18. Guo M, Li Y, Niu S, Zhang R, Shen X, Ma Y, et al. Oxidative stress-activated Nrf2 remitted polystyrene nanoplastic-induced mitochondrial damage and inflammatory response in HepG2 cells. Environ Toxicol Pharmacol. 2024;106:104385.
19. Kalyanaraman B, Darley-Usmar V, Davies KJA, Dennery PA, Forman HJ, Grisham MB, et al. Measuring reactive oxygen and nitrogen species with fluorescent probes: challenges and limitations. Free Radical Biology and Medicine. 2012;52(1):1-6.
20. Giordano ME, Lionetto F, Lionetto MG. Impact of polyethylene terephthalate nanoplastics (PET) on fibroblasts: a study on NIH-3T3 cells. Frontiers in Physiology. 2025;Volume 16 - 2025.
21. Schmidt A, da Silva Brito WA, Singer D, Mühl M, Berner J, Saadati F, et al. Short- and long-term polystyrene nano- and microplastic exposure promotes oxidative stress and divergently affects skin cell architecture and Wnt/beta-catenin signaling. Part Fibre Toxicol. 2023;20(1):3.
22. Hwang J, Choi D, Han S, Jung SY, Choi J, Hong J. Potential toxicity of polystyrene microplastic particles. Sci Rep. 2020;10(1):7391.
23. Yong CQY, Valiyaveettil S, Tang BL. Toxicity of Microplastics and Nanoplastics in Mammalian Systems. Int J Environ Res Public Health. 2020;17(5).
24. Lu YY, Cao M, Tian M, Huang Q. Internalization and cytotoxicity of polystyrene microplastics in human umbilical vein endothelial cells. J Appl Toxicol. 2023;43(2):262-71.
25. Michelini S, Mawas S, Kurešepi E, Barbero F, Šimunović K, Miremont D, et al. Pulmonary hazards of nanoplastic particles: a study using polystyrene in in vitro models of the alveolar and bronchial epithelium. J Nanobiotechnology. 2025;23(1):388.
26. Ma L, Wu Z, Lu Z, Yan L, Dong X, Dai Z, et al. Differences in toxicity induced by the various polymer types of nanoplastics on HepG2 cells. Sci Total Environ. 2024;918:170664.

# APPENDIX C

## C1 Spatial Heterogeneity of UVC-Induced Chemical Changes in PP Materials Revealed by ATR-FTIR

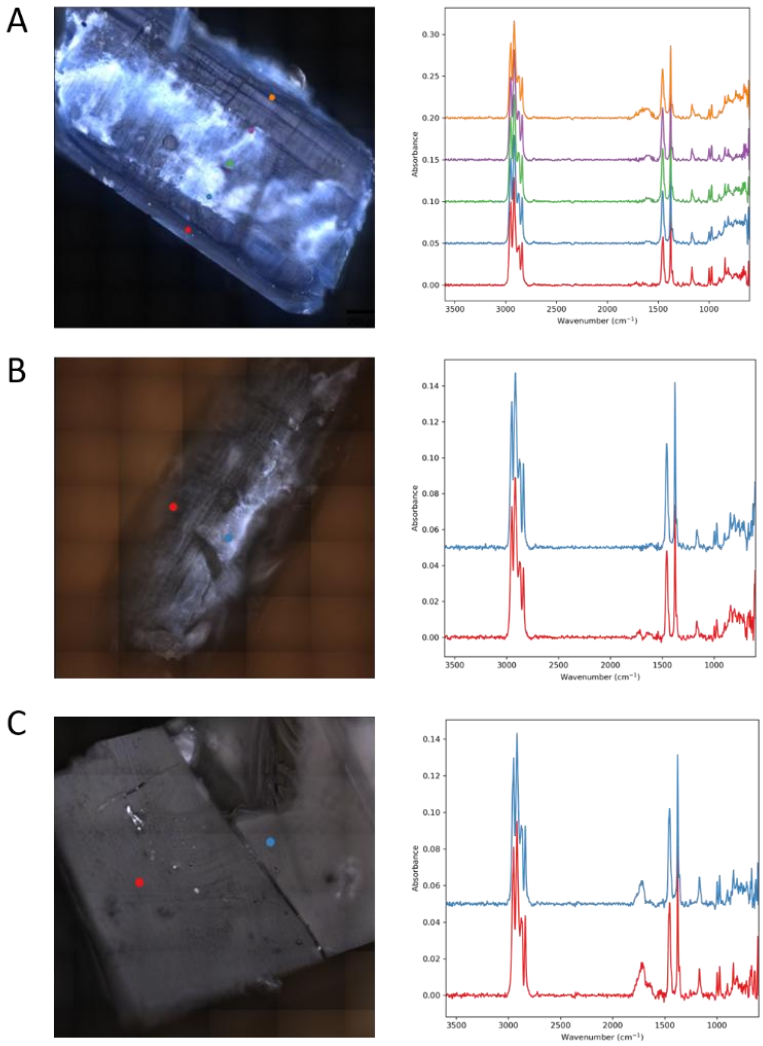


**Figure C1 Optical images of PP materials cross sections and ATR-FTIR spectra collected at selected positions.** (A) PPPB-L interior cross-section with five sampling points from the interior toward the UVC-exposed surface (red = point near the bottom face in contact with the bottle, orange = point near the directly exposed outer surface). (B) PPCT-L interior cross-section with two randomly selected points (red and blue). (C) PPCT-L exterior surface exposed to UVC, with two randomly selected surface points (red and blue). Colored points in the optical images

correspond to the ATR-FTIR spectra of the same colour in the right panels. These points indicate the sampling locations and do not represent the actual spatial extent of the ATR measurement. The blue dashed box highlights the carbonyl band region.

Figure C1 provides additional evidence that UVC-induced oxidation in PP materials was spatially heterogeneous rather than uniformly distributed throughout the particle or material body. ATR-FTIR spectra collected from different cross-sectional positions showed stronger carbonyl signals near the exposed surface and weaker signals toward the interior. This pattern supports a surface-initiated oxidation process, in which chemical modification develops first at the exterior and becomes progressively less pronounced with increasing depth from the exposed surface.

Nevertheless, the surface-to-interior decrease in carbonyl signal supports the interpretation that UVC aging was dominated by surface oxidation, and that particle size and thickness are important controls on the measured aging response.

## C2 Thermal Transition of PPCT and PPPB Across Size Fractions and UVC Exposure Levels

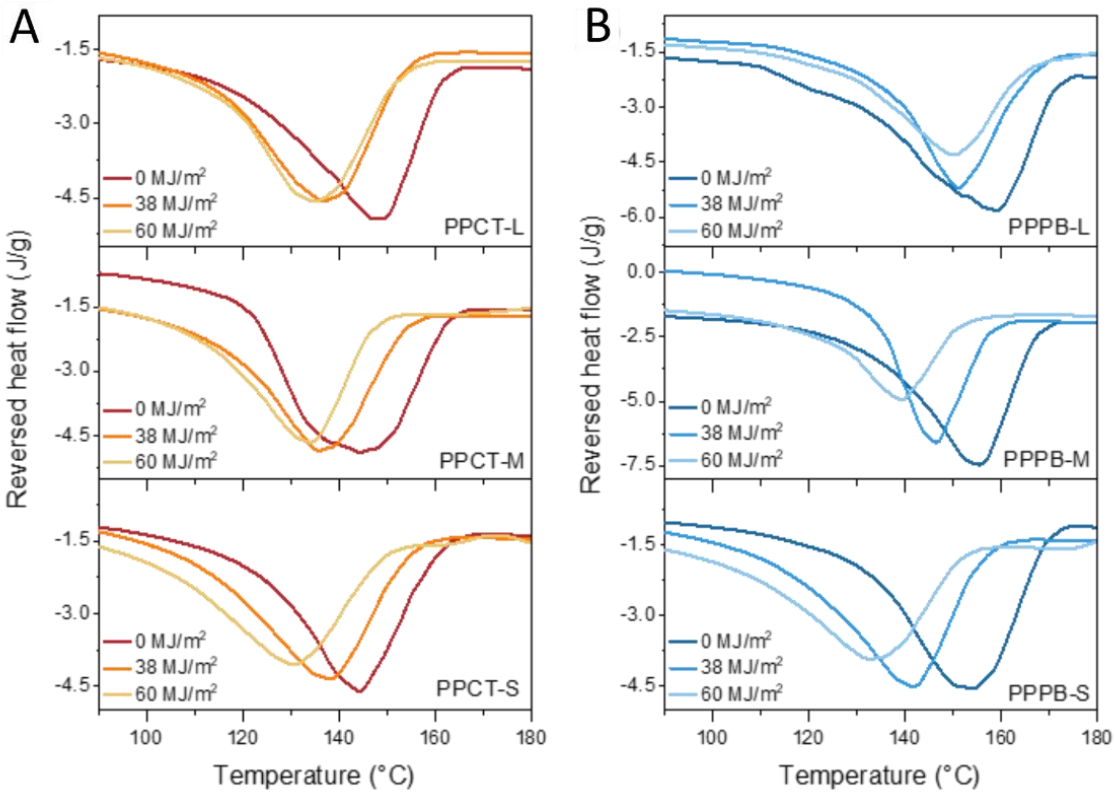


**Figure C2 MDSC thermograms of (A) PPCT and (B) PPPB in large (L), medium (M), and small (S) size fractions at selected UVC exposures of 0, 38, and 60 MJ/m$^2$.**

## C3 Principal Component Structure and Feature Contributions in PCA of Aging Descriptors

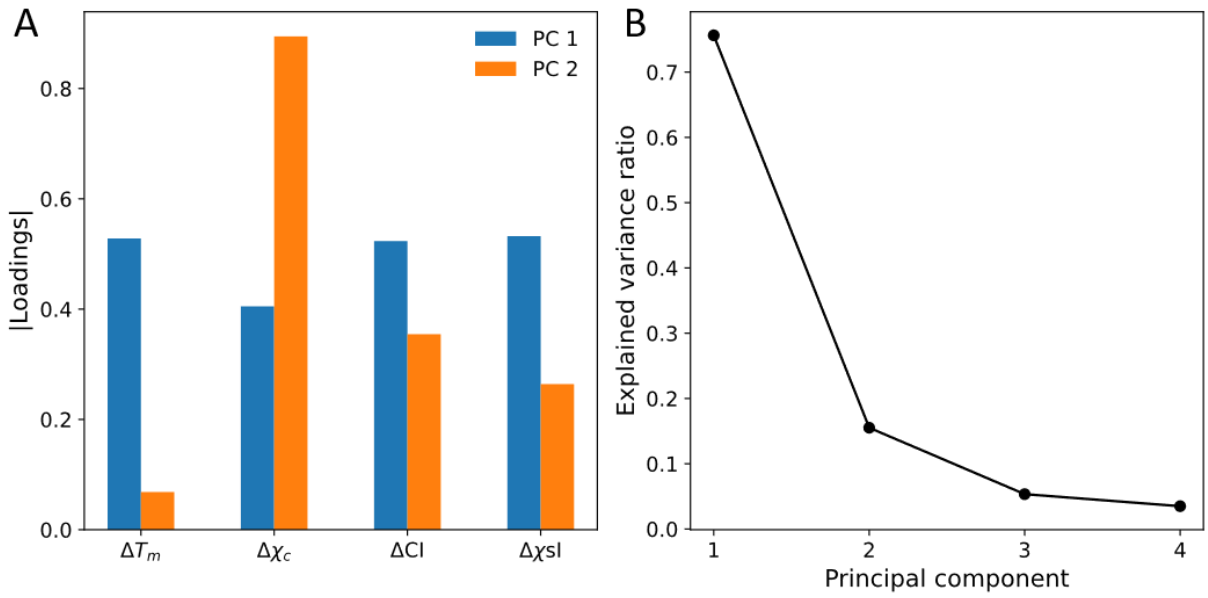


**Figure C3 (A) The loadings of the first 2 principal components (PC), demonstrating the contribution of each feature to the PC. PC1 is influenced by all features, but $\chi_c$ contributes the least, primarily contributing to PC 2. (B) Scree plot of the PCA, demonstrating the explained variance with respect to each principal component.** The PC 1 explains ~75% of the variance, followed by ~15% for PC 2. PC's 3 and 4 explain <10% of the variance and have minimal impact.

## C4 Consistency of Environmental and Lab-aged Microplastics by a PCA-Derived Aging Score

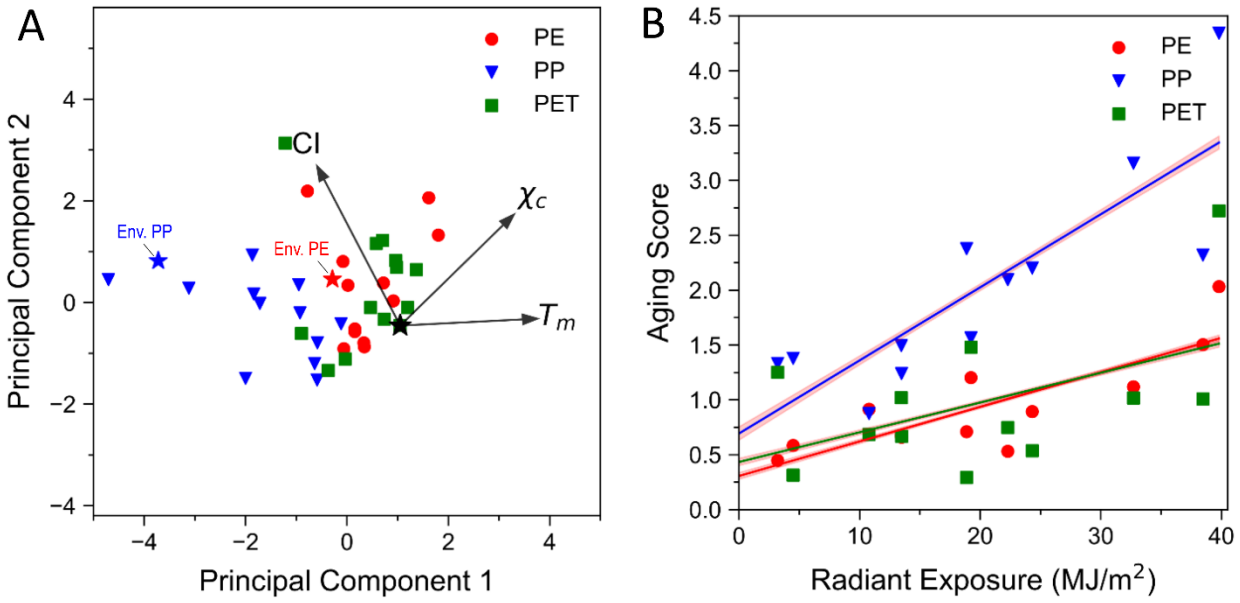


**Figure C4 (A) Principal component analysis of commercial microplastic powders of PE, PP, and PET. The degree of change in each measurement can be used to establish an aging score across different polymers. (B) Aging scores fitted for each plastic.** The red and blue points in (a) marked with stars represent environmental samples of PE and PP, respectively, indicating that their degree of change is consistent with the artificially aged samples. The aging rate of PP was much higher than that of PE and PET.